UNIVERSIDADE DE LISBOA
FACULDADE DE CIÊNCIAS

Microwave Imaging to Improve Breast Cancer Diagnosis

" Documento Definitivo"

Doutoramento em Engenharia Biomédica e Biofísica

Daniela Marques Godinho

Tese orientada por:
Doutora Raquel Cruz da Conceição
Professor Doutor Carlos António Cardoso Fernandes

Documento especialmente elaborado para a obtenção do grau de doutor

2022

UNIVERSIDADE DE LISBOA
FACULDADE DE CIÊNCIAS

Microwave Imaging to Improve Breast Cancer Diagnosis

Doutoramento em Engenharia Biomédica e Biofísica

Daniela Marques Godinho

Tese orientada por:
Doutora Raquel Cruz da Conceição
Professor Doutor Carlos António Cardoso Fernandes

Júri:

Presidente:

- Doutor José Manuel de Nunes Vicente e Rebordão, Investigador Coordenador e Presidente do Departamento de Física da Faculdade de Ciências da Universidade de Lisboa

Vogais:

- Doutora Milica Popovic, Associate Professor, Faculty of Engineering da McGill University (Canadá)
- Doutor Muhammad Adnan Elahi, Lecturer, College of Science and Engineering da National University of Ireland Galway (Irlanda)
- Doutor Nuno Miguel de Pinto Lobo e Matela, Professor Auxiliar, Faculdade de Ciências da Universidade de Lisboa
- Doutora Raquel Cruz da Conceição, Professora Auxiliar, Faculdade de Ciências da Universidade de Lisboa (orientadora)

Documento especialmente elaborado para a obtenção do grau de doutor

Trabalho financiado pela Fundação para a Ciência e Tecnologia (FCT) com a bolsa de doutoramento de referência SFRH/BD/129230/2017

2022

Acknowledgements

This work was possible thanks to the support from Fundação para a Ciência e a Tecnologia-FCT and European Social Fund under the fellowship SFRH/BD/129230/2017, and FCT/MEC (PIDDAC) under the Strategic Programme UID/BIO/00645/2013 and UIDB/00645/2020, and also in part by FEDER-PT2020 partnership agreement under project UIDB/50008/2020. I would also like to acknowledge the support of COST Actions BM1309 (EMF-MED) and CA17115 (MyWAVE) for giving me the opportunity to present my work in international conferences and meetings.

A PhD journey is always intense and full of ups and downs. Mine was also marked by a pandemic and lockdowns, and these last few years have been challenging. This thesis would not have been possible without the help and support of a significant number of people, and I would like to leave a word of appreciation to all of them.

I wish to express my most sincere gratitude to my supervisors Prof. Raquel Conceição and Prof. Carlos Fernandes. Thank you Raquel for everything you taught me, for giving me the opportunity to work with you, for your friendship and kindness, and for all your support. You are truly an inspiration to me, as a professional and as a person! Thank you Prof. Carlos for all the knowledge you shared with me, for introducing me this new world of antennas design, for all your patience during our meetings and your help during this journey. I am also sincerely grateful to João Felício. Although you are not officially my supervisor, I feel like you also are. Your help was crucial during the course of my PhD. Thank you for teaching me all about antennas, for your help with the simulations and measurements, for the conversations during lunch times and your kind support in my highs and lows.

I wish to thank everyone from Hospital da Luz for their collaboration in this work. I thank Nuno André Silva for helping establishing this partnership and introducing me to clinicians and technicians. I thank MD Lurdes Orvalho for receiving me and teaching me how to interpret MRI exams and all medical curiosities regarding breast cancer diagnosis. A special thanks to Tiago Castela, who coordinated the acquisition of MRI exams and was always available to answer my questions and receiving me in the

Hospital. Thank you also for giving up a bit of your time to test new things in MRI with my phantoms. Thanks to all technicians and administratives who helped collecting the exams and providing the medical reports. I would also like to thank Champalimaud Foundation for providing the CT image used to create the axillary region physical phantom used in this thesis.

I would also like to thank the staff of Instituto de Telecomunicações. A special thanks to António Almeida for building the axillary imaging prototype and giving me his support with the measurements and 3D-printing. I would also like to thank Jorge Farinha for his contribution in the creation of the breast imaging prototype.

I also wish to express my gratitude to Instituto de Biofísica e Engenharia Biomédica (IBEB) for serving as my host institution once again and all the people who work there. A special word of appreciation to Nuno Matela for all the support and interesting suggestions during the yearly evaluations.

Now, I would like to thank all my colleagues and friends in IBEB. Thank you Catarina Pelicano and Matteo Savazzi for your company in the lab, during lunch times and virtually, and for your help and motivation during most of my PhD. Thank you also to all internship and master students, specially Inês Jorge, Carolina Silva, Mariya Berezhanska and Catarina Moura, who work(ed) in our lab and contributed to make my days a bit more fresh. Thank you also to Nichal Gentilal for all the lunch invitations and for always making me laugh.

Thank you to all my friends, who supported me during this journey and always cheered me up. Thanks to Ana Simões, Bárbara Lopes and Rafael Simões for your friendship. Thanks to Jéssica Morais, Vera Salgado, Jéssica Costa, Daniela Medley, Jorge Borbinha and João Calisto, who are always very busy and I have only seen once or twice per year in the last few years. Thank you Raquel Almeida, who I missed the most to work with, for your friendship and all the happy memes you send me. Thanks to my long-time friends Cátia Seixas, Mariana Figueira, Paulo Pinheiro and João Lucas Munhão, for making me feel that no matter how much time passes by I can always count on you.

Thank you João for all these years. It is funny that I love you since the start of my PhD. But while my PhD is finished, my love with you is not. Thank you for all your support, for not letting me fall when I stumble in our (few) hikes, for cooking for me, for making fun of me and for letting me making fun of you, for your patience and for your love.

Finally, a special thanks to my family and because of whom I will switch to portuguese so they can understand. Obrigada por todos estes anos de apoio e paciência mesmo não me vendo durante muito tempo - especialmente nestes últimos anos. Obrigada avô Tózinho por todo o apoio durante os anos de escola, por todas as festas quando me vês e por todos os "beijinhooos" enviados por telefone. Obrigada avó Lurdinhas por todas as bolachas, bolos e pudins que sempre anseias me enviar quando te vou

ver. Obrigada por todas as chamadas, preocupação e apoio em todo o meu percurso. Obrigada Mãe por todo o apoio, por todos os passeios, por todos os risos, por todos os choros. Obrigada por seres uma referência para mim de trabalho, de coragem e de força. Obrigada por todos os conselhos e por estares sempre do meu lado.

Abstract

Breast cancer is the most prevalent type of cancer worldwide. The correct diagnosis of Axillary Lymph Nodes (ALNs) is important for an accurate staging of breast cancer. The performance of current imaging modalities for both breast cancer detection and staging is still unsatisfactory. Microwave Imaging (MWI) has been studied to aid breast cancer diagnosis. This thesis addresses several novel aspects of the development of air-operated MWI systems for both breast cancer detection and staging.

Firstly, refraction effects in air-operated setups are evaluated to understand whether refraction calculation should be included in image reconstruction algorithms. Then, the research completed towards the development of a MWI system to detect the ALNs is presented. Anthropomorphic numerical phantoms of the axillary region are created, and the dielectric properties of ALNs are estimated from Magnetic Resonance Imaging exams. The first pre-clinical MWI setup tailored to detect ALNs is numerically and experimentally tested. To complement MWI results, the feasibility of using machine learning algorithms to classify healthy and metastasised ALNs using microwave signals is analysed. Finally, an additional study towards breast cancer detection is presented by proposing a prototype which uses a focal system to focus the energy into the breast and decrease the coupling between antennas.

The results show refraction calculation may be neglected in low to moderate permittivity media. Moreover, MWI has the potential as an imaging technique to assess ALN diagnosis as estimation of dielectric properties indicate there is sufficient contrast between healthy and metastasised ALNs, and the imaging results obtained in this thesis are promising for ALN detection. The performance of classification models shows these models may potentially give complementary information to imaging results. The proposed breast imaging prototype also shows promising results for breast cancer detection.

Keywords: Axillary Region, Breast Cancer, Lymph Nodes, Medical Imaging, Microwave Imaging

Resumo

O cancro da mama é o mais comum em todo o mundo e o mais mortal entre as mulheres. As melhorias dos cuidados de saúde e aumento de campanhas de rastreio do cancro da mama têm mostrado que um diagnóstico precoce e um correto estadiamento são cruciais para reduzir a morbilidade e mortalidade das doentes. Em estadios mais avançados do cancro da mama, as células cancerígenas podem metastizar para os gânglios linfáticos vizinhos, nomeadamente os gânglios linfáticos axilares. O número de gânglios linfáticos afetados pelo cancro da mama é utilizado no estadiamento deste tipo de cancro. Neste sentido, o seu correto diagnóstico é importante para um estadiamento mais exato e para tomadas de decisão de terapêuticas mais ajustadas ao estado clínico. Atualmente, as modalidades de imagem utilizadas, quer para rastreio e deteção do cancro da mama, quer para a análise da existência de metástases na zona axilar, têm algumas limitações. No caso da deteção de metástases nos gânglios linfáticos, o método mais exato de diagnóstico é a Biópsia do Gânglio Sentinela, que é um procedimento cirúrgico, invasivo e que pode resultar na remoção desnecessária de gânglios linfáticos.

A Imagem por Micro-ondas (IMO) é uma técnica emergente de imagem que tem sido estudada nos últimos anos para rastreio e deteção do cancro da mama. É uma técnica de baixo-custo, não-invasiva e que usa radiação não-ionizante, baseada na diferença de propriedades dielétricas entre tecidos. A IMO consiste na iluminação de uma região do corpo com um impulso eletromagnético e a aquisição dos sinais refletidos pelos tecidos por uma ou mais antenas. Os sinais adquiridos são processados, nomeadamente para remoção de artefactos, por exemplo a reflexão da pele que tem uma resposta alta que pode mascarar a resposta dos tecidos de interesse. Grande parte dos protótipos de IMO da mama requerem a imersão da mama num líquido que funciona como um meio de acoplamento entre as antenas e o corpo, reduzindo assim a intensidade das reflexões da pele. No entanto, a utilização deste tipo de líquidos causa atenuação e dificulta a manutenção dos equipamentos e o seu saneamento. Recentemente, têm sido propostos novos protótipos com as antenas a operar em ar. Como consequência, a reflexão da pele tem uma maior amplitude mas estudos recentes mostram que existem algoritmos capazes da sua remoção com sucesso sem afetar a qualidade das imagens.

Esta tese aborda vários aspetos do desenvolvimento de sistemas de IMO sem meio de acoplamento para deteção do cancro da mama e o seu estadiamento.

Num primeiro estudo, é avaliado o efeito da refração em sistemas de IMO onde as antenas radiam em ar. A maior parte dos autores ignora o cálculo da refração entre o ar e o corpo na reconstrução das imagens e a consequência desta escolha na qualidade das imagens não tinha sido ainda quantificada. Neste estudo, o cálculo da refração é considerado utilizando algoritmos analíticos e de traçado de raios, dependendo da complexidade do fantoma considerado. Os efeitos de refração são avaliados variando parâmetros como a forma de propagação das ondas eletromagnéticas (esféricas ou planas), valores de permitividade relativa, tamanhos dos alvos, número de antenas e utilizando fantomas com diferentes graus de irregularidade. Os resultados com as imagens reconstruídas, considerando e não considerando refração, mostram que existem regiões cegas que podem afetar a deteção dos alvos perante ondas planas, ou perante ondas esféricas e meios com permitividade relativa alta. O tamanho dos alvos e número de antenas não influenciam o impacto do cálculo da refração na qualidade da imagem. As diferenças entre as imagens com e sem refração são negligenciáveis para valores de permitividade relativa do meio mais baixos, o que indica que o cálculo da refração pode ser ignorado, evitando um aumento do custo computacional desnecessário.

Posteriormente, é apresentado o tópico principal de investigação desta tese que visa o desenvolvimento de um sistema de IMO para diagnosticar os gânglios linfáticos axilares. Os estudos incluem a criação de fantomas antropomórficos, o estudo das propriedades dielétricas, o estudo experimental de imagem com condições realistas para deteção dos gânglios e a avaliação do potencial de algoritmos de classificação com o propósito de diagnosticar gânglios linfáticos.

A existência de fantomas antropomórficos com uma representação o mais exata possível das propriedades dielétricas dos tecidos é importante para a validação dos sistemas de IMO. Esta informação é ainda limitada na literatura e, nesse sentido, foi desenvolvida uma metodologia de processamento de exames de Imagem por Ressonância Magnética (IRM) com o objetivo de criar fantomas numéricos da região axilar e de inferir informação sobre as propriedades dielétricas dos gânglios. A estimativa das propriedades dielétricas baseia-se na hipótese das intensidades mais altas dos voxeis das imagens utilizadas estarem relacionadas com uma maior quantidade de água e, consequentemente, propriedades dielétricas mais elevadas. A estimativa das propriedades é efetuada para 100 gânglios linfáticos, tendo como base curvas de propriedades dielétricas já existentes na literatura e assumindo uma relação linear entre a intensidade dos voxeis e as propriedades dielétricas. A metodologia é validada em IRM com um fantoma impresso em 3D preenchido com líquidos com propriedades dielétricas conhecidas. Os resultados mostram um contraste dielétrico de 32% entre gânglios saudáveis e metastizados. Por outro lado, a validação com o fantoma mostra que os valores de contraste e das propriedades dielétricas podem encontrar-se sub-estimados.

Poucos estudos analisaram a utilização da IMO para fazer imagem da zona axilar,

focando-se apenas em simulações 2D. Um novo protótipo de IMO é avaliado em simulação 2D e posteriormente experimentalmente, considerando um cenário pré-clínico com uma configuração 3D. O protótipo é testado com um fantoma da zona axilar impresso em 3D correspondendo a uma situação em que a doente se encontra deitada de lado, com o braço estendido, e onde as antenas fazem um varrimento cilíndrico. O presente estudo apresenta as limitações de posicionamento das antenas, uma vez que não é possível fazer um varrimento em 360°, e os efeitos das concavidades e convexidades da região axilar dificultam a remoção dos artefactos. São apresentados os algoritmos adaptados para esta aplicação médica que incluem o algoritmo Decomposição em Valores Singulares (DVS) como algoritmo de remoção de artefactos (e otimização dos seus parâmetros), um filtro espacial que pretende restringir a região de interesse e que pode ser definido utilizando informação específica da doente e a escolha de antenas para cada algoritmo. São testadas experimentalmente quatro posições de um gânglio dentro do fantoma axilar. Os resultados mostram uma boa deteção com um rácio sinal-ruído de 2,77 dB e um erro de localização menor que 14,7 mm. Os resultados são promissores para a deteção dos gânglios com IMO mas são necessários mais testes para avaliar a robustez dos métodos apresentados.

As imagens resultantes do IMO podem ser complementadas com informação objetiva retirada dos modelos criados com algoritmos de aprendizagem automática utilizando sinais micro-ondas. Neste contexto, é efetuado um estudo de classificação entre gânglios linfáticos saudáveis e metastizados utilizando vários cenários em simulação. São considerados sessenta modelos de gânglios tendo em conta características reportadas na literatura, como o tamanho e forma. Quatro cenários são simulados com crescente nível de complexidade. Nos primeiros três cenários, apenas um gânglio é considerado dentro de um dielétrico, enquanto que no último cenário dois gânglios são considerados. São simuladas várias posições de antenas e os sinais gravados são utilizados para classificação. São testados vários tipos de sinais, extração de características e classificadores. O desempenho dos classificadores nos primeiros três cenários é semelhante, com exatidão superior a 90%, falhando apenas a classificação de 1 gânglio. Já quando vários gânglios são considerados, a distinção de uma zona axilar saudável de uma com gânglios metastizados é mais desafiante, falhando a classificação de 1 a 8 casos. Ainda assim, os resultados são promissores e mais níveis de complexidade devem ser considerados.

Um último estudo apresenta o potencial de um novo protótipo para IMO da mama que utiliza um sistema de focagem com uma lente dielétrica com o intuito de diminuir o acoplamento entre antenas e aumentar a energia transmitida para a mama. O protótipo consiste num emissor e uma lente por baixo da mama, que emitem um pulso eletromagnético, e uma ou mais antenas colocadas num plano coronal à volta da mama, que gravam o sinal transmitido. O protótipo proposto é testado com fantomas da mama com diferentes complexidades em simulação e experimentalmente. O algoritmo DVS é

também utilizado para remover os artefactos. É testada a possibilidade de focar certas regiões da mama com o feixe gerado pela lente e é feito um estudo de comparação da mesma configuração do protótipo com e sem lente. Os resultados são promissores para ambos fantomas homogéneos e heterogéneos da mama. A deteção de mais do que um alvo é melhorada quando a zona do alvo é iluminada pelo feixe. No entanto, mais estudos são necessários para encontrar uma evidência clara da vantagem deste protótipo em relação a outros com o mesmo propósito.

De uma forma geral, o trabalho desenvolvido mostra o potencial do desenvolvimento destes sistemas de IMO para diagnóstico dos gânglios linfáticos e deteção do cancro da mama.

Palavras-chave: Axila, Cancro da Mama, Gânglios Linfáticos, Imagem Médica, Imagem por Micro-ondas

Contents

List of Figures

List of Tables

Acronyms

ALN	Axillary Lymph Node
ALND	Axillary Lymph Node Dissection
BCS	Breast-Conserving Surgery
BI-RADS	Breast Imaging-Reporting and Data System
BMI	Body Mass Index
CNC	Computer Numerical Controlled
CR-DAS	Channel-Ranked Delay-And-Sum
CST	Computer Simulation Technology
CT	Computed Tomography
DAS	Delay-And-Sum
DE	Distance Error
DMAS	Delay-Multiply-And-Sum
DNA	DeoxyriboNucleic Acid
DT	Decision Trees
DWI	Diffusion-Weighted Imaging
EPT	Electrical Properties Tomography
FD	Frequency Domain
FEM	Feature Extraction Method
fl3D	Fast Low Angle Shot 3D
FNR	False Negative Rate
FWHM	Full Width Half Maximum
GMM	Gaussian Mixtures Model
IBEB	Instituto de Biofísica e Engenharia Biomédica/Institute of Biophysics and Biomedical Engineering

ICNIRP International Commission on Non Ionizing Radiation Protection
IDAS Improved Delay-And-Sum
IFFT Inverse Fast Fourier Transform
IT Instituto de Telecomunicações Lisboa/Institute of Telecommunications Lisbon
ITK Insight Toolkit

kNN k-Nearest Neighbours

LDA Linear Discriminant Analysis
LE Localisation Error

MCC Matthews Correlation Coefficient
MDAS Modified Delay-And-Sum
ML Machine Learning
MMR Maximum Magnitude Ratio
MPR Multiplanar Reconstruction
MR Magnetic Resonance
MRI Magnetic Resonance Imaging
MWI Microwave Imaging

NB Naïve Bayes

OECP Open-Ended Coaxial Probe

PCA Principal Component Analysis
PEC Perfect Electric Conductor
PET Positron Emission Tomography
PLA Polylactic Acid
PLRM Polynomial Linear Regression Model
PP Polypropylene

QDA Quadratic Discriminant Analysis

RBF Radial Basis Function
RF Radio Frequency
RFO Random Forests
RT Radiation Therapy

SAR Specific Absorption Rate
SCR Signal-to-Clutter Ratio
SLNB Sentinel Lymph Node Biopsy
SMR Signal-to-Mean Ratio
SPAIR SPectral Attenuated Inversion Recovery
STIR Short-Time Inversion Recovery
SVD Singular Value Decomposition
SVM Support Vector Machines

T_1-w T_1-weighted
T_2-w T_2-weighted
TD Time Domain
TE Echo Time
TR Repetition Time
TSE Turbo Spin Echo

US Ultrasound
UWB Ultra-Wide Band

VIBE Volumetric Interpolated Breath-hold Examination
VNA Vector Network Analyser
VOI Volume of Interest

XETS Crossed Exponential Tapered Slot Antenna

1 | Introduction

1.1 Context

Breast cancer is the most common cancer worldwide (Figure 1.1), with approximately 2.26 million new cancer cases in 2020 [1]. It is also the fifth deadliest cancer, with a position that has been decreasing in the past few years, mainly due to the increased awareness of early screening and improvement of diagnosis techniques.

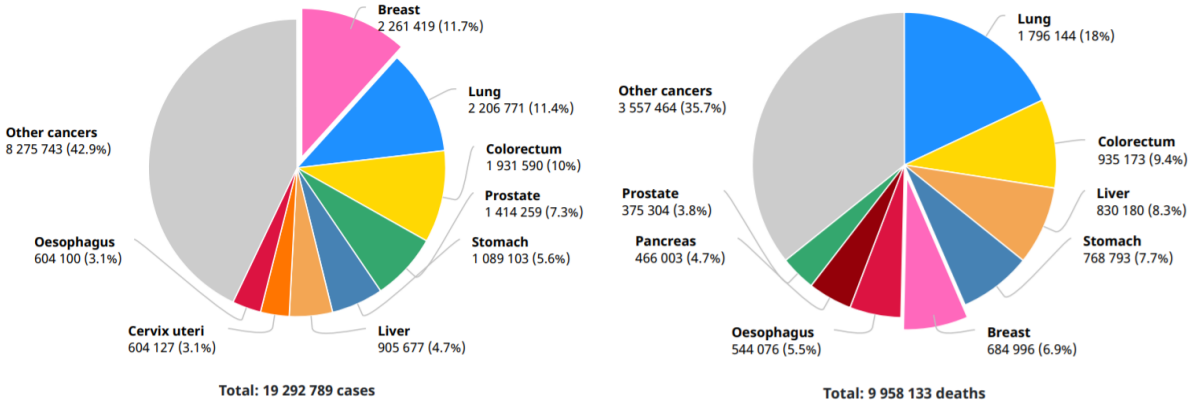

(a) New cases (b) Number of deaths

Figure 1.1: Estimated number of cancer cases in 2020, worldwide, all cancers, both sexes, all ages [1]. New cases are presented on the left and number of deaths on the right.

Both early breast cancer detection and correct breast cancer staging are important to ensure low mortality and/or morbidity among breast cancer patients and survivors. The dissemination of breast cancer cells to other parts of the body has a substantial impact on five-year survival rates. When breast cancer is diagnosed and cancer cells are still constrained in the breast region, the survival rate is around 95%. However, in 30% of invasive breast cancer cases, the tumour can drain cancer cells to surrounding lymph nodes, such as the Axillary Lymph Nodes (ALNs) [2]. In those cases, the survival rate can decrease by about 10%. In more advanced stages, when breast cancer cells have spread to other parts of the body, patients have a survival rate of approximately 30%. The treatment approaches highly depend on the cancer staging (Figure 1.2). It can vary from a more conservative approach using Breast-Conserving Surgery (BCS) and Radiation Therapy (RT), to mastectomy and chemotherapy. An incorrect breast

cancer staging can jeopardize the adoption of the correct treatment and have an impact on the patient's health and an economic impact on the healthcare system. Therefore, there has been an effort to continuously improve breast cancer detection and staging, while optimising current diagnosis techniques or developing other techniques based on emerging technologies.

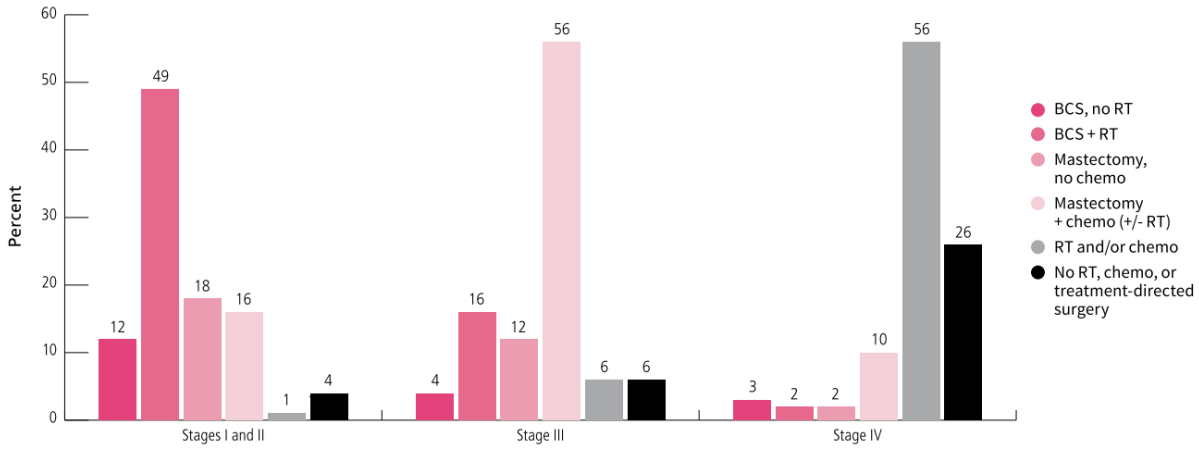

Figure 1.2: Breast cancer treatment approaches by type of cells dissemination in the United States from 2009 to 2015 [3]. BCS means Breast Conserving Surgery, RT means Radiation Therapy and Chemo stands for chemotherapy, targeted therapy and immunotherapy.

1.2 Current Screening Assessment

Currently, breast cancer screening is assessed using medical imaging modalities such as X-Ray mammography, Ultrasound (US), Computed Tomography (CT), Magnetic Resonance Imaging (MRI) or Positron Emission Tomography (PET). The assessment of the dissemination of breast cancer cells to lymph nodes is often performed, in a first stage, during breast cancer screening using imaging modalities. When a breast tumour is found, more detailed evaluation may be needed. The adopted imaging methods vary among institutions, their own protocols and available equipment [4].

X-Ray mammography and US are low-cost techniques and are widely used for mass-screening. X-Ray mammography relies on low-energy X-rays which are transmitted towards the breast and result in images reconstructed based on the contrast in X-ray attenuation between tissues. The main disadvantages of using X-Ray mammography is the required breast compression which causes patient discomfort, and the associated health risks of using ionising radiation. Also, the sensitivity (rate of tumours correctly identified) is not satisfactory, mainly for patients with denser breasts where sensitivity is reported to be around 63.2% [5], [6]. This means the false negative results can delay the detection of breast cancer and ultimately affect treatment efficiency. The specificity (rate of healthy tissue correctly identified) has a larger variability, ranging from 57.9% to 98.8% [5], [6]. X-Ray mammography is very limited in terms of ALNs screening since

only part of the axillary region is imaged, and its sensitivity ranges from 21% to 38.9% [7], [8].

US is based on sound waves and is often used to complement and/or confirm the observations of X-Ray mammography screening and to guide biopsies. Recently, automated imaging systems have been adopted for mass-screening [9] but the evaluation of suspicious masses with US is still user-dependent. Both sensitivity and specificity of US are higher compared to X-Ray mammography but they are still not satisfactory (sensitivity of 75.3% and specificity of 96.8% in denser breasts [5]). US can also be used to evaluate the whole axillary region and assess suspicious ALNs when a breast tumour is detected [10], as well as to guide biopsies in a technique called US-Guided Biopsy [11]. Studies report a large range of specificity and sensitivity values of US in the context of ALNs diagnosis, ranging from 55% to 97%, and from 49% to 87%, respectively [8], [12], [13]. US-Guided Biopsy has high specificity and could avoid additional procedures in 30% of the cases [14], but sensitivity is not satisfactory.

MRI and PET are imaging modalities with higher costs. MRI uses strong magnetic fields and radio waves to create high contrast and high spatial resolution images. It is more sensitive than US, with sensitivity values that can range from 88% to 100% [15], [16] but specificity has higher variability depending on the used sequences, ranging from 37% to 97% [15], [16]. MRI is particularly useful to determine the tumour extent and to evaluate dense breasts. The screening of the axillary region and the internal mammary lymph nodes with MRI is also addressed [17], [18]. However, the high-cost of MRI limits its usage by the overall population. It is also a time-consuming image modality and might be uncomfortable to claustrophobic patients. PET is a functional imaging technique which requires the use of radioactive agents to increase the contrast between healthy and diseased tissues. It is mostly used in more advanced breast cancer stages with suspicious metastases, in cases where the benefit-cost ratio is higher [19].

Recent studies show that these imaging modalities should be complementary for better assessment of ALN diagnosis [8], [13]. However, ALNs diagnosis using currently available imaging modalities is still unsatisfactory in terms of sensitivity and specificity, which can lead to incorrect breast cancer staging and negatively impact therapeutic decisions. The most accurate procedure to diagnose ALNs is the Sentinel Lymph Node Biopsy (SLNB). Several clinical trials showed 94% accurate identification rate of the sentinel node, the first lymph node receiving drainage from the tumour, and sensitivity around 80% to 90% [20]–[22]. SLNB is a procedure where the sentinel node is surgically removed to be analysed by pathologists, as exemplified in Figure 1.3. A radioactive substance and/or a dye are injected in the place where the tumour was excised, and the chemicals follow the drainage path until reaching the sentinel lymph node. Once the sentinel node is found, it is excised and sent to pathological analysis. In case of a positive result, i.e. metastasised ALN, Axillary Lymph Node Dissection (ALND) may be performed [23], [24]. ALND consists of the partial or complete removal of ALNs.

Despite the fact that SLNB has high sensitivity, a positive result does not mean that the remaining nodes are also metastasised, and the removal of more ALNs may be pre-emptive. The removal of too many lymph nodes can lead to patients' slower physical recovery, increase the risk of infection [25], lymphedema [26], and/or paraesthesia [25]. The reported morbidity associated with ALND is high when compared to SLNB [27], and ultimately, it is only used as a last resort. In case of negative SLNB, which is reported to be around 70% of the cases [28], [29], no additional procedure is performed which means the patient underwent an unnecessary surgical procedure. The False Negative Rate (FNR) of SLNB is approximately 10% [30], which is still unsatisfactory.

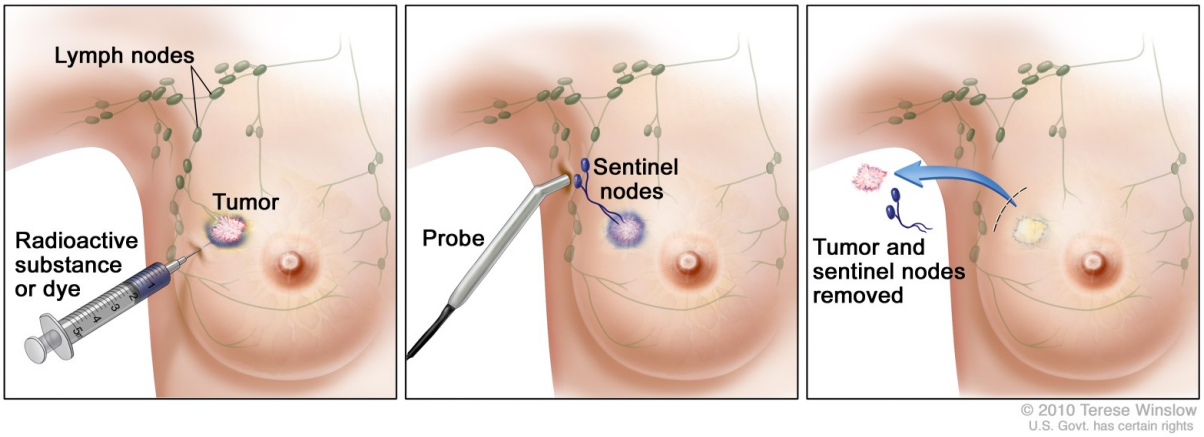

Figure 1.3: Procedure of the Sentinel Lymph Node Biopsy performed during Breast-Conserving Surgery. A radioactive substance or dye is injected in the tumour (first image), a probe is used to identify the sentinel nodes (second image), the tumour and sentinel nodes are removed for biopsy (third image).

Recent clinical studies [31], [32] have questioned the use of SLNB and mainly, ALND, and surgical approaches have been changing. Thus, the improvement of current modalities and the development of new complementary techniques is focused to provide minimally-invasive diagnoses. Furthermore, these complementary techniques are of great of importance to increase the accuracy of breast cancer detection and ALN diagnosis, leading to more accurate breast cancer staging.

1.3 Research Motivation

Microwave Imaging (MWI) is an emerging technique which has shown potential to early detect breast cancer [33]–[35], brain strokes [36], and to monitor bone health [37]. It is a low-cost technique which has some advantages when compared to other imaging modalities, since it uses non-ionising radiation, it does not need compression and it uses low-power [38], [39]. MWI is based on the differences of dielectric properties of tissues at microwave frequencies, typically from 500 MHz to 8 GHz. Cancer detection with MWI relies on the increase of vascularisation of cancerous tissues [40], which result in higher dielectric properties. MWI techniques can generally be divided in

three categories: Ultra-Wide Band (UWB) radar, tomography and holography [41]. The body region of interest is typically illuminated with an electromagnetic pulse and the resulting backscattered signals are recorded by antennas. In UWB radar, these signals are used to create an intensity profile with a reconstruction algorithm, allowing to detect potential tumours which are expected to yield high-intensity regions [42]. Both microwave tomography and holography involve solving forward and inverse scattering problems to represent the dielectric properties of tissues.

The main disadvantage of MWI is its limited resolution and low specificity which often results in many high-intensity regions in the resulting image, which may or may not correspond to tumours [43], [44]. Nonetheless, MWI is a promising technique, still under development and in clinical trials phase for breast cancer detection [34], [35], [45]. Its low-cost and user-independency endorses its implementation within breast screening protocols, specially in developing countries where access to high quality healthcare conditions may be limited. In this context, MWI has the potential to replace more expensive imaging modalities in early stages of diagnosis. In other contexts, it may be used as a complementary imaging modality.

In more advanced stages of development and validation of breast MWI prototypes, the breast is immersed in a liquid which serves as a coupling medium between the breast and the antennas to minimise the skin reflections and enhance the inner tissues detection. However, this liquid attenuates the transmission signals, imposes sanitation issues, patient discomfort, and the maintenance of the system is harder [41]. Recently, several air-operated radar systems with promising results have been presented where the antennas are in contact or a few centimetres away from the skin. Porter *et al.* [46] presented a low-cost wearable device with an antenna array placed in contact with the skin. Although promising results were showed compared to a conventional prototype where the patient is lying on the table with the breast immersed, no tumour detection studies were performed. Recently, Adachi *et al.* [47] validated a hand-held portable MWI device without the need of immersion liquid in 10 breast cancer cases. Additionally, some other authors have presented systems with antennas placed a few centimetres away from the skin [45], [48]–[51]. Felício *et al.* [49] showed that the absence of a coupling liquid can increase skin response up to 8 dB but it does not substantially affect the image quality.

In addition to the above mentioned limitations of using a coupling liquid, when imaging a part of the body such as the axillary region, immersing the body in a liquid is no longer practical. The first study using MWI to aid breast cancer staging through the detection of ALNs was presented by Eleutério *et al.* [52], [53]. The authors performed a 2D feasibility study using a planar antenna array with 17 elements placed over the skin. Several scenarios with 2D ALN numerical phantoms embedded in a uniform layer of adipose tissue were simulated. The results showed a good detection of isolated lymph nodes and a good distinction between healthy and metastasised ALNs. When a muscle

tissue was added, the detection was more challenging, due to the similar dielectric properties between ALNs and muscle. Liu *et al.* [54] also addressed the relevance of axillary MWI imaging and proposed using a planar configuration in future work, but they did not provide too much detail. Recently, Savazzi *et al.* [55], [56] presented a 2D numerical study with an anthropomorphic phantom corroborating the observations of Eleutério *et al.* [52], [53] regarding the challenges of detecting ALNs in the presence of muscle. Although these authors showed promising results, these were based on simulations in a 2D-geometry. Also, information regarding dielectric properties contrast between healthy and metastasised ALNs is still limited and inconclusive [55], [57], [58]. Therefore, a more detailed study with 3D configurations and anthropomorphic phantoms, and real measurement setups have yet to be completed.

Although all these authors proved the feasibility of air-operated systems with promising results for breast cancer detection and staging, there are some points which need to be addressed. The work developed in this thesis aims to contribute to the development of air-operated MWI radar systems to aid breast cancer staging through ALNs detection and also to breast cancer detection with a novel antenna configuration.

Firstly, this thesis addresses a gap in the literature regarding air-operated MWI systems, with relevance to different microwave medical applications:

- Evaluation of refraction effects at the air-body interface in MWI air-operated systems, since refraction calculation is computationally heavy and might hinder real-time image reconstruction.

The main topic of this thesis is the development of a MWI radar system to image the axillary region and detect and diagnose level I ALNs, the first nodes receiving drainage from the tumour, and comprises the following sub-topics:

- Creation of 3-D anatomically realistic phantoms of the axillary region, which were not available in the literature, with a real representation of ALN shapes, sizes and positioning;
- Estimation of dielectric properties of ALNs to improve the current knowledge on contrast between healthy and metastasised lymph nodes and to assess the feasibility of MWI for ALNs diagnosis;
- Experimental evaluation of the MWI prototype, which includes the definition of a valid examination positioning of the patient, antenna positioning and handling the inherent constraints of a real measurement setup;
- Development of dedicated algorithms for the axillary region application, both for artefact removal and image reconstruction;
- Evaluation of the feasibility of machine learning algorithms to inform and/or complement the information given by traditional microwave images.

Finally, one preliminary study of a new antenna configuration for breast cancer detection is presented, assessing relevant topics in the development of air-operated MWI systems:

- Minimisation of coupling between antennas in multistatic systems (systems with more than one radiating antenna), which can decrease the energy coupling to the breast and hamper the correct target detection;
- Maximisation of energy coupling to the breast by reshaping the antenna beam for enhanced illumination of the breast, in order to improve the detection;
- Increase spatial cross-range resolution with minimal increase of number of antennas.

1.4 Thesis Structure

The work included in this thesis was developed in Instituto de Biofísica e Engenharia Biomédica/Institute of Biophysics and Biomedical Engineering (IBEB) and Instituto de Telecomunicações Lisboa/Institute of Telecommunications Lisbon (IT) - Lisbon, with clinical collaborations with Fundação Champalimaud and Hospital da Luz Lisbon. The remainder of this document is organised as follows:

Chapter 2 presents a detailed review of the background of the work developed during this thesis, covering several distinct topics. Firstly, the anatomy of the breast and the differentiation between types of breast cancer are described. Secondly, the chapter presents the ALNs anatomy and the imaging features of ALNs described in the literature using current imaging modalities. Then, the concepts regarding the MWI technologies are described, highlighting some state-of-the-art MWI systems, how an electromagnetic exposure safety evaluation can be performed, artefact removal and image reconstruction algorithms. Then, the development of realistic phantoms for MWI validation is reviewed, including the different types of anatomically realistic phantoms, the state-of-the-art of both breast and ALNs dielectric properties, as well as the main concepts of MRI and the image processing algorithms which can be used to create anatomical phantoms from Magnetic Resonance (MR) images. Finally, the chapter describes the state-of-the-art of work regarding the classification of targets using MWI signals, and the commonly used feature extraction methods and classifiers.

Chapter 3 includes a study with relevance for several MWI applications. The refraction effects in MWI reconstructed images are analysed in order to evaluate when refraction computation can be avoided in air-operated MWI systems. To this end, refracted ray paths are calculated in spherical and more realistic shapes using different algorithms. The spherical phantom is used to test several combinations of parameters:

average relative permittivity, targets size and number of antennas. The realistic shapes are used to validate the conclusions drawn when using the spherical phantom.

The following three chapters comprise essential studies for the development of the MWI system to image the axillary region. **Chapter 4** proposes an imaging processing pipeline to create anatomically realistic phantoms of the axillary region and extract approximate dielectric properties of ALNs from MR images. The used MRI dataset is detailed and the step-by-step methodology and corresponding results are presented. An analysis of the estimated dielectric properties of ALNs is presented, considering 100 ALNs from 50 female patients. The resulting repository of axillary region phantoms is also described. The chapter finishes by presenting the validation of proposed methodology with a physical phantom with known dielectric properties in an MRI scanner.

Chapter 5 firstly presents a simulation-based study with 2D different shapes to mimic the axillary region, showing the challenges of artefact removal algorithms. Then, the first experimental prototype developed for imaging the axillary region using MWI technology is presented. The 3D-printed axillary region phantom used for the performed tests is detailed regarding the used tissue mimicking materials, the antenna and the measurement setup. The algorithms adopted for imaging the axillary region and detecting ALNs are detailed and the results are presented and discussed. Lastly, one of the proposed algorithms is tailored using patient-specific information collected from MRI exams, which is meant to improve the imaging results in a clinical scenario.

Chapter 6 proposes a complementary methodology based on machine learning algorithms to assess the diagnosis of ALNs with an MWI system. It describes how the ALN phantoms were created and simulated in several scenarios. These scenarios are presented with increased complexity, starting from a simplified case with homogeneous medium until an approximate realistic axillary region phantom with multiple ALNs. The classification pipeline is described. Lastly, classification results are presented and discussed.

Then, as a contribution to breast cancer detection, **Chapter 7** presents a preliminary study of a new breast MWI setup which uses a dielectric lens to focus the energy on the breast. Firstly, this setup is validated using simulations with a spherical and a realistic-shaped breast phantom, testing the system with one or two targets. In this simulated environment, the capability of selecting targets with the lens is evaluated. A safety evaluation is also performed. Finally, the first experimental tests with the dielectric lens are presented. A homogeneous and heterogeneous breast phantom are used and the setup with and without the lens are compared.

Finally, in **Chapter 8**, a summary of the work and general conclusions of this thesis are presented, as well as future work.

1.5 Thesis Contributions

The work developed during my PhD resulted in contributions in different areas of development of MWI systems aiding breast cancer and ALN diagnosis, as detailed below. These multidisciplinary studies provide an overview of the main challenges regarding the development of MWI systems.

- Study of refraction effects on imaging results using air-operated systems. This study is applied to regular and irregular-shaped phantoms with variable permittivity values of the phantom media, targets size and number of antennas.
- Creation of a methodology to estimate dielectric properties of biological tissues with limited dielectric property information from MRI scans. Specifically, dielectric properties are estimated from 100 ALNs and a comparison study is performed with healthy and metastasised ALNs.
- Creation of an open-access repository of 10 anatomically realistic phantoms of the axillary region with variable numbers of ALNs and Body Mass Index (BMI).
- Validation of the developed methodology for estimation of dielectric properties with the MRI evaluation of a physical phantom with known dielectric properties.
- Preliminary study of radar MWI system applied to the axillary region, using simulated 2D planes of anthropomorphic phantoms.
- Feasibility study of an experimental prototype to detect ALNs, which comprises developing and optimising signal processing algorithms specifically tailored to ALN detection, and testing an anatomically realistic phantom with ALNs placed in several positions in a setup mimicking a clinical scenario.
- Electromagnetic exposure risk evaluation of the axillary MWI prototype.
- Study of the performance of classification algorithms to classify between healthy and metastasised ALNs based on shape and size, using monostatic microwave signals.
- Preliminary feasibility study of a bistatic MWI radar system for breast cancer detection using a dielectric lens in a simulated environment. This study evaluates the possibility of using a dielectric lens to focus the energy radiated by the antenna in specific regions of the breast. A safety evaluation is also performed.
- Experimental evaluation of the proposed bistatic MWI prototype for breast cancer detection.

The publications and dissemination activities conducted related to my PhD work are listed below. They include 3 published journal papers, 1 journal paper under review, 5 published conference papers, and 3 awards.

Journal publications:

1. D. M. Godinho, C. Silva, C. Baleia, J. M. Felício, T. Castela, N. A. Silva, M. L. Orvalho, C. A. Fernandes, and R. C. Conceição, "Modelling Level I Axillary Lymph Nodes Location for Microwave Imaging", (under review in Physica Medica)

2. D. M. Godinho, J. M. Felício, C. A. Fernandes, and R. C. Conceição, "Experimental Evaluation of an Axillary Microwave Imaging System to Aid Breast Cancer Staging", *IEEE Journal of Electromagnetics, RF and Microwaves in Medicine and Biology*, vol. 6, no. 1, pp. 68-76, 2022, doi: 10.1109/JERM.2021.3097877

3. D. M. Godinho, J. M. Felício, T. Castela, N. A. Silva, M. L. Orvalho, C. A. Fernandes, and R. C. Conceição, "Development of MRI-based Axillary Numerical Models and Estimation of Axillary Lymph Node Dielectric Properties for Microwave Imaging", *Medical Physics*, vol. 48, no. 10, pp. 5974-5990, 2021, doi: 10.1002/mp.15143

4. D. M. Godinho, J. M. Felício, C. A. Fernandes, and R. C. Conceição, "Evaluation of Refraction Effects in Dry Medical Microwave Imaging Setups", *IEEE Antennas and Wireless Propagation Letters*, vol. 20, no. 4, pp. 617-621, 2021, doi: 10.1109/LAWP.2021.3059162

Conference publications:

1. D. M. Godinho, J. M. Felício, C. A. Fernandes, and R. C. Conceição, "Target Selection in Multistatic Microwave Breast Imaging Setup using Dielectric Lens", 16th European Conference on Antennas and Propagation (EuCAP), Madrid, Spain, 2022, doi: 10.23919/EuCAP53622.2022.9768984 (oral presentation)

2. D. M. Godinho, J. M. Felício, C. A. Fernandes, and R. C. Conceição, "Optimisation of Artefact Removal Algorithm for Microwave Imaging of the Axillary Region Using Experimental Prototype Signals", 15th European Conference on Antennas and Propagation (EuCAP), Düsseldorf, Germany, 2021, doi: 10.23919/EuCAP51087.2021.9411134 (oral presentation)

3. D. M. Godinho, J. M. Felício, C. A. Fernandes, and R. C. Conceição, "Study of the Refraction Effects in Microwave Breast Imaging Using a Dry Setup", 42nd Annual International Conferences of the IEEE Engineering in Medicine and Biology Society (EMBC), Montreal, Canada, 2020, doi: 10.1109/EMBC44109.2020.9176439 (oral presentation)

4. D. M. Godinho, J. M. Felício, T. Castela, N. A. Silva, M. L. Orvalho, C. A. Fernandes, and R. C. Conceição, "Extracting Dielectric Properties for MRI-based Phantoms for Axillary Microwave Imaging Device", 14th European Conference on Antennas and Propagation (EuCAP), Copenhagen, Denmark, 2020, doi: 10.23919/EuCAP48036.2020.9135980 (oral presentation)

5. D. M. Godinho, J. M. Felício, C. A. Fernandes, and R. C. Conceição, "Feasibility study of focal lens for multistatic microwave breast imaging", 23rd International Conference on Applied Electromagnetics and Communications (ICECOM), Dubrovnik, Croatia, 2019, doi: 10.1109/ICECOM48045.2019.9163628 (oral presentation)

Presentations in national and international meetings:

1. D. M. Godinho, J. M. Felício, T. Castela, N. A. Silva, M. L. Orvalho, C. A. Fernandes, and R. C. Conceição, "Estimating Dielectric Properties of the Axillary Region from Magnetic Resonance Imaging", 13th International Congress of Hyperthermic Oncology (ICHO), Rotherdam, The Netherlands, 6th to 8th of October of 2021 (oral presentation)

2. D. M. Godinho, J. M. Felício, C. A. Fernandes, and R. C. Conceição, "Classification of Axillary Lymph Nodes Metastasised by Breast Cancer using Microwave Imaging Signals", Encontro Ciência, Lisbon, Portugal, 28th to 30th of July of 2021 (poster)

3. D. M. Godinho, J. M. Felício, C. A. Fernandes, and R. C. Conceição, "Optimização do algoritmo de remoção de artefactos em imagem por micro-ondas da região axilar", 14.º Congresso do Comité Português da URSI, Online Event, Portugal, 2020 (oral presentation and winner of 2nd place of Best Student Paper Award)

4. D. M. Godinho, J. M. Felício, C. A. Fernandes, and R. C. Conceição, "Experimental Validation of an Axillary Microwave Imaging Prototype", Encontro Ciência, Lisbon, Portugal, 3rd to 4th of November of 2020 (presentation)

5. D. M. Godinho, and R. C. Conceição, "Axillary Region Numerical Models for a Microwave Imaging System", in mini-symposium "MICROWAVES in BIOMEDICAL APPLICATIONS – PART I: Breast Cancer Detection and Monitoring", 42nd Annual International Conferences of the IEEE Engineering in Medicine and Biology Society (EMBC), Montreal, Canada, 20th to 24th of July of 2020 (oral presentation)

6. D. M. Godinho, J. M. Felício, T. Castela, N. A. Silva, M. L. Orvalho, C. A. Fernandes, and R. C. Conceição, "Extracção de Propriedades Dieléctricas para

validação de Protótipo de Imagem por Microondas da Axila", 13.º Congresso do Comité Português da URSI 'Espaço: Desafios e Oportunidades', Lisbon, Portugal, 2019 (oral presentation and winner of 2nd place of Best Student Paper Award)

7. D. M. Godinho, J. M. Felício, C. A. Fernandes, and R. C. Conceição, "Experimental Validation of an Axillary Microwave Imaging Prototype", Ciências Research Day, Lisbon, Portugal, 2019 (poster)

8. D. M. Godinho, "A New Technique to Aid Breast Cancer Diagnosis", PhD Translational Fellowship Program by EIT Health, Oxford, United Kingdom, 2019 (oral presentation and selected as one of the 26 finalists)

9. D. M. Godinho, J. M. Felício, N. A. Silva, M. Lurdes Orvalho, C. A. Fernandes, and R. C. Conceição, "Axillary Region Numerical Models for a Microwave Imaging System", Encontro Ciência, Lisbon, Portugal, 8th to 10th of July of 2019 (poster)

10. D. M. Godinho, J. Felício, N. A. Silva, M. Lurdes Orvalho, C. A. Fernandes, and R. C. Conceição, "Axillary Region Numerical Models for a Microwave Imaging System", 11th edition of the Workshop on Biomedical Engineering, Lisbon, Portugal, 6th of April of 2019 (poster and winner of Best Poster Award)

11. D. M. Godinho, J. Felício, N. A. Silva, M. L. Orvalho, C. A. Fernandes, and R. C. Conceição, "Development of Axillary Region Models based on MRI Segmented Data to Aid Breast Cancer Staging", 1st EMF-Med World Conference on Biomedical Applications of Electromagnetic Fields, Split, Croatia, 2018 (oral presentation in a Convened Session)

2 | Background

This chapter reviews some important concepts to understand the work developed in this thesis. Understanding the breast anatomy and breast cancer is essential for the development of a Microwave Imaging (MWI) system to aid breast cancer diagnosis. In Section 2.1, the breast anatomy and the types of breast cancer are briefly reviewed. The anatomy and positioning of Axillary Lymph Nodes (ALNs) are also described.

The fundamentals regarding MWI are reviewed in Section 2.2, from the state-of-the-art of current imaging prototypes to the dielectric properties and imaging algorithms. Then, in Section 2.3, the state-of-the-art literature regarding phantom development for MWI validation is reviewed. In the same section, the main concepts of the generation of Magnetic Resonance (MR) images and state-of-the-art image processing methods are explained to understand how one can create Magnetic Resonance Imaging (MRI)-based phantoms and estimate approximate dielectric properties from this type of images. Finally, in Section 2.4, a review of the use of machine learning algorithms to classify targets in MWI is presented, including the commonly used feature extraction methods and classifiers.

2.1 Physiological Background

The following sections present the physiological background of the breast and ALNs.

2.1.1 Anatomy of the Breast

The breast is a modified skin gland which lies on the chest wall between the clavicle and sixth to eighth ribs [59] and anterior to the *pectoralis major* muscle. The female breast is responsible for producing milk ensuring the nutrition of neonates. It is surrounded by a skin layer, which is rich in melanocytes in the region of the nipple giving it a darker colour [60] (Figure 2.1). The composition of the interior of the breast can be summarised as follows: 1) glandular tissue which includes 15 to 20 lobes (which are subdivided into lobules) and breast (milk) ducts radiating from the nipple; 2) fibrous tissue, also called Cooper's ligament, which surrounds the glandular components and sustains all breast tissues; and 3) adipose tissue.

The shape and size of the breast depend on several factors such as genetics, race, diet, and age. The American College of Radiology defined Breast Imaging-Reporting and Data System (BI-RADS), an atlas used to classify breast observations in medical imaging reports [61]. One of its notations used for X-Ray Mammography aims to classify the breast composition into four categories (**a**, **b**, **c** and **d**):

a. The breasts are almost entirely composed by adipose tissue;

b. The breasts show areas with fibroglandular density;

c. The breasts present a heterogeneous density;

d. The breasts are extremely dense.

The evaluation of breast density is important mainly for two reasons. Firstly because breast density affects the performance of imaging modalities (e.g. the sensitivity of X-Ray Mammography) [5] and imaging results need to be careful analysed, and also because breast density is a risk factor to develop breast cancer [62].

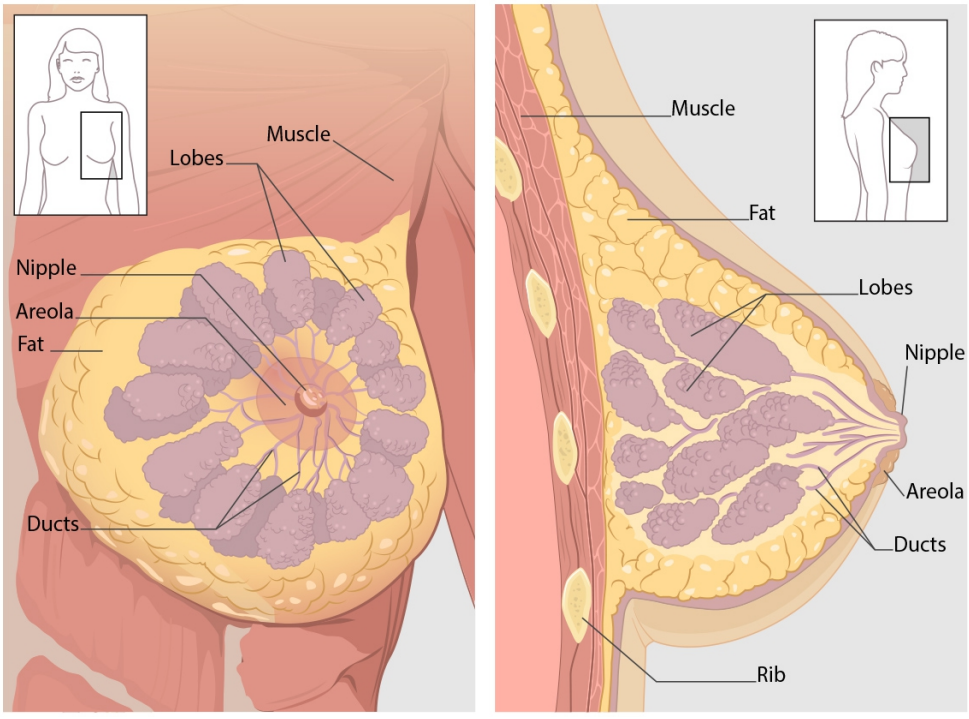

(a) (b)

Figure 2.1: Healthy breast composition in: (a) coronal and (b) sagittal planes [63].

2.1.2 Breast Cancer

The human body have several mechanisms to control the normal cell functioning. Cells may divide themselves in several situations replicating their genetic code (i.e. DeoxyriboNucleic Acid (DNA)). Mutations are likely to occur in the replication process and the

immune system is often capable of destroying these cells in a process called apoptosis. Tumour cells result from the failure of regulatory mechanisms which control how often and how much cells divide and die. If a mutation occurs when these mechanisms fail, the immune system response may fail to destroy all the mutated cells, resulting in a malignant tumour [64].

Benign tumours are an abnormal growth of non-cancerous cells which are limited to the tissue where they grow. Breast benign tumours include the Lobular Carcinoma *In-Situ* and other non-cancerous conditions such as simple cysts and fibroadenomas [65], [66]. Breast cancer (i.e. malignant tumours) can be classified in two main types: *in-situ* and invasive. The *in-situ* carcinomas are non-invasive cancers, limited to the ducts (Ductal Carcinoma *In-Situ*) or to the nipple (Paget's disease). When cancer cells spread into the surrounding breast tissues, the cancer is classified as an invasive carcinoma [65]. If the cancer starts to develop in the ducts it is called Invasive Ductal Carcinoma, if it starts in the lobules it is called Invasive Lobular Carcinoma. The invasive carcinoma can be metastatic when it spreads to the blood or lymphatic vessels and distant organs. Figure 2.2 exemplifies the behaviour of cancer cells in each type of cancer. Cancer cells proliferation is also characterised by an abnormal increase of vascularisation [67].

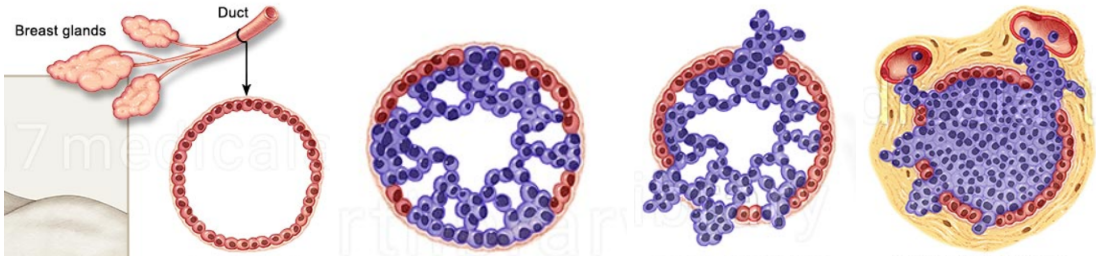

Figure 2.2: Evolution of cancer cells inside a breast duct: (a) Normal duct cells, (b) Ductal Carcinoma *In-Situ*, (c) invasive ductal carcinoma and (d) metastatic invasive ductal carcinoma. In (b), the cancer cells (in purple) are contained within the duct, in (c) those cells have spread through the duct wall into surrounding tissues, and in (d) the cancer cells have spread to the blood or lymphatic system. Adapted from [68].

One of the most widely used staging protocol is the TNM staging, proposed by the American Joint Committee on Cancer (AJCC) [65]. In the TNM acronym, T refers to the size and extent of the tumour, N to the presence of nearby metastasised lymph nodes and M to the metastases in other parts of the body [65]. The N category is divided in two subcategories, clinical and pathological staging. The categories vary from 0 to 3 and comprise the level of the metastasised lymph nodes, their mobility, the size of the metastases and the number of affected lymph nodes. The lymph nodes included in this staging are the ALNs and the internal mammary lymph nodes. In 2018, the 8th Edition of the AJCC Cancer Staging Manual added three new criteria to the staging protocol based on biomarkers [65]. These new criteria include the tumour grade, the expression of hormone receptors and the presence of oncogene HER2.

By combining these criteria, breast cancer can be categorised in five stages. Stages 0 to IV can be subdivided in A, B and C categories and result from several combinations of the TNM information and the new criteria. Figure 2.3 shows a general representation of four of the breast cancer stages. Stage 0 (not represented in the figure) comprises non-invasive tumours. Stage I is usually defined by the presence of a small tumour with no metastases or micro-metastases. Stage II includes tumours with more than 2 cm and/or metastases in lymph nodes. Stage III usually corresponds to situations where the tumour is larger or there are more metastases. Stage IV is metastatic due to the presence of metastases in distant organs, and does not depend on the size of the tumour or number of affected lymph nodes. ALNs metastases occur in some types of breast cancer in stage II, in most of the types in stage III and always in stage IV [65].

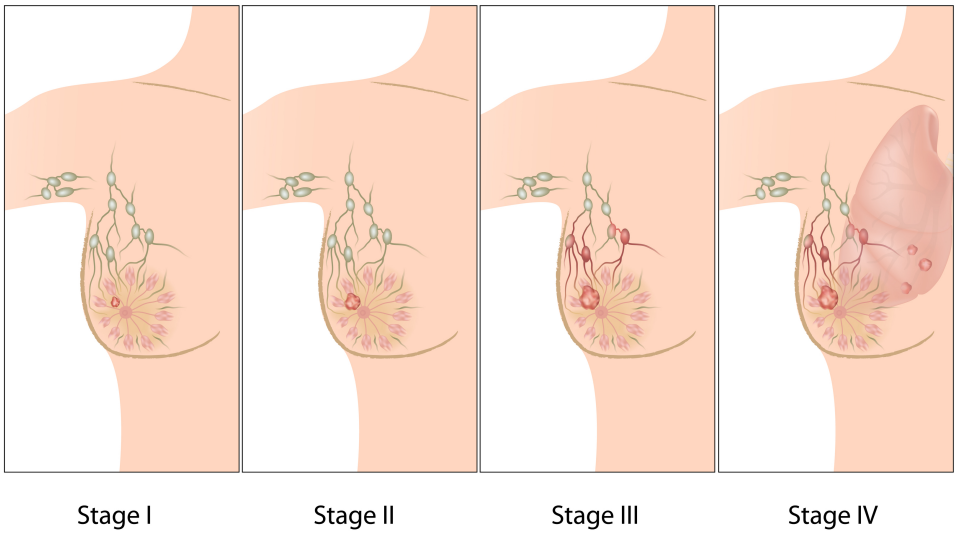

Figure 2.3: Main stages of breast cancer. Adapted from [69].

2.1.3 Axillary Lymph Nodes

Lymph nodes are small organs which are part of the lymphatic system. The lymphatic system is responsible for transporting lymphocytes and collecting excess interstitial fluid from the spaces between cells and conduct them as lymph through lymphatic vessels. Lymph nodes filter particles from the lymph and are a centre of activation, differentiation and proliferation of lymphocytes [70].

More than 75% of the lymph from the breast is drained to ALNs [60]. ALNs can be located in three levels, as shown in Figure 2.4(a), based on their relative anatomical location. Level I ALNs are the first to receive drainage from the breast and are lateral to the lateral border of the *pectoralis minor* muscle. They are also surrounded by other muscles such as the *latissimus dorsi* in the lateral side, the *serratus anterior* in the posterior side, and the *pectoralis major* muscle in the anterior side, as shown in Figure 2.4(b). Level II are located between the medial and lateral borders of the muscle, and level

III are medial to the medial margin of the muscle and inferior to the clavicle. Level I ALNs are usually the first nodes affected by breast cancer metastases, in around 97% of the cases [71], [72]. Level II and III nodes can have metastases in 22% and 10% of the cases, respectively. Cases where metastases skip level I nodes are rare and are often associated with more advanced stages of cancer [73]. The depth of ALNs was reported to vary from 1 to 12 cm [74], [75].

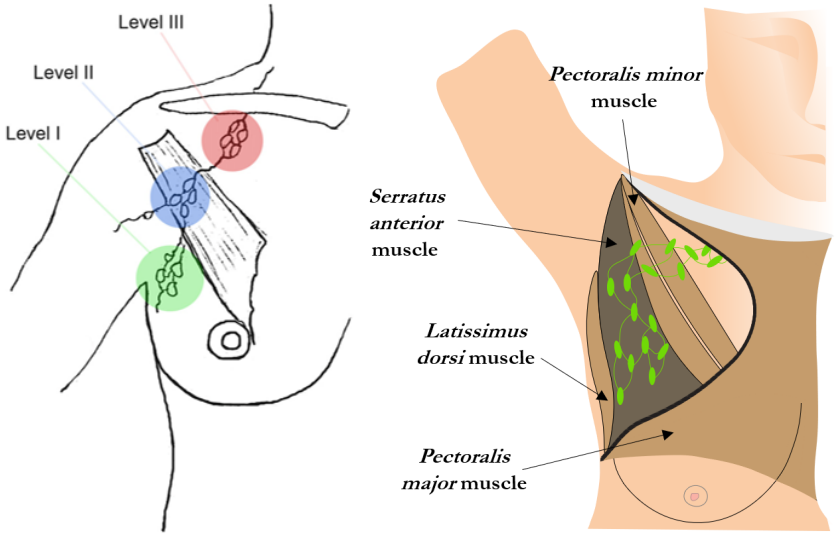

Figure 2.4: Anatomical organisation of ALNs levels [76] (left) and simplified representation of lymph nodes relatively to surrounding muscles (right). Level I are lateral to the muscle border, level II are within the muscle and level III are medial to the muscle and inferior to the clavicle.

A healthy lymph node has an ellipsoid shape and its size can range from 0.1 to 2.5 cm in its longest axis (Figure 2.5). It is surrounded by a capsule of collagen fibres and divided into lymphoid follicles where the lymphocytes and macrophages are maintained. The afferent lymph vessels carry the lymph into the node on its convex side. The lymph then moves through the follicles and leaves the node through an efferent lymphatic vessel which is located in a region called hilum [70], [77].

Metastasised, inflamed or healthy ALNs have overlapping imaging features which result in unsatisfactory sensitivity and specificity performances [76]. In fact, several recent studies show a stronger immune response, such as COVID-19 vaccination [78], may cause highly reactive ALNs. These reactive ALNs present similar characteristics to metastasised ALNs which may hamper cancer staging in breast cancer patients [78], [79].

Some authors have been trying to define objective criteria to distinguish healthy from metastasised ALNs in Ultrasound (US), Computed Tomography (CT) or MR images in order to maximise the diagnosis accuracy (Figure 2.6). These criteria can be summarised as follows:

- **Size:** Studies [80] have presented size thresholds to define whether an ALN is

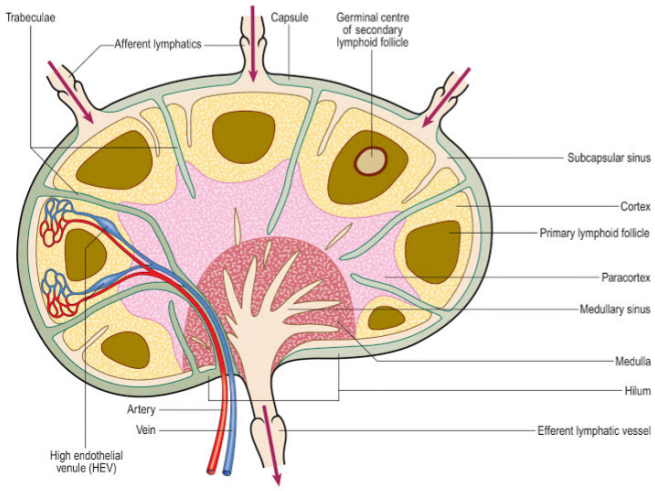

Figure 2.5: Structure of a lymph node [70] with its main structures: cortex, follicles and hilum.

healthy or metastasised. However, there is patient variability and healthy ALNs can be larger than metastasised ones. Size has been mostly useful to monitor the progression of metastases or the response to treatment in patients with confirmed carcinomas using US [81]. Chen *et al.* [82] performed a statistical analysis using measurements taken from CT images and 1490 ALNs, and verified a shorter-axis length higher than 9 mm can be used as a feature of metastasised ALNs.

- **Shape:** While healthy ALNs are characterised by its oval and elongated shape, metastasised ALNs are often described as spherical. A ratio between the longest

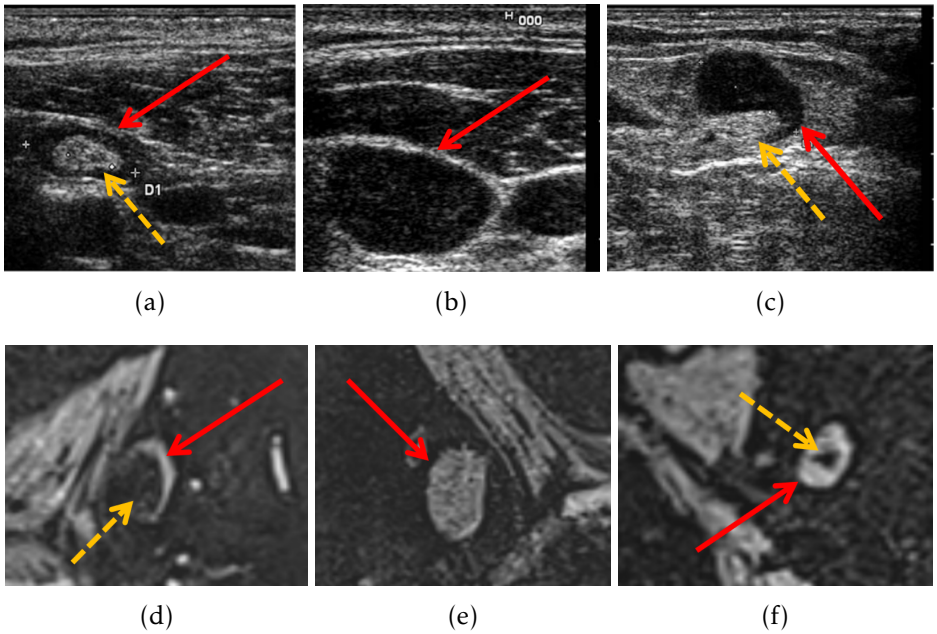

Figure 2.6: Examples of lymph nodes (red arrows) in (a,b,c) Ultrasound [10] and (d,e,f) T1-weighted with fat suppression MR images. Healthy lymph nodes with a fatty hilum (dashed yellow arrows) are shown in (a) and (d), metastasised lymph nodes without hilum are shown in (b) and (e), and round-shaped metastasised lymph nodes with hilum (dashed yellow arrows) and increased cortex thickness are shown in (c) and (f).

(L) and shortest (S) axes are often used to assess the shape of ALNs, such as L/S < 1.7 [82] for metastasised ALNs, or L/S < 2 [80] and L/S < 1.5 [83] for other metastasised lymph nodes.

- **Hilum:** It has similar response to fat tissue and is often identified as an echogenic (i.e. high intensity) structure in US. An absence of hilum is mostly observed in metastasised ALNs and is one of the features used to distinguish healthy and metastasised ALNs. However, some studies have verified hilum may not be visible in some healthy lymph nodes while metastasised lymph nodes may still show a hilum [10], [82] [Figure 2.6(c,f)].

- **Cortex:** Cortex is imaged as a thin and C-shaped structure in healthy ALNs [Figure 2.6(d)]. Inhomogeneous cortices or an increase of cortex thickness is a sign of probable metastasised ALNs. A thickness of less than 3 mm is often considered as normal [82].

- **Margins:** Healthy lymph nodes have sharp margins, while metastasised ALNs can present irregular and non-defined margins due to extracapsular spread [10], [18].

An increase of vascularisation of metastasised ALNs has also been observed in preliminary studies [84], [85] when compared to healthy or inflamed ALNs.

Computer-aided algorithms for lymph node detection and classification in medical images are still limited in the literature. Unal *et al.* [86] used segmentation methods which assumed lymph nodes had ellipsoid shapes to detect pelvic lymph nodes in MR images with contrast. However, this methodology was limited to the pelvic region and the applicability to other regions and to MR images without contrast cannot be assumed. Barbu *et al.* [87] presented a detailed lymph node detection method (patented by Siemens Corporation [88]) which allows to automatically detect axillary, abdominal and pelvic lymph nodes from 3D CT images. Their results yielded an 83% detection rate of ALNs. Ha *et al.* [89] and Liu *et al.* [90] presented a study with deep learning models to classify healthy and metastasised ALNs extracted from MR images and obtained an accuracy performance of 84.3% and 90.9%, respectively. The input images of the models comprised 2D images of manually segmented ALNs, which would require also a manual segmentation in clinical practice in order to use these models.

The ambiguity of ALNs features show the need for alternative imaging modalities to diagnose ALNs. MWI has the potential to assess this problem in a screening exam. However, crucial aspects to the development of such an MWI system were still unknown before this thesis, namely, the characteristics of the prototype, the optimal antenna positioning, the interaction between microwaves and the axillary region, and the dielectric contrast between ALNs and the axillary region tissues. These topics will

be reviewed in the following sections, which serve as a starting point for the work developed in this thesis.

2.2 Microwave Imaging

A short introduction to MWI was already presented in Section 1.3 but new concepts need to be introduced to understand the development of MWI systems. Firstly, theoretical concepts used to characterise radar MWI prototypes are described. Secondly, the exposure safety assessment which needs to be performed when developing MWI systems is explained. Finally, the state-of-the-art and theoretical concepts of the artefact removal and image reconstruction algorithms used for MWI are reviewed.

2.2.1 Prototype Characterisation

MWI systems usually comprise the use of a Vector Network Analyser (VNA), which is used to generate the microwave pulses. It is directly or indirectly connected through cables to one or more antennas, which are placed around the part of the body of interest. The effectiveness of the image reconstruction algorithms and consequent target detection requires a good characterisation of the used antennas and choosing the more suitable antenna configuration and positioning.

Radar MWI systems can be monostatic or multistatic. In a monostatic configuration, the signals are transmitted and received by the same antenna, while in a multistatic configuration each antenna transmits the radar signal, while the remaining antennas record the scattered signals. Bistatic systems are a particular case of multistatic, where only two antennas are used. The signals recorded are referred to as reflection or transmission coefficients. The reflection coefficient is often represented by $\mathbf{s}_{i,j}(f)$ with $i = j$ and it is a ratio between the received signal after reflection in the tissues and the incident signal. The transmission coefficient is also represented by $\mathbf{s}_{i,j}(f)$ but $i \neq j$, and it is a ratio between the received signal after transmission through the tissues and the incident signal. In both cases, i and j represent the number of the antenna and $\mathbf{s}$ is a complex signal in frequency domain.

Both monostatic and multistatic configurations have been used in several prototypes by different groups working in breast MWI [34], [43], [91]–[93]. Both monostatic or multistatic systems either use moving antennas to scan the body resulting in long acquisition times or use multiple antennas connected to a Radio Frequency (RF) switching system that selects which antenna radiates at each time. Systems with multiple antennas require less acquisition time than the ones that use only one antenna, at the expense of more complex signal processing algorithms due to coupling effects between antennas. As an example, Fear *et al.* [43] presented a monostatic prototype, where an antenna was moved across 200 positions, taking around 30 minutes to perform a

full scan. MVG Industries [34], [94] have used a breast imaging system for human patient studies with a multistatic setup of 18 antennas that moves vertically resulting in a scan time from 10 to 15 minutes. In contrast, Klemm *et al.* [92] presented a multistatic system with 60 antennas which was capable of performing all measurements in 10 seconds. Another advantage of using multistatic systems is the possibility to use power amplifiers in order to increase the dynamic range of the measurement, which is important in situations where the target can have a low amplitude response.

In multistatic systems, more than one interaction between the antennas can be observed, as illustrated in Figure 2.7. The waves transmitted by one antenna can be received directly by the other (in blue), they can be immediately reflected at the surface (in orange) or they can penetrate the body and be reflected by the tissues (in green). The latter is the interaction of interest in MWI since it allows to reconstruct the image based on the dielectric contrast between inner tissues of the body. The interaction between antennas represented in blue is called antenna coupling. During the design of the antennas configuration and positioning, these coupling effects need to be minimised.

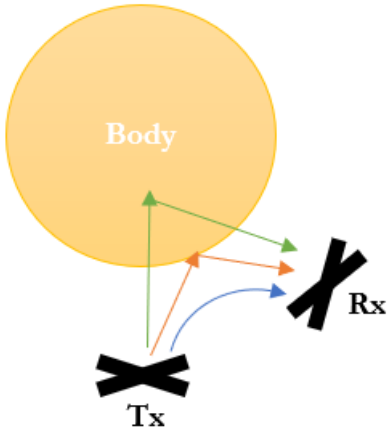

Figure 2.7: Schematic of possible interactions between neighbour antennas. Tx is the transmitting antenna, Rx is the receiving antenna, the blue arrow represents the direct interaction between both antennas, the orange arrow represents the signals reflected at the surface of the body and recorded by Rx, and the green arrow represents the signals of interest to MWI resulting from the reflections of the inner tissues recorded by Rx.

The optimal antenna positioning for MWI depends on the shape of the body region to image, tissue structures and properties. MWI systems can have planar or circular antenna positioning. As the name suggests, planar configurations mean that all antennas are placed or scan the body on a plane, while in circular configurations the antennas are positioned or scan around the body. Conceição *et al.* [38] compared the use of planar [33] and circular configurations [91] for breast imaging. When the patient is in a supine position, the antenna usually performs a planar scan above the region of interest. When the patient is lying in a prone position, the antenna performs a circular scan around the pending breast. The authors verified that circular configurations give generally better results independently of the tumour location. Eleutério *et al.* [52] used a planar configuration for ALNs detection. Recently, within my research group, Savazzi

et al. [56] presented a preliminary study with a quarter circular configuration also for ALNs detection.

Another component of the systems to consider is the medium between the antennas and the body. As explained in Section 1.3, air-operated systems have been proposed to address the sanitation and attenuation issues that immersing part of the body in a liquid imposes. Figure 2.8 shows examples of air-operated systems reported in the literature. The prototype presented by Islam *et al.* [48] consisted of a 9-element antenna array in a circular configuration around the breast in a multistatic system, using an RF switching system. It includes a portable stepper motor which allows to rotate the array in several positions. Vispa *et al.* [45]'s prototype has two antennas which work as transmitting and receiving antennas and are swept in several circular positions in circumferences with different radius. Reimer *et al.* [51] also proposed a prototype with two antennas but both are swept in the same radius circumference and can work as a monostatic or bistatic configuration. In contrast, Felício *et al.* [49] proposed a prototype with a single antenna rotating in a circular configuration.

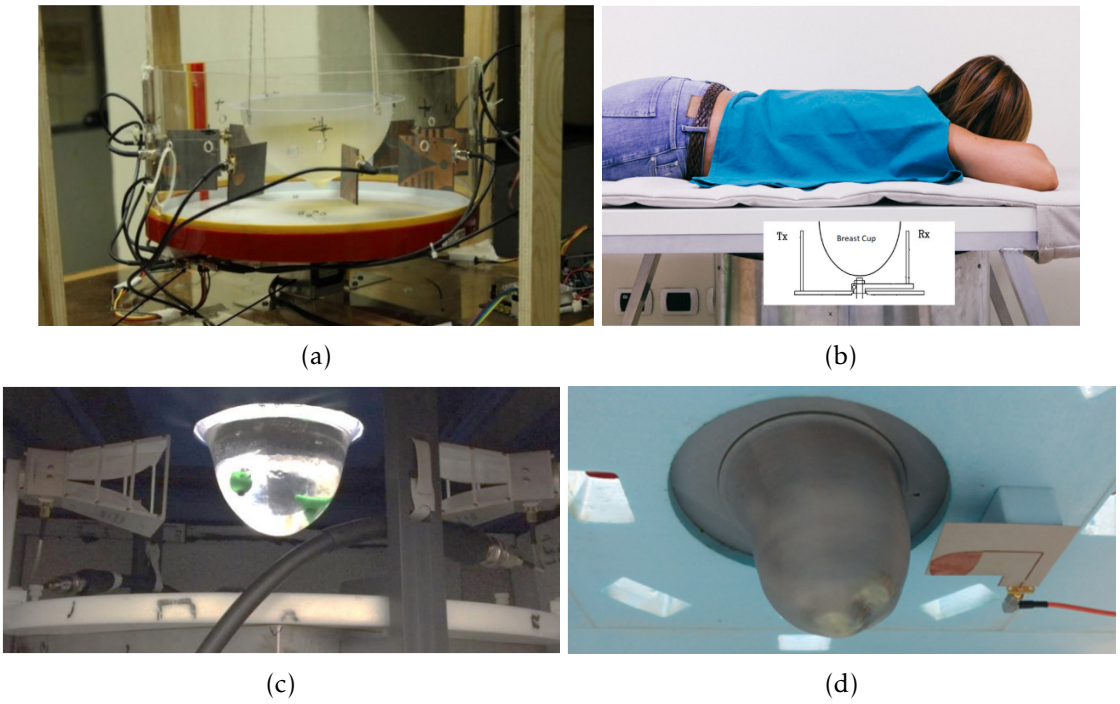

(a) (b)

(c) (d)

Figure 2.8: Prototypes of proposed air-operated microwave imaging systems in the literature. Multistatic systems by (a) Islam *et al.* [48] and (b) Vispa *et al.* [45], (c) monostatic or bistatic system by Reimer *et al.* [51] and (d) monostatic system by Felício *et al.* [49].

There are three main antenna-related characteristics that need to be considered to minimise and compensate adverse effects inherent to the setup that may hinder the quality of imaging results: the internal reflections, the "near-field phase centre" and the electrical distance offset of the antennas. The internal reflections inherent to any antenna can be the same order of magnitude as the tissues backscattering and mask the tissues response. The incorrect definition of the "near-field phase centre"

and the electrical distance offset may affect the distance calculations in image reconstruction algorithms. Felício *et al.* [95] have presented strategies to perform a proper antenna calibration by determining these antenna-related characteristics, and remove the undesired effects. The internal reflections can be eliminated by subtracting the measurement of the antenna(s) in free-space from the measurements in the presence of the body/phantom, while the "near-field phase centre" and the electrical distance offset of the antenna can be determined by performing an analysis of the antenna response in specific conditions [95].

2.2.2 Assessment of Electromagnetic Exposure Risk

The safety in terms of electromagnetic fields exposure needs to be evaluated when designing new radio-frequency devices. Specifically, the safety of MWI systems can be evaluated using Specific Absorption Rate (SAR). SAR is a measure of the rate at which energy is absorbed by the human body when exposed to an electromagnetic field and can be calculated as:

$$SAR = \frac{1}{V} \int \frac{\sigma(r)|\mathbf{E}(r)|^2}{\rho(r)} dr \tag{2.1}$$

where V is the volume considered for the calculation, σ is the conductivity measured in S/m, ρ is the density of the material in the considered volume and $\mathbf{E}$ is the root mean square electric field. SAR is expressed in W/kg.

The International Commission on Non Ionizing Radiation Protection (ICNIRP) establishes guidelines on limiting exposure to non-ionising radiation. In 2020, these guidelines were revised and published in a new document [96]. Table 2.1 shows the current limits for SAR in the microwave frequency band. For the breast and the axillary region, the SAR for local head/torso applies. In higher frequency ranges, localised SAR is not applicable, i.e., it does not need to be considered when determining the compliance of exposure.

MWI usually uses low-power and therefore SAR values are within the acceptable range, as previous studies have shown for breast [97] or brain [98] imaging. However, this assessment needs to be performed when developing devices with new antennas and varying antenna positioning.

2.2.3 Algorithms to Create Microwave Images

The recorded signals from an MWI prototype or simulation can be processed in time or frequency domains. Several domain-specific algorithms have been proposed in the past few decades both for image reconstruction [42], [99] and artefact removal [100], [101], which can provide better or worse results depending on the antenna configuration and part of the body to be imaged.

Table 2.1: Limits of electromagnetic exposure defined by ICNIRP [96] for exposures longer than 6 minutes.

Exposure scenario	**Frequency range**	**Whole-body average SAR (W/kg)**	**Local Head/Torso SAR (W/kg)**
Occupational	100 kHz to 6 GHz	0.4	10
	> 6 to 300 GHz	0.4	NA
General public	100 kHz to 6 GHz	0.08	2
	> 6 to 300 GHz	0.08	NA

NA: Not Applicable.

2.2.3.1 Image Reconstruction

One of the first radar-based image reconstruction algorithm for MWI ever presented was the Delay-And-Sum (DAS) [33]. The DAS is applied in time-domain signals and consists of applying a time-shift (delay) to the scattered signals and summing the resulting signals to obtain the contribution to each voxel, and integrated over a pre-defined time-window T_{win} [39]. The time delays are calculated considering the round-trip distance between each voxel and each antenna position and the average speed of propagation in the considered medium. If the voxel corresponds to a tumour location or a structure where there is high dielectric contrast, the signals will add coherently, resulting in a high intensity voxel. Otherwise, the signals will add incoherently and the intensity is lower. Generically, DAS can be formulated as follows [39]:

$$intensity(v) = \left[\sum_{i,j}^{N_a} \sum_{t=0}^{T_{win}} \mathbf{S}_{i,j}(t + \tau_{i,j,v}) \right]^2 \tag{2.2}$$

$$\tau_{i,j,v} = \frac{(d_{iv} + d_{vj})}{c} f_s \tag{2.3}$$

where d_{iv} and d_{vj} are the distances between each voxel v and each antenna position i and j respectively, accounting for the electrical distance offset of the antenna (d_{off}), the distance travelled in air (d_{air}) and the distance in the new medium (d_{diel}) considering the refractive index ($n_{diel} = \sqrt{\epsilon_{diel}}$), as $d_{air} + \sqrt{\epsilon_{diel}} d_{diel} + d_{off}$. The antenna positions are defined by the location of its "near-field phase centre". c is the speed of light, f_s is the sampling frequency, and N_a is the number of antennas. In a monostatic system, $\mathbf{S}_{i,j}$ are the reflection coefficients in time-domain with $i = j$, and in a multistatic system there are transmission coefficients in time-domain $\mathbf{S}_{i,j}$ where $i \neq j$.

Several extensions of DAS have been proposed in the literature. Both Improved Delay-And-Sum (IDAS) [102] and Modified Delay-And-Sum (MDAS) [103] propose two different methods to calculate a multiplication factor which gives higher weight

to coherent signals increasing the quality of the image. Channel-Ranked Delay-And-Sum (CR-DAS) [104] gives a higher weight to the antenna positions closer to the voxels, assuming the signals recorded by these antennas have more clear information, defined as $w_{i,j} = \frac{M - rank_{i,j}}{M(M-1)/2}$ where M is the number of multistatic signals and $rank_{i,j}$ is the rank of each antenna pair i, j in terms of distance to the voxel. In the case of monostatic signals the weight of each antenna can be simplified to $w_i = \frac{N_a - rank_i}{N_a}$. Delay-Multiply-And-Sum (DMAS) [42] consists of pairwise multiplying the scattered signals before summing the signals, which increase the range of resulting intensities, giving higher weight to the coherent signals. Iterative adaptations of DAS have also been recently studied [51], which use the fundamentals of Positron Emission Tomography (PET) image reconstruction.

In this thesis, DAS and CR-DAS are briefly used. The most adopted algorithm in this thesis is an adaptation of the DAS algorithm for frequency domain, based on the wave migration algorithm [105]. The algorithm can be written as:

$$intensity(v) = \left[\sum_{i,j}^{N_a} \sum_{f}^{N_f} \mathbf{s}_{i,j}(f) e^{jk_0(d_{iv} + d_{vj})} \right]^2 \tag{2.4}$$

where $\mathbf{s}_{i,j}$ is the complex signal response in frequency-domain, a vector $1 \times N_f$, where N_f is the number of frequency points. The wave number k_0 is given by $\frac{2\pi f}{c}$ for each frequency point f, with c as the speed of light.

2.2.3.2 Refraction Computation

Refraction is the change in direction of a wave passing from one medium to another, as a consequence of its change in velocity of propagation. The velocity of propagation is determined by the permittivity of the medium. In medical MWI, refraction effects are expected to occur between the media where the antennas are placed (e.g. air) and the body. The computation of these effects may increase the computational time, and, consequently, influence real-time image reconstruction.

The effect of refraction can be considered in image reconstruction algorithms through the calculation of the distances d_{air} and d_{diel}. Refraction paths can be calculated using Snell law in vector form, using the following equation [106]:

$$\left(\frac{1}{\sqrt{\epsilon_{diel}}} \hat{i} - \hat{t} \right) \times \hat{N} = 0 \tag{2.5}$$

where $\hat{i}$ is the unit vector in the incident direction, $\hat{N}$ is the unit normal vector inside the sphere, $\hat{t}$ is the unit vector in the direction of the refracted ray, and ϵ_{diel} is the relative permittivity value of the dielectric phantom. This formulation is described in more detail in Appendix A. Figure 2.9 illustrates the geometry for the propagating rays with and without refraction.

Some authors have considered refraction in the calculation of distances in their algorithms. Wang *et al.* [107] calculated refraction using Fermat's principle which calculates the entry point on an arbitrary surface ensuring the path between the antenna and each voxel corresponds to the lowest electrical path. The algorithm was tested with a numerical spherical breast with an average relative permittivity of 9 in a frequency band from 3.1 to 10.6 GHz, and the imaging result was presented. However, the authors did not provide a comparison to images where refraction was not considered nor presented quantitative performance metrics. Shao *et al.* [108] presented an imaging algorithm based on phase shift and sum method and assessed refraction calculation with an algorithm which considers multipath rays between the antenna and each voxel. The algorithm was validated with a cylindrical phantom in an experimental setup with an average relative permittivity of 7 in the working frequency band (1.5 to 7.7 GHz). They compared their algorithm performance to other algorithms but all of them considered refraction. The study was limited to uniform shapes, thus, the effects of neglecting refraction in imaging results are still lacking in the literature.

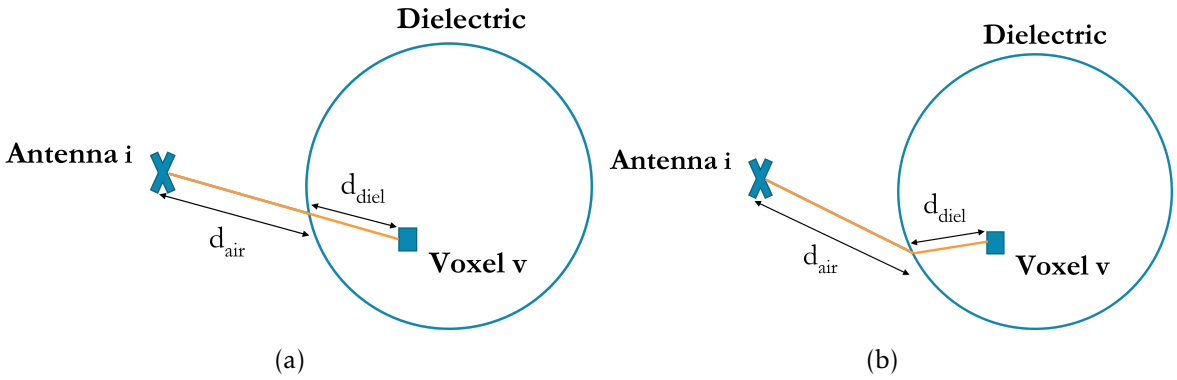

Figure 2.9: Schematic of the distances used in the image reconstruction algorithm where refraction effects (a) are not and (b) are considered. d_{air} and d_{diel} are the distances travelled in air and in the dielectric, respectively.

2.2.3.3 Artefact Removal

Raw microwave signals present artefacts that need to be removed to ensure reliable image reconstruction. Namely, an artefact removal algorithm is needed to remove high amplitude artefacts which can be created by the air-body interface (when using with air-operated MWI systems) or skin response (orange arrows in Figure 2.7). The optimal removal of such artefacts rely on the following assumptions:

- The artefact responses are an early-time artefact with the highest response which is recorded before the target response;
- The artefacts recorded by one antenna are similar within the neighbouring antennas, while the target response is usually different among them;

- The target response corresponds to the subtraction between the full measurement and an estimation of the artefacts.

An ideal artefact removal consists of using two groups of measurements: one with the target and another without the target. When subtracting the latter from the former the target response can be obtained. However, for obvious reasons, this is not possible in a real situation with patients. One of the simplest artefact removal algorithms is the rotation subtraction. It consists of subtracting, from each signal, the scattered signal recorded after shifting the antenna to a neighbouring position (or the scattered signal of a neighbouring antenna). Some authors have used this algorithm [45], [48], [109] but it presents limitations when the artefact varies between antenna positions, whether due to the irregular shape of the body or the variable distance between the antennas and the body. Another simple algorithm is the average subtraction [99], [108] which consists of subtracting the average of all measured signals, but it presents similar limitations as observed with the rotation subtraction algorithm.

More advanced artefact removal algorithms use adaptive filtering techniques [100], [110], [111] which estimate the early-time artefact response as a filtered combination of all signals. This type of algorithms can also be applied considering only the neighbouring antennas, which decreases the effect of the distance variability between the antennas and the body [112]. Ruvio *et al.* [113] and Felício *et al.* [49] proposed one adaptive algorithm based on Singular Value Decomposition (SVD), which is the algorithm explored in this thesis.

The scattering matrix $\mathbf{M}$ with reflection or transmission coefficients $\mathbf{s}_{i,j}$ is factorised using SVD, which applies an orthogonal linear transformation maximising the variance of the data. The algorithm decomposes the signals into singular vectors that represent the backscattered responses at different distances from the antenna, e.g. clutter, air-body interface or skin response, and target response. Considering a real or complex matrix $\mathbf{M}$ of dimensions $m \times n$, SVD computes the factorisation as follows:

$$\mathbf{M} = \mathbf{U}\Sigma\mathbf{V}^{*} \tag{2.6}$$

where $\mathbf{U}$ is an $m \times m$ unitary matrix, Σ is an $m \times n$ diagonal matrix with non-negative real numbers σ_l, for $l = 1, \ldots, \min[m; n]$, and $\mathbf{V}$ is an $n \times n$ unitary matrix. The columns of $\mathbf{U}$ and $\mathbf{V}$ are called the left-singular and right-singular vectors of $\mathbf{M}$, respectively, and the values σ_l of Σ are called singular values of $\mathbf{M}$. Matrix $\mathbf{M}$ can be created as follows: each column corresponds to the input reflection or transmission coefficient $\mathbf{s}_{i,j}$ and each row correspond to each frequency point of each input reflection or transmission coefficient.

The first singular vectors, i.e. the singular vectors with highest singular values, obtained from SVD represent the highest magnitude reflections which are common to all signals considered in matrix $\mathbf{M}$. These singular vectors are likely to correspond to the air-body interface response if that response is similar between all signals. The

signals without the air-body interface response ($\mathbf{M^{cal}}$) can be obtained by subtracting the contribution from the first n_{sv} singular vectors [49]:

$$\mathbf{M^{cal}} = \mathbf{M} - \sum_{l=0}^{n_{sv}} \sigma_l \mathbf{u_l} \mathbf{v_l^*} \tag{2.7}$$

The number n_{sv} of singular vectors which need to be subtracted to successfully remove the artefacts may vary with the complexity of the body shape. For a monostatic setup with an anthropomorphic breast model, Felício *et al.* [49] created an automatic procedure to find n_{sv}. In order to find n_{sv} for other antenna configurations or applications, further analysis needs to be completed.

Figure 2.10 shows an example of the response of a reflection coefficient ($\mathbf{s}_{i,j}$ where $i = j$) in spatial domain by applying the algorithm presented in equation 2.4. In this case, the voxel v is considered as a point in a 1D scenario and its position varies from 0 and 250 mm relatively to antenna i position. The $\mathbf{s}_{i,j}$ is recorded for a frequency band from 2 to 6 GHz. Figure 2.10(a) shows the signal over distance, with a high magnitude reflection corresponding to the surface of the body. Figure 2.10(b) shows the resulting response after an ideal artefact removal and Figure 2.10(c) shows the resulting response after an adaptive artefact removal based on SVD. Although the latter has a slightly lower magnitude signal than the former, the maximum magnitude is located at the target location.

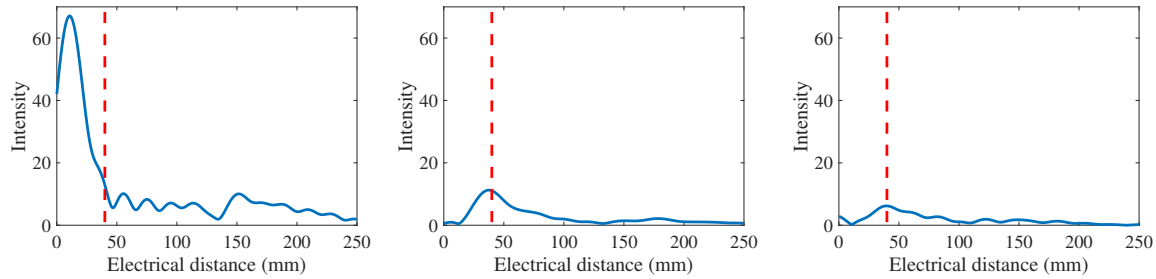

Figure 2.10: Examples of artefact removal algorithms performance. (a) shows the original response recorded by $\mathbf{s}_{i,j}$, where $i = j$, over distance, (b) and (c) show the resulting response after an ideal artefact removal and adaptive artefact removal with SVD, respectively. The red vertical line indicates the true location of the target.

2.2.4 Performance Metrics

Some metrics have been used to evaluate the imaging algorithms performance, assessing the quality of the detection of the targets under study. The target detection (T) is calculated considering the value of the voxel with highest intensity of the whole image ($\max(T)$) and the surrounding voxels connected to that voxel with intensity above half the maximum ($\max(T)/2$). The remaining voxels correspond to clutter (C), which is

originated by common and random reflections or unidentifiable sources. The following metrics are used to evaluate the imaging results obtained in this thesis:

- **Signal-to-Clutter Ratio (SCR)**: Ratio between the maximum intensity of the detection ($\max(T)$) and the maximum intensity of clutter ($\max(C)$). It is a measure of contrast between the target and the remaining image. Some authors [93], [114] define a positive detection when the SCR is higher than 1.5 dB.
- **Signal-to-Mean Ratio (SMR)**: Ratio between the maximum intensity of the detection ($\max(T)$) and the mean intensity of the clutter ($\text{mean}(C)$). It measures how easily the target can be identified within the image.
- **Full Width Half Maximum (FWHM)**: Average distance between the coordinates of the maximum intensity of the detection and the voxels where the intensity drops to half ($\max(T)/2$) in all dimensions of the image. It measures the extent of the detection and can be comparable with the dimensions of the target.
- **Localisation Error (LE)**: Distance between the coordinates of the maximum intensity of the detection ($\max(T)$) and the true location of the target. It measures the effectiveness of detecting the target in the correct position and can be considered acceptable if it is within the dimensions of the target.

2.3 Evaluation of Microwave Imaging with Phantoms

Anatomically realistic phantoms of the body are essential to complete a pre-clinical validation of medical MWI systems. These phantoms must represent the true dielectric behaviour of the tissues and the true shape and sizes of the structures of interest under examination. In the following sections, the relevant concepts for the development of such phantoms are presented. Firstly, the state-of-the-art of the dielectric properties of breast tissues and ALNs are reviewed. Secondly, the most used phantoms and tissue mimicking materials for pre-clinical MWI validation are described, including MRI-based phantoms. Finally, the basic concepts of MRI and image processing algorithms are reviewed.

2.3.1 Dielectric Properties

The interaction of biological tissues with electromagnetic fields is described by their dielectric properties. The information about the dielectric properties of the tissues one wants to image is relevant to perform feasibility studies of a new MWI device. The detection of targets in MWI is possible when there is dielectric contrast between tissues at microwave frequencies. Relative permittivity and conductivity are the most relevant dielectric properties at microwave frequencies, and largely depend on the water content

of the tissues. The complex relative permittivity, which corresponds to the dielectric constant, varies over frequency (ω) and is defined as follows:

$$\epsilon^*(\omega) = \frac{\epsilon}{\epsilon_0} = \epsilon_r'(\omega) - j\epsilon_r''(\omega) \tag{2.8}$$

where ϵ is the complex absolute permittivity, and $\epsilon_0 = 8.854 \times 10^{-12}$ F/m and corresponds to the permittivity of free-space. The real part of the relative permittivity (ϵ_r') is often called "relative permittivity" and is a measurement of how much energy from an external electric field is stored in a material [115]. The effective electrical conductivity (σ) is related to the dissipation of energy [115], is measured in Siemens per meter (S/m) and can be retrieved from the imaginary part of permittivity (ϵ_r'') through the following equation:

$$\sigma(\omega) = \omega\epsilon_0\epsilon_r''(\omega) \tag{2.9}$$

The ratio between ϵ_r'' and ϵ_r' is called dissipation factor or loss tangent and is often represented by $\tan\delta$ [115].

The frequency-dependent dielectric properties measurements are commonly fitted by Debye or Cole-Cole models, written as follows:

$$\epsilon^*(\omega) = \epsilon_\infty + \frac{\Delta\epsilon}{1 + (j\omega\tau)^{1-\alpha}} + \frac{\sigma_s}{j\omega\epsilon_0} \tag{2.10}$$

where ϵ_∞ is the permittivity at $\omega = \infty$; $\Delta\epsilon = \epsilon_s - \epsilon_\infty$ where ϵ_s is the static permittivity; σ_s is the static conductivity at $\omega = 0$; τ is the relaxation time constant, which is the time required for the displaced system, aligned with an electric field, to return to $1/e$ of its equilibrium value; and α allows to describe different spectral shapes. These five parameters are the Cole-Cole parameters which are calculated through the least-square fitting of measured data. The Debye model is defined by the same equation with $\alpha = 0$.

The dielectric properties of biological tissues have been widely studied in the last decades [116]. The most used conventional technique to measure dielectric properties of biological tissues is the Open-Ended Coaxial Probe (OECP) which measures the reflection coefficient ($\mathbf{s}_{1,1}$) which is then used to calculate the complex permittivity $\epsilon^*(\omega)$. There are several uncertainty factors which might affect the accuracy of the OECP [117], [118], which includes the amount of pressure done to the tissues with the probe, and the level of hydration and temperature of tissues. Some guidelines have been recently suggested to ensure a correct interpretation of dielectric property measurements [119]. Most studies are performed using *ex-vivo* measurements, which have raised some concerns regarding the reliability of these results [120], [121] mainly when stability of tissue hydration is not ensured [122]. So *ex-vivo* measurements need to be carefully analysed when extrapolated to *in-vivo* scenarios. Additionally, one of the main challenges of the OECP is the measurement of heterogeneous structures since the original design of this technique assumes the tissue under test is homogeneous [123]. The results of measurements of heterogeneous tissues have been recently associated to

corresponding histology composition [124]–[126]. Authors have also shown each tissue does not contribute equally to the measured coefficient [127] and a recent study [128] showed tissues can shrink by up to 90% during histology, which might decrease the accuracy of the analysis.

Despite these challenges, there are some studies using OECP which are a reference for dielectric properties of the breast. One of the most comprehensive studies of breast dielectric properties was performed by Lazebnik *et al.* in *ex-vivo* samples. In a first paper [125], the authors focused on analysing the properties of normal breast tissues which included glandular, fibrous and adipose tissues. They performed the analysis considering 354 measurements in the frequency range from 0.5 to 20 GHz from patients undergoing breast reduction surgery. The samples were histologically analysed and were divided into three groups according to their tissue composition:

- **Group 1** contained samples with 0-30% adipose tissue, corresponding to high water content samples and more fibroglandular tissue;
- **Group 2** contained samples with 31-84% adipose tissue;
- **Group 3** contained samples with 85-100% adipose tissue, corresponding to low water content samples.

In a second paper [126], the authors addressed the differences between healthy, benign and malignant breast tissues. They performed the analysis of 160 samples (85 normal, 10 benign and 60 malignant) using the same frequency band (0.5 to 20 GHz). Due to the limited number of benign samples, no statistical analysis was performed with those samples. The malignant measurements were also grouped according to the percentage of malignant tissue. In order to ensure the number of samples included in the analysis of malignant tissues was representative, only samples with a minimum of 30% malignant tissue content (49 samples) were considered for analysis. The measurements from the limited number of samples with minimum 50% or 70% malignant tissue were not visibly different from the ones with lower content. Figure 2.11 shows the first and third quartiles and median curves of measurements with the malignant tissues and Group 1, 2 and 3 of healthy tissues after a Cole-Cole model fitting. At 5 GHz, the authors verified a contrast of only 10% between Group 1 (mostly fibroglandular tissue) and malignant tissues.

More recently, Sugitani *et al.* [124] measured 102 breast samples with adipose, normal and malignant tissues from 0.5 to 20 GHz. An average contrast between malignant and normal tissues higher than the 10% reported in Lazebnik's study was observed. However, lower contrast was observed in some intra-patient measurements. The authors also studied the volume fraction of tumour cells, which was quantified using photomicrograph images of histology. They verified a direct correlation between the

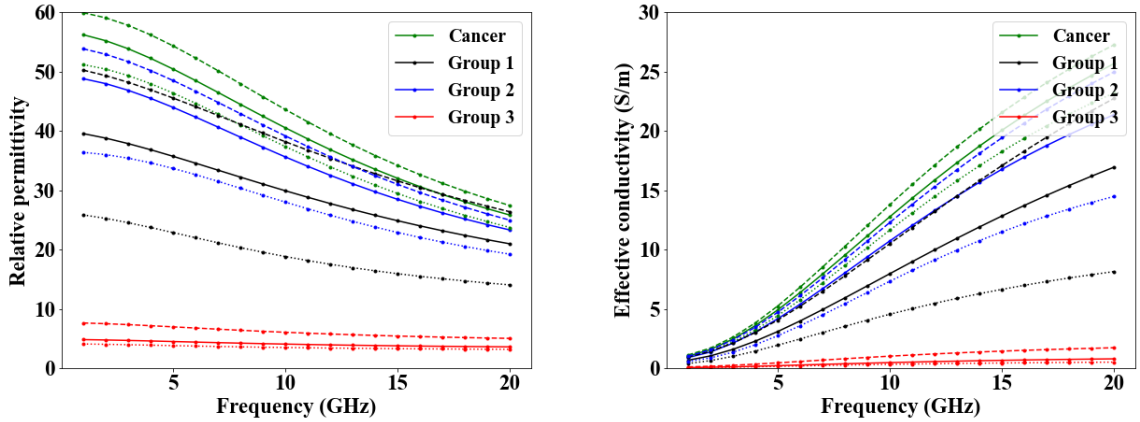

(a) (b)

Figure 2.11: Relative permittivity (left) and effective conductivity (right) of the measurements of normal and malignant breast tissues by Lazebnik *et al.* [126] over the frequency band from 0.5 to 20 GHz. The plots represent the first quartile (dotted line), median (solid line) and third quartile (dashed line) curves of each group: cancer tissue (more than 30% malignant tissue), group 1 (0-30% adipose tissue), group 2 (31-84% adipose tissue), and group 3 (85-100% adipose tissue).

volume fraction of tumour cells and dielectric properties, where a change of 0.5% of cell volume could result in a higher contrast of more than 10%.

Martellosio *et al.* [129] performed a similar study to Lazebnik *et al.*'s [125], [126] increasing the frequency range of study to 0.5 to 50 GHz. The authors conducted measurements in 166 samples of normal and 56 samples of tumourous tissues. The type of tumour was analysed in histology but no details were provided during the study. In the entire frequency range, the results showed a 20% to 30% contrast between high density healthy tissues and tumorous tissues, 45% to 55% contrast between medium density and tumorous tissues, and 80% to 90% contrast between low density and tumorous tissues. Considering how much the measured values of dielectric properties of healthy and unhealthy tissues intersected, the authors obtained a sensitivity of 86.5% and specificity of 73% on distinguishing both tissues in the entire frequency range.

The first study of dielectric properties measurements in lymph nodes was presented by Joines *et al.* [130], where only six metastasised lymph nodes were measured in a low frequency range from 50 to 900 MHz. Later, Choi *et al.* [57] performed measurements in 27 ALNs and 7 pure cancer tissues from 12 human patients in the frequency band from 0.5 to 30 GHz. They showed that both cancer tissues and metastasised ALNs have different responses from healthy ALNs, with a contrast of around 65% at 5 GHz, as shown in Figure 2.12. However, a detailed histology analysis was not presented neither was the accuracy of the measurements given the heterogeneity of the samples discussed.

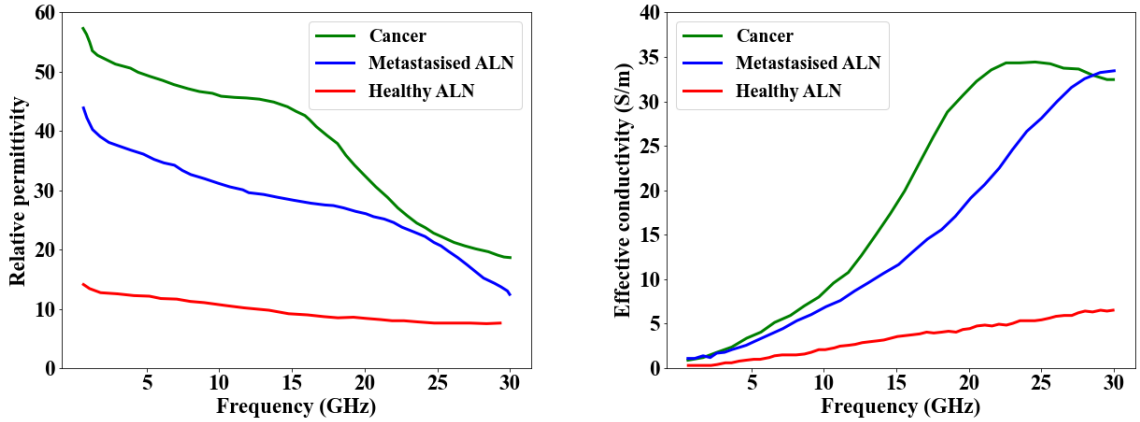

(a) (b)

Figure 2.12: Relative permittivity (left) and effective conductivity (right) of the measurements on healthy and metastasised ALNs, and cancer tissue by Choi *et al.* [57].

Cameron *et al.* [58] performed 30 measurements of 23 ALNs from 14 human patients in both external and cross-section surfaces. A large variability of relative permittivity values was observed within all measurements (5 to 55, at 5 GHz). They observed the measurements were highly affected by the adipose tissue surrounding the ALNs. Figure 2.13 shows the dielectric properties of 2 healthy and 1 metastasised ALNs. Healthy ALN 1 had 40% and 20% adipose tissue while Healthy ALN 2 had 47% and 10% adipose tissue, in the surface and cross-section measurements, respectively. The higher content of adipose layer on external surfaces measurements resulted in lower relative permittivity and conductivity. The Metastasised ALN 1 sample was measured with 34% and 60% of tumour content in the external and cross-section surfaces, respectively. No quantification of adipose content was reported in this case in order to explain the relationship between both healthy and metastasised ALNs. Additionally, the results were not conclusive due to the reduced number of measured samples and reported analysis.

Recently, Savazzi *et al.* [55] conducted a dielectric property study with 11 ALNs from 9 human patients and 8 ALNs from 2 sheep in the frequency range from 0.5 to 8.5 GHz. All ALNs were healthy verified pathologically. The human ALNs samples could not be punctured due to clinical constraints and these were only measured on the external surface in 3 to 5 points. The range of relative permittivity values was similar to the one of Cameron *et al.*'s study [58]: 5 to 55, at 5 GHz. The measurements were divided in three groups based on the range of relative permittivity values: Group 1-10, Group 10-40 and Group 40+. Group 1-10 corresponded to samples highly affected by adipose tissue and, therefore, the group was removed from the study. The authors suggested that measurements of Group 40+ are closer to the true ALN dielectric properties for two reasons: they corresponded to the samples where a larger amount of nearby adipose

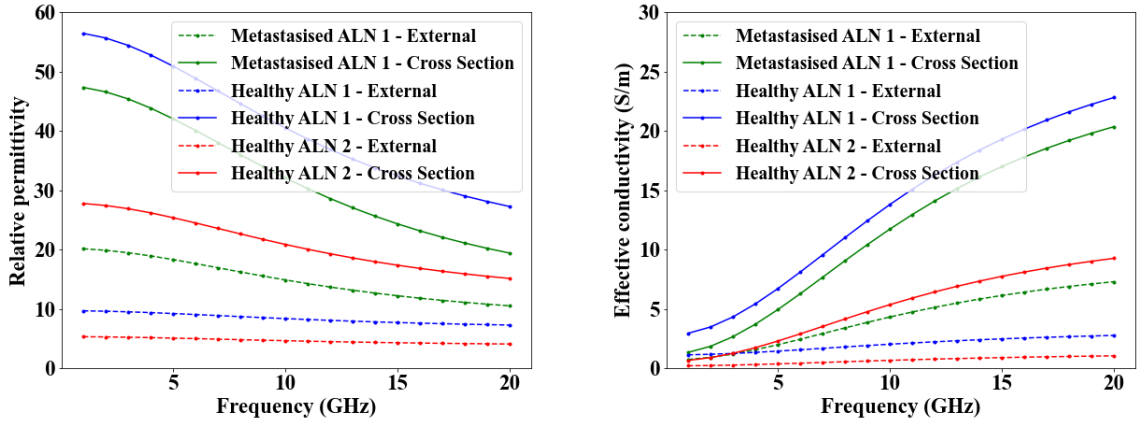

(a) (b)

Figure 2.13: Relative permittivity (left) and effective conductivity (right) of the measurements on healthy and metastasised ALNs by Cameron *et al.* [58].

tissue was successfully removed by the surgeon; and the measurements in this group showed a higher consistency across the same sample.

The sheep ALNs were measured both at the external and cross-section surfaces. They presented relative permittivity values ranging from 18 to 55 on the external surface and around 45 to 60 on cross-section surface at 5 GHz. The cross-section measurements with sheep ALNs showed higher dielectric properties than measurements with human ALNs on the external surface. Figure 2.14 shows the Cole-cole models fitted to the mean of the measurements of both Group 10-40 and Group 40+ of human ALNs and cross-section of sheep ALNs.

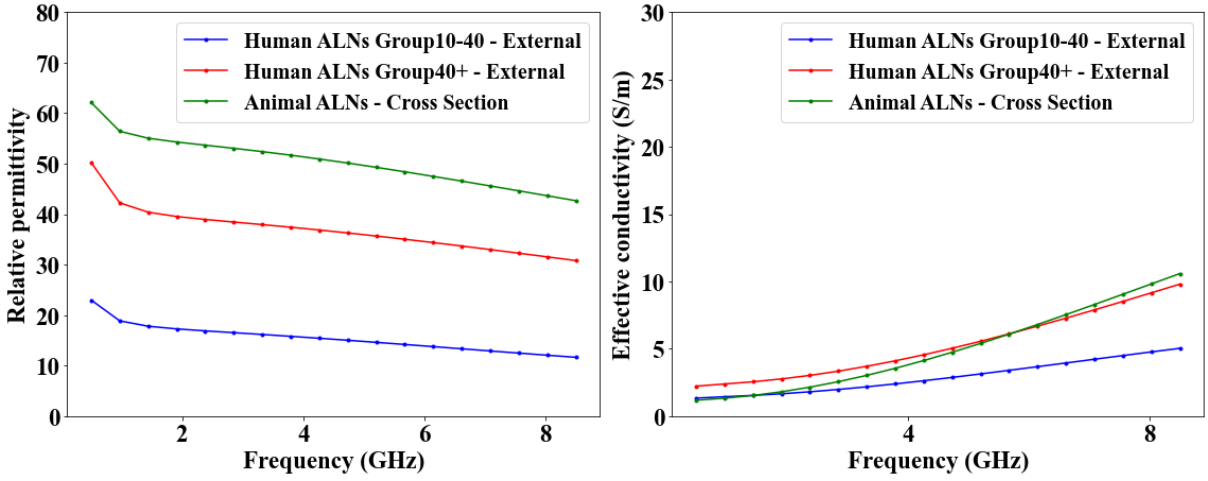

(a) (b)

Figure 2.14: Relative permittivity (left) and effective conductivity (right) of the measurements on healthy human and animal ALNs by Savazzi *et al.* [55].

Yu *et al.* [131] measured human intrathoracic lymph nodes (178 healthy and 41

metastasised) removed from lung cancer surgeries of 76 patients. Although the variability of the measurements was not shown in detail, the standard deviation showed a larger variability in healthy lymph nodes than in metastasised lymph nodes. Statistical tests demonstrated that differences between healthy and metastasised lymph nodes within the considered frequency range were significant. The results showed metastasised lymph nodes presented higher dielectric properties than healthy lymph nodes. However, the contrast decreases with frequency (from 19.8% to 18%) and the frequency range (1 MHz to 4 GHz) does not cover all the frequencies of interest for MWI applications (in most cases typically comprised in the 0.5 to 8 GHz range). Also, the cancer and LNs in the thorax region may not be comparable with ALNs metastasised by breast cancer.

In summary, there is still uncertainty regarding the level of contrast between malignant and glandular breast tissues and information about the dielectric properties of lymph nodes is still limited.

2.3.2 Phantoms and Tissue Mimicking Materials

MWI systems have been developed using simplified phantoms (e.g. spherical or cylindrical phantoms in the case of the breast) [110], [132] or MRI-based anthropomorphic phantoms. The latter are essential to ensure correct validation of MWI systems.

Numerical phantoms allow testing and validating algorithms in a more controlled environment using electromagnetic simulations. Several authors created MRI-based numerical breast phantoms for MWI validation [133]–[138] and three of them have shared them with the community. Zastrow *et al.* [133] provided an online repository with 9 MRI-based anatomically realistic breast numerical phantoms. This repository comprises healthy breasts divided in the four BI-RADS categories of breast density. Each breast is segmented into skin, muscle, and three levels of adipose and fibroglandular tissues inspired by the Group 1 and Group 3 curves of Lazebnik *et al.*'s paper [125] (see Section 2.3.1). Omer *et al.* [139] also created a repository with 12 breast numerical phantoms of 6 patients, one of them with carcinoma in the left breast. This repository provided phantoms in different format files and adaptable to vary the complexity of the phantom through different clusters of fibroglandular tissue. More recently, within my research group, Pelicano *et al.* [138] presented a repository with MRI-based numerical breast models and tumours.

Axillary region phantoms are more limited in the literature. Conceição *et al.* [140] implemented an algorithm to create a model of the axillary region, using CT data from Champalimaud Foundation. This was a preliminary study where the K-means clustering algorithm was used to segment tissues. However, these CT scans had low resolution between slices. Virtual population models [141] also include the axillary region but have limitations for MWI use. Namely, the positioning of the arm does not

allow a direct access to the axillary region, which is needed in an MWI device, and the model does not present variability of ALN shapes and pathology status.

The tissue dielectric properties are often associated to these numerical phantoms created for MWI validation. The dielectric properties are defined considering an average value for each tissue [137], [139] or considering an interpolation between voxel intensities of MRI and known dielectric properties curves [99], [133], [135], [138].

In more advanced steps of development, experimental validation of MWI systems becomes crucial and appropriate physical phantoms need to be developed. Generally, physical phantoms can be divided in two groups depending on the type of tissue mimicking materials used: solid phantoms and compartment phantoms filled with liquids.

In solid phantoms, each tissue is mimicked using solid mixtures with similar dielectric properties to the tissue of interest. Some authors have used TX151 with polythene powder and different amounts of water [103], gelatin and oil [142], or mixtures of carbon black, graphite and polyurethane [143], [144]. The dielectric properties of TX151-polythene powder-water mixtures can be unstable due to water evaporation, while gelatin and oil mixtures are sensitive to the environment and its shape can deteriorate in a short amount of time [145]. Carbon black, graphite and polyurethane mixtures are known for preserving dielectric properties over time but the creation of homogeneous mixtures with high dielectric properties can be challenging and limits the creation of complex shapes [146].

Compartment phantoms are the mostly used phantoms and comprise shells delimiting the different tissues cavities. Each compartment is then filled with a liquid mixture mimicking the corresponding dielectric properties of the tissue [147], [148]. Joachimowicz *et al.* [145] presented methodologies to achieve suitable mixtures of Triton® X-100 (TX-100) surfactant, water and salt (NaCl) which mimic the dielectric properties reported by Lazebnik *et al.*'s papers [125], [126] for breast adipose, fibroglandular and tumour tissues. Although liquid tissue mimicking materials are practical to use, they need to be carefully conserved in order to avoid water evaporation and consequent variation of dielectric properties. Rydholm *et al.* [149] have shown concerns regarding the effects of plastic shells of compartment phantoms in imaging results but other authors [55] have shown the differences with a numerical phantom with and without plastic are negligible.

A 3D-printed version of one breast phantom of Wisconsin-Madison repository was firstly presented by Burfeindt *et al.* [147] with cavities for adipose and fibroglandular tissue, and then adapted by Joachimowicz *et al.* [148] who added cavities to insert a tumour phantom. Recently, Reimer *et al.* [150] created 3D-printed phantoms of the remaining numerical phantoms. A first physical phantom of the axillary region was created by Savazzi *et al.* [55] from a CT image. This comprises compartments of the torso (partially), the muscles (including *pectoralis minor* and *major* muscles, *latissimum dorsi*, *serratus anterior*, and rib-cage muscles) and lung (partially), and a 3D-printed

solid bone structure. The lymph nodes were created as hollow ellipsoids, which can be filled with the suitable tissue mimicking liquid and can be attached to the muscle structure using a nylon string.

2.3.3 Magnetic Resonance Imaging for Phantom Development

As mentioned in Section 2.3.2, many numerical and physical phantoms are based on MR exams and several authors have used MRI information to model the dielectric properties of the tissues within the phantoms [99], [133], [135], [137]–[139]. In this thesis, we explore this methodology further to estimate the dielectric properties of ALNs. In this section, the basic concepts of MRI are explained in order to understand how a direct relationship between dielectric properties and voxel intensities can be assumed and how MR images are processed in order to create anthropomorphic models.

2.3.3.1 Main Concepts of Magnetic Resonance Imaging

MR images are based on the magnetisation of the angular momentum of Hydrogen nuclei by applying a static magnetic field (B_0) and magnetic field gradient (B_1). Several different sequences of excitations are used to give different information about different tissues allowing the visualisation of different tissues and detection of several pathologies.

The magnitude of the MR signal is related to the longitudinal magnetisation increase and the transverse magnetisation decrease which are often called T_1 recovery and T_2 decay, respectively (Figure 2.15). T_1 recovery is caused by the energy exchange between the nuclei and the surrounding environment and T_2 decay is caused by the magnetic fields of nuclei interacting with each other. The rate of recovery and decay are called relaxation times. Each tissue has different T_1 and T_2 relaxation times, which depend on the inherent energy of the tissue, how closely packed the molecules are and how well the molecular tumbling rate matches the frequency defined by the B_0 field (Larmor frequency) [151], [152].

Larger molecules like fat, which contain atoms of hydrogen closely packed with carbon and oxygen atoms, have slow molecular tumbling rates. The tumbling rate matches the Larmor frequency and therefore the energy exchange from hydrogen nuclei to the surrounding atoms is higher, which allows the T_1 recovery to be relatively fast. Since atoms are closely packed, the interaction between nuclei is more likely to occur, which means the T_2 decay is fast. Water molecules (H_2O) are usually spaced apart and their tumbling rate is relatively fast. This means it has both low T_1 recovery and T_2 decay since the energy exchange from hydrogen nuclei and the surrounding environment is low and the interactions are less likely to occur, respectively. These differences are exemplified in Figure 2.16.

Images with different contrast, such as T_1-weighted (T_1-w) and T_2-weighted (T_2-w) images, can be obtained by varying acquisition parameters, namely Repetition Time (TR) and Echo Time (TE). Since each tissue has its own magnetisation curve, the amplitude of the signal is different for each acquisition time.

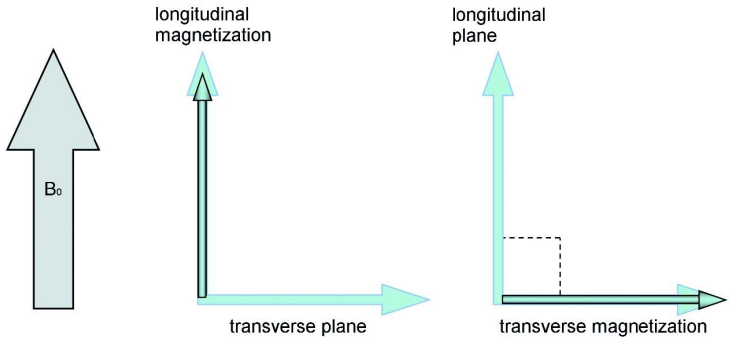

Figure 2.15: Magnitude of longitudinal and transverse magnetisation [151].

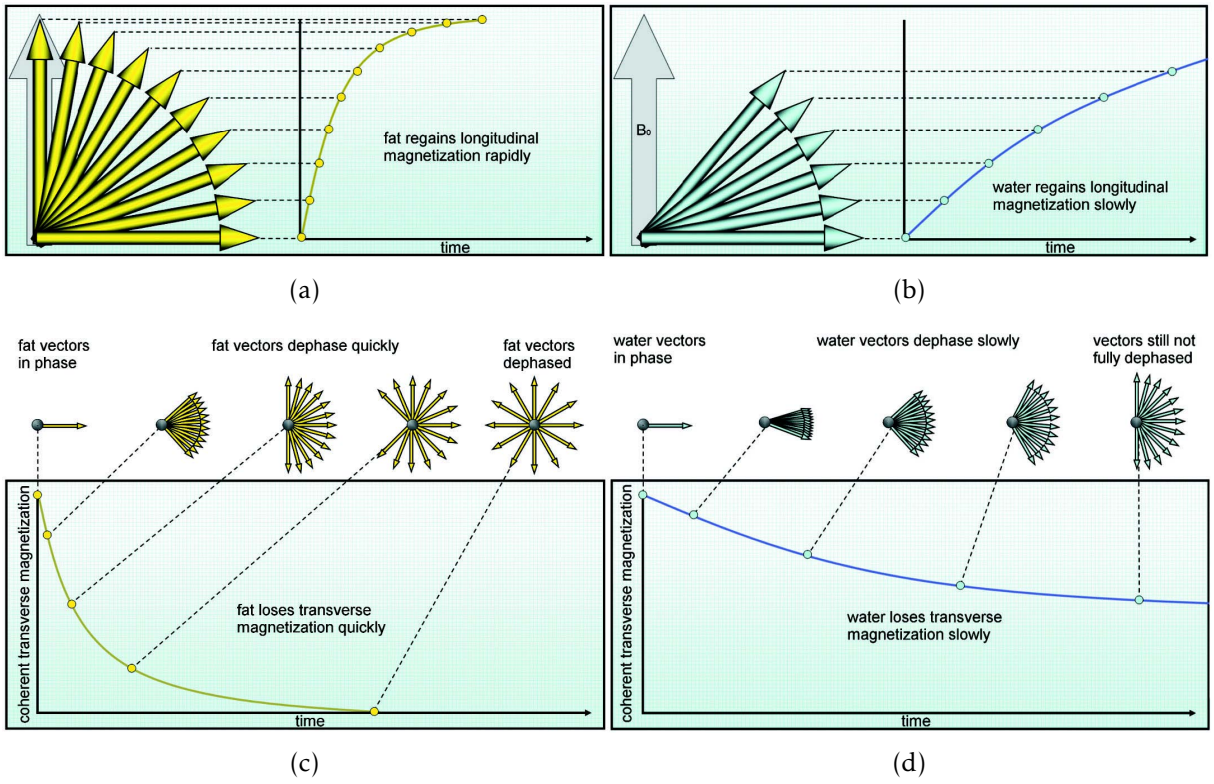

Figure 2.16: T_1 and T_2 relaxation times in both fat and water. (a) and (b) show the longitudinal magnetisation and T_1 relaxation time and (c) and (d) show the transverse magnetisation and T_2 relaxation time in fat and water, respectively [151].

One of the main image sequences used in the work developed in this thesis is the Dixon sequence [153]. The Dixon sequence [153] is not often considered in breast screening protocols because there are other sequences with faster acquisition that give similar clinical information. However, it has several advantages for image processing. It provides four set of images with different contrasts between tissues, which allows combining different image features. Several variations of this technique have been

presented but the original implementation consisted in acquiring images when both water and fat molecules had their angular momentum in phase (Dixon-IN) and when they were in opposed-phase (Dixon-OPP). The Dixon-Fat (Dixon-F) image is obtained from the difference between Dixon-IN and Dixon-OPP, and Dixon-Water (Dixon-W) image is obtained by summing both images. The inherent image combination between Dixon-IN and Dixon-OPP images reduces the artefacts due to inhomogeneities of the magnetic field.

Figure 2.17 shows examples of Dixon-W and Dixon-F images obtained with T_1-w and T_2-w Dixon sequences. The relation between intensities on each type of image is summarised in Table 2.2. In general, in T_1-w images, the voxel intensities are directly related to the amount of Hydrogen nuclei present in tissues, not only free water, and in T_2-w, higher voxel intensities are directly related to free water content. T_1-w Dixon-W provides a good contrast between tissues, except between muscle and bone, while T_2-w does not.

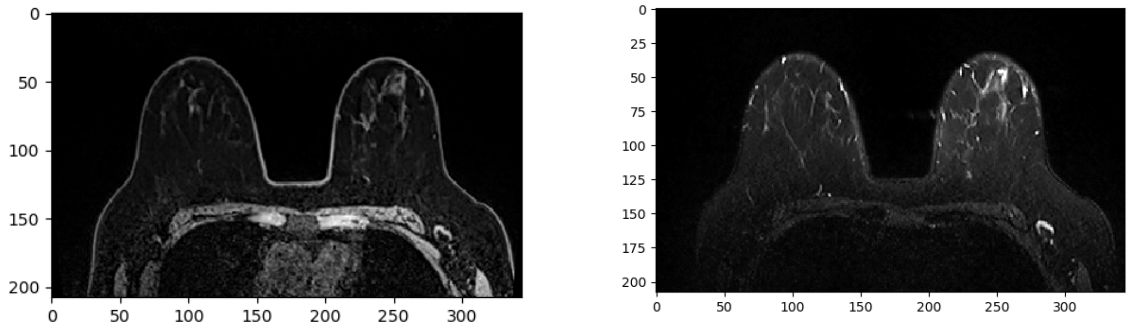

(a) (b)

Figure 2.17: Identical axial slices of (a) T_1-w Dixon-W and (b) T_2-w Dixon-W images. The voxel intensities are related to the water content of tissues and are different between the sequences.

2.3.3.2 Image Processing Algorithms

The state-of-the-art of image processing algorithms is vast but there are some algorithms which are commonly used for processing MR images, whether to improve the image quality or segmenting tissues. In the following sections, pre-processing and segmentation algorithms used in this thesis are described.

Inhomogeneity Artefacts Removal One of the main artefacts in MR images is the inhomogeneity of intensities of the same tissue within the image, which is often called bias field. The bias field is an artefact produced during the MRI acquisition due to the magnetic field, the patient and coil positions. This effect is observed mainly on the body

Table 2.2: Summary of image qualitative intensities in Dixon-W images.

	Qualitative intensity in Dixon-W	
Tissue	**T_1-w**	**T_2-w**
Water	Light Grey	Bright
Fat	Dark	Dark
Bone	Dark Grey	Dark Grey
Cartilage	Bright	Dark Grey
Muscle	Light Grey	Dark Grey
Air	Dark	Dark
Skin	Light Grey	Dark Grey
Fibroglandular	Light Grey	Light Grey
Lymph Nodes	Light Grey	Bright

parts further away from the coil and when the body is not symmetrically positioned relative to the coil.

Many bias field removal algorithms have been proposed, mainly for brain applications [154], [155]. A point-by-point methodology for bias field removal was also presented for breast bias field removal [135] but, since it is not an automatic process, this is not viable for larger volumes of the part of the body under study. An algorithm called N4 bias field removal [156], which is based on an improved non-parametric non-uniform intensity normalisation, has also shown promising results in removing bias field from breast MR images [137].

Considering a noise-free image, the N4 algorithm [156] can be written in the form $v(\mathbf{x}) = u(\mathbf{x})f(\mathbf{x})$, where v is the original image, u is the image without bias field and f is the bias field. The algorithm iteratively estimates the resulting image without bias field using a B-spline approximator, which creates smooth surfaces considering reference points of the image.

Noise Removal MR images are often corrupted by noise, such as Gaussian noise or salt and pepper noise, which result from inherent limitations of the acquisition system. The amount of noise can vary with field strength or voxel volume.

Spatial filters can be used for image noise removal and are applied by scanning the original image voxel by voxel considering the neighbour voxels defined by a kernel. The resulting voxel value can be calculated by applying the convolution between the voxels of the original image and the kernel, or by applying specific calculations to the voxels. The resulting image can be defined as a 3D function $g(x,y,z)$. The 3D-convolution between the original image $f(x,y,z)$ and a filter of size $(2a+1)\times(2b+1)\times(2c+1)$ for

each position (x, y, z) can be written as:

$$g(x,y,z) = h * f(x,y,z) = \sum_{dx=-a}^{a} \sum_{dy=-b}^{b} \sum_{dz=-c}^{c} h(dx,dy,dz) f(x+dx, y+dy, z+dz) \qquad (2.11)$$

where $h(dx, dy, dz)$ is the weight of the filter position (dx, dy, dz).

The conventional spatial filters used for image noise removal include the Gaussian and median filters. Both filters are able to remove isolated high intensity voxels and smooth transitions. The Gaussian filter is based on the Gaussian 1D-function $G(x) = \frac{1}{\sqrt{2\pi}\sigma} e^{-\frac{x^2}{2\sigma^2}}$, where σ is the standard deviation, which can be adapted for higher dimensions. Figure 2.18 shows an example of a 2D-convolution of an image with a Gaussian filter with $\sigma = 1$ for a specific pixel. The median filter calculates the median of the voxels in the considering kernel size. Considering the example of Figure 2.18, the resulting value of the highlighted pixel after applying a median filter corresponds to the median of $[23, 22, 21; 20, 50, 25; 27, 30, 25]$ which is 25. The median filter is quite effective for salt and pepper noise removal and causes less blurring effects than the Gaussian filter.

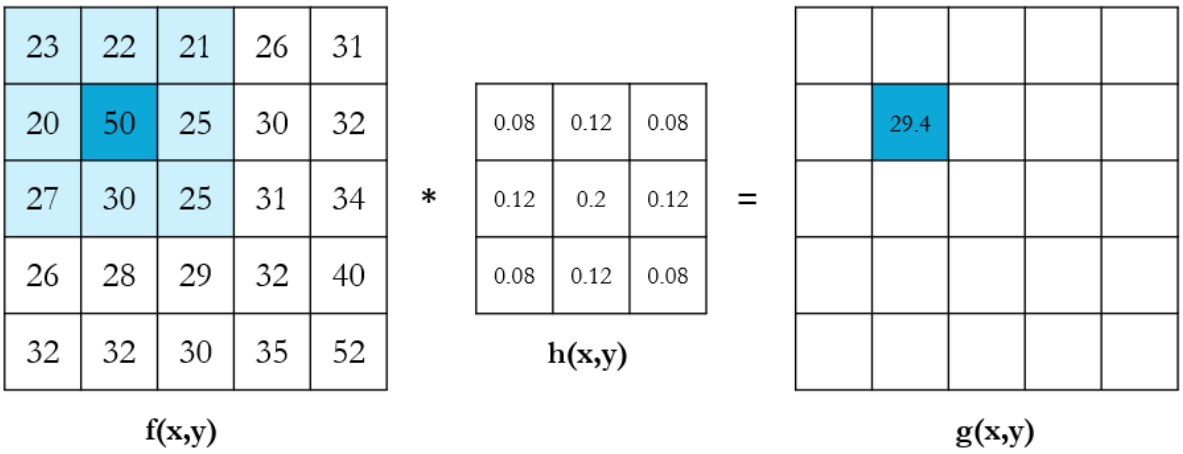

Figure 2.18: Example of a 2D spatial Gaussian filter of dimensions 3×3 with standard deviation $\sigma = 1$ applied to the highlighted pixel of a 2D image. $f(x, y)$ represents the original image, $h(x, y)$ represents the Gaussian filter and $g(x, y)$ is the resulting image.

Morphological Operations Morphological operations are non-linear operations which quantify shape or structural features in images. Although they can be applied to grey scale images, they are commonly used to process binary images and can also be used for noise removal.

The most common operations are called erosion, dilation, opening and closing and result from scanning an original binary image A with a structuring element S which can vary its shape [157]. Figure 2.19 shows an example of the four operations where the structuring element is a cross. The erosion operation removes the boundaries of

a binary object as well as isolated points. A voxel (x, y, z) becomes 1 in the resulting image only if the structuring element S is contained in the original image A:

$$A \ominus S = \{(x, y, z) : S_{(x,y,z)} \subset A\} \tag{2.12}$$

Dilation, as opposed to erosion, increases the size of the objects. A voxel (x, y, z) becomes 1 if at least one element under S is 1, which results in the union between S and A at each voxel:

$$A \oplus S = \bigcup_{(x,y,z) \in A} S_{(x,y,z)} \tag{2.13}$$

Opening and closing are two common compound operations which are the combination of erosion and dilation. Opening results from an erosion followed by a dilation and is often used to remove noise, while maintaining the overall shape of the objects. Closing is used to close small holes inside the objects and results from a dilation followed by an erosion.

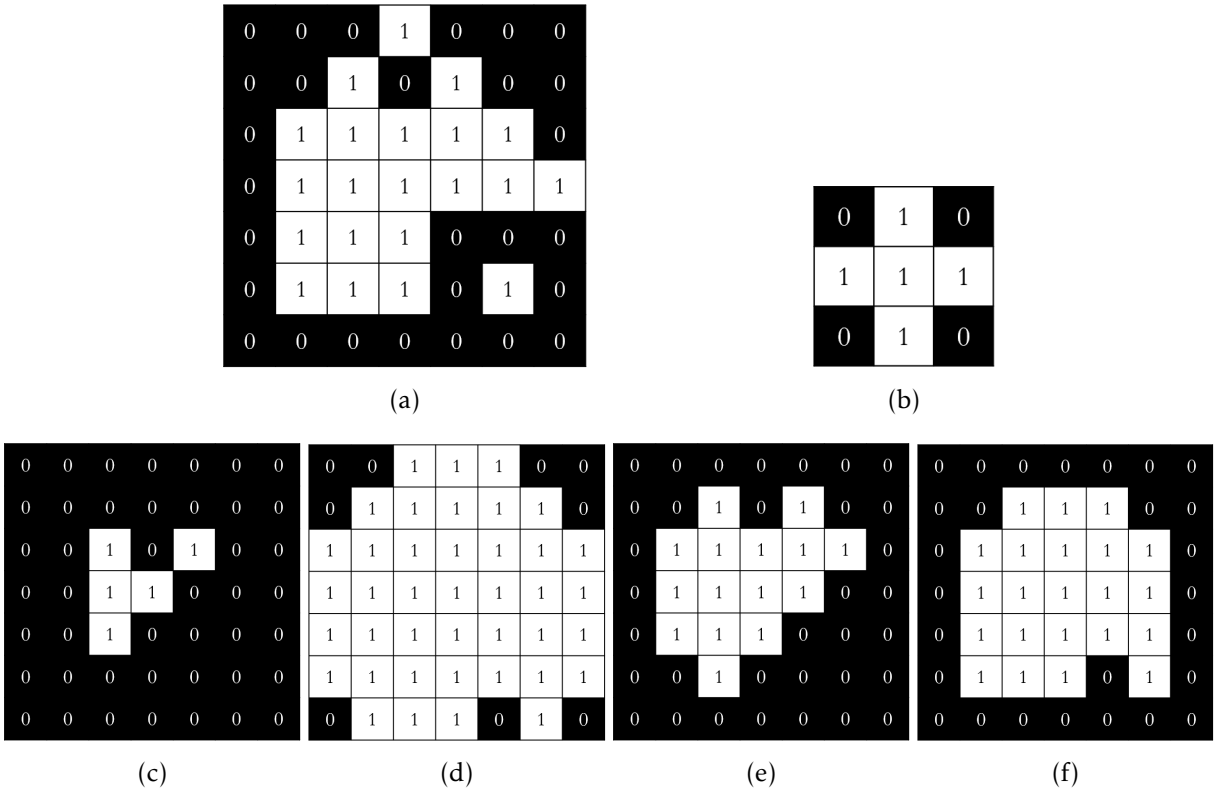

Figure 2.19: Examples of morphological operations applied to a binary 2D image. (a) represents the original image, (b) the structural element, resulting images after (c) erosion, (d) dilation, (e) opening and (f) closing operations.

Segmentation Segmentation algorithms are conventionally used to separate objects in digital images and can be divided in different categories based on their fundamentals. Thresholding, region-based and clustering methods are briefly described in this section, as a thorough description is out of the scope of this thesis.

Thresholding methods are computational fast algorithms which may provide satisfactory results. They can be used in a simple scenario where one wants to separate one object or multiple objects from the background. These methods consist of dividing the image in two classes (C_1 and C_2), by replacing each voxel of the image by 1 if the intensity value is greater than a defined threshold t and by 0 otherwise. In manual thresholding, the threshold t is empirically defined by the user considering prior knowledge, while other automatic thresholding methods use iterative processes to find the optimal value of t.

One of these automatic methods is the Otsu's thresholding [158] which is well-known for several applications including medical imaging segmentation [137], [159]. Otsu's method finds the optimal threshold through an iteration process aiming to maximise the inter-class variance ($\sigma_B^2(t)$) of the histogram of an image.

The Gaussian Mixtures Model (GMM) has also been used to segment adipose and fibroglandular tissues in breast MR images [133]–[135]. This algorithm comprises the fitting of two Gaussian curves to the histogram and uses the mean, standard deviation or FWHM to define a threshold t.

Region-based methods can be useful to segment multiple objects by considering the similarity of surrounding voxels. Region-growing algorithm is one of the most well-known region-based methods. Given a seed (i.e. the coordinates of a voxel) and the similarity feature (e.g. intensity value range, texture, colour), this algorithm segments the surrounding voxels as part of the region around the seed.

Connected-component labelling [160], as opposed to region-growing algorithm, does not need a seed to segment the objects. For grey-scale images, a similarity feature needs to be given, while for binary images, no additional input is needed. The algorithm consists of scanning the image considering an S structure element which defines the neighbouring voxels. Generally, the implementation of this algorithm can be described as the following: 1) the algorithm assigns one label to each voxel and creates an equivalence table which saves the labels of the neighbouring voxels; 2) Then, the label of each voxel is updated based on the equivalence table for the minimum label within each group of neighbours. Figure 2.20 shows an example of this algorithm.

Clustering methods are machine learning-based algorithms and can be used when one wants to segment multiple objects in one image based on its intensity values or other features, other than the voxels location. Clustering methods are non-supervised learning algorithms, which means that only the data is provided to the algorithm, i.e. no labels are provided. In medical imaging applications, the most commonly used clustering method for segmentation is K-means. K-means has shown good results handling MRI intensity inhomogeneities and noise [161] for brain tumor segmentation [162], and breast tissues segmentation [136]. K-means iteratively separates the data into K clusters/groups minimising the distance of the cluster centre (i.e. mean of the cluster) and each point of the cluster. It requires a dataset of one or more features

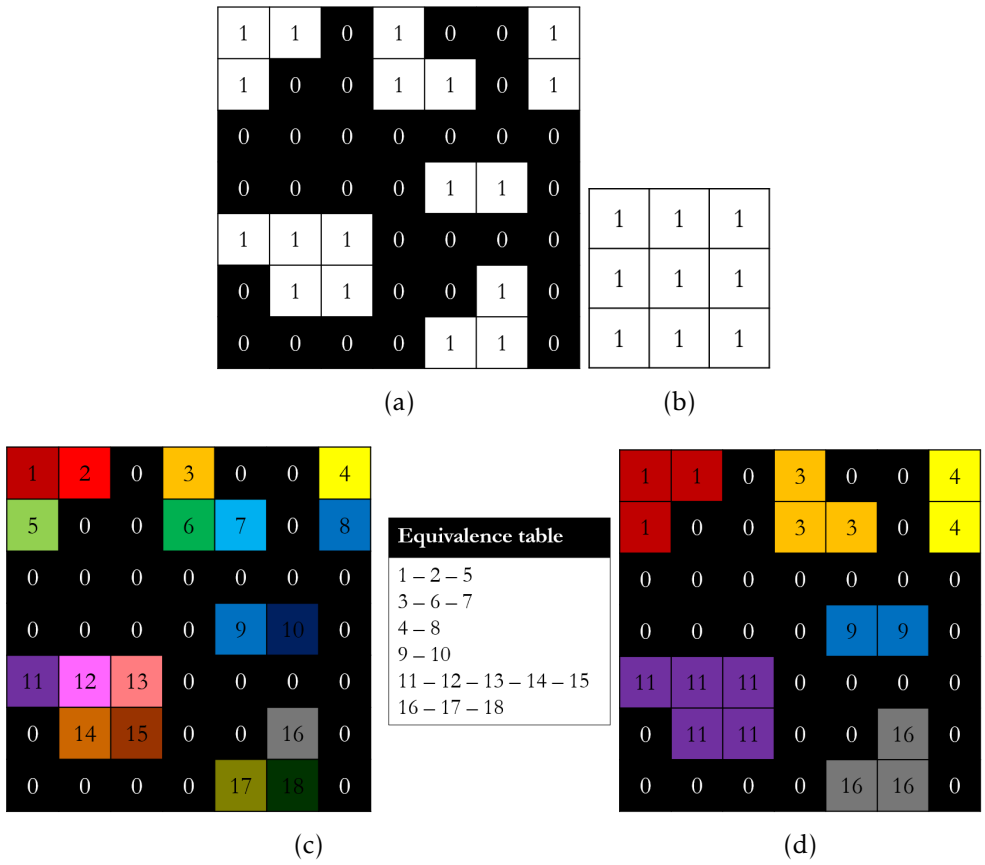

Figure 2.20: Example of a connected-component labelling algorithm applied to a binary 2D image. (a) represents the original image, (b) represents the structural element defining the neighbouring pixels, (c) represents the resulting image after the first scan with an equivalence table, and (d) represents the final image which segmented 6 objects based on their location.

and a parameter K which defines the number of clusters. K-means algorithm can be described in the following steps:

1. Randomly select K data points as the initial cluster centres;

2. Each data point is assigned to the closest cluster centre based on the shortest Euclidean distance;

3. The cluster centre is updated calculating the mean of the resulting clusters;

4. Step 2) and 3) are repeated until no further change of the cluster centres is verified.

In medical images, the common procedure is to use the intensity values as a single feature and the K parameter roughly corresponds to the number of tissues to segment. Other versions of this algorithm such as fuzzy C-means have also been developed. Contrarily to K-means, in fuzzy C-means, each data point has a probability value to belong to each cluster, which means each data point can belong to more than one cluster [163].

2.4 Supervised Machine Learning applied to Microwave Imaging

MWI signals carry different signatures depending on the observed target (e.g. tumour) and/or dielectric contrast. These signatures can be identified by Machine Learning (ML) algorithms and used to create models which can predict distinct scenarios. The information given by these algorithms can be important to complement imaging results. It can be used to differentiate between healthy from unhealthy tissues, or to help classifying multiple targets (e.g. tumours), since the main information in the image is their intensity value and may be challenging to interpret. Ultimately, when the quality of radar-based microwave images is hampered by other body structures, ML can also provide additional information that can not be observed in the reconstructed images with traditional algorithms (as the ones presented in Section 2.2.3). This information can be either used to feed image reconstruction algorithms, e.g. as has been done for head [164] or breast MWI [165], or to help the clinicians interpret the images and produce a preliminary diagnosis.

In particular, ML algorithms have been used to assess breast tumour detection i.e. to classify whether a breast has or does not have a tumour [166]–[169]. Another approach followed by other authors was to classify breast tumours as benign or malignant [170]–[174]. In these papers, the benign and malignant phantoms were created with distinct shapes and sizes. Benign tumours are often represented as round, while malignant tumours are represented as spiculated. Teo *et al.* [175] and Chen *et al.* [176] observed these phantom features have an effect on MWI signals. Accuracy values up to 96% were obtained when classifying benign and malignant tumour phantoms in simplified homogeneous breast phantoms [174]. Classification is more accurate when classifying tumours based on their sizes rather than their shape [170]. Recently, this type of algorithms has been implemented in prototypes used in clinical trials [94], [177], by estimating the probability of malignancy of breast masses and considering features extracted directly from microwave images. The breast tumours were classified with a 88.5% of accuracy [94]. These papers presented methodologies which can also be applied to lymph node classification in MWI prototypes based on their morphological features (see Section 2.1.3). To the best of my knowledge, no lymph node classification using MWI signals was ever performed.

In supervised learning, ML models receive the features of the data and their labels, which contain the class information of each data point, as input. In a binary classification, the classes can be, for instance, benign or malignant, or healthy or metastasised. The models are created through a training process which iteratively finds the patterns within each class in the given data. To perform the training process, the data can be divided into training, testing and validation set. The terminology of this division is

often interchanged in different research areas, but in this thesis they are defined as follows. The training set is used to train the classification model, based on the given labels, and the testing set is used to evaluate the performance of the model and optimise the classifier hyperparameters. The validation set corresponds to unseen data which gives a final performance evaluation of the created model.

A process named cross-validation is often used to generalise the results. One of the most common types of cross-validation is K-fold cross-validation. It consists of dividing the dataset into K groups, and perform K training iterations where $K-1$ groups are used for training and the remaining group is used for testing, ensuring the whole dataset is tested and each observation is tested only once. Leave-one-out cross-validation is a particular case of K-fold cross-validation where K is equal to the number of observations.

The performance of the models can be evaluated using several metrics, such as the accuracy, defined as the ratio between the correct classifications and the total number of observations. An accuracy value is considered good when it is substantially higher than the chance-level accuracy. In datasets with the same number of observations per classes (i.e. balanced) the chance-level accuracy is 50%. In unbalanced datasets, accuracy may be misleading when not compared with the chance-level accuracy, and metrics such as Matthews Correlation Coefficient (MCC) [178] may be used to help the interpretation of the results. MCC considers all the metrics from the confusion matrix as follows:

$$MCC = \frac{TP \times TN - FP \times FN}{\sqrt{(TP+FP)(TP+FN)(TN+FP)(TN+FN)}} \tag{2.14}$$

where TP is the number of true positives, TN is the number of true negatives, FP is the number of false positives, and FN is the number of false negatives. MCC takes values between -1 and 1, where $+1$ means a perfect classification, 0 means a random classification and -1 represents an inverse classification. Sensitivity (true positive rate) and specificity (true negative rate) are also used to measure the performance of the models.

In the following subsections, the commonly used Feature Extraction Methods (FEMs) and classifiers to classify MWI signals are reviewed.

2.4.1 Feature Extraction Methods

One of the most important steps of the machine learning and classification process is feature extraction. This step consists of finding the best features to represent the data one aims to use to train a model. When classifying MWI signals, the signals themselves can be used as features, i.e. each time or frequency sample corresponds to a feature. Nonetheless, other methods have been studied to extract features from these signals.

Principal Component Analysis (PCA) is one of the most used FEMs [166], [170], [172], [174], [179]. PCA applies an orthogonal linear transformation to multivariate data by maximising its variance. Considering a matrix $\mathbf{M}$ of dimensions $m \times n$, where m is the number of signals and n is the number of time or frequency samples, PCA transformation can be written as:

$$\mathbf{P} = \mathbf{MW} \tag{2.15}$$

where $\mathbf{W}$ is an $l \times l$ matrix of eigenvalues, where $l = \min[m; n]$, and $\mathbf{P}$ is the transformation matrix with the dimensions $m \times l$. The columns of $\mathbf{P}$ correspond to each principal component, which are independent between each other, and are ordered by decreased variance. Thus, the first components represent the major differences within the data. PCA can also be used for feature reduction, since the number of columns of $\mathbf{P}$ can be reduced, while maintaining the meaningful information needed to classify the data.

Customised FEMs have also showed promising results in multistatic MWI signals classification. These features may include time-domain features as the amplitudes and locations of peaks or variance, autocorrelation features or periodogram features [173].

2.4.2 Classifiers

A large range of classifiers have been used to classify MWI signals: linear and quadratic discriminant analysis [166], [170], [179], spiking neural networks [172], Naïve Bayes (NB) [174], k-Nearest Neighbours (kNN) [174], Support Vector Machines (SVM) [166], [179], [180], Decision Trees (DT) [174], Random Forests (RFO) [173] or even deep learning techniques [181], [182]. Exploring several types of classifiers with different characteristics is important when assessing new applications. Classifiers handle data differently, and therefore they can have different performances for different types of data. The following paragraphs address the basic fundamentals of some of these algorithms and the hyperparameters which need to be optimised when training a dataset.

The discriminant analysis algorithms include Linear Discriminant Analysis (LDA) and Quadratic Discriminant Analysis (QDA). LDA allows discrimination of classes with multivariate normal Gaussian distributions and similar covariance matrices. It calculates a linear combination as a weighted sum of the features. If the data has two features, LDA creates a line separator, while if it has more than two features, LDA creates a hyperplane. QDA allows discrimination of data which have different class-specific covariance matrices and multivariate normal Gaussian distributions with the same mean. The advantage of these algorithms is that they do not require a large amount of data and the computation is fast. There are two parameters that can be optimised: δ (only for LDA), which defines the minimum value of the coefficients in the weighted sum, and γ, which defines the amount of regularisation of the covariance matrices.

The NB is a probabilistic algorithm which assumes the features are independent. It is based on Bayes Theorem and considers conditional probabilities, i.e. the likelihood of each class occurring based on the occurrence of certain features. This algorithm also does not require a large dataset and has only one important hyperparameter to optimise: the type of distribution of the features.

The kNN algorithm classifies the data calculating the distance between each test data sample and the data used for training. The class assigned to each data point results from the majority vote of the k nearest neighbours [183]. The hyperparameters of kNN are the number of neighbours k and the function used to calculate the distance between data points.

The SVM classifier maps the input vectors into a high-dimensional feature space using a kernel and calculates a hyperplane that separates the data into classes [184]. The hyperparameter optimisation in SVM is of great importance to guarantee good classification results. The hyperparameters include the type of kernel used to separate the data and the inherent parameters of the kernel. One kernel example is the Radial Basis Function (RBF) which has a scaling factor γ used to control how the data is grouped. Another hyperparameter is the penalty parameter of the error term, usually represented by C, which balances the trade-off between the misclassified data and the margin of separation between classes [185]. SVM is effective in high dimensional spaces but the optimisation of hyperparameters may be time-consuming.

DT create models with a tree structure, splitting the training set into smaller learning problems [186]. DT include several hyperparameters. Two of the most important parameters are the split and pruning criteria, which define how the tree is created and how to decide which nodes are redundant and can be excluded from the tree, respectively. Missing values or outliers do not substantially affect the performance of decision trees but a small change on the data can affect the model. RFO are a combination of decision trees, which allows to reduce overfitting and improve generalisation of results when compared to an individual decision tree. In RFO, a random selection of the independent variables is implemented, generating independent vectors assigned to each decision tree [187]. Similarly to kNN, the classification result is the majority vote of all decision trees. The number of trees in the forest needs to be optimised, considering that for each dataset there is a value for which the performance saturates and stops improving [188]. All hyperparameters of DT are also hyperparameters of RFO.

2.5 Chapter Conclusions

This chapter presented important concepts that support the work developed in this thesis. Firstly, the breast and ALNs composition was presented showing the heterogeneity of both structures. Secondly, MWI systems concepts were reviewed, including the

type of systems and how the assessment of electromagnetic exposure safety can be performed. An overview about artefact removal and image reconstruction algorithms was also presented. Thirdly, a dielectric properties literature review was presented, showing the limitations and challenges of the measurements in breast and ALNs tissues. The type of phantoms and tissue mimicking materials used to validate the systems were described, as well as the main concepts of MRI and image processing methods which can be used to create anatomically realistic phantoms. Finally, ML applications in MWI were reviewed showing the viability of using such algorithms to classify structures using microwave signals.

The next chapter presents the evaluation of refraction effects in air-operated MWI systems, which precedes the presentation of the studies of two air-operated MWI systems to aid breast cancer diagnosis.

3 Refraction Effects in Air-Operated Microwave Imaging Systems

This chapter presents a qualitative and quantitative study of refraction effects on imaging results when using air-operated Microwave Imaging (MWI) systems. Refraction effects are more evident in air-operated imaging setups, which do not use immersion liquid for impedance matching, and are gradually receiving more attention in the literature. Authors have been considering a direct path between the antenna and the voxel on image reconstruction and the consequences of this assumption have yet to be quantified. Accounting for refraction computation in the image reconstruction algorithms can significantly increase the computational burden and be time consuming, which may hamper real-time image reconstruction. Therefore, it is relevant to know if these effects can be neglected without compromising the quality of the resulting images.

The results of this study can be generalised for different applications, although the examples represent some specific applications. Firstly, the refraction effects are evaluated with a numerical spherical phantom which can represent a simplified phantom of the breast or the head. Usually, antennas in the near-field produce spherical waves, but in specific cases the waves can become planar, as Chapter 7 will show. Hence, in this chapter, results with antennas producing spherical and planar waves are compared. Also, the influence of three parameters of the phantoms are analysed, namely: the average relative permittivity of the phantom medium, the targets size and the number of antennas. The relative permittivity of the medium is expected to be the major factor influencing the refraction effects since the physical phenomenon of refraction is directly related to the relative permittivity. Secondly, the refraction effects are analysed in realistic-shaped phantoms of the breast and the axillary region, in order to validate the observations performed in regular shapes. The computational time of the current implementations is also reported with both regular and irregular-shaped phantoms, using a computer with an Intel Core i7-7700 processor and 16 GB of RAM.

3.1 Formulation of Refraction Calculation

Refraction calculation is based on Snell's law as described in Section 2.2.3.2 and consists of calculating the incident and refracted ray paths to be included in the distances d_{air} and d_{diel} of the imaging algorithm (described in Section 2.2.3.1) as shown in Figure 3.1(a). However, the complexity of calculating the ray paths highly depend on the shape of the surface the ray paths go through. In the following sub-sections, two methods to calculate refraction are described.

3.1.1 Analytical Form

In spherical-shaped phantoms, the normal vector is radial to the surface, which simplifies the calculation of refraction [Figure 3.1(b)]. In this case, the Snell's law can be applied analytically (detailed in Appendix A). However, the calculation of the entry point on the surface for each voxel may result in multiple solutions. The appropriate solution is obtained by discarding imaginary solutions or by setting spatial restrictions (for instance, selecting shorter d_{diel}). Due to its efficiency in analytical calculations, the Wolfram Mathematica® software was used to compute the distances d^*_{air} and d^*_{diel} using the analytical form.

3.1.2 Ray Tracing Algorithm

For irregular-shaped phantoms where the normal vector is not easily determined, the analytical formulation is no longer viable. One alternative method is to compute refraction locally following the ray paths in a 2D scenario.

Given a 2D contour of the phantom and the coordinates of an antenna, several incident rays are traced towards the phantom [Figure 3.1(c)]. The refracted rays are then locally calculated with Snell's law at the intersection point between each incident ray and the phantom, assuming the refractive index n_{diel}. The distances d^*_{air} and d^*_{diel} are calculated from the rays that intersect each voxel v. When multiple refracted rays intersect a voxel v for the same antenna position, the voxel intensity is calculated as the contribution of the shortest ray path.

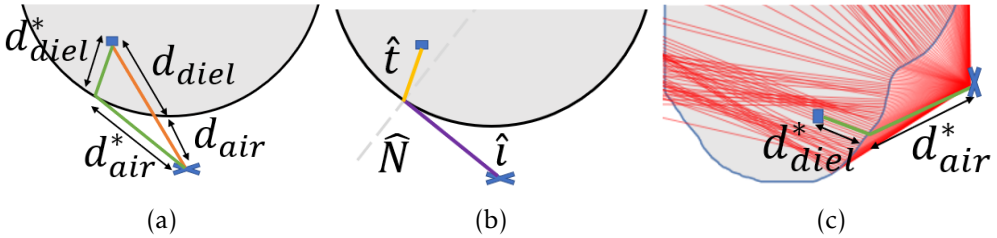

(a) (b) (c)

Figure 3.1: Schematics for refraction calculation with (a,b) analytical form and (c) ray tracing algorithm. The distances travelled in air (white background) and through the dielectric (grey background) when refraction is not considered are d_{air} and d_{diel}, and when refraction is considered are d^*_{air} and d^*_{diel}, respectively.

This algorithm was implemented in MATLAB® software to compute the distances d^*_{air} and d^*_{diel}.

3.2 Evaluation with Regular Phantoms

This section presents the study of refraction effects in regular shapes using a spherical phantom with two targets inside. The analytical formulation presented in Section 3.1.1 was considered to calculate the refracted ray paths.

All elements in this study were simulated using Computer Simulation Technology (CST) Studio Suite® software [189], which allows designing antennas and objects, and simulating the propagation of the electric and magnetic fields produced by antennas. The simulated signals are then used to reconstruct the images with and without the calculation of refraction. An ideal artefact removal is considered to avoid adding other confounders to the study. This means $\mathbf{s}_{i,j}$ is the difference between the simulated response with all components (dielectric phantom, targets and antennas) and the simulated response without the targets.

The state-of-the-art performance metrics Signal-to-Clutter Ratio (SCR), Signal-to-Mean Ratio (SMR), Full Width Half Maximum (FWHM), and Localisation Error (LE) (defined in Section 2.2.4), are used to quantitatively evaluate the refraction effects. Two additional metrics are considered in this study, the Maximum Magnitude Ratio (MMR) and Distance Error (DE). MMR is the ratio between the maximum magnitude of the image when refraction is not considered and the maximum magnitude of the corresponding image when refraction is considered. MMR equal to 1 means the magnitude does not change between compared images. DE is the average difference between the full electrical distance ($d_{air}+n_{diel}d_{diel}$) between each antenna position i and each voxel v when considering or not considering refraction. DE can be compared to the theoretical range resolution, which can be defined as:

$$\Delta d = \frac{c}{2n_{diel}\Delta f} \tag{3.1}$$

where c is the speed of light in vacuum, n_{diel} is the refractive index of the dielectric and Δf is the frequency bandwidth.

3.2.1 Geometry for Numerical Analysis

The geometry for the numerical analysis comprised a 50 mm radius homogeneous dielectric sphere with a relative permittivity ϵ_r and a loss tangent $\tan(\delta) = 0.1$. Two Perfect Electric Conductor (PEC) spheres with radius r_t were embedded in the phantom and used as targets. To illustrate the refraction effects in a scenario with targets placed

in asymmetrical positions, they were placed at coordinates $(x, y, z) = (-10, 30, 0)$ and $(20, -20, 0)$ mm.

The system was simulated in a monostatic configuration using a planar slot-based single-layer printed antenna formed by two crossed exponential slots, called Crossed Exponential Tapered Slot Antenna (XETS) [190], [191] [Figure 3.2(a)]. The antenna is impedance matched from 2 to 6 GHz and has the dimensions of 28 mm radius and 0.26 mm thickness. This antenna has a highly stable radiation pattern and phase centre, as well as pure linear polarisation along the entire bandwidth. Figure 3.2(b) shows the corresponding reflection coefficient plot. $\mathbf{s}_{1,1}$ is less than -10 dB in the working frequency band, which ensures a good performance of the antenna. This frequency band is commonly used for medical MWI applications, including imaging of the breast and the head [49], [192].

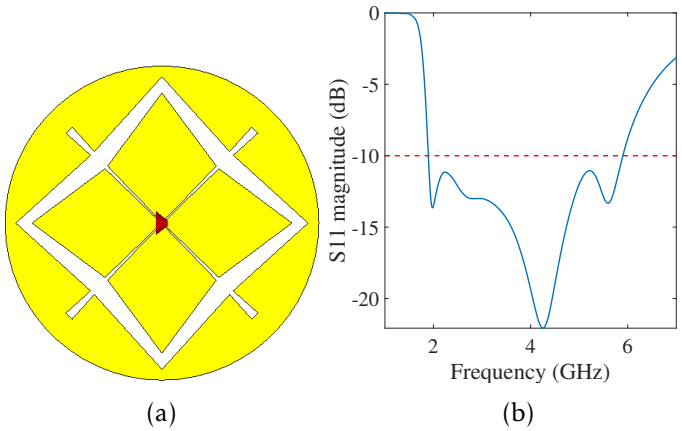

Figure 3.2: (a) Schematic of XETS and (b) plot of the corresponding S-Parameter (magnitude in dB).

The XETS is swept around the spherical phantom in an 80 mm radius circumference (i.e. 30 mm away from the sphere surface) contained in the plane $z = 0$ mm. The antenna is simulated in a total of equidistant N_a positions, with an angular step of $\frac{360^\circ}{N_a}$. Figure 3.3 shows the positioning of the antenna for three different values of N_a. This positioning of the antennas means $z = 0$ mm is the plane with highest resolution. Therefore, although the refraction calculations are performed considering a 3D geometry, only the results from the 2D plane $z = 0$ mm are analysed.

Before proceeding with MWI studies, the electrical distance offset of the antenna needs to be calculated so it can be included in the image reconstruction algorithm as mentioned in Section 2.2.3.1. To this end, a PEC plane is simulated in front of the XETS. The difference between the highest reflection point and the physical distance to the PEC plane corresponds to the electrical distance offset. Figure 3.4(a) shows the XETS placed at a distance of 100 mm away from the PEC plane, while Figure 3.4(b) shows the plot of the signal intensities reconstructed with the imaging algorithm in 1D, where the highest reflection point is shown at 138 mm. Therefore, the electrical

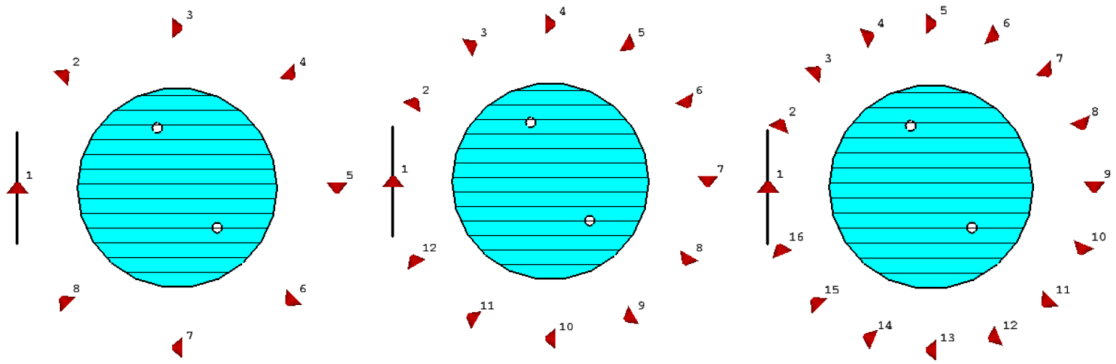

(a) $N_a = 8$ (b) $N_a = 12$ (c) $N_a = 16$

Figure 3.3: Schematics of varying number of equidistant antenna positions (N_a) around the spherical phantom.

distance offset of the XETS is 38 mm.

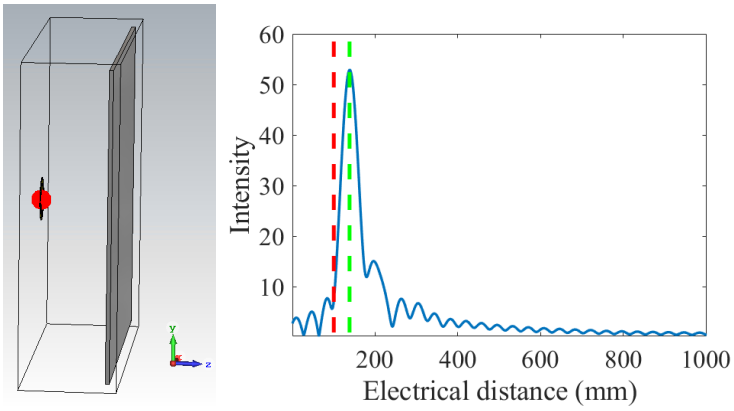

(a) (b)

Figure 3.4: Screenshots from the CST simulation with a PEC in front of the XETS antenna. (a) shows the setup and (b) the plot of the signal intensities reconstructed with the imaging algorithm in 1D, where the red dashed line corresponds to the physical location of the PEC plane and the green dashed line corresponds to the maximum value of intensity.

In the following sections, the refraction effects are qualitatively analysed when spherical and planar waves can be considered for two average relative permittivity values: $\epsilon_r = 4$ and 40. Then, the influence of the three parameters (relative permittivity, targets size and number of antennas) are presented and discussed quantitatively. The average relative permittivity of the phantom takes the values $\epsilon_r = 4, 8, 20, 40$, targets radii take the values $r_t = 2.5, 5, 7.5$ mm and the number of antennas takes the values $N_a = 8, 12, 16$. The average relative permittivity values were chosen to represent different applications. A value of $\epsilon_r = 4$ or 8 represents a fatty breast, while $\epsilon_r = 40$ represents average head tissues.

3.2.2 Spherical and Planar Waves

An XETS antenna in the near-field radiates in the radial direction which results in spherical waves. If the antenna is placed at a large distance away from the phantom, the waves can be considered planar. In this sub-section, the refraction effects in both situations are analysed, in order to evaluate whether imaging results are differently affected when spherical or planar waves are present, and analyse the existence of blind regions. To this end, the resulting images are reconstructed using only one antenna position.

When considering spherical waves, the antenna is located at coordinates $(x, y, z) = (0, -80, 0)$, and phantoms with average relative permittivity media $\epsilon_r = 4$ and 40 are compared. The target size is fixed at $r_t = 5$ mm. Figure 3.5 shows the resulting images considering spherical waves with the two average relative permittivity values. When $\epsilon_r = 4$, both targets are detected, but the target nearest to the antenna position is detected with higher magnitude and, as expected, the response of the farther away target is attenuated by the medium. In both cases when refraction is and is not considered, there is only a slight change in the shape of the detection but its location is similar. When $\epsilon_r = 40$, the farthest target from the antenna is not detected. Two main reasons justify this observation: 1) a high average permittivity medium implies higher attenuation of electromagnetic waves; 2) there is a blind region in the location of the target, which can be observed when using the algorithm of refraction computation [Figure 3.5(d)]. Also, for high permittivity media, the detection of the target nearest to the antenna position is more accurate when refraction is considered than when it is not. The existence of blind regions might hamper the detection of targets in high average permittivity phantoms.

For a very specific case where the waves are planar, the antenna is located at coordinates $(x, y, z) = (0, -305, 0)$. The targets are symmetrical in position $(x, y, z) = (\pm 30, 0, 0)$ in order to avoid adding confounders to the interpretation of refraction effects. Figure 3.6 shows the resulting images considering only a permittivity value ($\epsilon_r = 4$) which shows the existence of a blind region even for this low permittivity value, in contrast with what happens with spherical waves [Figure 3.5(a-b)]. This means that even when considering low average permittivity values, planar waves might result in blind regions, hampering target detection.

In both cases (spherical and planar waves), the effects of these blind regions can be reduced if more antenna positions are used, as the blind regions of different antenna positions are not completely superimposed.

3.2.3 Relative Permittivity

Figure 3.7 shows the performance metrics when refraction is or is not considered in the image reconstruction algorithm for average relative permittivity values, with fixed

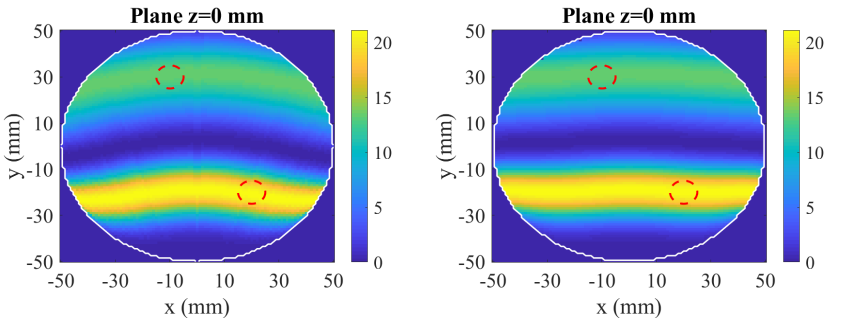

(a) $\epsilon_r = 4$, No Refraction (b) $\epsilon_r = 4$, Refraction

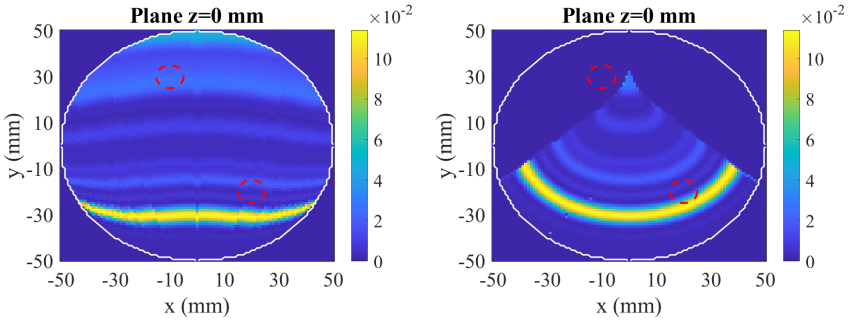

(c) $\epsilon_r = 40$, No Refraction (d) $\epsilon_r = 40$, Refraction

Figure 3.5: Reconstructed images in the xy-plane of the spherical phantom with only one antenna position and fixed $r_t = 5$ mm, while considering spherical waves. (a,b) show the images considering a medium with $\epsilon_r = 4$, and (c,d) show the images considering a medium with $\epsilon_r = 40$, when (a,c) not considering and (b,d) considering refraction. The red dashed circles represent the true location and size of the targets.

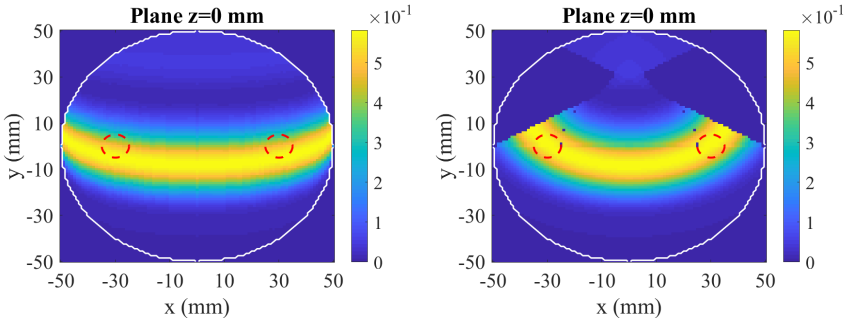

(a) $\epsilon_r = 4$, No Refraction (b) $\epsilon_r = 4$, Refraction

Figure 3.6: Reconstructed images in the xy-plane of the spherical phantom with only one antenna position, $\epsilon_r = 4$ and fixed $r_t = 5$ mm, while considering planar waves, when (a) not considering and (b) considering refraction. The red dashed circles represent the true location and size of the targets.

$r_t = 5$ mm and $N_a = 16$. Figure 3.8 shows the corresponding imaging results.

As illustrated in Figure 3.8(a-d), for low to moderate average relative permittivity values ($\epsilon_r = 4$ and 8) refraction calculation may be discarded, as the target is detected correctly in both cases. The targets are detected with different magnitudes whether refraction is or is not considered due to the different positioning of the targets in relation to the surface. MMR is lower than 1 when refraction is considered, thus showing better energy focusing. However, both SCR and SMR are comparable when refraction is or is not considered for both average relative permittivity values, as shown in Figure

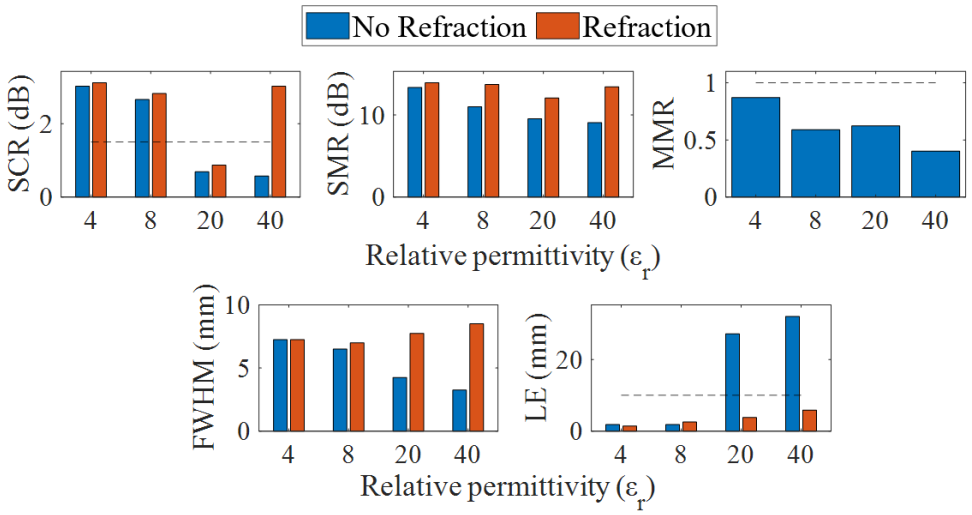

Figure 3.7: Performance metrics when varying the relative permittivity value ($\epsilon_r = 4, 8, 20, 40$) of the spherical phantom for fixed values $r_t = 5$ mm and $N_a = 16$.

3.7(a-b). Both FWHM and LE are within the targets size (10 mm diameter) and do not change substantially when refraction is considered.

When ϵ_r increases, the benefits of refraction calculation are observed, which is an indication it should be considered in image reconstruction. Figure 3.8(e-h) shows that, for both $\epsilon_r = 20$ and 40, the image is better focused when considering refraction, which results in an MMR lower than 0.5. The effect of the blind regions can be observed in Figure 3.8(f,h) but the effects are minimised since the number of antennas is sufficient to compensate the blind regions and cover the imaged region. When considering a phantom with $\epsilon_r = 40$, SCR indicates that the targets detection is only possible when refraction is considered [Figure 3.7(c)]. SMR also increases and shows the improvement of the detection when refraction is considered. Moreover, FWHM increases when considering refraction, which is a result of the focusing of the rays in the correct location. LE decreases when considering refraction, with both targets detected correctly. When $\epsilon_r = 20$, FWHM and LE behaviour is similar when refraction is considered which indicates that targets are focused and detected in the correct location. However, low SCR, even when refraction is considered, means the identification of the targets is not reliable. This can be explained by the level of clutter around the target which can be observed in Figure 3.8(f).

DE is 3.1, 11.9, 23.7 and 38.9 mm for $\epsilon_r = 4$, 8, 20 and 40, respectively. These values illustrate there is a large difference in the computation of distances when refraction is or is not considered for higher average relative permittivity ϵ_r. Furthermore, the range resolution Δd is 18.7, 13.3, 8.4 and 5.9 mm for $\epsilon_r = 4$, 8, 20 and 40, respectively. DE is not higher than Δd for lower average relative permittivity, which corroborates refraction may be disregarded in these conditions. For higher average relative permittivity, refraction computation has a clear impact on imaging results and should be computed.

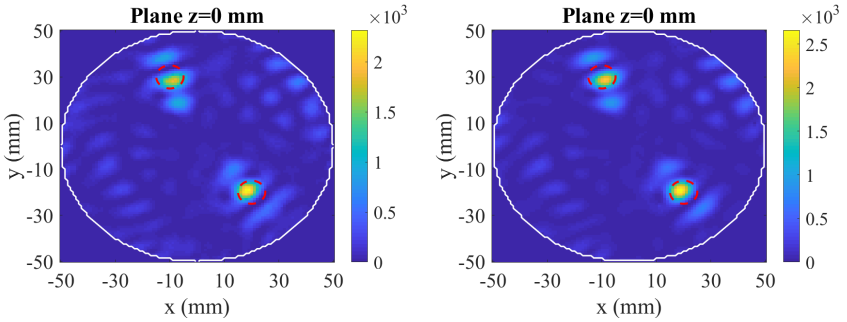

(a) $\epsilon_r = 4$, No Refraction

(b) $\epsilon_r = 4$, Refraction

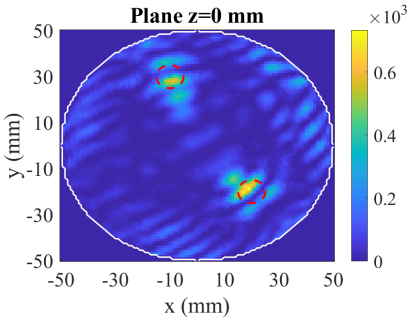

(c) $\epsilon_r = 8$, No Refraction

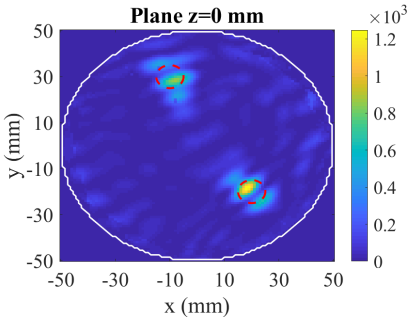

(d) $\epsilon_r = 8$, Refraction

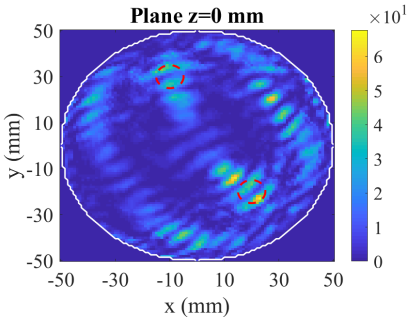

(e) $\epsilon_r = 20$, No Refraction

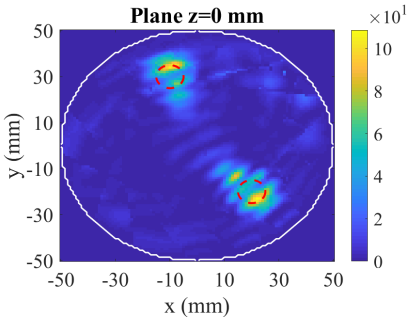

(f) $\epsilon_r = 20$, Refraction

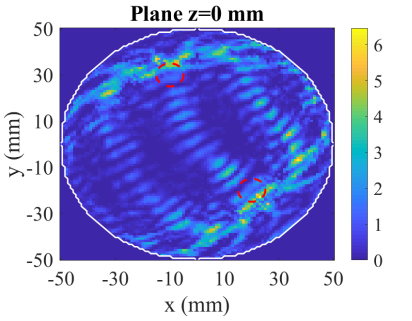

(g) $\epsilon_r = 40$, No Refraction

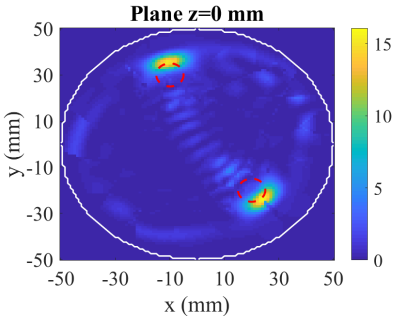

(h) $\epsilon_r = 40$, Refraction

Figure 3.8: Reconstructed images in the xy-plane of the spherical phantom with fixed $r_t = 5$ mm and $N_a = 16$, when not considering (left) and considering (right) refraction. The red dashed circles represent the true location and size of the targets.

3.2.4 Size of Targets

For conciseness, the refraction effects on imaging phantoms with different targets size are presented using only $\epsilon_r = 4$ and 40, and $N_a = 16$. Two additional targets size were

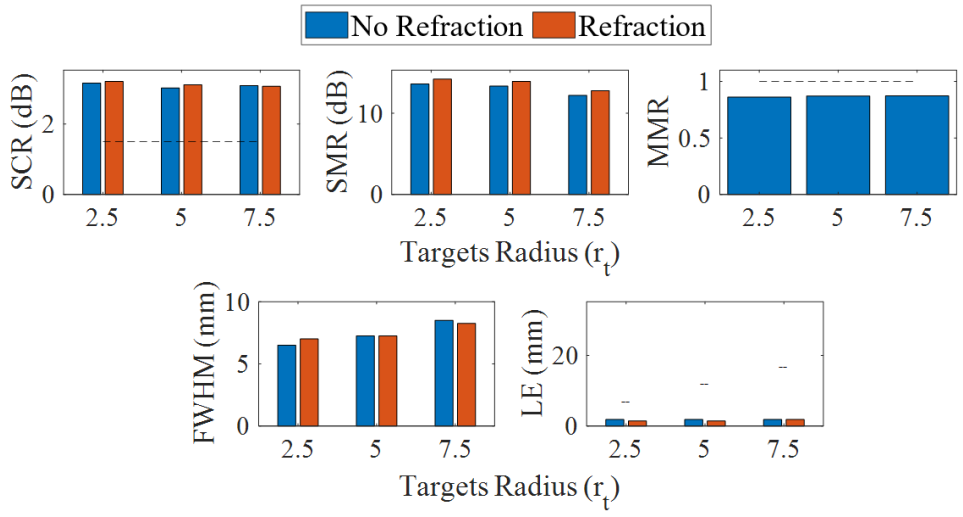

(a) $\epsilon_r = 4$

(b) $\epsilon_r = 40$

Figure 3.9: Performance metrics when varying the targets radius ($r_t = 2.5, 5, 7.5$) embedded in the spherical phantom ($\epsilon_r = 4, 40$ and $N_a = 16$).

assumed: 2.5 and 7.5 mm in radius.

Figure 3.9 presents the resulting performance metrics. Figure 3.10 shows the resulting reconstructed images which can be compared to Figure 3.8(a,b,g,h) where $r_t = 5$ mm. The impact of computing refraction on SCR, SMR and FWHM does not depend on the size of the targets considered, for both average relative permittivity values (ϵ_r). LE behaviour only changes for a particular test where $\epsilon_r = 40$ and $r_t = 7.5$ mm. In this test, LE is within the size of the targets whether refraction is or is not considered. Nonetheless, refraction is relevant to ensure the target is detected with high SCR and a FWHM within the targets dimensions, as shown in Figure 3.10(g-h). The size of the targets does not affect DE.

These results demonstrate that the influence of refraction on the targets detection in both low and high average relative permittivity phantoms is independent of the size

of the targets, which is unknown in most cases.

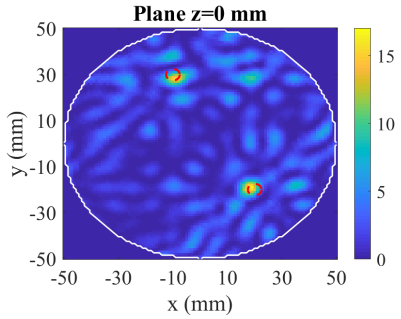

(a) $\epsilon_r = 4$, $r_t = 2.5$ mm, No Refraction

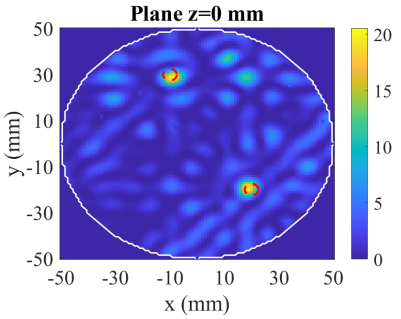

(b) $\epsilon_r = 4$, $r_t = 2.5$ mm, Refraction

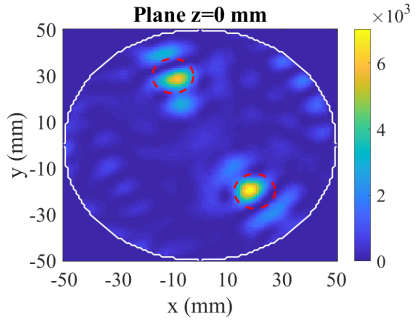

(c) $\epsilon_r = 4$, $r_t = 7.5$ mm, No Refraction

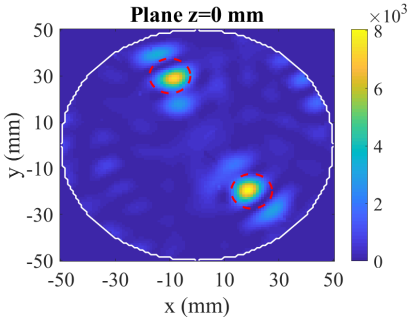

(d) $\epsilon_r = 4$, $r_t = 7.5$ mm, Refraction

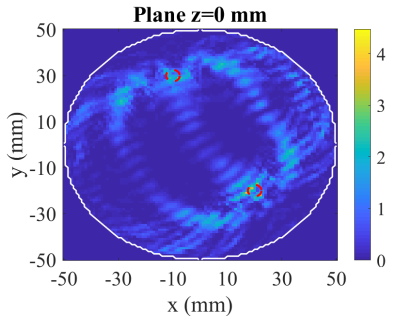

(e) $\epsilon_r = 40$, $r_t = 2.5$ mm, No Refraction

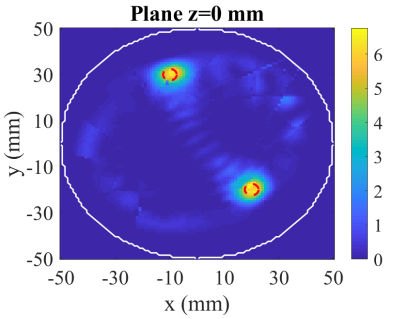

(f) $\epsilon_r = 40$, $r_t = 2.5$ mm, Refraction

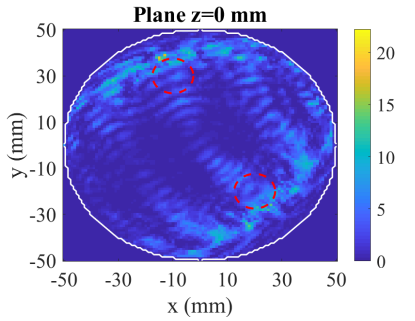

(g) $\epsilon_r = 40$, $r_t = 7.5$ mm, No Refraction

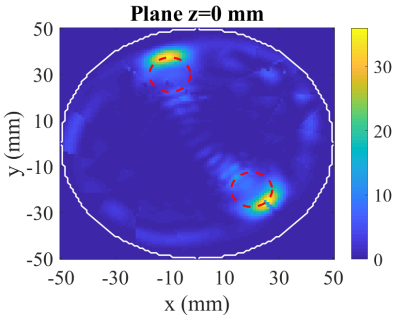

(h) $\epsilon_r = 40$, $r_t = 7.5$ mm, Refraction

Figure 3.10: Reconstructed images in the xy-plane of the spherical phantom with fixed $N_a = 16$, when not considering (left) and considering (right) refraction. The red dashed circles represent the true location and size of the targets.

3.2.5 Number of Antennas

The results of the study with varying number of antennas were obtained using $\epsilon_r = 4$ and 40 and $r_t = 5$ mm. Three different sets of number of antenna were compared: $N_a = 8$, 12 and 16. These antennas were placed around the spherical phantom as shown in Figure 3.3.

Figure 3.11 shows the resulting performance metrics and Figure 3.12 shows the reconstructed images where $N_a = 12$ and 8. These can be compared with the images in Figure 3.8(a,b,g,h), which were reconstructed with $N_a = 16$. For low average permittivity values, in particular $\epsilon_r = 4$, refraction does not impact imaging results regardless the number of antennas used. When the average permittivity value is higher, in particular $\epsilon_r = 40$, refraction is important to improve imaging results for both $N_a = 16$ and 12. SCR and SMR increase in both cases when refraction is considered with an SCR higher than 1.5 dB. For a lower number of antennas, the targets are not detected whether refraction is considered or not. This can be explained by the existing blind regions, reported in Section 3.2.2, which are larger when a lower number of antennas is used. Varying the number of antennas does not affect DE.

3.2.6 Computational Cost

The computational cost of refraction computation is addressed implementing the calculation of distances considering and not considering refraction. As mentioned in Section 3.1.1, Wolfram Mathematica® software was used to compute these distances using the analytical form.

The average computational time of distances calculation for the considered geometry when refraction is not considered is 19.20 seconds, conversely when refraction is considered, the calculation takes 1610.59 seconds. This means that, in this example, the inclusion of refraction increases image reconstruction time by approximately 84 times.

3.2.7 Partial Conclusions

The results with a spherical phantom show refraction effects are important to be considered in high average relative permittivity media regardless the size of the targets. Moreover, the results corroborate that one should use the largest number of antennas as possible around the phantom, to ensure better focusing of the image. This is observed when refraction computation does not substantially improve the imaging results when a low number of antennas is used. In situations of low to moderate average relative permittivity phantoms, the improvement of imaging results when considering refraction is not sufficient to justify the associated increase of computational cost, independently of the target size and number of antennas used.

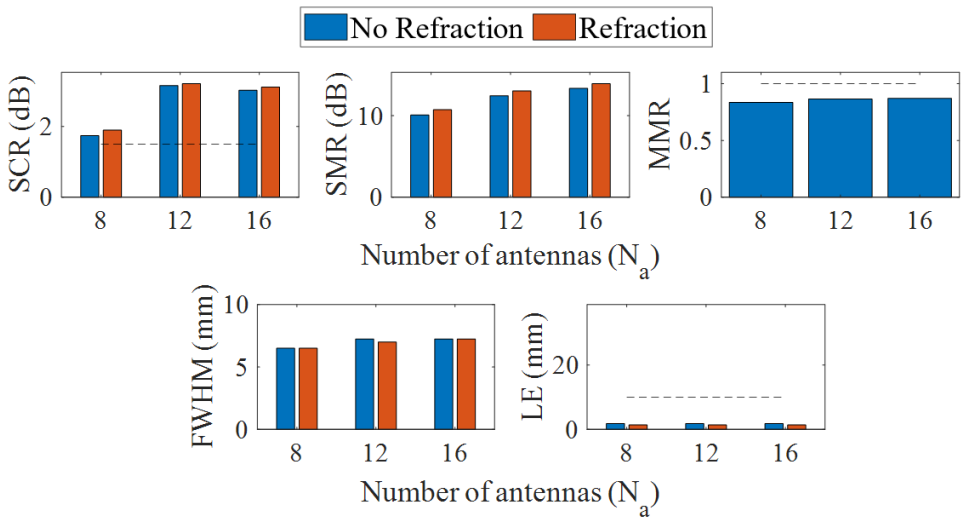

(a) $\epsilon_r = 4$

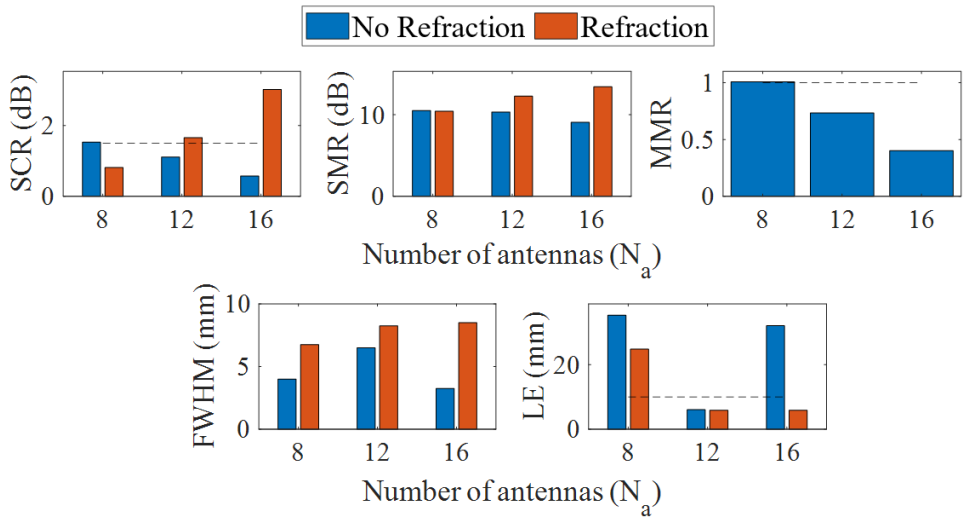

(b) $\epsilon_r = 40$

Figure 3.11: Performance metrics when varying the number of antennas ($N_a = 8, 12, 16$) used to obtain the images of the phantom ($\epsilon_r = 4, 40$ and $r_t = 5$ mm).

3.3 Validation with Anthropomorphic Phantoms

In this section, realistic-shaped phantoms are used to confirm if the conclusions regarding refraction computation with the spherical phantom can be generalised for more complex shapes.

Therefore, the ray tracing algorithm described in Section 3.1.2 is used to calculate the refracted ray paths. The same artefact removal algorithm and performance metrics, as presented in Section 3.2, are used in the setups considered in this section.

Refraction is evaluated in two distinct monostatic setups: 1) a realistic breast phantom using the simulated signals on CST; 2) an axillary region phantom using an experimental prototype. These two different phantoms are motivated by the fact that breast is mostly convex, while the axillary region has both concave and convex surfaces,

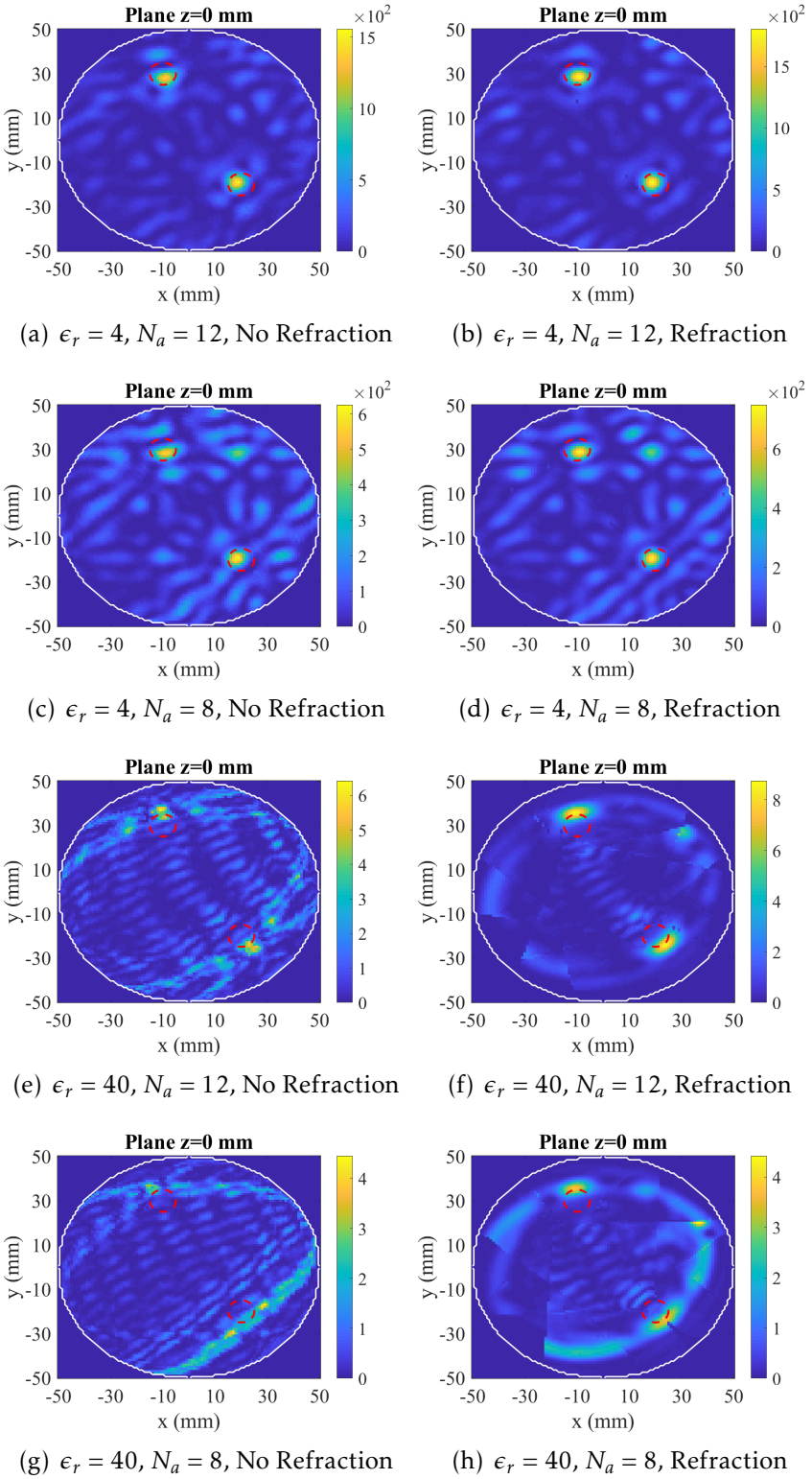

(a) $\epsilon_r = 4$, $N_a = 12$, No Refraction

(b) $\epsilon_r = 4$, $N_a = 12$, Refraction

(c) $\epsilon_r = 4$, $N_a = 8$, No Refraction

(d) $\epsilon_r = 4$, $N_a = 8$, Refraction

(e) $\epsilon_r = 40$, $N_a = 12$, No Refraction

(f) $\epsilon_r = 40$, $N_a = 12$, Refraction

(g) $\epsilon_r = 40$, $N_a = 8$, No Refraction

(h) $\epsilon_r = 40$, $N_a = 8$, Refraction

Figure 3.12: Reconstructed images in the xy-plane of the spherical phantom with fixed $r_t = 5$ mm, when not considering (left) and considering (right) refraction. The red dashed circles represent the true location and size of the targets.

which can result in different refraction effects. Figure 3.13 summarises the performance metrics with both phantoms.

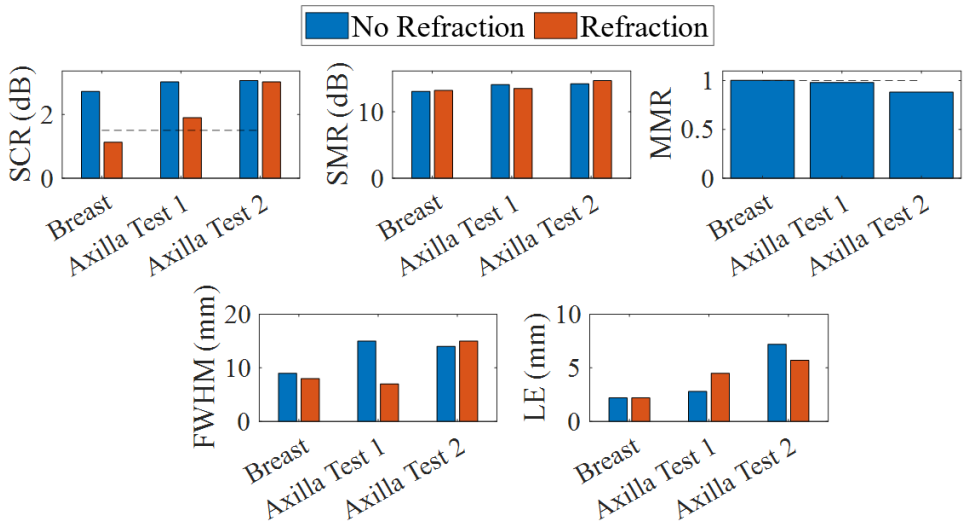

Figure 3.13: Performance metrics with anthropomorphic phantoms: a breast phantom and two planes of an axillary region phantom with $\epsilon_r = 8$.

3.3.1 Anthropomorphic Breast Phantom

A Magnetic Resonance Imaging (MRI)-derived breast phantom from the University of Wisconsin-Madison repository (ID: 062204) [147] was considered. It has a homogeneous medium of $\epsilon_r = 8$ and loss tangent of 0.1, which corresponds to the upper limit of adipose tissue permittivity [125]. A PEC target was embedded in the breast phantom at coordinates $(x, y, z) = (25, 0, -30)$ mm. Figure 3.14 shows the numerical setup of the anthropomorphic breast, where the antennas are placed in the xz-plane. The 2D shape of the breast in the xy-plane is more irregular, while the 2D shape on the xy-plane is similar to a circle (which was already studied in the Section 3.2). The XETS swept the breast with a radius of 80 mm in 7 equidistant antenna positions (angular step of 30°).

Figure 3.15 shows the imaging results of an axial plane of the breast, with antenna positions marked in magenta. The target is correctly detected, with LE within the target dimensions in both cases, as shown in Figure 3.13. MMR is 1 and no change is observed in SMR. SCR and FWHM decrease when considering refraction. However, no relevant artefacts in the resulting image are observed outside the region of the target when refraction is considered. DE is 7.9 mm which is in the same order of magnitude of Δd (13.3 mm).

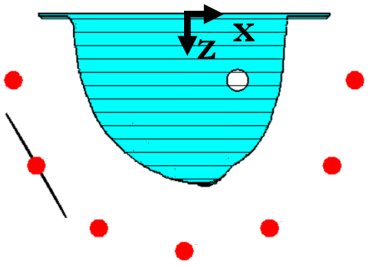

Figure 3.14: Numerical setup of the anthropomorphic breast with 7 antenna positions (represented by red dots) in the xz-plane.

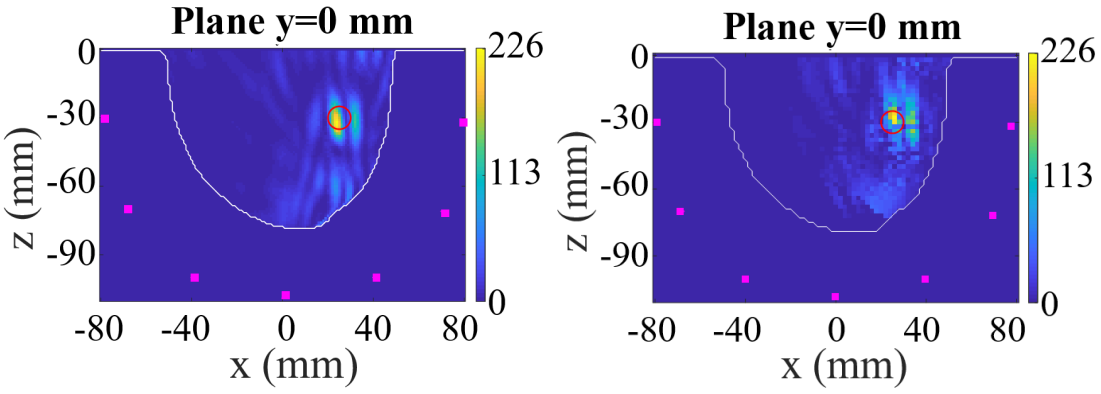

(a) (b)

Figure 3.15: Reconstructed images in the xz-plane of a realistic breast phantom with $\epsilon_r = 8$ when not considering (left) and considering refraction (right). The breast contour is represented in white. The red circle represents the true location and size of the target, and the magenta points represent the antenna positions surrounding the breast.

3.3.2 Anthropomorphic Axillary Region Phantom

The refraction effects in a 3D-printed axillary region phantom segmented from a Computed Tomography (CT) image were evaluated using an experimental prototype. This prototype was developed during this thesis and is described in detail in Chapter 5. The tests presented in this section result in placing a 3D-printed model of an Axillary Lymph Node (ALN) in two different positions inside the compartment of the axillary region phantom. The ALN model is a kidney-shaped model with dimensions $23.6 \times 17.6 \times 12$ mm^3. Both axillary region and ALN phantoms were filled with liquid mixtures [145] in order to mimic the dielectric properties of adipose tissue and ALNs, respectively. At 4 GHz, the dielectric properties were $\epsilon_r = 4$ and 55 and $\sigma = 0.01$ and 3.5 S/m for adipose and ALN mimicking mixtures, respectively.

A Vivaldi antenna was used to perform this study (originally presented in [95]) as it showed better imaging results in experimental tests [95]. This antenna is impedance-matched in the 2 – 7 GHz frequency band but the same frequency band used in the previous studies (2 – 6 GHz) was considered for image reconstruction. The Vivaldi antenna was swept in a total of 9 positions, with an angular step of 10°, in the same xy-plane as the target.

Figure 3.16 shows the imaging results of the two ALNs placed in different xy-planes of the axillary phantom, which correspond to axial planes of the torso. The results of both considered planes (test 1 and test 2) are similar, even though the axillary region shape is quite different between these planes. The ALN is correctly detected whether refraction is or is not considered.

DE is 6.2 and 12.1 mm for test 1 and 2, respectively, which are within the order of magnitude of Δd (18.7 mm). Both LE and FWHM are within the target dimensions in both tests whether refraction is considered or not. In test 1, SCR, SMR and FWHM decrease when refraction is considered and MMR is close to 1, as shown in Figure

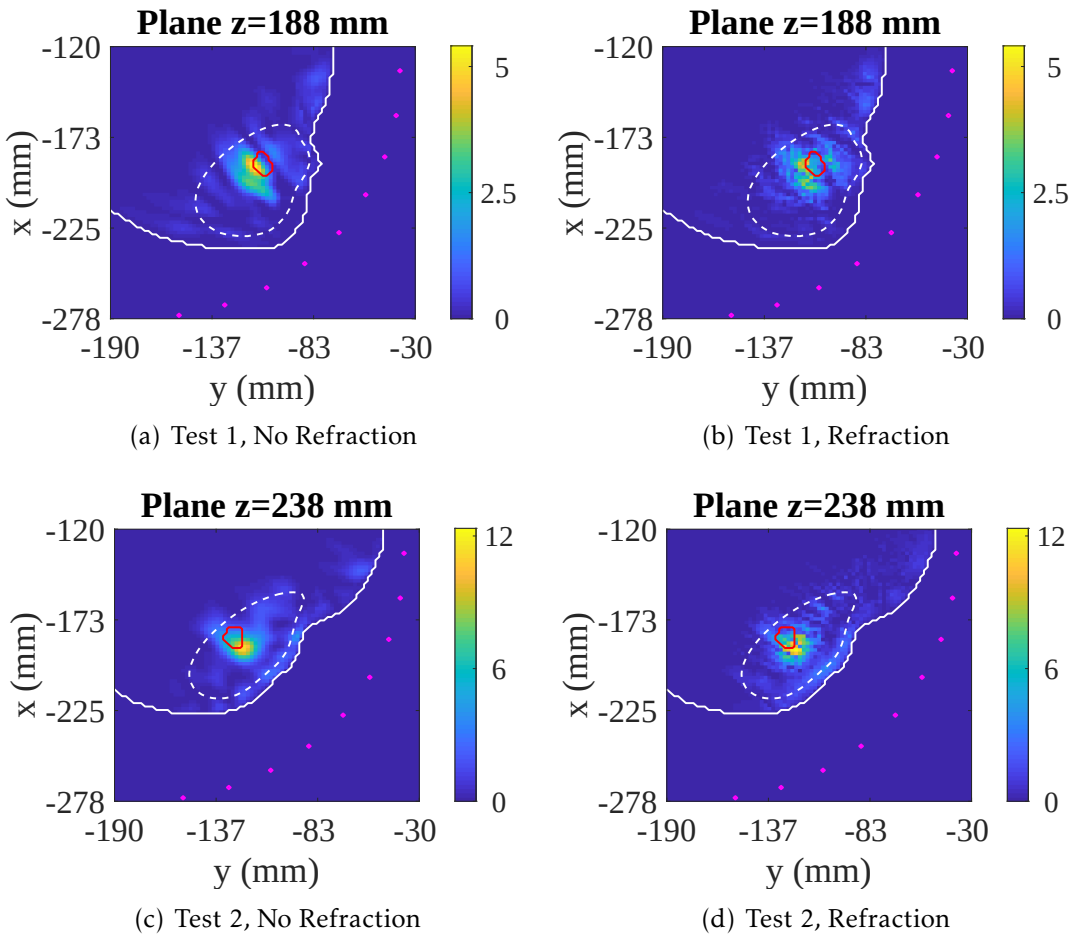

(a) Test 1, No Refraction

(b) Test 1, Refraction

(c) Test 2, No Refraction

(d) Test 2, Refraction

Figure 3.16: Reconstructed images in the xy-plane of an axillary region phantom when not considering (left) and considering (right) refraction. The red contour represents the true location and size of the target, the white solid contour represents the breast contour, the white dashed contour represents the region where the lymph nodes are likely to be located and the magenta points represent the antenna positions.

3.13. However, the ALN detection is still satisfactory, and no relevant artefacts are observed in Figure 3.16(a, b). In test 2, no substantial differences are observed in the performance metrics whether refraction is considered or not [Figure 3.16(c, d)].

3.3.3 Computational Cost

In contrast to the implementation of the calculation of distances using the analytical form with Wolfram Mathematica®, the ray tracing algorithm was implemented in MATLAB®. These values are not directly comparable to the ones presented in Section 3.2.6, since a different software was used. In this case, the computational time of refraction computation highly depends on the shape complexity and the size of the imaged region.

For the breast shape, the computational time of the calculation of distances for the considered geometry is 0.76 seconds when refraction is not considered, and increases to 99.31 seconds when refraction is computed. This means an increase of about 131 times.

For the axillary region shapes, the computational time is 3.26 and 27.80 seconds when refraction is not considered for test 1 and test 2, respectively. When refraction is considered, the computational time of the algorithm is 175.44 and 275.65 seconds, for test 1 and test 2, respectively. This results in a 54 and 10 times increase, respectively for tests 1 and 2.

3.3.4 Partial Conclusions

Despite the differences between the shapes of the breast and both axillary region planes, the effects of refraction in the imaging results are negligible in the three test cases, probably due to the low to moderate average relative permittivity of the phantom media (ϵ_r = 4 and 8), in agreement to the conclusions drawn from Section 3.2.

3.4 Chapter Conclusions

In this chapter, the refraction effects on imaging results using MWI systems were evaluated. The study was completed with both simulated and experimental data, and using regular shapes (a spherical phantom) and realistic shapes (a breast and an axillary region phantoms).

The spherical phantom allowed studying the influence of varying the average relative permittivity of the phantom, the targets size and number of antennas on refraction effects. The results demonstrated refraction effects are negligible for low to moderate values of average permittivity (ϵ_r <= 8). MMR may decrease but the image quality is not substantially affected when refraction is not considered, yielding high SCR and SMR and low LE. Conversely, for higher average permittivity values (ϵ_r > 8), imaging results may present clutter and artefacts, and refraction computation is relevant to ensure a resulting image with high quality. Clutter and artefacts effects aggravate when the number of antennas used is reduced. Targets size does not seem to have an influence on the impact of refraction. The realistic phantoms confirmed the previous conclusions. These phantoms were studied with low to moderate values of average permittivity, which mimic properties for breast and axillary region applications. The results showed refraction computation can be neglected without compromising the targets detection.

This study is the most complete study of refraction effects available in the literature and is especially important in the development of air-operated MWI systems. A thorough analysis of refraction effects in several conditions was performed. The presented results indicate that the conditions where refraction should be computed can be generally considered. Therefore, these conclusions can be used for researchers to decide whether refraction computation should be implemented in the image reconstruction

algorithm, at the expense of increasing the computational time, which, as shown in Section 3.2.6 and 3.3.3, can increase by 10 to 131 times.

The major effect of refraction happens in the air-phantom interface as this is a large interface common to all ray paths starting from each antenna position. In heterogeneous phantoms, refraction effects may happen between inner tissues (e.g. in the case of the breast between adipose and fibroglandular tissues) but the irregularity and size of the tissues may produce other effects such as diffraction, which are more complex to account for. In future work, refraction effects on heterogeneous phantoms may be evaluated, while considering that in a clinical scenario there is no prior knowledge of the interfaces of the inner tissues.

The following chapters present the studies to address the development of a novel MWI system to aid ALNs detection and a preliminary study of an MWI system to aid breast cancer detection with a dielectric lens.

4 Anthropomorphic Numerical Models and Estimation of Dielectric Properties

This chapter presents the development of an image processing pipeline aimed to create anatomically realistic numerical phantoms of the axillary region and to estimate dielectric properties of Axillary Lymph Nodes (ALNs) using breast Magnetic Resonance (MR) images. Our group presented a physical axillary region phantom from a Computed Tomography (CT) image but the ALNs included in the model were an approximation of the true ALN shapes and their positioning [55]. As reported in Section 2.3.1, the information regarding dielectric properties of ALNs is still limited. Firstly, only a very limited number of metastasised ALNs was measured [55], [58], [130]. Secondly, the heterogeneity of ALNs needs to be considered.

Many Magnetic Resonance Imaging (MRI)-based breast phantoms have been described in the literature [133]–[137], as well as the methodology to create these phantoms. However, regions farther away from an MRI coil, such as the axillary region, have not been assessed, and the segmentation of these regions present some challenges. Most significantly, the same type of tissue can have lower voxel intensities if they are not near a coil. This effect is even more evident in patients with higher Body Mass Index (BMI). The estimation of dielectric properties of biological tissues from MRI is not addressed in [133]–[137]. Only MR-based Electrical Properties Tomography (EPT) has been studied [193], [194] for that purpose. However, EPT is limited to estimate dielectric properties at the Larmor's frequency (up to 300 MHz), which is lower than the frequency range of interest for Microwave Imaging (MWI).

The study presented in this chapter is the first one using common MRI sequences data to infer unknown dielectric properties based on state-of-the-art dielectric properties, independently of the frequency of the MRI acquisition. MRI is not quantitative and therefore a careful analysis is needed when relating MR images to water content. Nonetheless, a relative comparison between signal intensities is possible when the correct image processing is applied. Firstly, the dataset and the developed image processing pipeline are described. Secondly, the estimated dielectric properties of both

healthy and metastasised ALNs in inter- and intra-patient studies are compared. Then, the final open-access repository with the developed anthropomorphic numerical phantoms of the axillary region is presented. Finally, a study to validate the method of dielectric property estimation in MRI is presented. The accuracy of the method of dielectric property estimation is difficult to quantify, as we could not directly measure the dielectric properties of the tissues of the imaged patients. Hence, a physical phantom filled with mixtures with known dielectric properties is tested in an MRI scanner and used to calculate the error associated with the dielectric properties estimation.

4.1 Dataset

The breast MRI dataset includes exams from female patients acquired with a 3T clinical MR system (Magnetom Vida, Siemens Healthineers) with an 18-channel dedicated breast coil, at Hospital da Luz Lisbon, during regular breast cancer screenings or follow-ups. This study was approved in September of 2019 and November of 2020 by the Scientific and Ethical Commission under references CES/44/2019/ME and CES/34/2020/ME, and an informed consent was obtained from all patients.

This study includes 50 MRI exams of female patients, retrieved from a dataset with a total of 448 MRI exams, ensuring patient variability and equal proportion of patients with healthy ALNs and patients with one or more metastasised ALNs. To that end, 25 exams of patients with only healthy ALNs were selected from the available dataset, ensuring the representativeness of the sample in terms of BMI. Only exams from patients with visible lymph nodes were considered. The remaining 25 exams are from patients with metastasised ALNs, 10 more patients than the ones included in the study presented in the published journal paper [195]. The demographic data of the patients included in the study of this chapter are shown in Table 4.1.

Table 4.1: Demographic data of patients from the MRI database.

	Patients with only Healthy ALNs (n=25)			**Patients with Metastasised ALNs (n=25)**		
	Mean	**Std**	**Range**	**Mean**	**Std**	**Range**
Age	49	10	34 to 73	55	13	38 to 81
BMI	28	6	17 to 44	27	4	19 to 36

ALNs: Axillary Lymph Nodes; BMI: Body Mass Index;
Std: Standard deviation

In collaboration with the technicians of Hospital da Luz, the regular MRI acquisition protocol was adapted in order to include both clinicians requirements and the

objectives of our study. The adopted breast MRI acquisition protocol is presented in Table 4.2.

The first sequence in three acquisition planes was included in the protocol so it could be considered to retrieve the overall shape of the axillary region and all contours of the upper torso. For the purpose of this study, only the T_1-weighted (T_1-w) localisation image sequence acquired in the axial plane was used. Although T_1-w localisation image is not isotropic, it has enough resolution to allow for Multiplanar Reconstruction (MPR) at sagittal and coronal planes, for a complete anatomical evaluation. Due to its low acquisition time (approximately 9 seconds), the overall shape of the upper torso is obtained avoiding a substantial increase of the duration of the MRI exam, at the expense of lower signal-to-noise ratio.

The 2D T_2-weighted (T_2-w) Short-Time Inversion Recovery (STIR) is the most used sequence by radiologists to detect ALNs, since ALNs are usually very well-detected in images reconstructed with this sequence. However, such a 2D image sequence has low resolution in the transversal and sagittal planes, meaning an additional sequence must be used to complement the detection of ALNs. Regarding the contrast between tissues, the T_2-w STIR is similar to T_2-w Dixon-W image sequences (shown in Figure 2.17).

Although T_1-w SPectral Attenuated Inversion Recovery (SPAIR) is often collected in breast MRI protocols, the performance of segmentation algorithms applied to these images was not satisfactory mainly due to the bias field effect (described in Section 2.3.3). Alternatively, T_1-w Dixon images were acquired since the bias field effect is reduced in this type of images. Additionally, the T_1-w Dixon image sequence provides good contrast between "internal" tissues, such as muscle, adipose and fibroglandular

Table 4.2: Breast MRI sequence acquisition protocol.

Sequence name	Acquisition plane	Voxel size
3D T_1-w fl3D VIBE localisation	Axial	$0.86 \times 0.86 \times 1.8$ mm^3
	Sagittal	$0.86 \times 0.86 \times 0.86$ mm^3
	Coronal	$0.86 \times 0.86 \times 0.86$ mm^3
2D T_2-w TSE with STIR pulse	Coronal	$4 \times 0.75 \times 0.75$ mm^3
Isotropic 3D T_1-w 3D VIBE Dixon	Axial	$1.48 \times 1.48 \times 1$ mm^3
	Coronal	$0.99 \times 0.99 \times 1$ mm^3
2D DWI STIR	Axial	$0.94 \times 0.94 \times 4$ mm^3
3D T_1-w SPAIR	Axial	$1.07 \times 1.07 \times 1$ mm^3

T_1-w: T_1-weighted; T_2-w: T_2-weighted; DWI: Diffusion-Weighted Imaging;
STIR: Short-Time Inversion Recovery; SPAIR: SPectral Attenuated Inversion Recovery;
VIBE: Volumetric Interpolated Breath-hold Examination; fl3D: Fast Low Angle Shot 3D;
TSE: Turbo Spin Echo

tissues. The image sequence acquired in the coronal plane is used for the study, which allows an MPR in all anatomical planes without major image artefacts and provides a wider view of the axillary region. As explained in Section 2.3.3, this image sequence provides four image sets with different contrasts. For the purpose of this study, the Water (W) and Fat (F) image contrasts are used. Although one can assume higher water content tissues are represented with higher signal voxel intensity values in T_1-w Dixon-W, in order to assume a direct relationship between them (and consequently dielectric properties), this assumption needs to be carefully confirmed for each tissue type individually.

Diffusion-Weighted Imaging (DWI) STIR and T_1-w SPAIR image sequences are not used since they do not provide anatomical information and require contrast agent, respectively. In summary, only four types of images are used in the implemented pipeline: T_1-w localisation, T_2-w STIR, T_1-w Dixon with W and F contrasts.

In the acquired breast MR images, eight main types of tissues are imaged: adipose tissue, fibroglandular tissue, skin, lung, muscle, bone, costal cartilage, and, finally, ALNs. Only level I ALNs are included. ALNs of other levels are embedded between muscles and are frequently not visible in MRI. Table 4.3 shows the relationship between intensities on T_1-w Dixon-W images, water content and the state-of-the-art dielectric properties of each tissue at 5 GHz. The water content of the lung is not shown since it is usually reported depending on its individual structures [196], which include air, parenchyma and blood vessels. The accuracy of the signal voxel intensities is affected by the large distance to the coil which is not tailored to image the lung, and, as a result, its different sub-structures are not detected. Therefore, the relationship between signal voxel intensities, water content and dielectric properties cannot be correctly inferred.

Table 4.3: Tissue analysis by qualitative intensity of T_1-w Dixon-W images, water content and dielectric properties (at 5 GHz).

Tissue	**Qualitative intensity**	**Water content (%)**	ϵ_r	σ **(S/m)**
Adipose	Dark	6-36 [197]	3.8-7.0 [125]	0.1-0.4 [125]
Lung	Dark	-	19.0 [116]	1.7 [116]
Bone	Dark Grey	12-40 [196], [197]	10.0 [116]	1.0 [116]
Fibroglandular	Dark Grey/ Light Gray	30-73 [196]	33.7-48.5 [125]	2.7-4.7 [125]
Muscle	Light Grey	70-79 [197], [198]	49.5 [116]	4.0 [116]
Skin	Light Grey	58-72 [196], [197]	35.8 [116]	3.1 [116]
Costal cartilage	Bright	60-75 [196], [199]	33.6 [116]	4.1 [116]

Among the remaining tissues (i.e. adipose, bone, fibroglandular, muscle, skin and costal cartilage), only skin and costal cartilage do not have a direct relationship between water content, dielectric properties and qualitative voxel intensities. Although skin presents similar signal voxel intensities to muscle, it has lower water content (and permittivity) when compared to muscle. This is explained by the skin proximity to the coil placed around the breast, which inherently results in higher signal voxel intensity values. Costal cartilage is mainly composed by water and collagen, which, due to its high number of Hydrogen atoms, results in increased intensities in T_1-w Dixon-W images. However, this tissue is not relevant when imaging the axillary region. For the remaining tissues, a direct relationship between dielectric properties, water content and intensity values can be assumed.

For the purpose of imaging the axillary region, skin, adipose tissue, ALNs and muscle are the most relevant tissues. In this region, bones and muscles are indistinguishable and the MRI contrast between them is very low so it is not possible to segment them separately. For the purpose of MWI, this does not pose a problem since the location of muscle in the axillary region is shallower than bone. For that reason, bone response yields higher attenuation and its MWI response is much lower than muscle's.

4.2 Image Processing Pipeline

The methodology pipeline includes pre-processing steps and semi-automatic segmentation required towards the estimation of ALNs dielectric properties and the creation of axillary region numerical models.

The processing pipeline was fully implemented in Python™ and was applied to T_1-w localisation, T_1-w Dixon with both Water and Fat contrasts and T_2-w STIR. A flowchart of the implemented pipeline is shown in Figures 4.1 and 4.2 and it is summarised in the following points:

- Image pre-processing:
  - Image registration
  - Bias field removal
  - Selection of region of interest
  - Filters and normalisation
- Image segmentation:
  - Background
  - Internal tissues
  - Lung cavity

  - Skin
  - ALNs

- Estimation of ALNs dielectric properties
- Creation of Axillary Region Numerical Models

4.2.1 Image Pre-processing

In this sub-section, the image pre-processing pipeline is described. The following steps must be applied to ensure an optimal performance of the segmentation of tissues.

4.2.1.1 Image Registration

T_1-w localisation, T_2-w STIR and T_1-w Dixon image sequences have different spatial resolutions and dimensions, as shown in Figure 4.3(a-f). In order to be able to correctly superimpose them, they need to be spatially registered to the same spatial reference system.

The Insight Toolkit (ITK)'s implementation [200] of an affine registration with linear interpolation is used to register both T_1-w localisation and T_2-w STIR (moving images) to T_1-w Dixon (static image). This combination of moving and static images is chosen since the T_1-w Dixon has higher resolution and includes the most important information. This type of registration uses the coordinates of each referential system relatively to the MRI machine, to rotate, translate and scale the moving image. The resulting images are transformed to the same referential and have the same dimensions and resolution of the static image, as shown in Figure 4.3(g-l). In order to preserve the information in T_1-w localisation image, before applying the registration algorithm, the image size of T_1-w Dixon is increased without changing its resolution [Figure 4.3(d,j)].

4.2.1.2 Bias Field Removal

As explained in Section 2.3.3, the bias field is an unrealistic variation of intensities within the tissues of the same type. The bias field removal step is of particular importance in images of patients with higher BMI where this effect is more evident. Bias field removal is essential for the remaining pipeline for mainly two reasons:

1. **Improve image segmentation:** Most of segmentation algorithms are highly dependent on signal voxel intensities. Hence, the voxel intensities within each tissue should be similar in order to be correctly segmented.

2. **Ensure reliability of estimated ALN dielectric properties:** The voxel intensities of all tissues are important to infer ALN dielectric properties. Additionally,

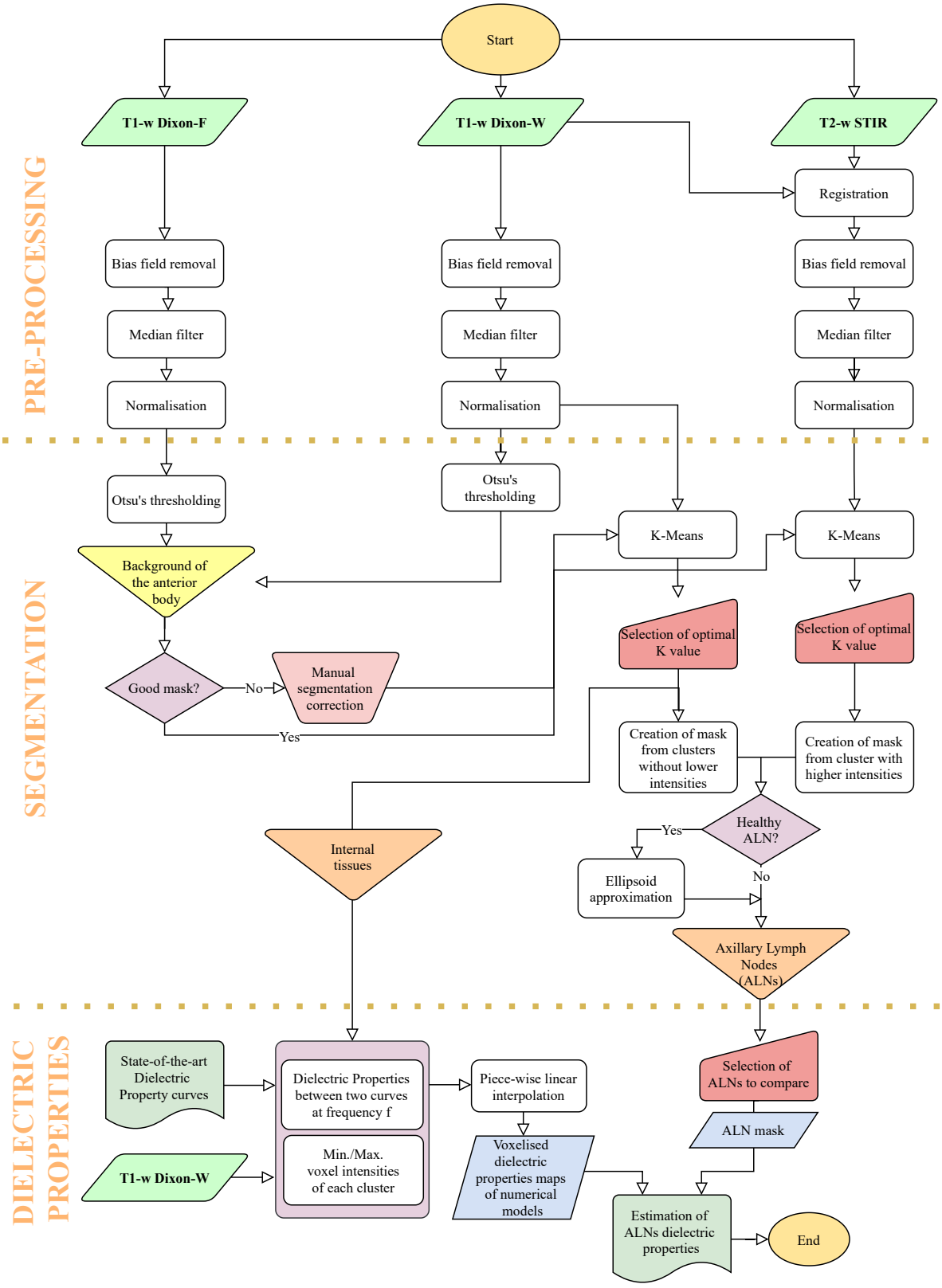

Figure 4.1: Flowchart of the processing pipeline for the estimation of dielectric properties.

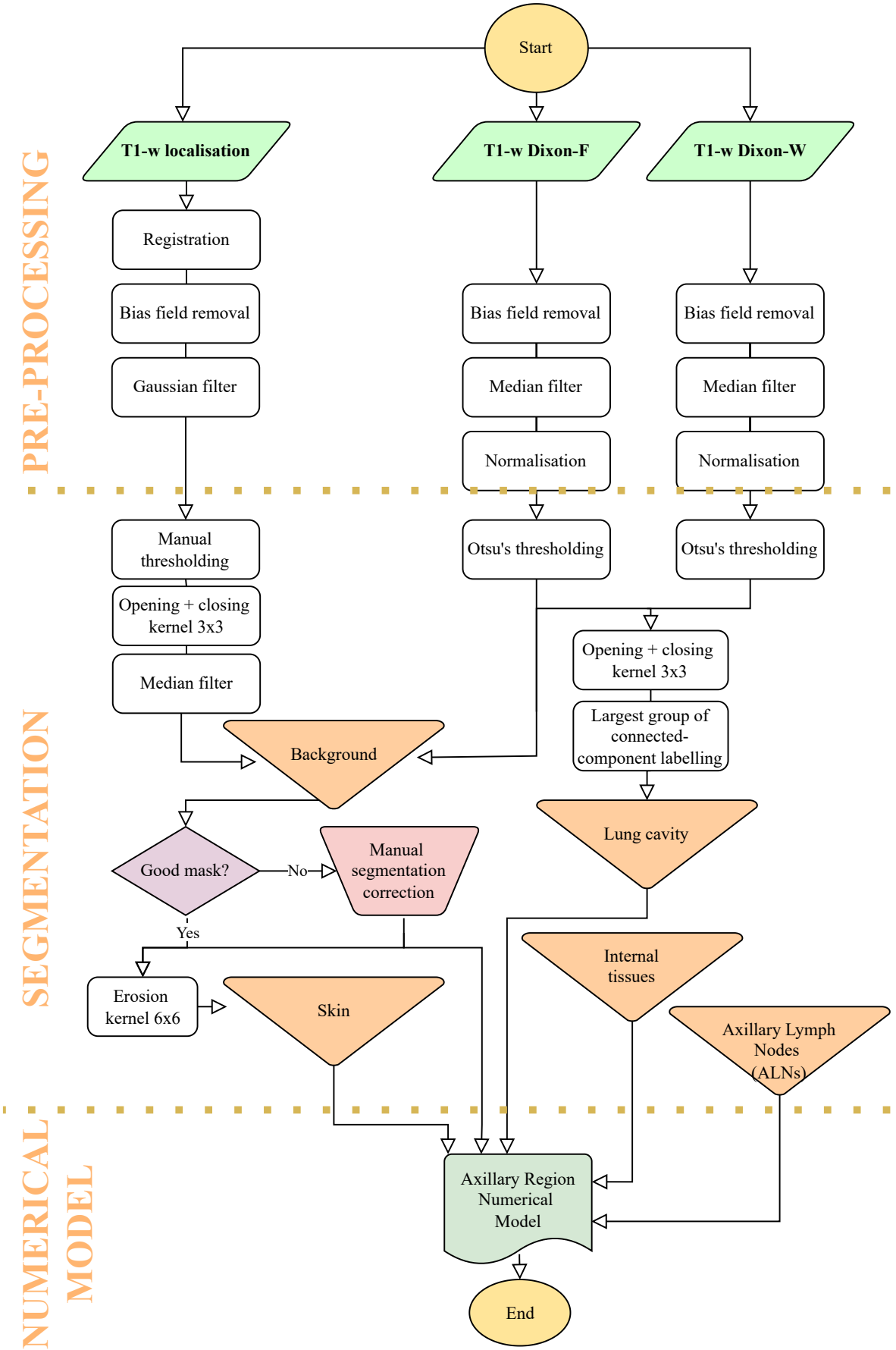

Figure 4.2: Flowchart of the processing pipeline for the creation of axillary region numerical models using segmented tissues obtained with the flowchart of Figure 4.1.

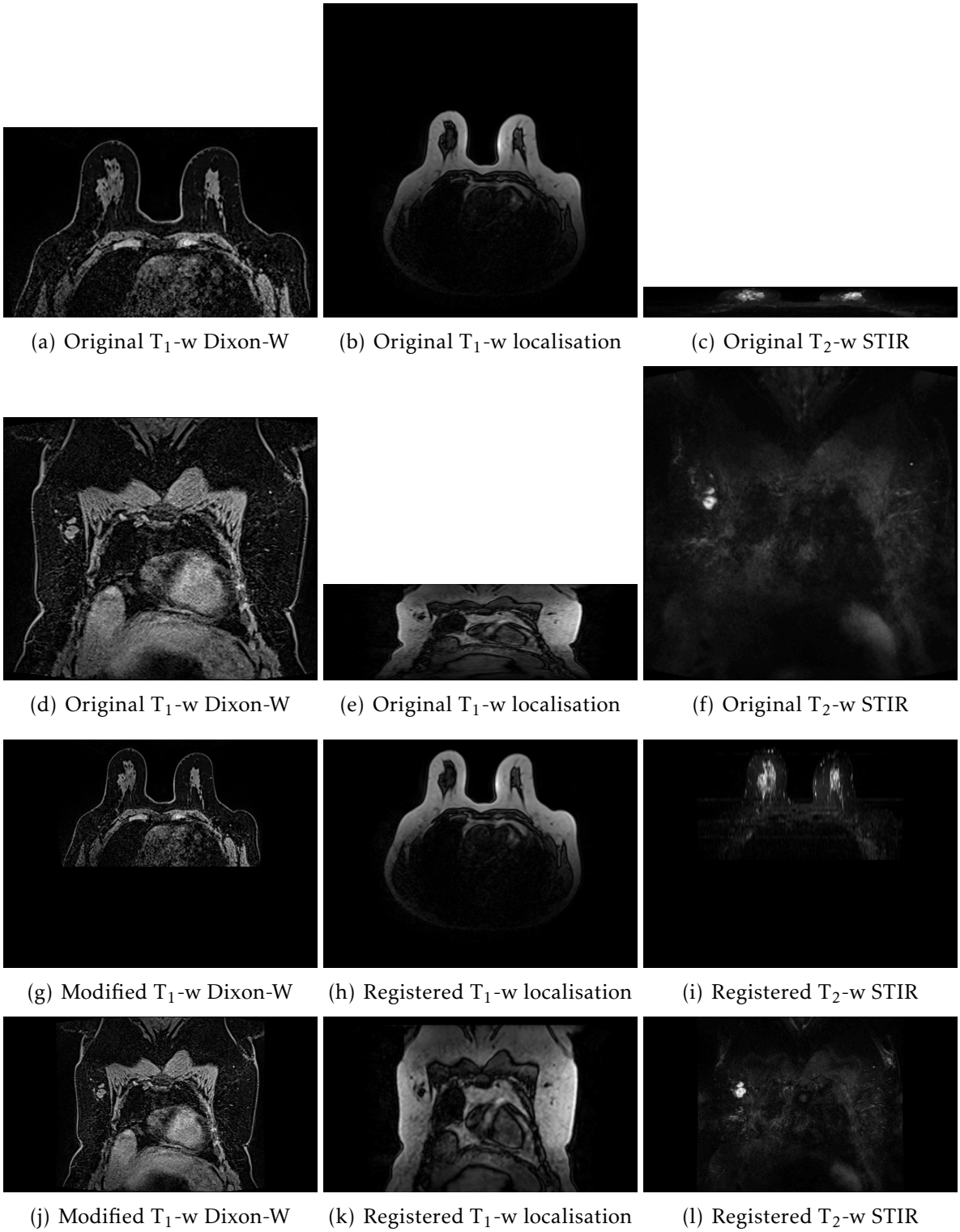

(a) Original T_1-w Dixon-W (b) Original T_1-w localisation (c) Original T_2-w STIR

(d) Original T_1-w Dixon-W (e) Original T_1-w localisation (f) Original T_2-w STIR

(g) Modified T_1-w Dixon-W (h) Registered T_1-w localisation (i) Registered T_2-w STIR

(j) Modified T_1-w Dixon-W (k) Registered T_1-w localisation (l) Registered T_2-w STIR

Figure 4.3: Example of registration of the three image sequences: T_1-w Dixon-W as static image and T_1-w localisation and T_2-w STIR as moving images. (a-c) and (g-i) represent axial slices, and (d-f) and (j-l) represent coronal slices. The size of the images represent the true dimensions of the MR images.

tissues with the same molecular composition in both sides of the body should be represented in MR images with similar signal voxel intensities in order to compare different ALNs from both axillary regions.

The ITK's implementation [156] of bias field removal is applied to T_1-w localisation

and T_1-w Dixon images. The algorithm receives as input the original image and a negative binary mask of the adipose tissue obtained from the original image after applying an Otsu's thresholding. One or more iterations are applied until a satisfactory bias field removal is obtained. The algorithm is also applied to T_2-w images, although there is no clear advantage when processing this type of images.

Figure 4.4 shows the result of applying a bias field removal algorithm to two axial slices, at the breast and at the axillary regions planes. In this case, the bias field is more intense in the internal region of the breast near the coil and the axillary regions are asymmetric. The voxel intensities are more homogeneous after applying the bias field removal [Figure 4.4(b,f)]. Figure 4.4(d,h) shows that the value of voxel intensities between the right and left side of the patient yield similar orders of magnitude after applying the bias field removal.

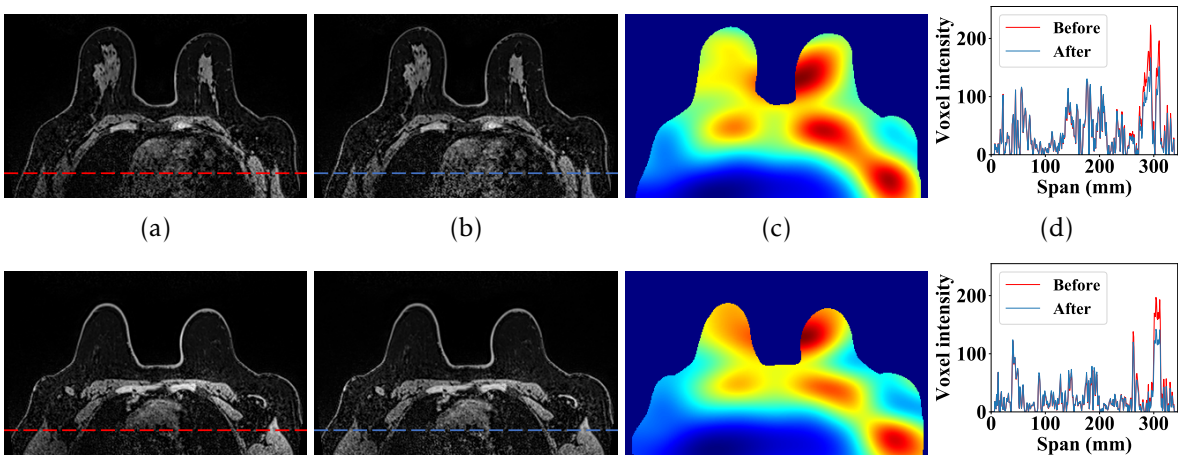

Figure 4.4: Bias field removal results in (a-d) inferior and (e-g) superior axial slices of a breast MR T_1-w Dixon-W image. The images show the slices (a,e) before and (b,f) after the bias field removal is applied, (c,g) the computed bias field, and (d,h) voxel intensities variation over the red and blue lines represented in (a,b,e,f). Blue and red colours in (c,g) represent a smaller and larger inhomogeneity between voxel signal intensities, respectively.

4.2.1.3 Selection of Region of Interest

A region of interest in each image is selected for the next steps of the pipeline to avoid including regions of the body of little interest to this study, which could compromise the algorithms performance. The selection of a region of interest is optional but it yields improved results.

T_1-w localisation and T_1-w Dixon-W images should contain both breasts and axillary regions, while only the axillary region needs to be included in the T_2-w image. The region of interest is selected by visual inspection using the following criteria for each type of image sequence:

- **T_1-w localisation image sequence:**

  - Axial plane: From the inferior part of the neck to the inferior part of the breast

- **T_1-w Dixon image sequence:**
  - Axial plane: From the inferior part of the neck to the inferior part of the breast
  - Coronal plane: From the nipple to the posterior parts of the axillary region
- **T_2-w STIR image sequence:**
  - Axial plane: From the inferior part of the neck to the inferior part of the axillary region
  - Coronal plane: From the anterior to the posterior parts of the axillary region
  - Sagittal plane: From the lateral to the medial parts of each axillary region

4.2.1.4 Filters and Normalisation

A median filter is applied to remove noise and to smooth the voxel intensity differences within each tissue, for both T_1-w Dixon-W and T_2-w STIR images. Figure 4.5 shows two examples of T_1-w Dixon-W image before and after the median filter is applied, where it is possible to observe the smoothing effect on voxel intensity values. A more powerful filter needs to be used for T_1-w localisation image to remove the noise. Hence, a Gaussian filter with $\sigma = 1$ is used.

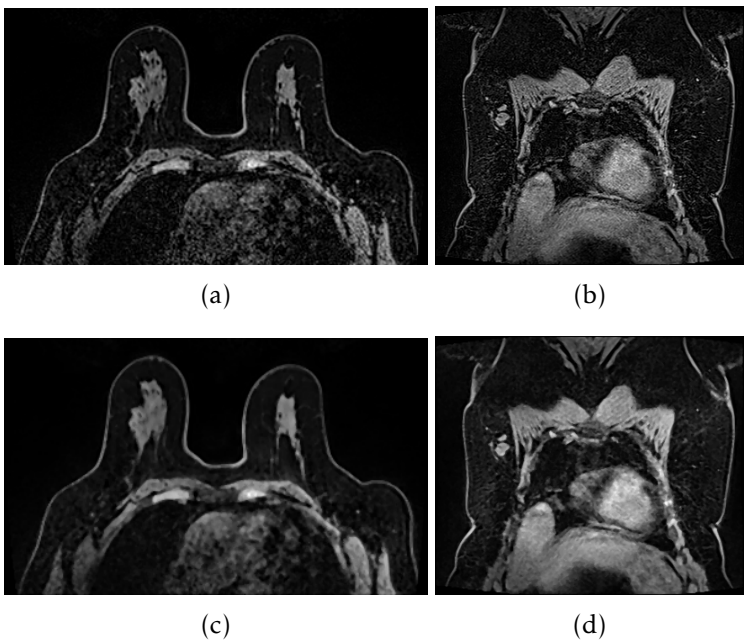

Figure 4.5: Comparison between slices of T_1-w Dixon-W image (a,b) before and (c,d) after applying a median filter. The figures only show the region of interest of the image. (a,c) represent axial slices, and (b,d) represent coronal slices.

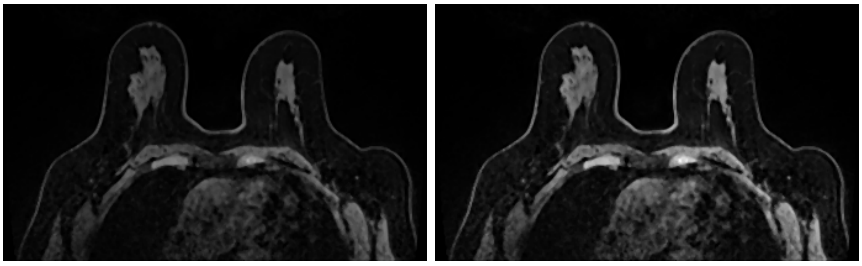

(a) (b)

Figure 4.6: Comparison of the axial slices (a) before and (b) after normalising a T_1-w Dixon-W image. The figures only show the region of interest of the image.

Then, a minimum-maximum normalisation is applied to the voxel intensities of each image, which is important for dielectric properties assignment, later presented in Section 4.3. The normalisation does not have an impact on the quality of the images, since the contrast between tissues is not changed, as observed in Figure 4.6.

4.2.2 Image Segmentation

Five segmentation methods are applied to the breast MR images to segmented different type of tissues, which are described in the following sub-sections.

4.2.2.1 Background

Contrarily to previous studies with MRI [133]–[137] where only the breast region was segmented, the lateral and posterior part of the body also need to be retrieved to create an axillary region phantom. In this thesis, the background is segmented in two steps, as shown in Figure 4.7. Firstly, the background of the anterior part of the body is segmented. This segmentation results from the binarisation of both T_1-w Dixon-W and T_1-w Dixon-F images using Otsu's thresholding [Figure 4.7(b, d)] and applying the union of both binarised images (masks), as shown in equation 4.1. Then, a post-processing step is applied where each axial slice of the resulting mask is scanned from the anterior to the posterior part of the mask, filling any holes within the body region [Figure 4.7(e)]. This background mask is also used to improve the results of the next segmentation step by removing the artefacts of the background on the T_1-w Dixon-W image.

$$\begin{aligned}\mathbf{mask}_{background} = \text{Post-processing}\Big[&\Big(\text{Bin}_{\text{intensity>OTSU threshold}}(\text{T}_1\text{-w Dixon-W})\Big) \cup \\ &\Big(\text{Bin}_{\text{intensity>OTSU threshold}}(\text{T}_1\text{-w Dixon-F})\Big)\Big]\end{aligned} \tag{4.1}$$

Secondly, the background of the posterior part of the body is segmented so it can be used in the final axillary region models. This background is obtained using the T_1-w

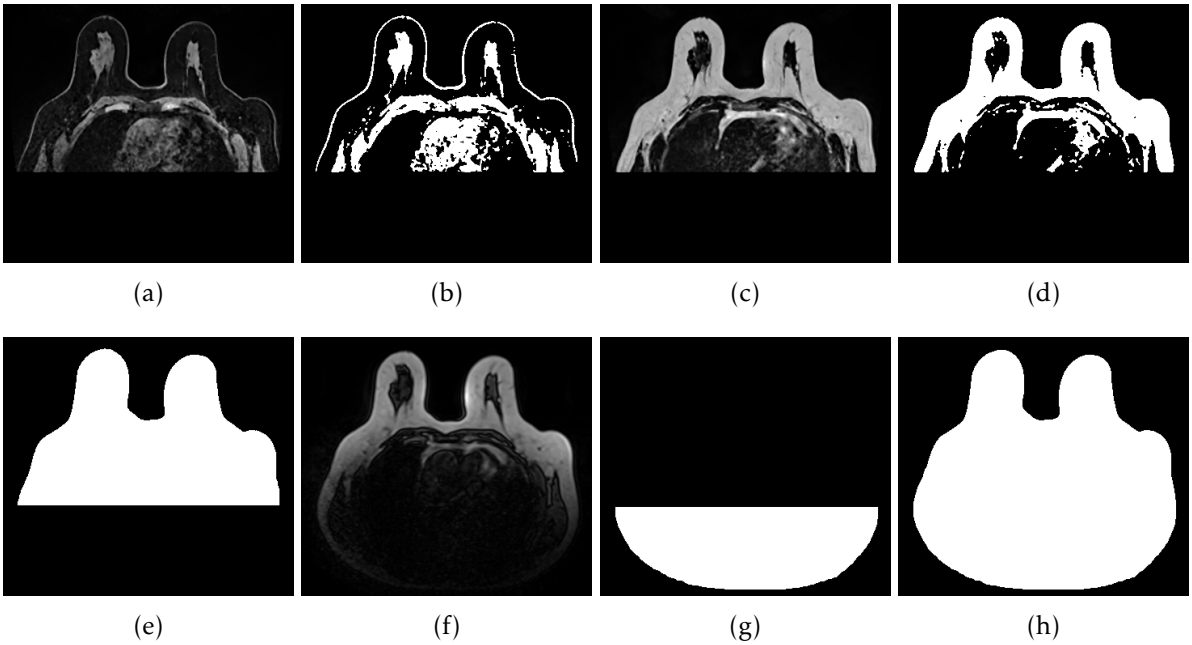

Figure 4.7: Example of background segmentation of an axial slice of a breast MR image. The images show (a) T_1-w Dixon-W and (c) T_1-w Dixon-F images, and the corresponding results of Otsu's thresholding in (b) and (d). The combination of (b) and (d) and after filling the holes within the body region result in (e). T_1-w localisation image is presented in (f) and the resulting image of the background segmentation is presented in (g). The final background is presented in (h), a combination of (e) and (g).

localisation image [Figure 4.7(f)], which is the only image sequence which contains the posterior part of the body. The segmentation results from a manual thresholding, followed by opening and closing operations with a kernel 3×3 and a median filter.

Then, both background masks of the anterior [Figure 4.7(e)] and posterior part of the body [Figure 4.7(g)] are combined [Figure 4.7(h)]. The final background can have some unexpected errors, e.g. discontinuities between slices, since T_1-w localisation image sequence has low contrast in the posterior part. These errors can be corrected by manual segmentation and by applying a univariate smoothing spline interpolation in the sagittal plane, as shown in Figure 4.8.

4.2.2.2 Internal Tissues

The internal tissues are segmented using the K-Means algorithm (presented in Section 2.3.3.2). Several values for the number of clusters K are compared, from 3 to 10. The best value is empirically retrieved considering some qualitative criteria. The following criteria are considered for the T_1-w Dixon-W images:

1. Good distinction between the following tissues: fibroglandular tissue, adipose tissue, and muscle;

2. Lymph nodes can be identified in more than one cluster but should be isolated from the surrounding tissues;

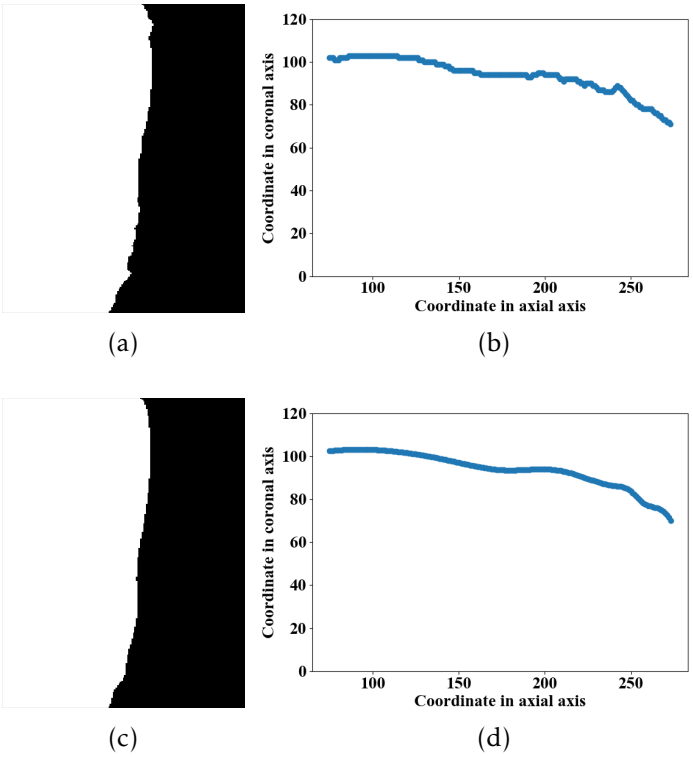

Figure 4.8: Example of univariate smoothing spline interpolation applied to a sagittal slice of the background. (a) and (c) shows the sagittal binary slice before and after the interpolation is applied, respectively. The plots in (b) and (d) shows how the interpolation is applied using the coordinates of the surface.

3. One single main tissue cannot be identified in more than three clusters.

K-Means algorithm is also applied to T_2-w STIR images, but only one criterion is used: all ALNs need to be segmented in one cluster with no other tissues.

Figure 4.9 shows some examples of the results with the K-Means algorithm applied to a T_1-w Dixon-W image for different K values. Independently of the considered K, multiple groups of tissues are identified within the same cluster since they have similar range of voxel signal intensities: skin and muscle are segmented and identified in the same clusters as the fibroglandular tissue, adipose tissue is identified in more than one cluster, and the lung cavity is identified in the same clusters as adipose tissue. Even though fibroglandular tissue and muscle are identified in the same clusters, they are visually distinguishable. Regarding the ALNs, their cortex is identified as belonging to the same cluster as fibroglandular tissue, while their hilum is identified as belonging to the same clusters as adipose tissue. Therefore, extra segmentation steps are needed to individually segment skin, the lung cavity and ALNs as detailed in the following sub-sections. In the presented example in Figure 4.9, a value of K between 4 and 6 would be sufficient to segment the remaining tissues, i.e. adipose, fibroglandular tissue and muscle, as higher values of K do not provide more advantages for the following steps.

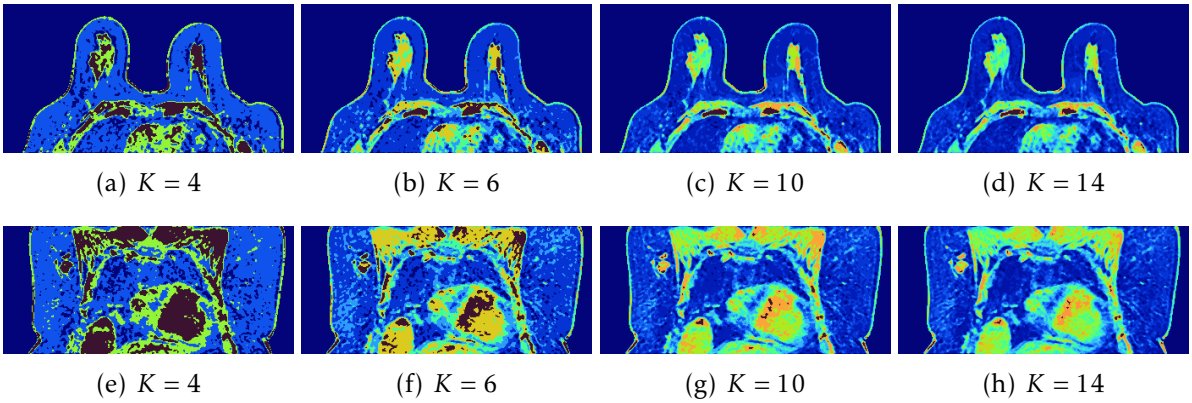

(a) $K = 4$ (b) $K = 6$ (c) $K = 10$ (d) $K = 14$

(e) $K = 4$ (f) $K = 6$ (g) $K = 10$ (h) $K = 14$

Figure 4.9: Comparison of segmentation with K-Means algorithm for different K values. The figures only show the region of interest of the image. (a-d) represent axial slices, and (e-h) represent coronal slices.

4.2.2.3 Lung Cavity

The lung cavity is usually segmented in the same cluster as adipose tissue. Hence, an additional step is required to segment this part of the torso. The segmentation of this structure is not usually addressed in breast MR images and it is only roughly estimated [201]. Although the lung has a minimal importance to MWI applications since it is deep and located behind the muscles in the axillary region, it is included in the axillary region models to ensure a realistic anatomical representation.

The segmentation of the lung cavity results from the intersection between the binarisation using Otsu's thresholding of both T_1-w Dixon-W and T_1-w Dixon-F images, as shown in the equation 4.2. The resulting mask may include some voxels which do not belong to the lung cavity. Hence, some post-processing steps are applied. These steps include applying opening and closing operations with a kernel 3×3, and applying a connected-component labelling method, which is used to select the largest group that will indeed correspond to the lung cavity.

$$\begin{aligned}\mathbf{mask}_{lung} = \text{Post-processing}\Big[\Big(\text{Bin}_{\text{intensity<OTSU threshold}}(\text{T}_1\text{-w Dixon-W})\Big) \cap \\ \Big(\text{Bin}_{\text{intensity<OTSU threshold}}(\text{T}_1\text{-w Dixon-F})\Big)\Big]\end{aligned} \tag{4.2}$$

The segmentation results of the lung cavity are shown in Figure 4.10, showing a successful segmentation. To note that lungs are asymmetrical.

4.2.2.4 Skin

The skin is usually segmented in the same cluster as fibroglandular tissue or in more than one cluster, so an additional step is required to segment the skin tissues. Most authors added an artificial layer of skin with a fixed thickness to their breast models

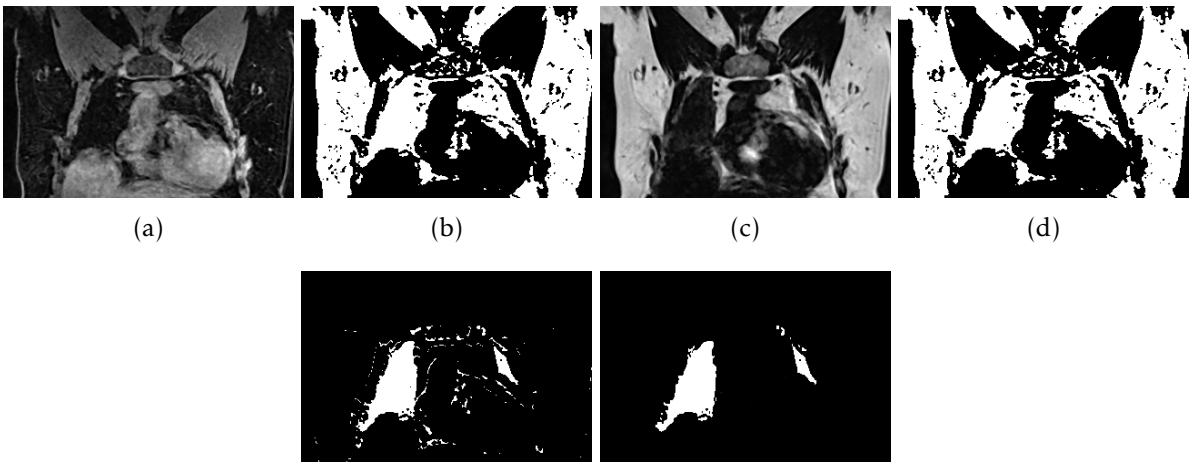

Figure 4.10: Examples of coronal slices of the lung cavity segmentation. The original images of T_1-w Dixon-W and T_1-w Dixon-F are shown in (a) and (c), respectively, and the corresponding resulting images after Otsu's thresholding are shown in (b) and (d), respectively. (e) shows the resulting image of the intersection between (b) and (d), and (f) shows the final result after the processing steps.

[133], [136], [137]. Tunçay *et al.* [135] removed a layer of the breast model and added a skin layer with a lower thickness than the thickness of the removed layer. Pelicano *et al.* [138] combined the the binary masks of several MR images in order to retrieve the true thickness of the skin in the breast region.

In this thesis, several methods were tested to segment this tissue in the overall torso. The first implemented method consists of using the resulting segmentation from K-Means, and scanning the axial slices in both directions, considering the skin is the first segmented tissue. The second method uses the manual segmented background mask and considers the contour of the mask as the skin tissue. And the third method uses the T_1-w Dixon-F image, considering the skin as the contour of the binarised image with Otsu's thresholding.

The final algorithm was chosen based on its performance and low computational cost. It is based on the second method, where an erosion operation is applied to each axial slice of the background mask. The kernel size of the erosion is defined as twice the ideal skin thickness. For most cases, a kernel size of 6×6 is sufficient. The skin layer is obtained from the subtraction between the background mask and the resulting image after the erosion operation, as shown in equation 4.3. It has the disadvantage of considering a uniform skin thickness in all regions of the torso. Figure 4.11 shows the results of skin segmentation in axial and coronal planes.

$$\mathbf{mask}_{skin} = \mathbf{mask}_{background} - \mathbf{mask}_{background\_eroded} \tag{4.3}$$

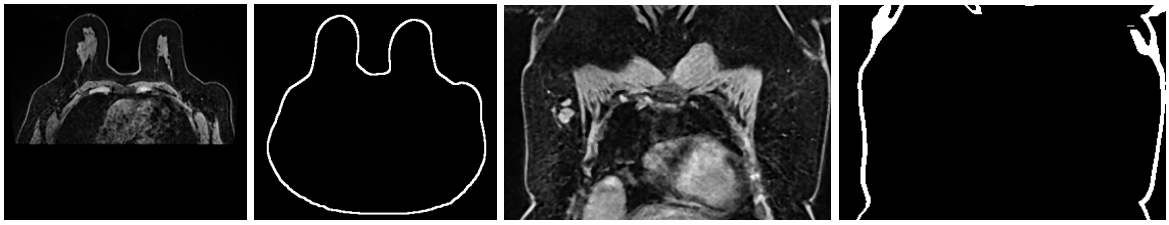

(a) (b) (c) (d)

Figure 4.11: Examples of skin segmentation results in the (b) axial and (d) coronal planes and the corresponding original (a, c) T_1-w Dixon-W image.

4.2.2.5 Axillary Lymph Nodes

Ideally, the K-Means algorithm should segment ALNs in only one cluster. But this is often not possible without compromising the segmentation of other tissues. Previous studies of breast or torso segmentation [133], [135], [136] have not included ALNs in their models. Other studies [86], [87], [89] have addressed ALN segmentation but surrounding tissues were not segmented. The segmentation of the surrounding tissues is important for the purpose of our study where a relationship between ALNs and the remaining tissues is needed. To this end, the resulting segmentations from K-Means of T_1-w Dixon-W and T_2-w STIR images are combined.

Figure 4.12 shows the step-by-step results of ALNs segmentation. In the represented coronal slice, only one matted metastasised ALN (i.e. more than one ALN very close to each other and visually indistinguishable) is segmented but each slice can include multiple ALNs. As observed, the T_2-w STIR image sequence does not provide a good separation between all tissues but provides a good detection of ALNs in higher intensities. The ALNs mask is created from the intersection between the $(K-3)$ highest-intensity clusters from T_1-w Dixon-W segmentation [Figure 4.12(e)] and the highest-intensity cluster from T_2-w STIR image segmentation [Figure 4.12(f)], as shown in equation 4.4. The resulting image from the intersection represents a more accurate representation of the lymph node shape and size, due to the higher resolution of T_1-w Dixon-W.

As an example, if the optimal K value for T_1-w Dixon-W segmentation is $K = 5$, the ALNs mask is created considering the fourth and fifth clusters which correspond to tissues with higher signal intensities (ignoring adipose and intermediate tissues). For T_2-w STIR segmentation, only the cluster with higher signal intensities is selected, which includes the ALNs.

$$\mathbf{mask}_{ALN} = \Big(\text{Bin}_{\text{(K-3)}^{\text{th}},\ldots,\text{K}^{\text{th}}\text{ clusters}}(\text{T}_1\text{-w Dixon-W})\Big) \cap \Big(\text{Bin}_{\text{K}^{\text{th}}\text{ cluster}}(\text{T}_2\text{-w STIR})\Big) \quad (4.4)$$

As shown in Figure 2.6, only the cortex of healthy ALNs has high voxel intensities in T_1-w Dixon-W, and only this structure is included in the resulting segmentation. In

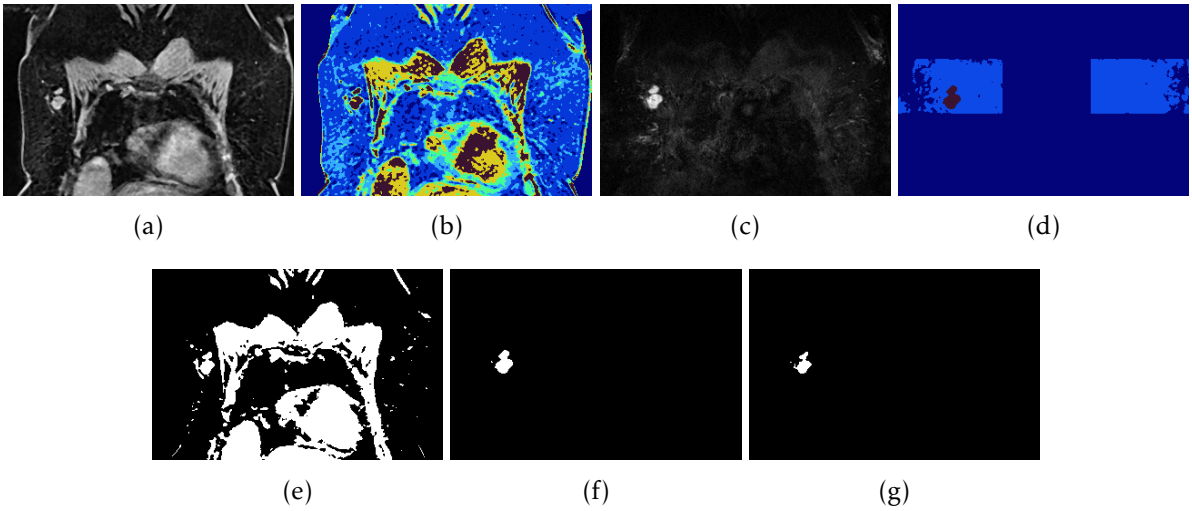

Figure 4.12: Coronal slices of step-by-step segmentation of an ALN. The original images T_1-w Dixon-W and T_2-w STIR images are shown in (a) and (c), respectively, and the corresponding K-means segmentation results are shown in (b) and (d), respectively. The masks generated from (b) and (d) and their intersection are shown in (e), (f) and (g), respectively.

order to include the entire structure of healthy ALNs, the resulting segmentation of each ALN is used to estimate an ellipsoid which includes the hilum for each detected healthy ALN.

The ellipsoid fitting method is adapted from an open-access code repository [202]. It applies a linear least squared algorithm [203] considering the algebraic form of an ellipsoid (equation 4.5) and a constraint (equation 4.6) [204].

$$Ax^2 + By^2 + Cz^2 + Dxy + Exz + Fyz + Gx + Hy + Iz + J = 0 \tag{4.5}$$

$$A + B + C = 3 \tag{4.6}$$

After solving the equation system, the ellipsoid axes lengths (a, b and c), its center and orientation are obtained. These parameters are then used to create an ellipsoid mask in the image which matches the true ALN shape, as shown in Figure 4.13.

4.3 Estimation of Axillary Lymph Nodes Dielectric Properties

The dielectric properties are assigned to MRI-based numerical models considering state-of-the-art dielectric properties of tissues (in particular, adipose and fibroglandular tissues). In this section, this information is used to estimate ALNs dielectric properties.

To this end, a similar approach proposed by [133], [135]–[138] for the breast was considered to create dielectric property maps of the axillary region model. Zastrow *et al.* [133] mapped permittivity and conductivity values to the images considering

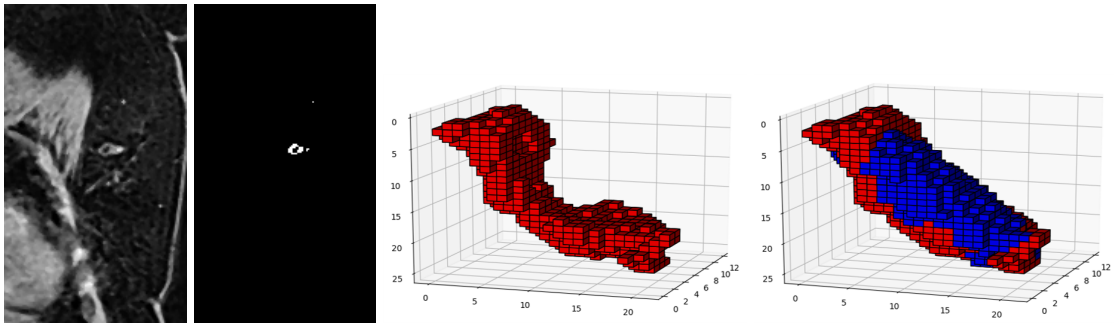

(a) (b) (c) (d)

Figure 4.13: Ellipsoid estimation from a healthy ALN. Coronal slice of the original (a) T_1-w Dixon-W image and (b) its resulting mask. (c) 3D segmented volume and (d) resulting 3D volume from ellipsoid estimation. Voxels in red represent the ALN cortex and voxels in blue represent the hilum.

a Gaussian fitting and a linear relation between each MRI signal voxel intensity and dielectric properties. Tunçay *et al.* [135] applied a polynomial cubic interpolation to assign dielectric properties. More recently, other authors [136], [137] subdivided the main breast tissues in several clusters, and assigned one single dielectric property value per frequency per cluster. In the axillary region, some details of the proposed methods cannot be applied. As the axillary region includes more than two tissues, a Gaussian fitting cannot be used, and there is also no advantage of considering sub-clusters as proposed by [136], [137] as no additional dielectric property curves need to be fitted to the model. Also, no substantial differences were observed between a linear and a polynomial cubic interpolation so a linear interpolation will be adopted since it has a simpler implementation to create dielectric maps.

In order to create the dielectric property maps, six curves of dielectric properties for permittivity and conductivity are considered, as shown in Figure 4.14. These curves are based on Lazebnik *et al.* [125], [133]: two curves to limit both fibroglandular and adipose tissues, one minimum and one maximum curve. Choosing these curves will inherently impose the maximum value of dielectric properties for ALNs as those of fibroglandular tissue. However, no other curves, such as the water curve, are viable to use with this methodology since no free-water tissues are present in the images.

Each cluster obtained from the K-Means segmentation is then assigned to an interval between two curves. Table 4.4 and Figure 4.15 show an example of how each original cluster is assigned to an interval between the dielectric property curves when $K = 5$, which is one of the values of K that provides realistic segmentation results. For lower values of K, some of the intermediate curves need to be neglected, while for higher values of K, some of the clusters need to be grouped. At each frequency, the minimum and maximum voxel intensities of each cluster are assigned to the dielectric properties values of the chosen two curves. The voxel intensities are then mapped to a value

between the selected curves using a piecewise linear interpolation:

$$dp(w,f) = w(v) \times c_{upper}(f) + [1 - w(v)] \times c_{lower}(f) \tag{4.7}$$

$$w(v) = \frac{v - v_{min}}{v_{max} - v_{min}} \tag{4.8}$$

where c_{upper} and c_{lower} are the dielectric property values at the upper and lower bound curves considered in interpolation, respectively, at a specific frequency f. v is the voxel intensity, and v_{min} and v_{max} are the minimum and maximum voxel intensity of the corresponding cluster, respectively. w is a value between 0 and 1. Following this procedure, voxelised dielectric property maps (i.e. each voxel has the intensity value matching each dielectric property) are created for frequencies from 1 to 20 GHz, with a step of 1 GHz. Figure 4.16 shows an example of a resulting map of both permittivity and conductivity for a frequency of 5 GHz.

After assigning the dielectric properties to each cluster and generating the dielectric property maps, the properties of ALNs can be estimated by superimposing the ALNs mask with the resulting dielectric property maps. For the purpose of this study, one ALN from each axillary region is selected for comparison. In exams of patients with metastasised ALNs, one metastasised and one healthy ALNs in opposite axillary regions are compared.

In order to select a specific ALN, a connected-component labelling method is applied to the ALNs mask. The whole ALN is selected when the coordinates of a point in the ALN are given. The selected ALNs are mostly level I ALNs and may sometimes include level II ALNs. Then, the dielectric properties of an ALN, per frequency, are obtained by averaging the assigned dielectric properties to each voxel of the ALN. A Mann-Whitney statistical test is then applied to evaluate the difference of dielectric

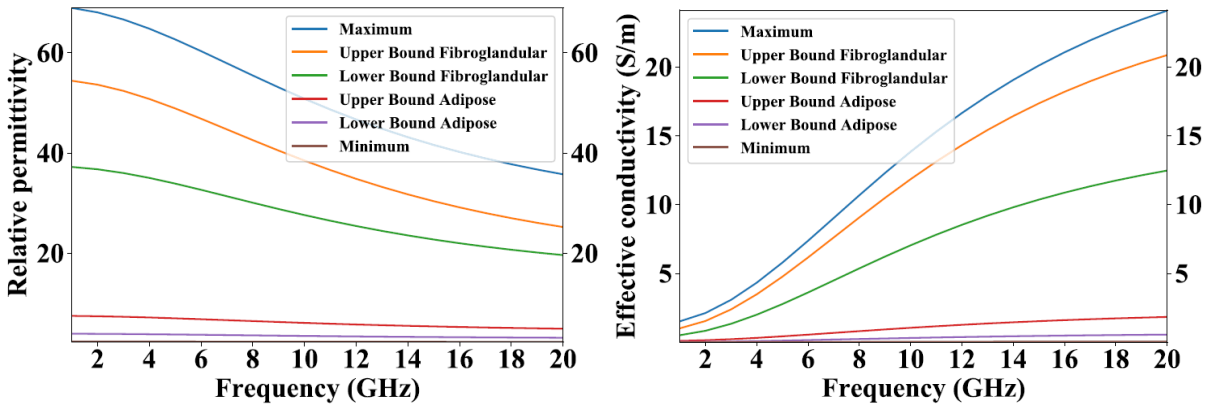

Figure 4.14: Relative permittivity (left) and effective conductivity (right) curves of breast tissues reported in [125], [133].

Table 4.4: Correspondence between cluster numbers, dielectric property curves and tissues that may be detected in the clusters.

Cluster number	v_{min}	v_{max}	c_{lower}	c_{upper}	**Detected tissues**
1	I_m	I_{a1}	P_m	P_{a1}	Adipose, lung
2	I_{a1}	I_{a2}	P_{a1}	P_{a2}	Adipose, lung
3	I_{a2}	I_{fg1}	P_{a2}	P_{fg1}	Adipose
4	I_{fg1}	I_{fg2}	P_{fg1}	P_{fg2}	Fibroglandular, muscle, skin, ALNs
5	I_{fg2}	I_M	P_{fg2}	P_M	Fibroglandular, muscle, skin, ALNs

I: voxel intensity; P: dielectric property; m: minimum curve; a1: lower bound of adipose tissue; a2: upper bound of adipose tissue; fg1: lower bound of fibroglandular tissue; fg2: upper bound of fibroglandular tissue; M: maximum curve

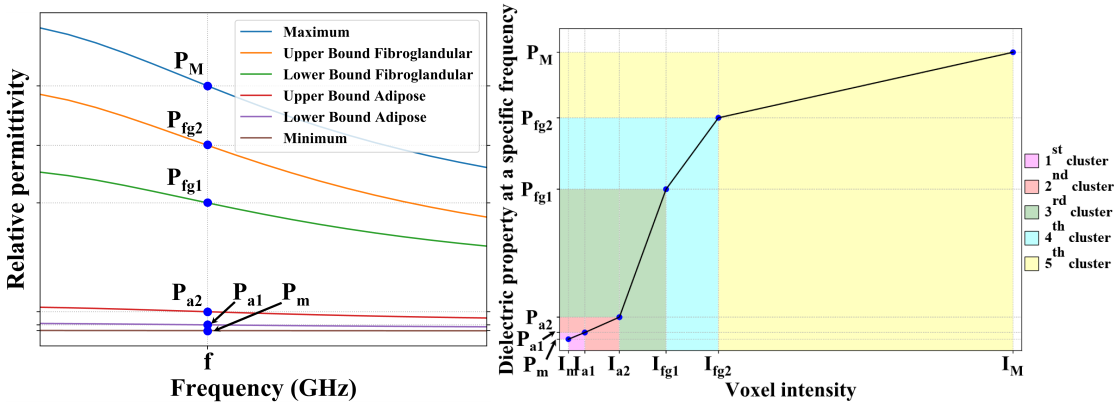

(a) (b)

Figure 4.15: Interpolation between dielectric properties values and voxel intensities at a specific frequency f. (a) shows an example of reference points of relative permittivity curves and (b) shows the piecewise linear interpolation considering 5 clusters.

properties between both groups of healthy and metastasised ALNs. A p-value ≤ 0.05 is considered as statistically significant.

The entire analysis resulted in estimating dielectric properties from 25 metastasised ALNs and 75 healthy ALNs, i.e. 2 healthy ALNs from each of the 25 patients with only healthy ALNs, and 1 healthy and 1 metastasised ALNs from the 25 patients with metastasised ALNs. Figure 4.17 shows the results of the estimated dielectric properties for each ALN over frequency.

The curves of the first, second and third quartiles for both healthy and metastasised ALNs are shown in Figure 4.17. The corresponding Debye parameters (presented in Table 4.5) are calculated by fitting a Debye model using the non-linear least squares method. Healthy ALNs have a large variability of dielectric property values, ranging from 15.9 to 41.4 average relative permittivity at 5 GHz. In contrast, metastasised ALNs

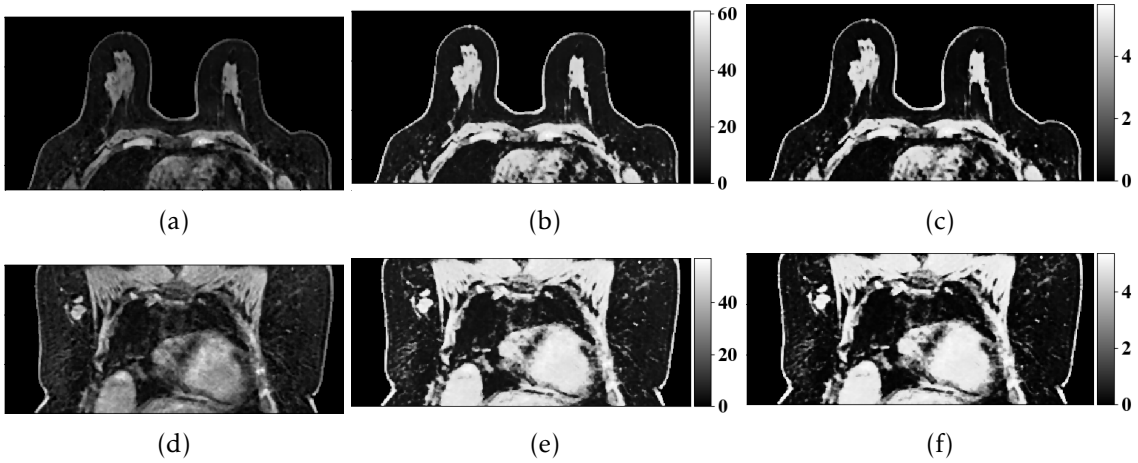

Figure 4.16: Example of dielectric property map at 5 GHz in (a-c) axial and (d-f) coronal planes. The original image is shown on the left, and the resulting relative permittivity and conductivity maps are shown on the centre and right, respectively.

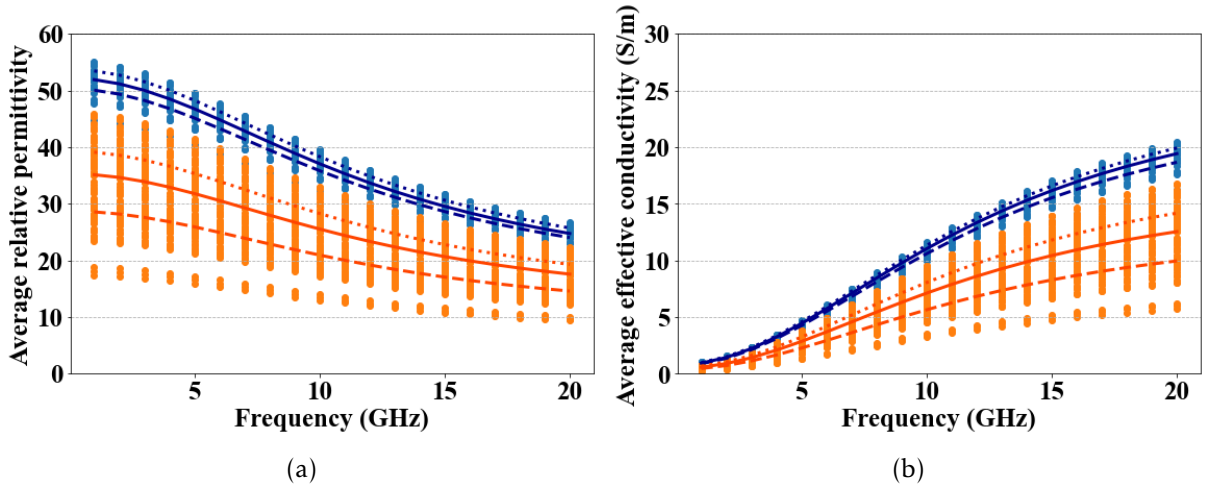

Figure 4.17: Relative permittivity (left) and effective conductivity (right) of healthy (orange) and metastasised (blue) ALNs estimated from MR images, over frequency. The dashed, solid and dotted lines represent the first, second and third quartiles of both healthy and metastasised ALNs, respectively.

have higher dielectric properties and the variability is much lower than healthy ALNs, with an average relative permittivity ranging from 40.5 to 49.7 at 5 GHz. The estimated dielectric properties of both healthy and metastasised ALNs are statistically different with a p-value of 10^{-14} for both relative permittivity and conductivity at 5 GHz. The dielectric contrast between the median of both healthy and metastasised groups is 31.8% at 5 GHz. The following analysis focuses on average relative permittivity values as they highlight absolute differences, but comparable conclusions can be drawn from conductivity results.

One factor that may explain the variability of permittivity values for healthy ALNs is the variability of their size. Figure 4.18 shows how average relative permittivity values change over the ALN larger axis length (i.e. the larger dimension of the ALN within the three image planes) and volume. A trend between relative permittivity and the ALN larger axis is observed in Figure 4.18(a). Comparatively, this trend is more

Table 4.5: Debye model parameters for healthy and metastasised ALNs applied to 1 to 20 GHz frequency range.

	Healthy ALNs			**Metastasised ALNs**		
Quartile	Q1	Q2	Q3	Q1	Q2	Q3
ϵ_∞	9.33	10.94	11.81	14.18	14.49	15.22
σ_s (S/m)	0.36	0.48	0.56	0.75	0.77	0.83
$\Delta\epsilon$	19.37	24.35	27.49	36.14	37.67	38.54
τ (ps)	13.00	13.00	13.00	13.00	13.00	13.00

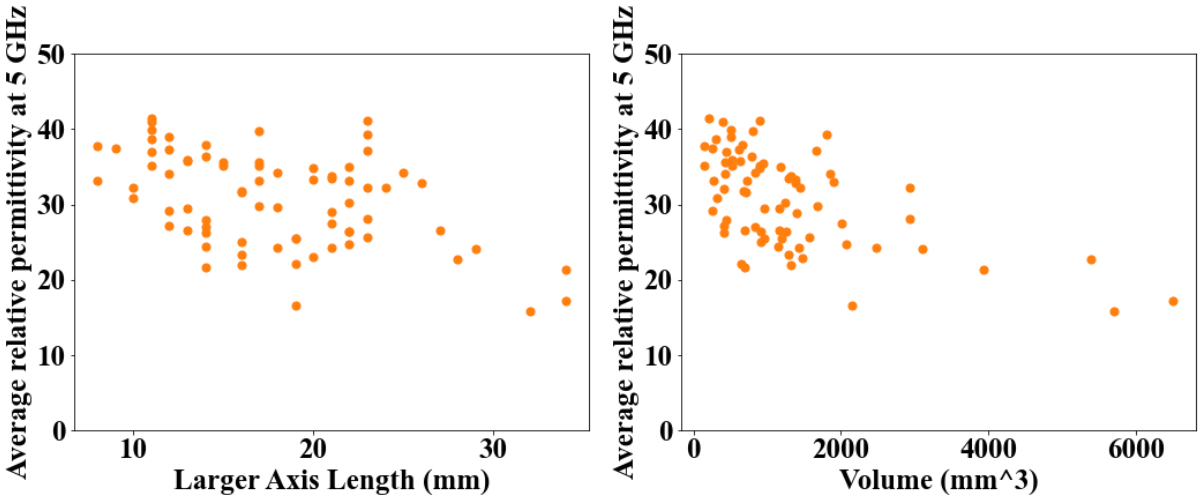

(a) (b)

Figure 4.18: Estimated relative permittivity at 5 GHz of each healthy ALN over its larger axis length (left) and volume (right).

evident considering the total ALN volume [Figure 4.18(b)]: smaller ALNs have higher average relative permittivity values. This can be due to the fact that smaller ALNs have a smaller hilum, which means the cortex is the ALN structure contributing more to the average dielectric properties of the ALN.

Figure 4.19 shows the relative permittivity change over the patients' BMI. BMI could have an impact on bias field removal performance which would result in changes of voxel signal intensities and, consequently, in estimated dielectric properties. However, Figure 4.19 shows that average relative permittivity values change independently of BMI, for both healthy and metastasised ALNs, indicating that this methodology is sufficiently robust for all patients' BMI.

The robustness of this methodology can also be evaluated by analysing patient-specific results. Figure 4.20 shows a comparison between the resulting average relative permittivity values of ALNs within the same patient. The values vary between patients but they are all within a similar range of values. This indicates that the estimated permittivity values with this methodology are not within different intervals of values

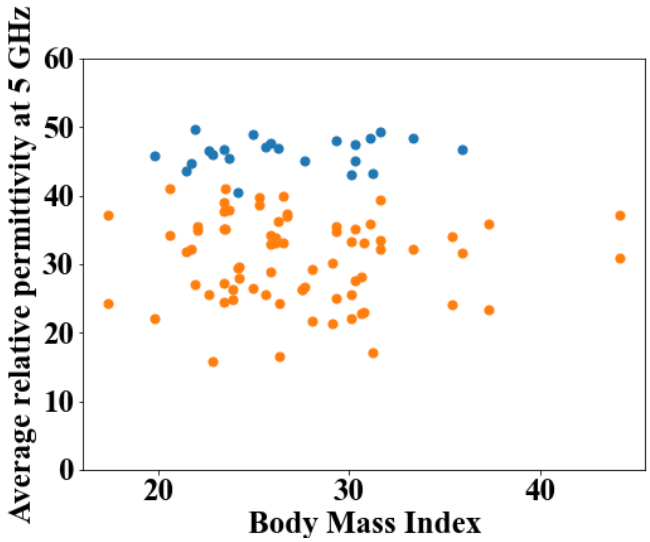

Figure 4.19: Estimated relative permittivity at 5 GHz of each ALN over the patient's BMI. Healthy ALNs are represented in orange and metastasised ALNs in blue.

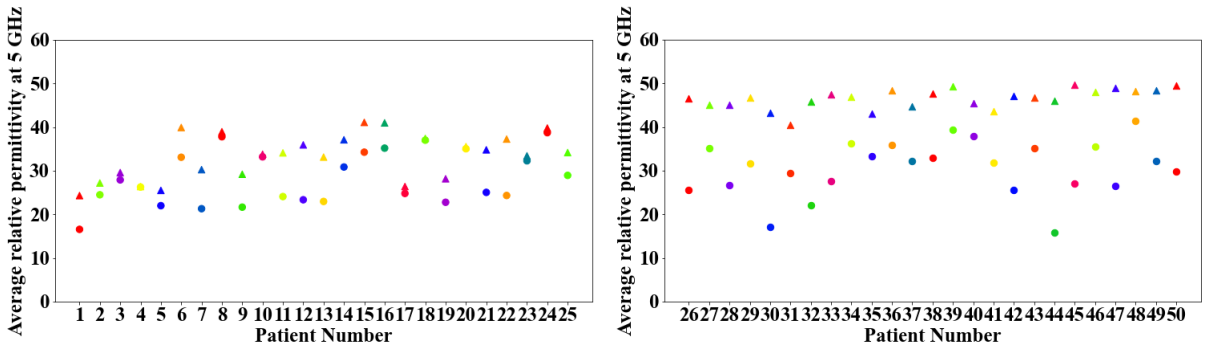

(a) (b)

Figure 4.20: Comparison of estimated average relative permittivity within each patient for 5 GHz. (a) shows a comparison between healthy ALNs and (b) shows a comparison between healthy and metastasised ALNs. In (a) both circles and triangles are healthy ALNs, while in (b) circles represent healthy ALNs and triangles represent metastasised ALNs.

per patient or neither the same interval across all patients. The contrast of relative permittivity between healthy and metastasised ALNs within the same patient is larger (on average 34%) than between healthy ALNs (on average 16%). This analysis confirms that the dielectric property results are not due to variability between MR images but between the ALNs themselves.

The assumptions behind this methodology do not allow a direct comparison of absolute dielectric property values with state-of-the-art values measured with traditional methods, such as Open-Ended Coaxial Probe (OECP) [55], [58]. Furthermore, a comparison to actual OECP measurements of ALNs of the patients included in this study is not possible since no follow-up of the patients was done. Nevertheless, these results can be compared to the main conclusions drawn from those studies. The large range of dielectric property values is common across studies. While in the case of OECP this

large range might be due to sample handling and limitations on measuring heterogeneous samples, in this study it can be explained by the inherent heterogeneity of the ALN and variability intra- and inter-patient. The range of the relative permittivity we can estimate from MRI varies from 15.9 to 49.7 at 5 GHz which is lower when compared from 4.9 to 49.6 measured with OECP [58]. This may have three explanations: 1) the estimated dielectric properties are limited by a minimum and maximum dielectric property curve obtained from measurements of fibroglandular tissues and ALNs could have higher properties than this type of tissue; 2) the voxel intensity values of ALNs can be affected by the distance to the coil even if this effect is reduced by the bias field removal algorithm; 3) OECP measurements may not be sensitive to the heterogeneity of the samples, providing a weighted average of the properties of the measured sensing volume of the ALN, and may be hampered by adipose tissue. Despite these points, this study is an important contribution to the understanding of the dielectric contrast between healthy and metastasised ALNs. Additionally, the observed contrast between healthy and metastasised ALNs (31.8% and 34% for inter- and intra-patient) is a good indicator for the feasibility of an MWI system aiming to diagnose ALNs. In Section 4.5, a validation of this methodology will be presented.

4.4 Creation of Axillary Region Numerical Models

The axillary region numerical models are created after adapting the segmented results from the image processing pipeline. To anatomically represent the tissues of interest, the obtained clusters from K-Means are grouped into two clusters: adipose and muscle/fibroglandular tissue. Multiple ALNs are included in the numerical models after being selected using the connected-component labelling method (introduced in Section 4.3). This method also allows to remove artefacts generated by vessel structures as it removes smaller sub-clusters within muscle/fibroglandular tissue cluster. The resulting models have a total of 6 groups of tissues: adipose tissue, muscle/fibroglandular tissue, skin, lungs, healthy ALNs and metastasised ALNs. Bone was the only large structure which was not included since MRI does not allow a good contrast between bone and the surrounding tissues. However, as mentioned before, this structure is deeper than muscle, which would attenuate bone MWI response, and therefore its MWI response in the axillary region is negligible. Moreover, the model is divided into two sections of each axillary region (right and left), using the nipples as the medial limit and the bottom part of the breasts as the inferior limit.

A repository was made available for download on GitHub [205] and includes axillary region numerical models of 5 patients. These models were created from a selection of patients from the larger dataset of 448 patients, ensuring the representativeness of axillary regions with both healthy and metastasised ALNs. The presented models have

Table 4.6: Specifications of axillary region models.

Model AR_	Patient BMI	Side	Dimensions A	Dimensions C	Dimensions S	Resolution A	Resolution C	Resolution S	# H ALNs	# M ALNs
001	21	R	190	298	121	0.99	0.99	1	1	2+1 Matted
		L	190	298	126				3	0
002	24	R	204	297	144	0.99	0.99	1	0	6
		L	204	297	105				4	0
003	26	R	169	325	114	1.07	1.07	1	3	0
		L	169	325	111				1	1 Matted
004	26	R	213	360	144	0.99	0.99	1	1	2
		L	213	360	154				3	0
005	31	R	217	443	169	0.99	0.99	1	1	1
		L	217	443	138				2	0

BMI: Body Mass Index; ALNs: Axillary Lymph Nodes; R: Right; L: Left;
A: Axial Direction; C: Coronal Direction; S: Sagittal Direction; H: Healthy; M: Metastasised

variability in terms of number of metastasised ALNs and BMI, as shown in Table 4.6. When considering models of patients with different BMIs, the models present variability of ALNs depth and positioning in relation to the surrounding muscles. Different types of metastasised ALNs are also included in the models, such as single ALNs, multiple clearly separated ALNs, or matted ALNs. Figure 4.21 shows three examples of the numerical models in 3D and more details of each model are presented in Appendices B, C, D, E and F.

Each patient folder includes two sub-folders with the corresponding right and left axillary region numerical models. A single file is provided for each group of tissues so the users can combine and create models with different levels of complexity. Each

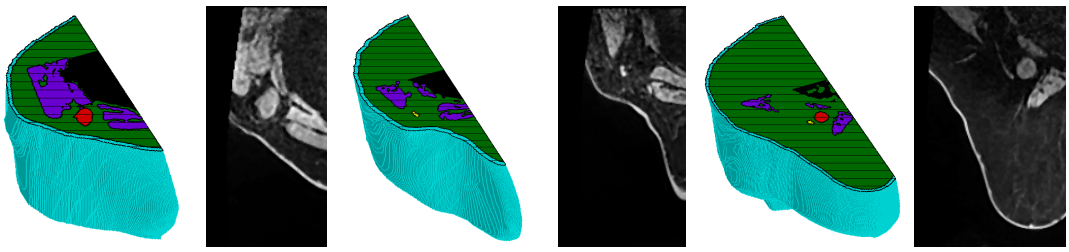

(a) (b) (c) (d) (e) (f)

Figure 4.21: 3D representation with a 2D axial view and the corresponding MRI slice of (a,b) AR_001, (c,d) AR_003, and (e,f) AR_005 right axillary region models. Light blue colour represents the skin layer, green represents adipose tissue, purple represents muscle, black represents lung cavity, yellow represents healthy lymph node, and red represents metastasised lymph node.

Table 4.7: Debye model parameters for skin, muscle, lung and adipose tissue (valid from 1 to 20 GHz) [116], [125], [133].

	Skin	**Muscle**	**Lung**	**Adipose**
ϵ_∞	15.93	21.66	7.62	3.12
σ_s (S/m)	0.83	0.89	0.81	0.05
$\Delta\epsilon$	23.83	33.24	14.03	1.59
τ (ps)	13.00	13.00	13.00	13.00

numerical model includes a maximum of 6 groups of tissues: adipose tissue, muscles and fibroglandular tissue, skin, lung, healthy ALNs and metastasised ALNs.

The files are provided in MAT, RAW and STL formats. The numerical models are created with the original resolution of the MRI scans, so users might need to use post-processing steps such as interpolation or smoothing filters to fit the electromagnetic simulation software requirements or for 3D-printing. Two additional files for adipose and skin without cavities are provided in STL format to allow the user to combine post-processing STL files.

The user has two options to assign the dielectric properties to the numerical phantoms. The first option consists of implementing the Debye models presented in Tables 4.5 and 4.7. The second option consists of associating a dielectric property map for each frequency, which can be obtained from the interpolation between MRI voxel intensities and dielectric properties. For this option, 2 additional files in MAT and RAW formats for each axillary region model are provided: $\mathbf{label}_{\text{map}}$ and $\mathbf{weight}_{\text{map}}$. The $\mathbf{label}_{\text{map}}$ file has a matrix where each voxel is represented by one of 7 labels, as shown in Table 4.8. Each label defines which dielectric properties curves should be used to interpolate the voxel intensities into the corresponding dielectric properties. The $\mathbf{weight}_{\text{map}}$ file includes the weight of each voxel calculated using equation 4.8. The corresponding dielectric property map can then be calculated using equation 4.7.

This repository is an important contribution to the community and is a useful tool for the development and validation of dedicated algorithms for MWI systems designed to diagnose ALNs.

4.5 Validation of Dielectric Properties Estimation with Phantom

As mentioned in Section 4.3, no OECP measurements of ALNs of the patients included in the study were possible. Hence, the accuracy of the presented methodology and the estimated dielectric properties could not be calculated. In order to address this gap in the analysis, a phantom with mixtures with known dielectric properties is used to

Table 4.8: Correspondence between labels and Debye models for interpolation (valid from 1 to 20 GHz) [116], [125], [133].

Cluster number	**Dielectric property curve**	ϵ_∞	σ_s **(S/m)**	$\Delta\epsilon$	τ **(ps)**
-2	Skin	15.93	0.83	23.83	13.00
-1	Lung	7.62	0.81	14.03	13.00
0	-	-	-	-	-
1	Minimum	2.31	0.005	0.09	13.00
	Lower Bound Adipose	2.85	0.05	1.10	13.00
2	Lower Bound Adipose	2.85	0.05	1.10	13.00
	Upper Bound Adipose	3.99	3.55	0.08	13.00
3	Lower Bound Fibroglandular	12.99	0.40	24.40	13.00
	Upper Bound Fibroglandular	14.20	0.82	40.49	13.00
4	Upper Bound Fibroglandular	14.20	0.82	40.49	13.00
	Maximum	23.20	1.31	46.05	13.00

validate the adopted assumptions in the methodology, while replicating a breast MRI exam. The purpose of this study is to compare the estimated dielectric properties using the developed methodology with the known dielectric properties. The impact of other effects, such as the distance to the coil and bias field effect, in the estimated dielectric properties is also evaluated.

The following sections describe the creation of the phantom and the used mimicking materials, the methodology used for the MRI acquisition and the dielectric properties estimation, and the main results.

4.5.1 Phantom Creation

A physical phantom was created so it could be used in the dedicated breast MRI coil. To that end, a breast-shaped phantom was created to ensure similar interaction of the magnetic fields and similar behaviour of MRI artefacts (e.g. the bias field) to what happens in a real patient exam. The phantom comprised several compartments where breast tissues mimicking mixtures could be inserted.

The anthropomorphic physical phantom of the breast and part of the axillary region was created from the breast MR images collected and described in Section 4.1. A patient exam with a small breast size was chosen so both the breast and part of the axillary

region could be printed in Form 3 3D-printer (Formlabs [206]), which is limited to a volume of $145 \times 145 \times 180$ mm^3. Firstly, a numerical phantom was created following the procedure described in Section 4.2.2.1. The numerical phantom was then divided in two parts, the left and the right sides. Only the left side was used in the following steps. The phantom was partially cut to fit within the volume of the 3D-printer and converted to a STL file, as shown in Figure 4.22(a).

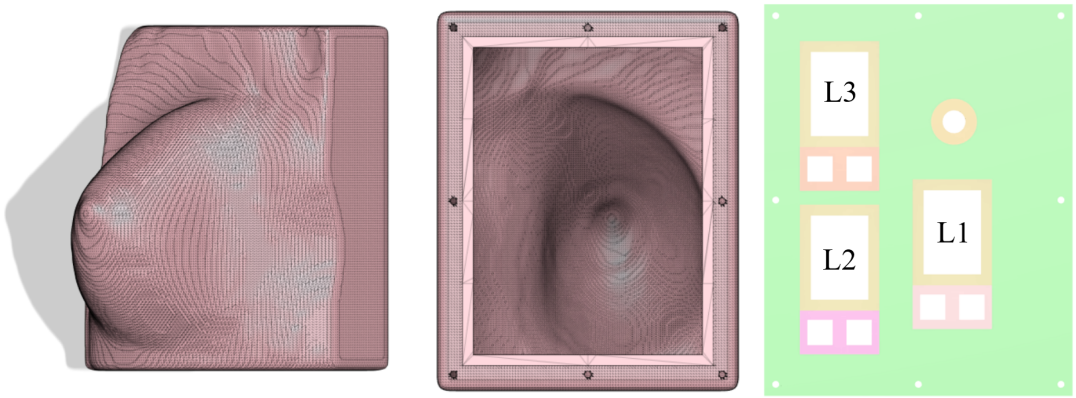

(a) (b) (c)

Figure 4.22: Numerical model of the breast and axillary region phantom in (a) perspective view, in (b) axial view showing the opening of the phantom, and (c) the corresponding cover with three opening for the compartments. L1, L2 and L3 are the labels of each compartment location.

The remaining steps were performed using Meshlab™ and Autodesk® Fusion 360®. The phantom was made hollow, with a wall-thickness of 2 mm. In order to create a phantom that could be adaptable for other tests, an opening in the corresponding posterior part of the body was created which could then be closed with a corresponding cover. To this end, a border around the opening was maintained in order to enable the insertion of holes for 8 nylon screws [Figure 4.22(b)], which were used to attach the cover of the model. The corresponding cover [Figure 4.22(c)] was designed also with 8 holes, 3 rectangular openings where compartments for several liquid tissue mimicking mixtures would be fixed, 6 squared openings where solid tissue mimicking mixtures would be fixed, and one circular opening to give access to the main volume. The rectangular and squared openings were created in different locations so the effects of MRI artefacts could be evaluated between the same mixtures: near the nipple (L1), lateral to the breast in the inferior part (L2) and lateral to the breast in the superior part (near the axillary region) (L3).

Each rectangular opening was designed for a compartment, divided into six smaller compartments in order to hold 6 liquid tissue mimicking mixtures in each of the three locations (L1, L2, L3). L1 has a height of 113 mm, L2 has a height of 43 mm, and L3 has a height of 38 mm, as shown in Figure 4.23(a). Each smaller compartment has dimensions 10×10 mm^2 and are separated by 1.5 mm. The two squared openings next to each compartment location [Figure 4.22(c)] were designed to hold 2 solid tissue

mimicking mixtures. More details in those mixtures will be given in the following section (Section 4.5.2). The corresponding covers for these compartments were created so that the compartments could be totally sealed to avoid any sanitation issues in transportation and during the MRI exam [Figure 4.23(b)].

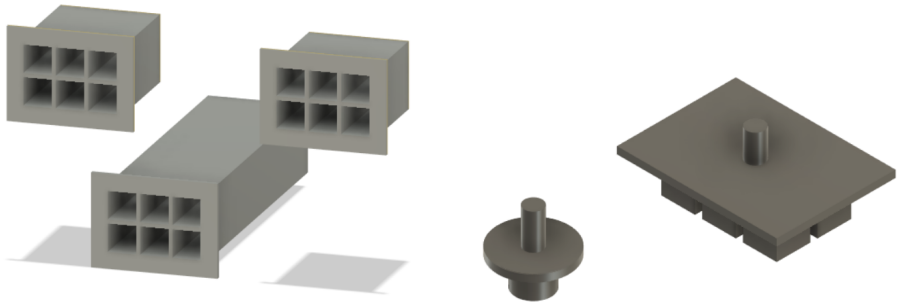

(a) (b)

Figure 4.23: (a) Numerical models of L1 (bottom), L2 (top left) and L3 (top right) compartments, and (b) numerical models of individual covers.

All the components of the phantom were printed in Form 3 3D-printer (Formlabs [206]) using the Clear Resin polymer. The main cover was attached to the model with nylon screws, as shown in Figure 4.24.

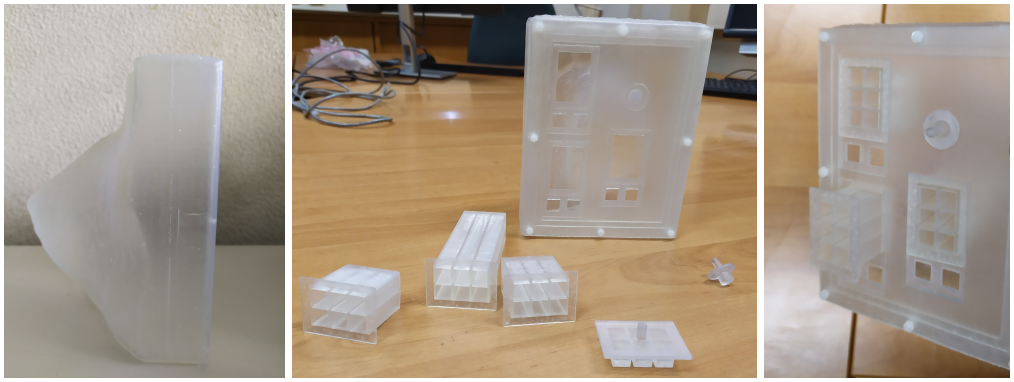

(a) (b) (c)

Figure 4.24: 3D-printed phantom and compartments.

4.5.2 Tissue Mimicking Materials

As explained in Section 2.3.3, the MRI response depends on the interaction between molecules. Therefore, it can vary with the state of the matter under study. Therefore, different states of matter are considered for tissue mimicking materials in this study, allowing to evaluate the MRI response for mixtures with the same dielectric properties but in a different state.

Seven liquid mimicking mixtures and two solid tissue mimicking mixtures are considered. One of the liquids is the main liquid in the phantom to mimic adipose

Table 4.9: Composition of the mixtures used in the phantom and reported average dielectric properties at 5 GHz.

Mixture Composition	**Mixture Symbol**								
	G3	**B**	**G2**	**G1**	**T**	**WN**	**W**	**S-**	**S+**
TX-100 (%)	100	75	40	28	21	0	0	-	-
Water (%)	0	25	60	72	79	100	100	-	-
Salt (g/L)	0	0.8	4.28	5.7	6.2	11.69	0	-	-
Polyurethane part-A (%)	-	-	-	-	-	-	-	40	32
Polyurethane part-B (%)	-	-	-	-	-	-	-	40	32
Graphite (%)	-	-	-	-	-	-	-	20	30
Carbon-black (%)	-	-	-	-	-	-	-	0	6
Acetone (mL/100 g)	-	-	-	-	-	-	-	0	3
ϵ_r	5	10	32	44	50	71	74	8	30
σ **(S/m)**	0.2	1	3	4	4	1	1	0.1	2

tissue, the remaining six were inserted in the compartments presented in the previous section and the two solid mixtures were embedded in the main liquid.

The mixtures are based on well-reported recipes of tissue mimicking materials for MWI frequencies. The liquids are mixtures of Triton® X-100 surfactant, destilled water and salt (NaCl), following the recipes of Joachimowicz *et al.* [145], [207] in order to represent a wide range of dielectric properties in 0.5 to 10 GHz frequency band. The solids are mixtures of polyurethane, graphite, carbon-black and acetone, following the recipes of Oliveira *et al.* [146]. These mixtures were chosen due to the availability of the materials and, although they have some challenges, they are relatively easy to produce. Table 4.9 shows a summary of the composition of the mixtures. G3, G2 and G1 mimic Lazebnik *et al.* [125] measurements of breast tissues, representing low-density, medium-density, and high-density breast tissues, respectively. B stands for bone, T stands for tumour, WN stands for water with NaCl, and W stands for water. S stands for solid, - and + represent the lowest and highest dielectric property mixture, respectively. The solid mixtures were created using a mould [Figure 4.25(a)] and reshaped afterwards into a parallelepiped [Figure 4.25(b)] to fit within the phantom.

The dielectric properties of all the mixtures were measured using the OECP method 3 to 6 hours prior the acquisition in MRI. The measurements were performed over the frequency band 0.5 to 10 GHz using a Keysight N1501A dielectric slimform probe kit (comprised by a probe, a cable and a probe stand) and connected to a Keysight E5063A Vector Network Analyser (VNA) [Figure 4.25(c)]. As standard procedure, the system was calibrated using the open/short/load method before all measurements [208]. Distilled water was used as a standard load. Each liquid was measured up to

(a) (b) (c)

Figure 4.25: Solid tissue mimicking mixtures (a) before and (b) after reshaping, and (c) while measuring the dielectric properties with the Keysight slim form probe and controlling pressure with a scale.

3 times and the results are shown in Figure 4.26. Each solid was measured 3 times in four different points and the pressure was controlled with a scale [Figure 4.25(c)]. The results of the solid mixtures are shown in Figure 4.27. The results show the dielectric properties of liquids are more consistent over repetition. The variation of the measured dielectric properties in the solid mixtures in the same measurement point is higher than the one observed with liquids. The variation between different points is also substantial. These differences are even more evident for the S+ mixture, which has the highest dielectric properties. This can be explained by the fact that liquids are more homogeneous and the existence of air bubbles during the dielectric measurement is easier to control. Conversely, the homogeneity of solid mixtures could not be ensured and the OECP is sensitive to the pressure and contact between the solid and the probe. As more graphite and carbon-black powder are added during the production of the mixtures, the more difficult is to mix all the components. Therefore, mixtures with higher dielectric properties may be more heterogeneous and have air bubbles inside. Due to time constraints, no other type of solid mixtures were produced and these mixtures were used in the performed tests in the MRI.

4.5.3 Imaging Acquisition

One to two hours before the imaging acquisition, the compartments were filled with the liquid mixtures and the solid mixtures were placed inside the phantom immersed in the main liquid. The mixtures were randomly positioned inside the compartments, as shown in Figure 4.28(a), ensuring the repetition of each mixture in locations L1, L2 and L3. All liquids were easily inserted in the whole compartment, except for the G2 mixture, which was viscous and ensuring the absence of air bubbles inside the compartment was not possible. The phantom was then sealed with silicone and with tape to avoid leakage [Figure 4.28(b-c)].

The phantom was imaged in a 3.0T clinical MR system (Magnetom Vida, Siemens

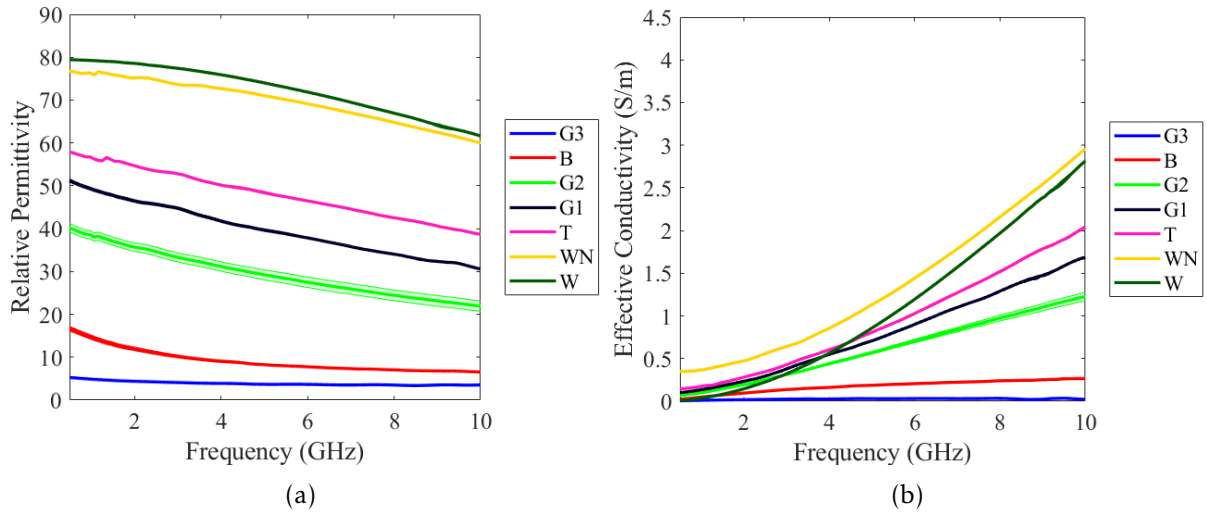

Figure 4.26: Relative permittivity (left) and effective conductivity (right) of the measurements on liquid tissue mimicking mixtures over the frequency band 0.5 to 10 GHz. Each liquid is represented by the average curve of all measurements and a band of the same colour which represents the average minus and plus the standard deviation of the measurements.

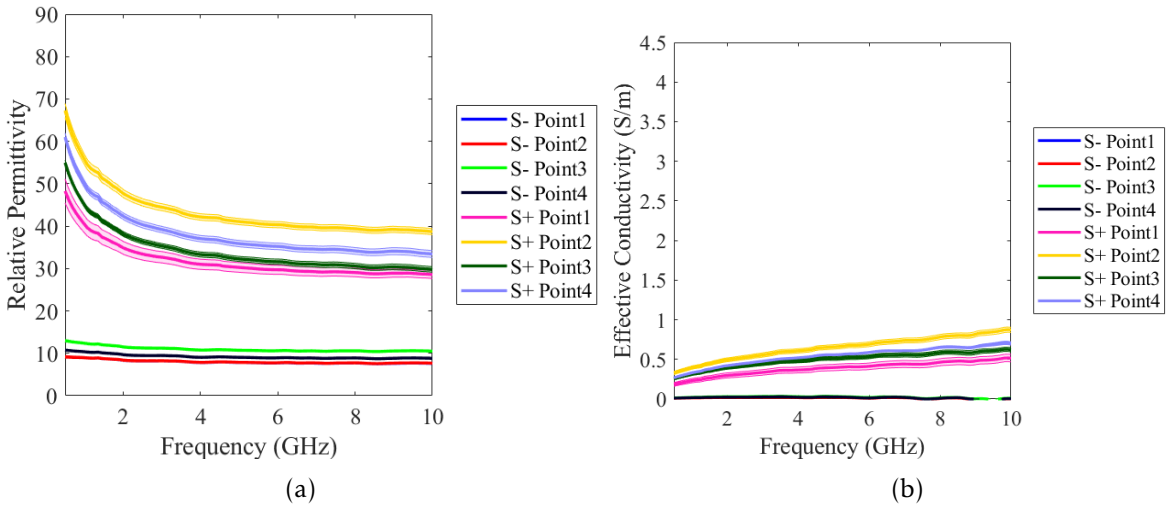

Figure 4.27: Relative permittivity (left) and effective conductivity (right) of the measurements on solid tissue mimicking mixtures over the frequency band 0.5 to 10 GHz. Each solid is represented by the average curve the measurements in each point of measurement and a band of the same colour which represents the average minus and plus the standard deviation of the measurements.

Healthineers), as shown in Figure 4.29. The used MRI sequences comprise the majority of the sequences used in the patient study (Table 4.2), excluding the DWI STIR and T_1-w SPAIR image sequences, and a new sequence: T_2-w TSE VIBE Dixon. This image sequence also creates a set of images with different contrasts (Dixon-IN, Dixon-OPP, Dixon-F and Dixon-W, as explained in Section 2.3.3), and it is acquired in the axial plane with voxel size of $1.48 \times 1.48 \times 1$ mm^3.

Figure 4.30 shows the original images acquired in the same axial plane. The T_1-w localisation and T_2-w STIR sequences are excluded from the study as they do not provide additional information. As can be observed in all images, the solid mixtures produce a magnetic susceptibility artefact, causing some image distortion. In fact, this behaviour

(a) (b) (c)

Figure 4.28: Positioning of the mixtures inside the phantom (left) and final phantom in axial (centre) and sagittal (right) views.

(a) (b) (c)

Figure 4.29: Phantom inside the breast MRI coil in the MRI scanner table in three different perspectives. The dashed black contour in (c) represents the approximate position and shape of the breast coil.

is common in paramagnetic materials [209], which attract the external magnetic field and create local induced magnetic fields. However, this was not expected to happen because polyurethane, graphite and carbon-black are diamagnetic materials [210], i.e. do not attract magnetic fields. However, graphite may show paramagnetic behaviour when its structure is disordered, which may have happened when mixing it with the other components [211]. Unfortunately, these results mean that no comparison between solid and liquid mixtures can be done as the solid mixtures have to be disregarded. Due to time constraints, no other solid mixtures were prepared to overcome this problem. As expected due to its viscosity, the compartment with the G2 mixture presents air bubbles, as can be observed in the L1 compartment in Figure 4.30(e-i). Although these artefacts affect some of the images, it is possible to observe that liquid mixtures are imaged with distinct voxel intensities in the different image sequences and the contrast between the mixtures is also different. Contrarily to what happened in breast patient exams, the T_1-w Dixon-W image sequence is the sequence where the contrast between

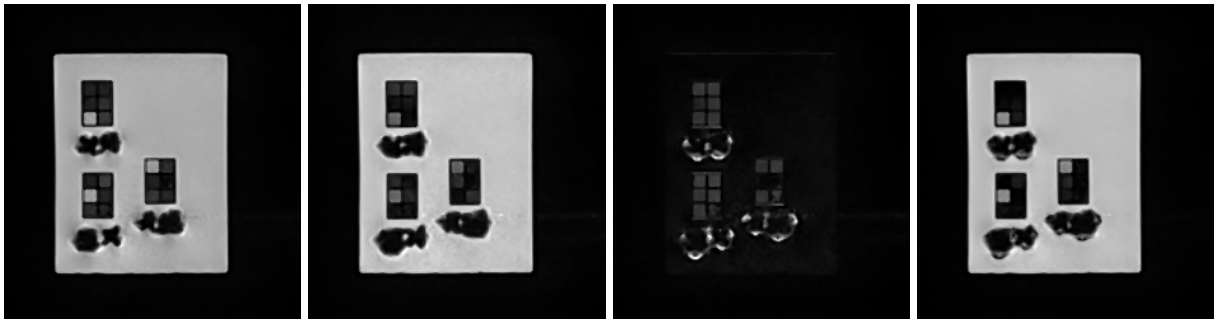

(a) T_1-w Dixon-IN (b) T_1-w Dixon-OPP (c) T_1-w Dixon-W (d) T_1-w Dixon-F

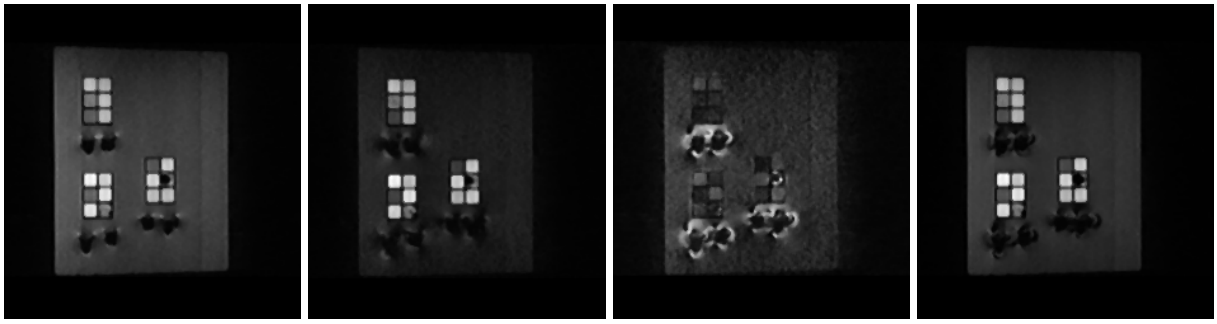

(e) T_2-w Dixon-IN (f) T_2-w Dixon-OPP (g) T_2-w Dixon-W (h) T_2-w Dixon-F

Figure 4.30: Original MR images acquired with the phantom.

the mixtures is the smallest. The image sequences with the best contrast between the mixtures are the T_2-w Dixon-IN, T_2-w Dixon-OPP or T_2-w Dixon-F. Similarly to the patient study, the image sequences with best contrast between the structures of interest should be the ones used for estimation of dielectric properties. Therefore, T_2-w Dixon-IN, T_2-w Dixon-OPP or T_2-w Dixon-F are the ones that should be used for that purpose.

4.5.4 Dielectric Properties Estimation

Some adaptations to the methodology presented in Sections 4.2 and 4.3 are performed in order to process the obtained images.

Firstly, a ground truth mask from the numerical model is created to label the mixtures under study and to remove artefacts that might hamper the segmentation of the mixtures [Figure 4.31(a)]. The removal of artefacts comprises the removal of the following: 1) artefacts of the phantom walls by applying a morphological dilation to the actual wall [Figure 4.31(b)]; 2) the region where the solid mixtures are, by using a binary mask of the T_1-w Dixon-F sequence and applying a morphological dilation to the artefacts [Figure 4.31(c)]; 3) air bubbles by considering the intersection between the binary mask of T_2-w Dixon-IN and the interior of the compartments [Figure 4.31(d)].

Prior to the dielectric property estimation, the image processing steps comprise part of the pipeline presented in Section 4.2. T_2-w Dixon is registered to T_1-w Dixon.

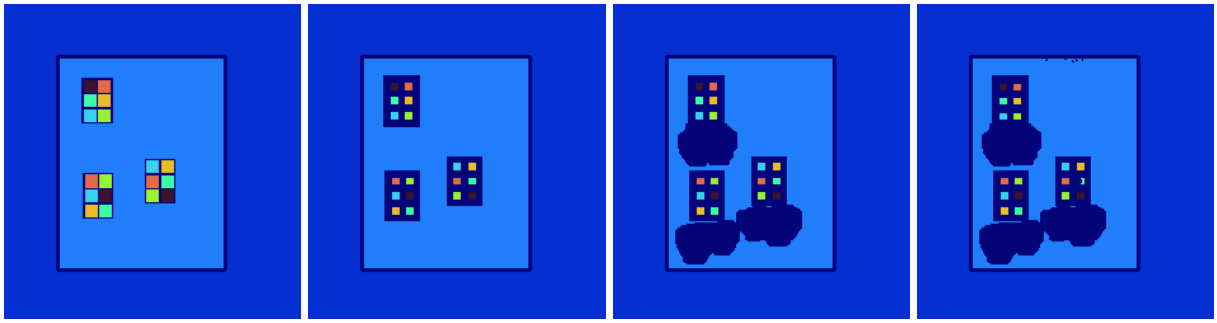

(a) (b) (c) (d)

Figure 4.31: Steps for creating the ground truth mask. (a) represents the original numerical model, in (b) the regions where artefacts produced by phantom walls are excluded, in (c) the regions where the solid mixtures are excluded, and in (d) the regions with air bubbles are excluded.

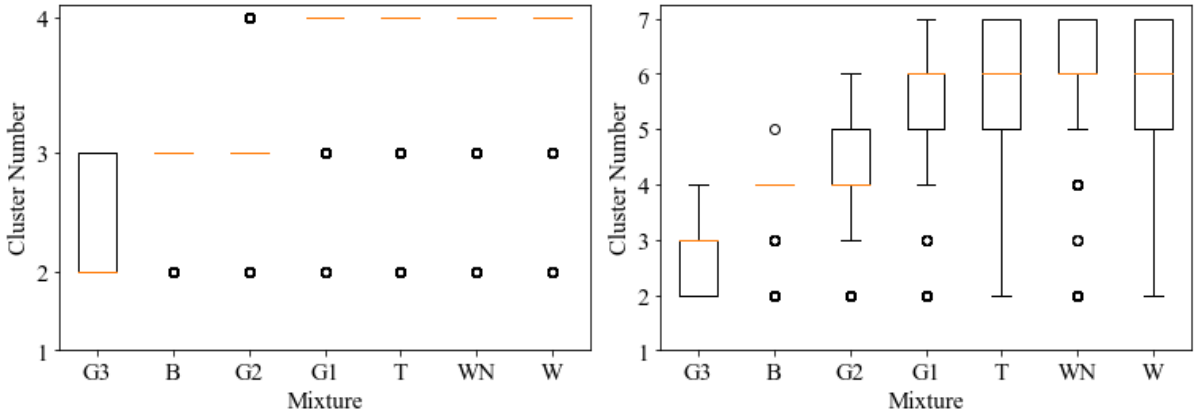

Figure 4.32: Box plots of the distribution of clusters for each liquid mixture for (a) $K = 4$, and (b) $K = 7$ applied to T_2-w Dixon-OPP image. The orange line represents the median, the boxes represent the first and third quartile of the distribution, and the dots represent the outliers.

The bias field removal is applied, as well as the median filter to remove noise, and the images are normalised. The segmentation of the mixtures is performed with K-Means. The best K value is chosen by maximising the separation of the mixtures in the clusters, while minimising the number of clusters where the same mixture is present. This criterion can be applied by visually analysing the images, as in the case with the patient exams, or, as a ground truth mask exists, this criterion can be analysed through plots similar to the ones represented in Figure 4.32. The examples in the figure show that $K = 4$ is more suitable since each mixture is present in less clusters.

The dielectric property estimation is performed following the same procedure presented in Section 4.3 while considering the Debye models fitted to the curves of Figure 4.26. In order to decrease the effect of limiting the range of values for the true dielectric properties, G3 curve is replaced by a lower bound curve corresponding to G3 curve minus 5% and the W curve is replaced by an upper bound curve corresponding to W curve plus 5%. Figure 4.33 shows the resulting curves of relative permittivity and an example of the piece-wise linear mapping to voxel intensities at 5 GHz when $K = 4$. In

this case, when $K = 4$, the background and air bubbles are exclusively included in one of the clusters, and therefore only 3 clusters are mapping. As the number of clusters is lower than the number of curves, some of the curves need to be neglected. The first

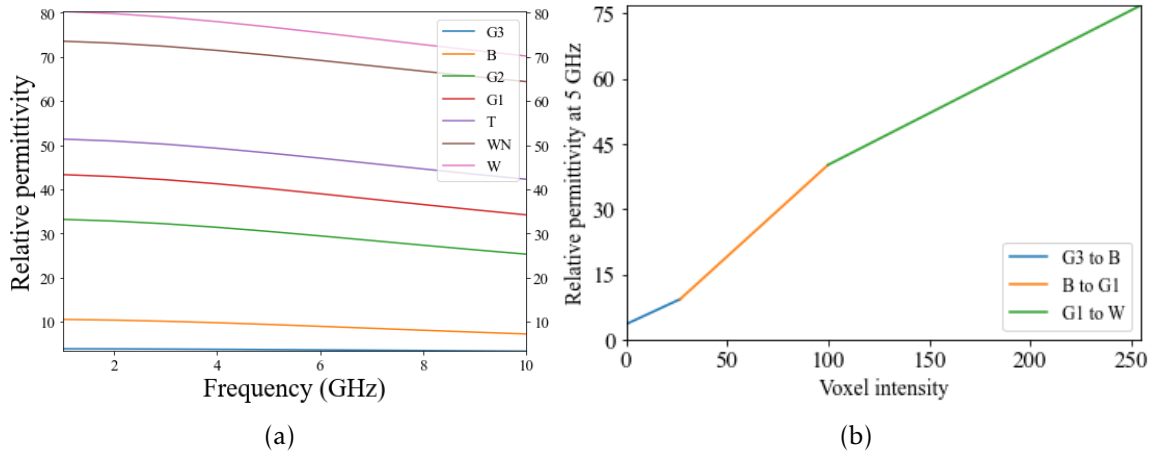

(a) (b)

Figure 4.33: Relative permittivity curves of liquid mixtures after fitting a Debye model and considering a variation of 5% in the G3 and W curves (left), and relative permittivity mapping to voxel intensities at 5 GHz when considering $K = 4$ in K-Means applied to T_2-w Dixon-OPP image (right).

cluster is mapped between G3 and B curves, the second cluster is mapped between B and G1 curves, and, finally, the third cluster is mapped between G1 and W curves. As shown in Figure 4.33(b), the resulting overall mapping is approximately linear.

Figure 4.34 presents the voxel intensities, the known dielectric properties of each liquid mixture for 5 GHz and the estimation of dielectric properties of the whole 3D volume considering T_2-w Dixon-OPP, one of the sequences with best contrast between the mixtures. The figure shows that the voxel intensities, and the corresponding estimated dielectric properties, for each mixture increase as the water content of mixtures increases, as expected. However, both the voxel intensities and estimated dielectric properties are within a large range of values for each mixture. The tendency is also not completely linear and does not follow the same behaviour as the dielectric properties. Besides the inherent artefacts of MRI scans due to field inhomogeneities, the response of the mixtures at MRI frequencies (127.74 MHz) may very well show different behaviour than at MWI frequencies (500 MHz to 20 GHz). Hence, although a linear relationship between voxel intensities and dielectric properties is a good approximation, this assumption can result in some errors.

Furthermore, the dielectric properties of some of the mixtures are under- or overestimated, which is more evident in the case of G3, B2, WN and W. This is one of the disadvantages of the method, as was also observed in Section 4.3. The minimum and maximum curves influences the estimation of dielectric properties, limiting the range of properties. Small artefacts or inhomogeneities of the image may affect the minimum and maximum voxel intensities of the clusters, which are then assigned to the minimum and maximum curves, resulting in under- or overestimation of the properties. In

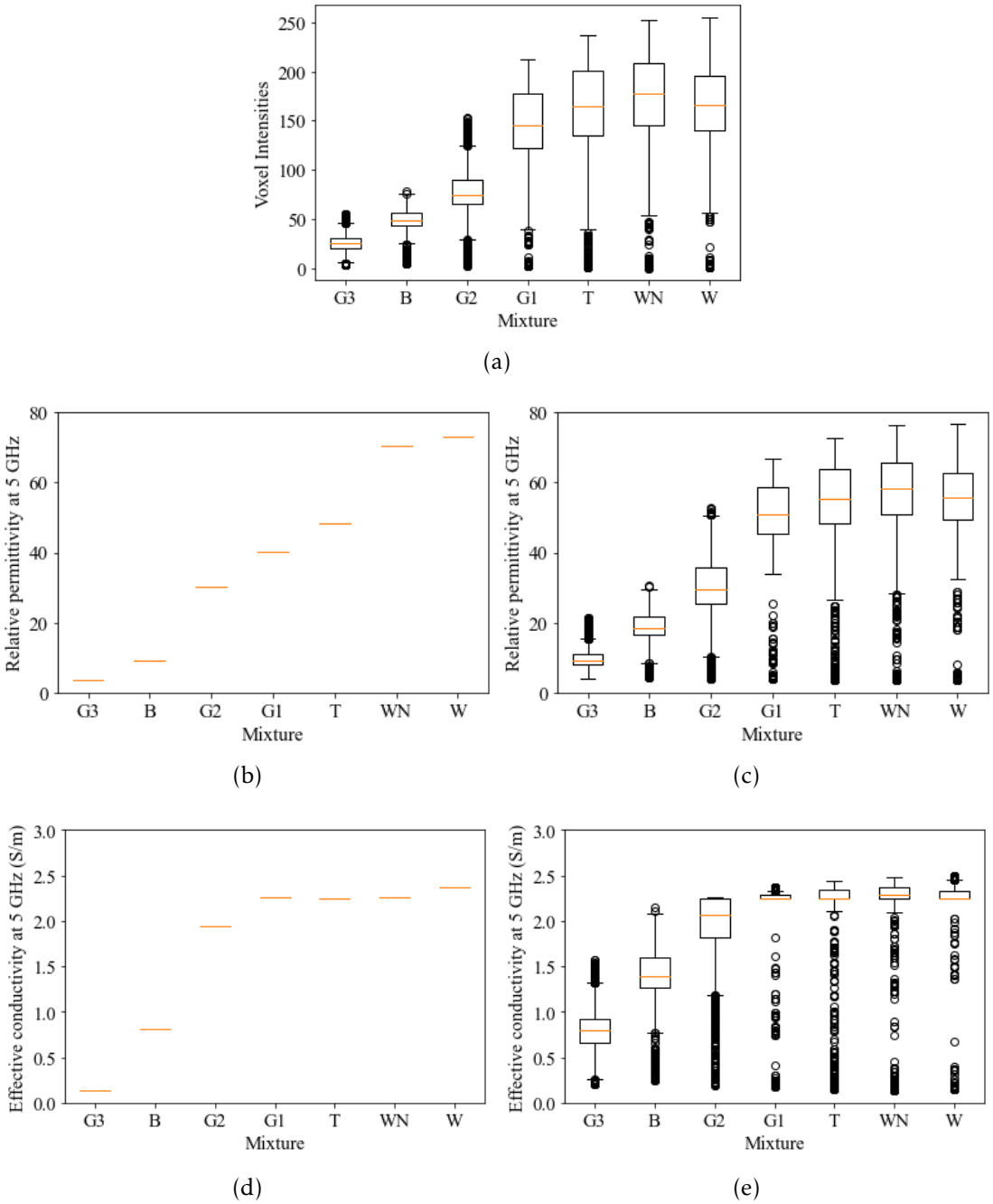

Figure 4.34: Box plots of the distribution of (a) voxel intensities, true (b) relative permittivity and (d) effective conductivity, and estimated (c) relative permittivity and (e) effective conductivity for each liquid mixture, using the 3D volume of T_2-w Dixon-OPP image. The orange line represents the median, the boxes represent the first and third quartile of the distribution, and the dots represent the outliers.

fact, the estimation of the dielectric properties from this phantom is more challenging since the properties of 7 different mixtures are meant to be estimated. In the case of the patient study, 5 curves are available to model the range of dielectric property values for adipose and fibroglandular tissues, and ALNs properties are estimated considering those curves. Moreover, the MR image sequences are not fine-tuned for this type of mixtures, considering their chemical composition, as they are for breast tissues, which can result in less accurate contrast between the mixtures.

To address the causes of the variability observed in the 3D results, the same processing steps are performed to a 2D slice. Additionally, the dielectric properties are also estimated for the mixtures inside each compartment (L1, L2, and L3) separately. For conciseness, the analysis is only shown for permittivity but a similar analysis could be done for conductivity. Figure 4.35 shows the estimated permittivity in a 2D axial slice where all compartments are visible. The range of permittivity values decreases

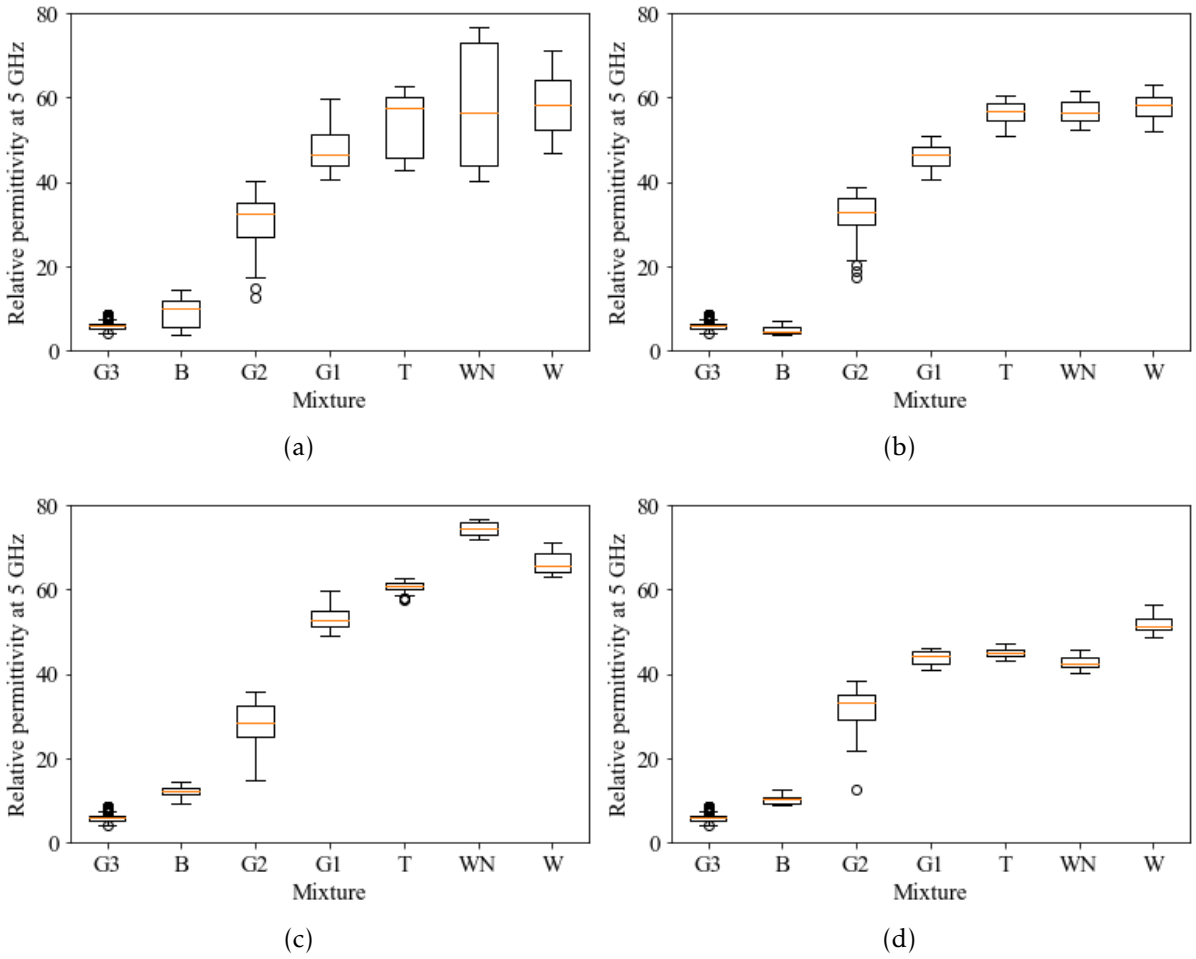

Figure 4.35: Box plots of the distribution of the estimated permittivity values for each liquid mixture for (a) 2D slice, (b) L1, (c) L2 and (d) L3, using T_2-w Dixon-OPP image. Orange line represents the median, box represents the first and third quartile of the distribution, and dots represent outliers.

when considering a 2D slice. This can be explained by the effects of inhomogeneities of the magnetic field and proximity to the coil which may not have been completely removed by the pre-processing steps. Different compartments also have slightly different estimated permittivity values. In particular, as can be observed in Figure 4.29, the L2 compartment is the one closest to the coil, which explains the higher voxel intensities and, therefore, corresponding higher dielectric properties.

The mean absolute errors of estimated dielectric properties in value and percentage considering the 3D volume and the 2D slice are shown in Figure 4.36. As a consequence of the under- and overestimation of the dielectric properties, the error of estimated

permittivity ranges from 2 to 17.2. As observed in previous results, the error is larger when considering the 3D volume. The error in percentage is larger for mixtures with the lowest permittivity values, reaching around 150% and 50% considering the 3D and 2D images, respectively. For mixtures G2, G1, T, WN and W, the percentage error is around 25%. Although these values are not satisfactory, the evaluation of the accuracy of the estimated contrast is relevant for the study of the contrast between healthy and metastasised ALNs.

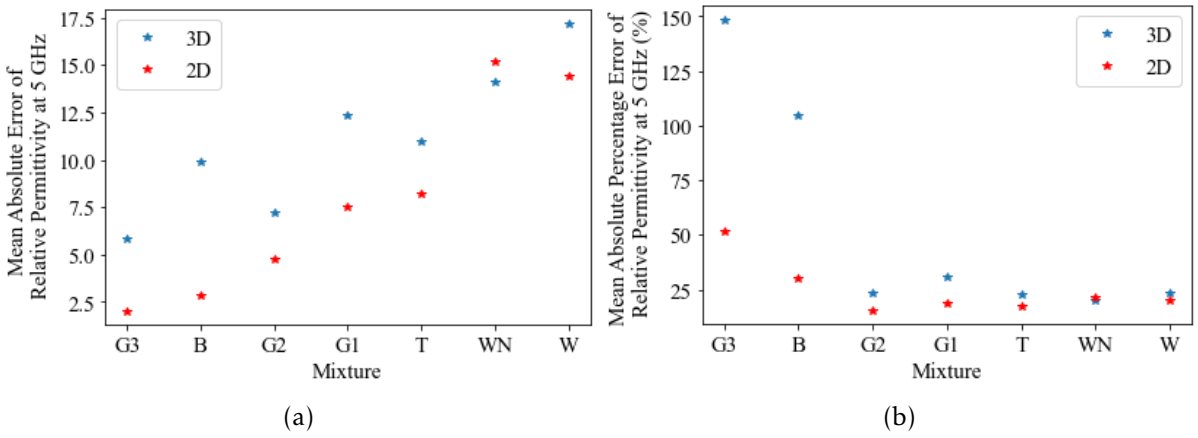

Figure 4.36: Mean absolute error of relative permittivity at 5 GHz of each mixture, in (a) absolute value and (b) percentage, considering 3D volume and 2D slice.

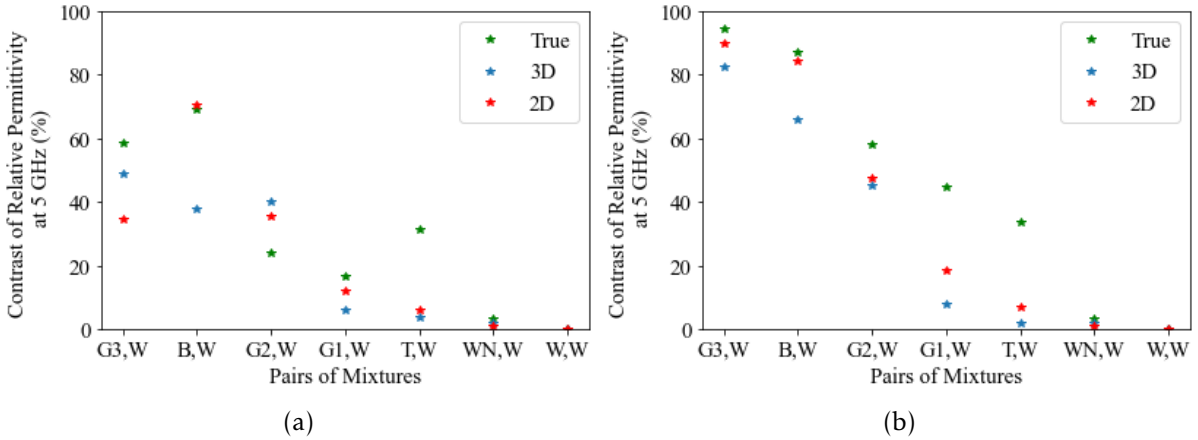

Figure 4.37: Contrast of relative permittivity at 5 GHz between (a) each pair of prior and consequent mixtures with ascending properties, and (b) between each mixture and the W mixture.

Figure 4.37 shows the contrast calculated between the average estimated permittivities of each mixture and a reference mixture, in comparison with the true contrast between the mixtures. The first plot considers the reference mixture as the mixture with consequent high permittivity value. The second plot considers the reference mixture as the W mixture. Figure 4.37 shows the contrast is underestimated in most of the cases. The exception is the B mixture when considering the contrast relatively to G2, and the G2 mixture when considering the contrast relatively to G1. As the G2 mixture

presented different characteristics (viscosity), this observation is not considered relevant. In the remaining cases, the difference between the true contrast and the estimated contrast can be up to 20%. These results indicate that even though the absolute error of estimated properties is not satisfactory, the estimated contrast is not compromised by overestimation.

In summary, the results with the validation phantom indicate that the relationship between voxel intensities and dielectric properties is not entirely linear. The estimated properties of ALNs may be underestimated, as well as the contrast between them. Moreover, it seems unlikely that the properties and the contrast are overestimated.

4.6 Chapter Conclusions

This chapter comprised the development of an image pipeline applied to MR breast images of patient exams with two purposes, both important to the development of microwave-based medical devices: the creation of anatomically realistic models of the axillary region with information about the dielectric properties and the estimation of dielectric properties of ALNs. The methodology used to estimate dielectric properties of ALNs was then validated with a phantom with mixtures with known dielectric properties.

Dielectric properties measurements of ALNs are still limited and inconclusive due to the reduced number of measured samples or their heterogeneity which influences the accuracy of the measurements. Thus, this study provided a way to address the dielectric properties of both healthy and metastasised ALNs and the contrast between both type of ALNs. A high variability of dielectric properties of healthy ALNs was observed, in line with what is reported in state-of-the-art traditional dielectric property measurements. And most importantly, a 31.8% contrast between healthy and metastasised ALNs was obtained, which is a good indicator for the validation of MWI systems to detect and diagnose ALNs. The validation with the breast phantom indicated that the error of the method for dielectric properties estimation varies with the magnitude of the properties values, ranging from 2 to 17.2 of absolute points of permittivity. Nonetheless, the results indicated the estimated properties can result in an underestimated contrast, rather than overestimated. This is a good indicator for MWI as it means the average contrast between healthy and metastasised ALNs may be higher than the one observed in this study. Ten axillary region region models of 5 patients were created and have been made available in an open-access online repository [205], which can be used towards the validation of new electromagnetic medical devices.

In the following chapter, a simpler physical axillary region phantom created from another exam is considered to experimentally validate an MWI system to aid the detection of ALNs. Future work should consider the developed models and the observed

dielectric contrast presented in this chapter.

5 Evaluation of an Axillary Microwave Imaging System

This chapter presents the evaluation of a novel Microwave Imaging (MWI) prototype to aid breast cancer staging through the detection of Axillary Lymph Nodes (ALNs). In particular, level I ALNs, which are the shallowest ALNs. Firstly, a preliminary simulation study is performed, followed by an experimental evaluation in a pre-clinical scenario.

Imaging the axillary region poses some new challenges compared to the state-of-the-art breast and brain MWI systems, which are described as follows:

1. **The location and size of the axillary region limits the options of antenna positioning:** Eleutério *et. al* [52] considered a planar antenna positioning over the surface of the axillary region phantom. However, the antenna dimensions for microwave frequencies of 2 to 6 GHz (a few centimetres) and the small size of the axillary region limit the number of antennas that can be used. Consequently, the reduced number of antennas substantially affects the resolution of the system. A cylindrical configuration is an alternative to improve resolution but, in contrast to breast or head imaging, a 360° sweep, which would have been important to improve image resolution, is not possible since the axillary region is in the torso.

2. **The axillary region presents both concave and convex surfaces:** The irregularity of the body in this region can hinder the effectiveness of common artefact removal algorithms mainly due to two reasons. Firstly, the distances between the antenna positions and the body are not constant, which means the response of the surface of the body is recorded at different distances for each antenna position. Secondly, each antenna position can record the reflection from different points of the surface of the body at different distances, which means each antenna position can record more than one reflection of the body surface.

3. **Immersing the axillary region in a coupling medium is not feasible in a real situation:** The advantages and disadvantages of using a coupling medium have been already addressed in previous chapters. In the axillary region application,

using a coupling medium is not practical, and therefore the reflections at air-dielectric interface have to be compensated.

4. **Location of ALNs**: In patients with low Body Mass Index (BMI), level I ALNs are known to be close to the skin, which may hinder the performance of air-dielectric response removal.

5. **Muscles response**: ALNs are surrounded by muscles which may have comparable microwave response and hamper the ALNs detection.

Prior to the presentation of the experimental validation, a brief study of radar imaging in a 2D simulated scenario with realistic-shaped axillary regions is presented. This study aims to evaluate the challenges of axillary imaging in a more simplified and controlled scenario, analysing the algorithms performance. Then, in the following sections, an experimental setup for axillary imaging is described, as well as the physical models and tissue mimicking materials used to test the system. The dedicated algorithms developed to detect the targets inside the axillary region are also presented. These dedicated algorithms include the definition of a volume of interest inside the axillary region. Patient-specific information is then used to fine-tune this method. Finally, an electromagnetic exposure risk assessment is performed using a numerical phantom in simulation using Computer Simulation Technology (CST) Studio Suite® software [189]. Challenges 4 and 5 mentioned above are still not fully addressed in this thesis.

5.1 Numerical Evaluation in 2D Simulation

This section presents a preliminary investigation of the challenges of imaging the axillary region using MWI in a 2D simplified scenario. In particular, the limitation of the antenna positioning and the irregularity of the shape are analysed. The performance of image reconstruction and artefact removal algorithms is evaluated.

5.1.1 Geometry for Numerical Analysis

A simulator [212], developed and implemented in Wolfram Mathematica®, was used to simulate the reflection coefficients considering 2D shapes of axillary region phantoms. This simulator receives the contour of the body and the target, and the average permittivity of the media, and computes the reflection coefficients $\mathbf{s}_{i,i}$ considering the contributions from all the visible points of the 2D contour. Each contribution is calculated considering the rays propagation and their direction in the corresponding medium. The antennas are modelled as ideal source points, which means the behaviour of a real antenna is not modelled.

The simulations were performed with two different axial slices of an axillary region phantom based on a Computed Tomography (CT) exam developed in my research

group [55] and one slice from two of the axillary region phantoms created in Chapter 4. These four 2D shapes (shown in Figure 5.1) were used to represent different realistic axillary region shapes. In the first two slices (shape A and B), the target is a circle with 6 mm radius placed in an arbitrary location, while in the last two slices (shape C and D), the target takes the real size and real position of the ALN. Shape A and C are more regular shapes and most of the contour visible in the field of view of the antennas has a convex shape. Contrarily, shape B and D present both convex and concave shapes. The depth of the ALN in shapes A, B, C and D are 29, 20, 23, and 83 mm, respectively. The axillary region and the ALN were simulated with $\epsilon_r = 4$ and $\epsilon_r = 50$, respectively, and a loss tangent $\tan(\delta) = 0.1$. No skin layer was considered at this stage.

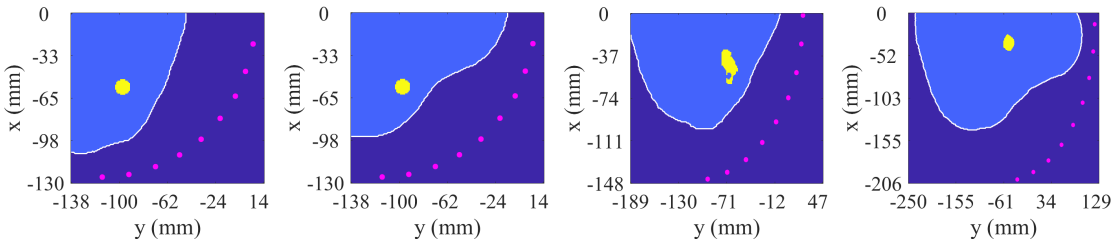

(a) Shape A (b) Shape B (c) Shape C (d) Shape D

Figure 5.1: Axial slices with different shapes considered for this study. The shapes are not represented within the same space (shown by x and y-axis). The light blue shape and the white solid contour represent the axillary region, the yellow shape represents the true location and size of the target, and the magenta points represent the source points surrounding the axillary region.

The axillary shapes were simulated without coupling medium, where 9 source points are placed in air. They are placed in a semi-circle around the region where the target is located, in a 90° angular range with a 10° angular step (magenta points in Figure 5.1). The positions of the source points are determined considering the known 3D-volume of the phantom. The first angular position is placed at the sagittal plane (x-plane) of the nipple, and the centre of rotation is determined so the last angular position is located close to the mid-coronal plane (y-plane which divides the body in half).

Figure 5.1 reflects some of the challenges in the positioning of the source points. Shape A and B are slices of the same axillary region phantom at different depth. To ensure the source point positioning comply with a cylindrical configuration, the source points were placed at the same (x,y) coordinates. Consequently, the distance between the axillary region surface and the source points vary approximately from 21 mm to 54 mm. This means that the air-phantom interface is recorded at different distances for each source point, and the signals recorded at each source point have different magnitudes, which may hamper the performance of both artefact removal and image reconstruction algorithms. For shapes C and D, the antennas were also placed considering the remaining 3D-volume of the phantom. In the particular case of shape D, the breast size limits the angular positioning of the source points.

Each source point was simulated in the frequency band 2 to 6 GHz, which is within the range of frequencies used for radar breast MWI [49], [93]. This frequency band was chosen as a starting point as the shallower tissues in the axillary region have similar properties to the breast tissues.

5.1.2 Signal Processing Algorithms

In this section the algorithms used to perform this first analysis are described.

5.1.2.1 Artefact Removal Algorithm

Several artefact removal algorithms are used in order to remove the air-phantom interface response which masks the response of interest - the ALN response. For conciseness, only the results of three artefact removal algorithms are presented: the rotation subtraction algorithm, the average subtraction algorithm and an adaptive filtering algorithm (described in Section 2.2.3.3).

The chosen adaptive filtering algorithm is Singular Value Decomposition (SVD) (also described in Section 2.2.3.3). In this study, the matrix $\mathbf{M}$ is an $N_f \times N_s$ matrix where each column corresponds to the input reflection coefficient $\mathbf{s}_{i,i}$. N_f is the number of frequency points and N_s is the number of source points considered for the matrix factorisation. The resulting signals without the air-phantom interface response are denominated $\mathbf{s}_{i,i}^{cal}$. This artefact removal algorithm relies on the similarity between signals, which is affected by the distance between the antenna and the phantom surface. As mentioned in Section 5.1.1, this distance has a large variability among all the antenna positions. Therefore, the matrix $\mathbf{M}$ should actually only contain a subset of antenna positions neighbouring the antenna position under analysis. Additionally, to remove the air-phantom interface response, the optimal number of singular vectors which are removed (n_{sv}) needs to be determined. Two points are considered: 1) the air-phantom interface response can be present in more than one singular vector due to the irregular shape of the axillary region; and 2) one needs to guarantee the ALN response is not present in the removed singular vectors.

In this study, for each source point, the matrix $\mathbf{M}$ is created with its own signal and the signals from the neighbouring two source points: $\mathbf{s}_{i-2,i-2}, \mathbf{s}_{i-1,i-1}, \mathbf{s}_{i,i}, \mathbf{s}_{i+1,i+1}, \mathbf{s}_{i+2,i+2}$. For the source points at the extremities, only three neighbouring source points are considered. Two methods to find the number of singular vectors to be removed (n_{sv}) are used: 1) considering a fixed n_{sv} for all source points and analysing the results by visual inspection, and 2) adapting the algorithm proposed by Felício *et al.* [49] where n_{sv} is found for each source point by minimising the response at the air-phantom interface. To implement the second method, the resulting signals after removing 1 to $N_s - 1$ singular vectors are automatically analysed, where N_s is the number of signals in matrix $\mathbf{M}$ and corresponds to the maximum number of singular vectors. The number

n_{sv} is determined by ensuring the ratios between the magnitudes of each signal at the electrical distances to the first air-phantom interface ($m_{\mathrm{d}_{min}}$) and to the air-phantom interface at the back wall ($m_{\mathrm{d}_{back}}$) is less than half of the maximum magnitude of each resulting signal (m_{sv}): $m_{\mathrm{d}_{min}}/m_{sv} \leq 0.5$ and $m_{\mathrm{d}_{back}}/m_{sv} \leq 0.5$. Figure 5.2 shows how the corresponding physical distances are calculated. These interfaces correspond to the walls of the phantom, but in a clinical scenario the first air-phantom interface corresponds to the skin and the back wall corresponds to the reflection at internal tissues of the torso, e.g. the muscles.

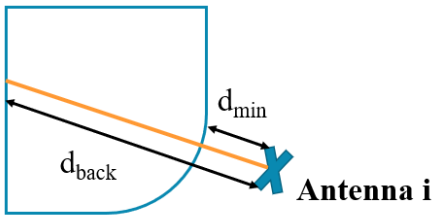

Figure 5.2: Illustration of the physical distances used to infer the reflection at the first air-phantom interface (d_{min}) and the air-phantom interface at the back wall (d_{back}).

5.1.2.2 Image Reconstruction Algorithm

Three image reconstruction algorithms are evaluated. The first algorithm is based on the wave-migration algorithm, as described in Section 2.2.3.1, where the input signals are $\mathbf{s}_{i,i}^{cal}$, after the artefacts are removed. The second and third algorithm are Delay-And-Sum (DAS) and Channel-Ranked Delay-And-Sum (CR-DAS) with implementation in the time-domain signals.

The images are reconstructed in the frequency band 2 to 6 GHz. As observed with the results of Section 3.3.2, the computation of refraction does not substantially impact the imaging results in the current conditions of the phantom under study. Hence, refraction is not included in the calculations. At this stage, the image quality is only evaluated by visual inspection.

5.1.3 Results and Discussion

Figure 5.3 shows the reconstructed images of shape A considering the 3 different artefact removal algorithms. As expected, because of the different distances between source points and the surface of the axillary region, the rotation subtraction and average subtraction algorithms do not yield good detection of the target. SVD algorithm yields a good detection when n_{sv} is 2 [Figure 5.3(c,g)], i.e., 2 singular vectors were removed from the original signals in order to remove the air-phantom interface response. The automatic method to find n_{sv} yields slightly worse results regarding the location of the detection relatively to the ALN true location, but the air-phantom interface response is successfully removed. Similar results regarding the performance of artefact

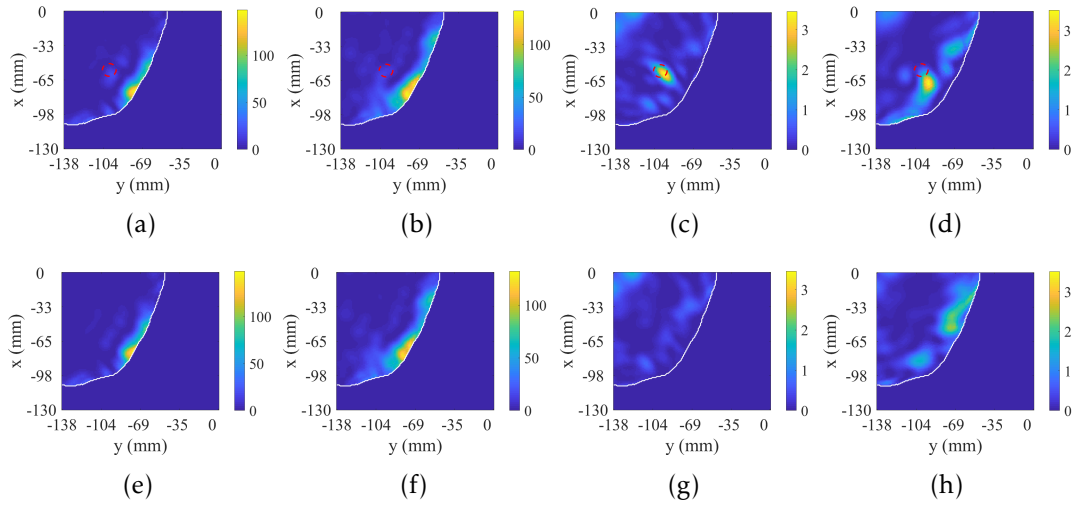

Figure 5.3: Reconstructed images of shape A (a-d) with the target and (e-h) without the target inside. (a,e) show the images after applying the rotation subtraction algorithm, (b,f) show the images after applying the average subtraction algorithm, (c,g) show the images after applying SVD by removing a fixed n_{sv}, and (d,h) show the images after applying SVD with the automatic method. The white solid contour represents the phantom limit and the red dash contour represents the true location and shape of the target.

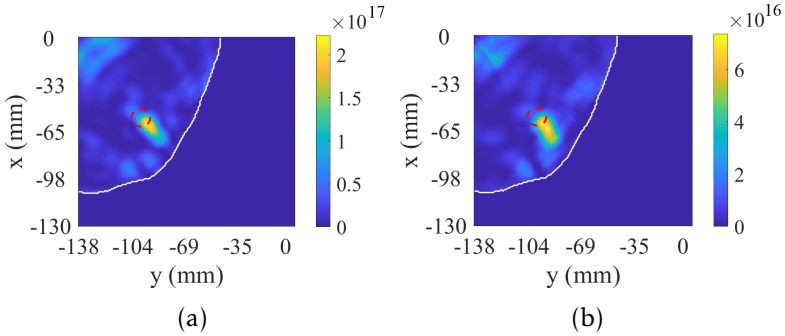

Figure 5.4: Reconstructed images of shape A using (a) DAS, and (b) CR-DAS reconstruction algorithms, after applying SVD considering $n_{sv} = 2$. The white solid contours represent the phantom limit and the red dash contour represents the true location and shape of the target.

removal algorithms are obtained with the remaining shapes. As the SVD algorithm shows promising results, this is the chosen algorithm to process the remaining tests.

Figure 5.4 shows the reconstructed images of shape A using DAS and CR-DAS image reconstruction algorithms, considering SVD algorithm with fixed n_{sv}. The resulting images show there is no substantial difference in the image quality and detection of the target between these algorithms and the wave-migration algorithm used in Figure 5.3. Hence, the remaining tests are performed using the wave-migration algorithm, which provides faster reconstruction of the images.

Figure 5.5 shows the reconstructed images of shape B. For this shape and this position of the ALN, the best imaging results are also obtained considering $n_{sv} = 2$. However, there is an artefact at the back of the phantom, which probably corresponds to the reflection of the back wall. This region is of little interest for the ALN imaging as it corresponds to the region where other tissues of the torso are present (e.g. muscles,

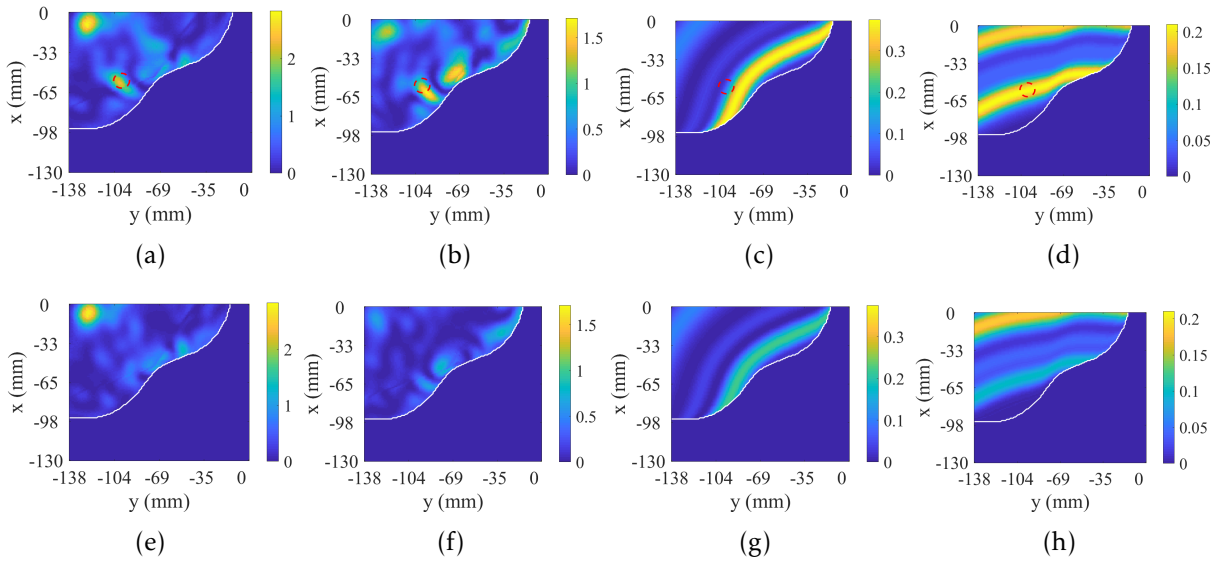

Figure 5.5: Reconstructed images of shape B (a-d) with the target and (e-h) without the target inside. (a,e) show the images after applying SVD considering $n_{sv} = 2$, (b,f) show the images after applying SVD automatic method, (c,g) show the images the individual response of source point 4 after applying SVD considering $n_{sv} = 1$, and (d,h) show the images the individual response of source point 8 after applying SVD considering $n_{sv} = 1$. The white solid contour represents the phantom limit and the red dash contour represents the true location and shape of the target.

bones). Therefore, these artefacts may be removed using a spatial filter that selects only the region of interest, as will be seen in the following sections. The automatic method also does not provide a clean detection of the ALN, showing an artefact near the first air-phantom interface. For this shape in particular, the challenges of both concave and convex shapes can be observed in the individual responses of distinct source points. Figure 5.5(c,g) and (d,h) shows the response of source points 4 and 8, respectively, when removing 1 singular vector from the original signal. The automatic algorithm chooses $n_{sv} = 1$ for these source points, as the reflection of the first air-phantom interface is not observed. However, the concave and convex shapes create more reflections, which are seen by source point 4 and do not correspond to the target response. Considering a wider range of distances of exclusion in the criteria of the automatic algorithm, so $n_{sv} = 2$ would be chosen, could be an alternative, but it would result in also removing the target response. In the case of source point 8, the detection matches both the location of the ALN and one part of the concave air-phantom interface. As these two regions are located at similar distances from the source point, their responses are represented in the same singular vectors, which means SVD may not be able to completely remove the interface response. This can also create a focusing region inside the phantom when summing the contribution from all the source points. As more source points in distinct locations are used, the more this effect can be reduced. However, one must remember the angular sweep around the axillary region is limited. The effects observed in this 2D scenario are expected to be even more evident in a 3D-volume with both concave and convex surfaces, decreasing the efficiency of the artefact removal algorithm.

Figure 5.6 presents the reconstructed images of both shape C and D after applying the SVD algorithm and considering both methods of calculating n_{sv}. The ALN is successfully detected in shape C with both methods. The images show an artefact at the back of the phantom, a region that is part of the torso but no longer belongs to the axillary region - which corroborates the need for a spatial filter to select the region of interest. The detection of the ALN in shape D is more challenging as the air-phantom interface response was not successfully removed with any of the methods. This can be explained by the distance between the ALN and the source points, which in this case is highly affected by the depth of the ALN and the positioning of the source points. This results in a weaker response of the ALN, hampering the performance of the SVD algorithm.

This study provided an overview of the main challenges when imaging the axillary region. SVD is the considered artefact removal algorithm that yields better imaging results. Using a constant n_{sv} for all the source points yields either similar or better imaging results than when using an automatic method that finds the optimal n_{sv} for each source point. The concavities and convexities of the axillary region may hamper the performance of the algorithms. In the following section, an experimental evaluation in a 3D configuration for MWI of ALNs is presented.

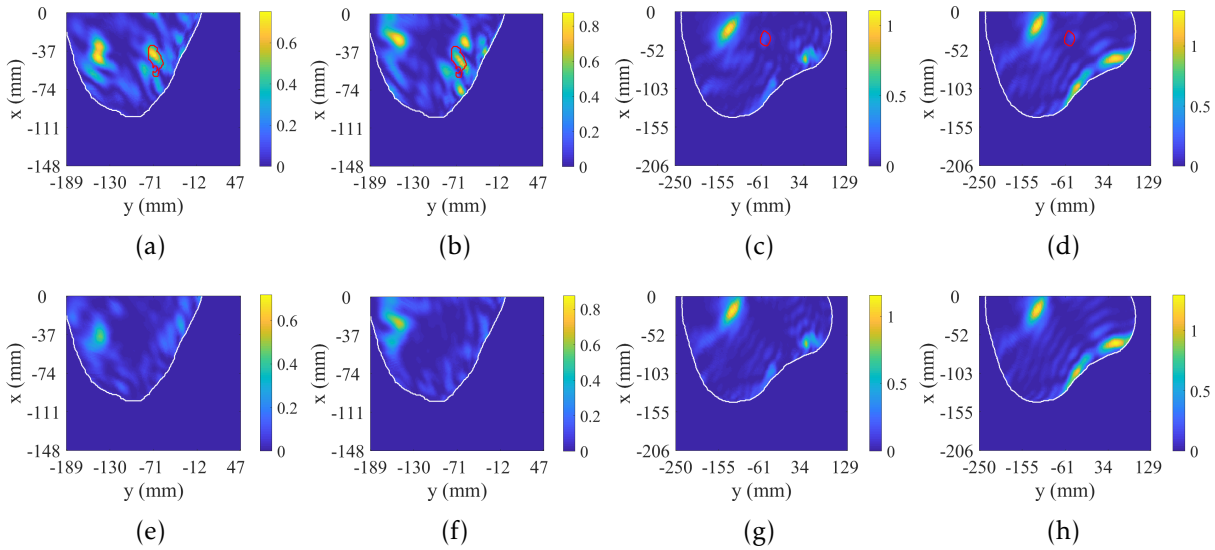

Figure 5.6: Reconstructed images of shapes C and D (a-d) with the target and (e-h) without the target inside, using two methods for artefact removal. (a,e) show the images of shape C after applying SVD considering $n_{sv} = 2$, (b,f) show the images of shape C after applying SVD automatic method, (c,g) show the images of shape D after applying SVD considering $n_{sv} = 2$, and (d,h) show the images of shape D after applying SVD automatic method. The white solid contour represents the phantom contour and the red contour represents the true location and shape of the target.

5.2 Experimental Setup

The developed ALN-MWI system consists of a position scanning system of a single antenna, the Radio Frequency (RF) equipment, the signal acquisition hardware and signal post-processing algorithms. The system is tested with an anthropomorphic physical phantom of the axillary region with a single level I ALN model in several positions. The prototype configuration is designed to be as close as possible to an actual clinical scenario, where the patient lies sideways on one side, with the arm along the head.

In the following sections, all components used to perform the first tests using the developed prototype for ALN-MWI will be presented. Some of the tasks were completed by the Instituto de Telecomunicações Lisboa/Institute of Telecommunications Lisbon (IT) and Instituto de Biofísica e Engenharia Biomédica/Institute of Biophysics and Biomedical Engineering (IBEB) team and others by myself.

5.2.1 Physical Phantom Development

An anatomically realistic physical phantom of the axillary region was created by other members of my research group. It was 3D-printed from a previously processed image created from a CT breast exam acquired in Champalimaud Foundation under protocol "MMWave" (17/10/2018) (Figure 5.7). The BMI of the patient was 19 kg/m^2, which is considered normal weight. Only a part of the image was selected to be printed, which comprised the head (for reference purpose), a part of the arm, and the torso from the neck until below the breast. The phantom was then printed in parts using an Ultimaker 3 Extended 3D-printer (Ultimaker [213]). The printing material was Polylactic Acid (PLA), with relative permittivity ranging from 2.75 and 2.9 and dissipation factor $\tan(\delta) = 0.01$ [214]. The parts of the phantom were glued and impermeabilised with epoxy resine. The axillary region is hollow and has an opening in the yz-plane to enable access to the compartment where a tissue mimicking liquid is placed. No skin layer was added to the phantom, but the air-phantom interface response is comparable to the response of an actual skin layer [49]. Using models without skin is common practice to validate MWI systems [207], [215].

Then, the structures to be placed inside the axillary region phantom were created. The models of ALNs and a simplified version of the muscle were designed to represent approximate shapes using CST Studio Suite® software [189]. The dimensions of each component were adjusted to the axillary phantom, considering reported dimensions in the literature [70], [82] and measurements from the Magnetic Resonance Imaging (MRI) exams acquired in Hospital da Luz - Lisboa.

An ALN model was created using an open-source STL model of a kidney [216], which is similar to the shape of an ALN albeit different dimensions (described in Section

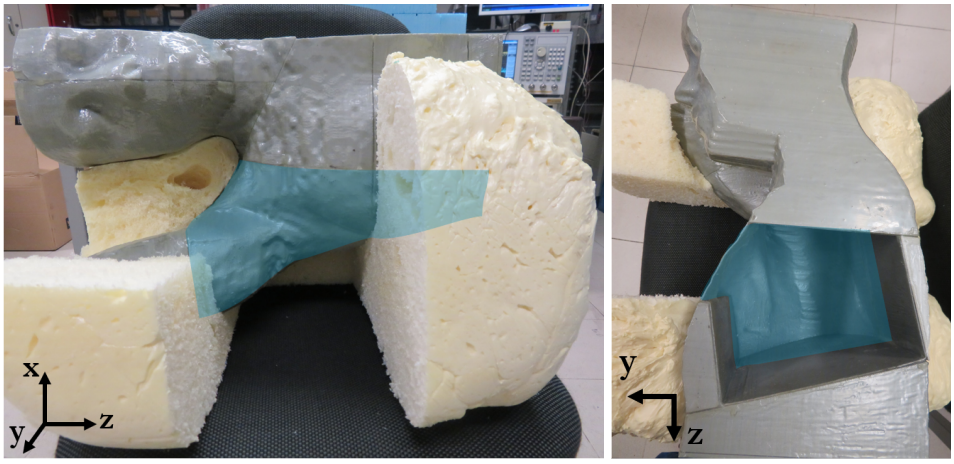

(a) (b)

Figure 5.7: 3D-printed phantom of axillary region in (a) coronal and (b) sagittal planes. The blue shade corresponds to the volume used for image reconstruction, comprising the volume where the ALNs were placed.

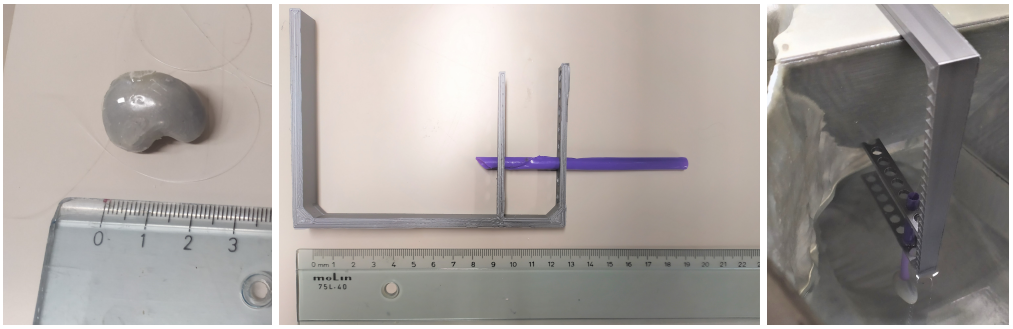

(a) (b) (c)

Figure 5.8: 3D-printed models of (a) the ALN and (b) plastic support designed to control the ALNs positioning, and (c) actual ALN positioning inside the axillary region phantom.

2.1.3). The model was reshaped and resized to fit the characteristics of metastasised ALNs, i.e. large and round. An ALN was 3D-printed with a 1.2 mm thickness wall and filled with an appropriate tissue mimicking liquid (described in Section 5.2.2) through a 1 mm hole, which was sealed with epoxy resin afterwards. Its dimensions were 23.6×17.6×12 mm^3 [Figure 5.8(a)]. The ALN was placed inside the axillary region phantom connected by a nylon string which was fixed in a pre-determined position with the help of a plastic support, as shown in Figure 5.8(b,c). The ALN used in this study was positioned in four locations inside the phantom at depths varying between 20 to 30 mm from the phantom surface.

The muscle phantom was inspired by a simplified version of the *pectoralis minor* muscle, one of the closest muscles to the ALNs and the muscle used as a reference to classify the ALNs levels (as described in Section 2.1.3). The muscle was 190 mm long with a diameter ranging from 30 to 50 mm, as shown in Figure 5.9. The muscle was designed to be fixed to the phantom wall with a rectangular platform which was designed to have the exact dimensions of the wall.

(a) (b)

Figure 5.9: 3D-printed simplified phantom of the *pectoralis minor* muscle.

5.2.2 Tissue Mimicking Materials

The phantom cavities were filled with mixtures of Triton® X-100 (TX-100), distilled water and salt (NaCl) in order to mimic the dielectric properties of the tissues as the tissue mimicking materials reported by Joachimowicz *et al.* [145]. For the purpose of this study, three mixtures, already prepared by the IT team, were considered to mimic adipose tissue, muscle, and metastasised ALNs.

As the information about dielectric properties of ALNs is very limited, as mentioned in Chapters 2 and 4, an approximation of their dielectric properties was considered. The contrast observed in Chapter 4 was not considered in this chapter since those results had not been obtained when this experimental study was performed. The used dielectric properties approximation was based on preliminary results [58], which seemed to indicate that healthy ALNs have similar dielectric properties to breast fibroglandular tissue, while metastasised ALNs have higher properties. Figure 5.10 shows the dielectric property measurements of the three mixtures considered. The G3, G1 and T mixtures reported by Joachimowicz *et al.* [145] were considered to mimic adipose tissue, muscle, and the metastasised ALN, respectively.

5.2.3 Antenna and Measurement Setup

The prototype consists in an Ultra-Wide Band (UWB) low-power radar monostatic system. The RF measurements were acquired with an Agilent E5071C Vector Network Analyser (VNA). The signals were measured with a signal power of 10 dBm and signal IF bandwidth of 7 kHz. A Vivaldi antenna was used to record the monostatic signals, calibrated with a Keysight Electronic Calibration (E-cal). This antenna is impedance-matched in the 2 – 7 GHz frequency band and linearly polarised in the x-axis. An adjustable arm is attached to the antenna in order to enable scanning the axillary region in a cylindrical configuration (Figure 5.11). The position of the antenna is adjusted horizontally in the z-axis using an aperture which is handled manually and rotated

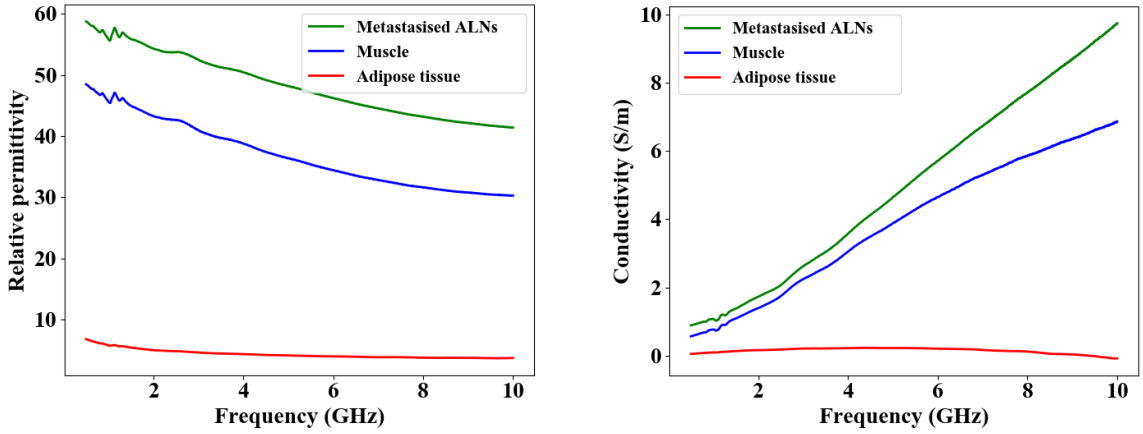

(a) (b)

Figure 5.10: Relative permittivity (left) and effective conductivity (right) of the measurements of the used tissue mimicking mixtures in the setup, over the frequency band 0.5 to 10 GHz.

around the z_0-axis using the angular positioner. The angular positioner is connected to a power supply, a multimeter and a controller. The controller is used to rotate the arm, where the measured resistance by the multimeter is the reference for each rotation angle.

The antenna positioning is defined through a measurement grid ($\mathbf{G_M}$), as shown in Figure 5.12. As mentioned in Section 5.1, the anatomical shape of the torso limits the antenna angular range, and, therefore, only a 90° angular range is covered. The limits of this measurement grid are defined considering four anatomical references: the first angular position (A) considers the sagittal plane (x-plane) of the nipple; the last angular position (I) considers the mid-coronal plane (y-plane which divides the body in half); the first horizontal position (1) considers the axial plane (x-plane) of the clavicle; and the last horizontal position (8) considers the axial plane across the nipple. These anatomical references may result in a $\mathbf{G_M}$ of variable size for different patients, while covering different volumes and maintaining the spacing between antennas. The volume of interest where the ALNs are located is expected to vary from patient to patient.

The defined $\mathbf{G_M}$ is the one shown in Figure 5.12. A total of 72 antenna positions are considered. These positions are distributed in 9 angular positions (A to I) with a 10° angular step, and 8 horizontal antenna positions (1 to 8) with 10 mm step. The radial distance between each antenna position and the phantom surface ranges from 4 to 56 mm, with an average of 35 mm, as shown in Figure 5.13.

The remaining grids represented in Figure 5.12 are used for the signal processing algorithms presented in the following sections. A free-space measurement was also performed for calibration purposes. A total of $N_f = 1401$ frequency points were acquired for each antenna position.

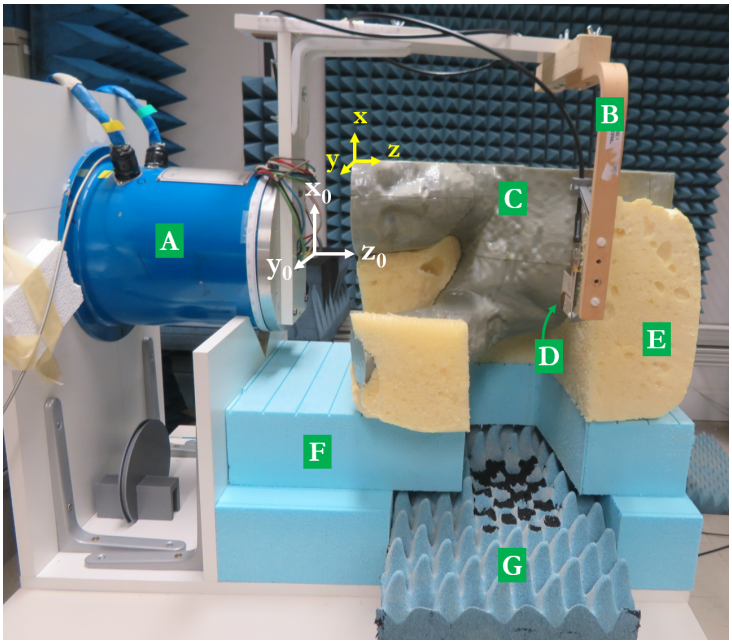

(a)

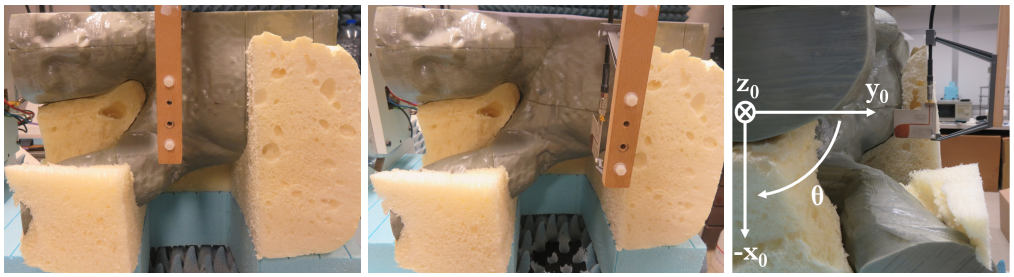

(b) (c) (d)

Figure 5.11: Measurement setup with (a) all components ([A] roll positioner, [B] antenna support arm, [C] phantom and [D] the antenna). (b) shows a closer picture of the first horizontal and angular position in the coronal view, (c) and (d) show the last horizontal and first angular position in the coronal and axial view, respectively. The yellow and blue pieces [E, F] supporting the phantom are styrofoam and the blue piece at the bottom [G] is an electromagnetic absorber. The white coordinate system in (a) and (d) is used for the rotation and translation movements of the arm, and the yellow coordinate system in (a) is used as a reference for the image reconstruction algorithm.

5.2.4 Signal Processing Algorithms

In the following sections, the developed algorithms to image the axillary region are presented. Following the findings in Section 5.1, they were specifically adapted for the axillary imaging application considering the volume of interest is smaller than the volume of the experimental phantom and that its surface is irregular. In a clinical scenario, the shape of the body needs to be retrieved so it can be considered in the image reconstruction algorithms. This can be performed using very low-cost optical devices such as a webcam [49] or more complex laser systems [217]. For the purpose of this study, this information is assumed available.

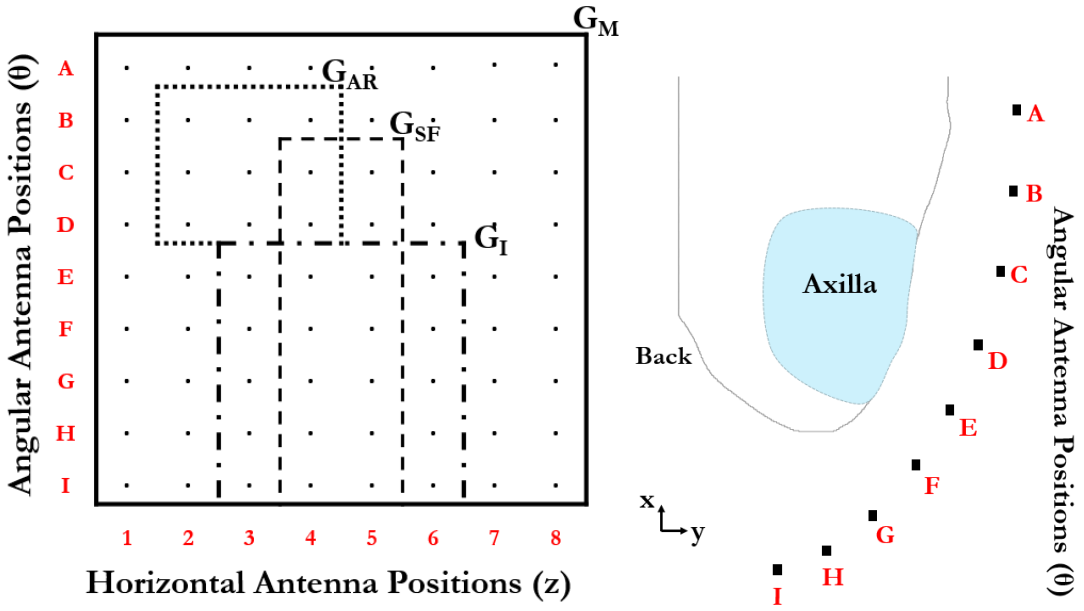

Figure 5.12: Schematic of the grid of antenna positions in (a) a flattened view in the *xz*-plane and (b) angular positions in the *xy*-plane. In (a), $\mathbf{G_M}$ (delimited by the solid line) corresponds to the measurement grid; $\mathbf{G_{AR}}$ (delimited by the dotted line) is an example of the subset of neighbour antenna positions of (C,3) antenna position used for artefact removal; $\mathbf{G_{SF}}$ (delimited by the dashed line) is the subset used to create the spatial filter; and $\mathbf{G_I}$ (delimited by dash-dot line) is the subset of antenna positions used for image reconstruction.

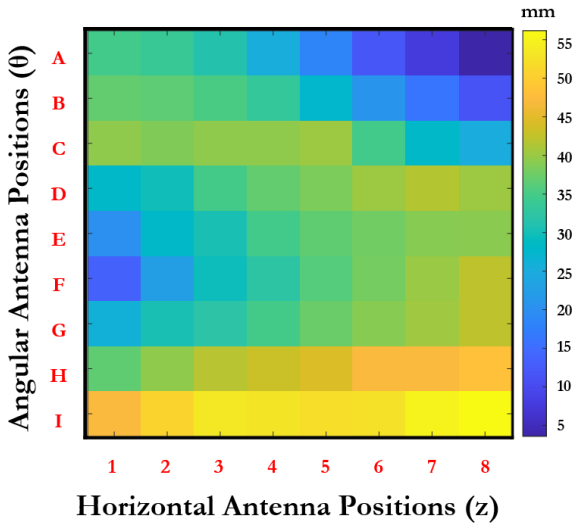

Figure 5.13: Radial distance (in millimetres) between each antenna position and the phantom surface represented in a flattened view of the cylindrical antenna position grid.

5.2.4.1 Artefact Removal Algorithm

The SVD is used as artefact removal algorithm to remove the air-phantom interface response. Similarly to Section 5.1.2.1, the matrix $\mathbf{M}$ is a $N_f \times N_s$ matrix where each column corresponds to the input reflection coefficient $\mathbf{s}_{a,h}$. The indices a and h correspond to the indices of each angular and horizontal antenna positions, respectively. $\mathbf{s}_{a,h}$ is the difference between the measured input reflection coefficient in the presence of the phantom and the measured coefficient in free-space. This subtraction is meant to remove the internal reflections of the antenna [95]. N_f is the number of frequency points and N_s is the number of antenna positions considered for the factorisation. The resulting signals without the air-phantom interface response are designated $\mathbf{s}^{cal}_{a,h}$.

As explained in Section 5.1.2.1, the matrix $\mathbf{M}$ should be created considering the neighbouring antenna positions of each antenna position. As shown in Figure 5.13, the distance between the antenna and the phantom surface has a large variability among all the antenna positions. The optimal number of singular vectors which needs to be removed (n_{sv}) also needs to be defined. The results with the numerical phantoms (Section 5.1) showed that, for the axillary region, an automatic algorithm that finds the optimal n_{sv} for each antenna position may not necessarily yield better results than a constant n_{sv} for all antennas. Therefore, a thorough methodology was developed to find the optimal combination of subset of antenna positions ($\mathbf{G_{AR}}$) for a 3D scenario and the number of singular vectors to be removed (n_{sv}), ensuring a successful target detection with the best imaging performance metrics. Six subsets of antenna positions are tested, based on the neighbouring positions with different patterns. Figure 5.14 shows the different subsets of antenna positions, which include 3 to 9 antenna positions and are named according to their shape and number of antenna positions: Vertical 3, Horizontal 3, Diagonal 3, Cross 5, Diagonal 5 and Block 9. As an example, if Block 9 is used, the factorisation of $\mathbf{s}_{a,h}$ is performed considering the surrounding 8 neighbours and the signal itself: $\mathbf{s}_{a+\Delta_N,h+\Delta_N}$ where $\Delta_N = [-1, 0, 1]$. Then, a range of different number of singular vectors (n_{sv}) are removed. For each subset of antenna positions, this number is limited by $N_s - 1$. For instance, if the number of signals of matrix $\mathbf{M}$ (N_s) is 3, only a maximum of 2 singular vectors can be removed. The performance of each combination is evaluated analysing the performance metrics of the imaging results.

5.2.4.2 Image Reconstruction Algorithm

The used image reconstruction algorithm is based on the wave-migration algorithm (as described in Section 2.2.3.1) where the input signals are $\mathbf{s}^{cal}_{a,h}$. It was tested for several frequency bands included in the frequency band of the antenna but due to space constraints only the best results, which were obtained from 2 to 5 GHz, will be presented. Refraction is also not included in the calculations. The resulting images were

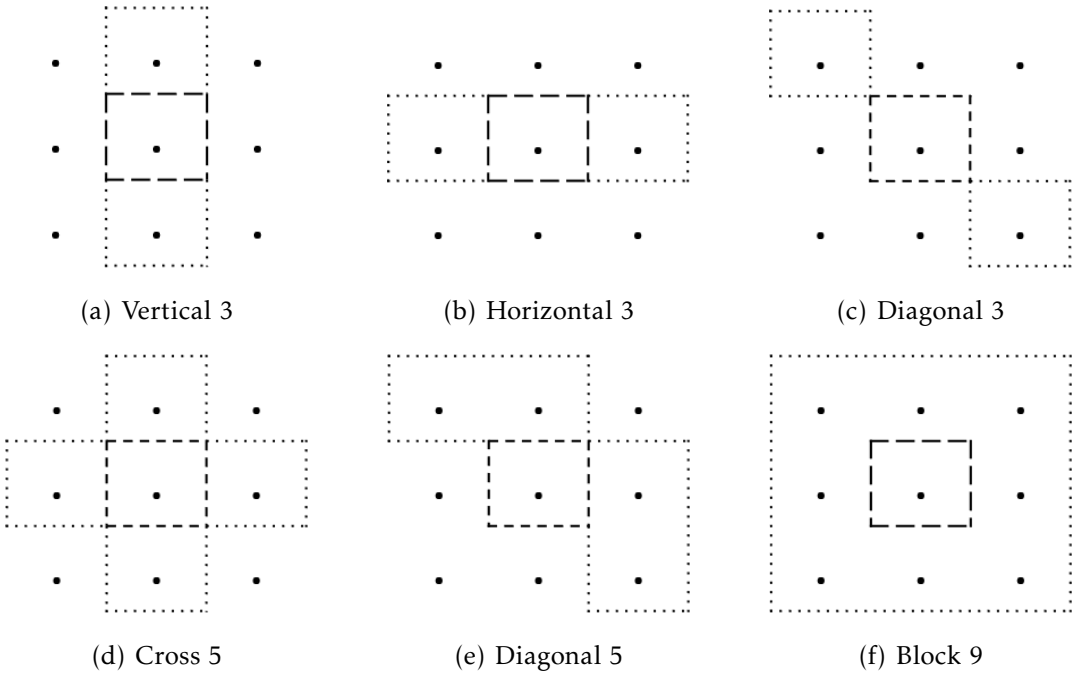

(a) Vertical 3 (b) Horizontal 3 (c) Diagonal 3

(d) Cross 5 (e) Diagonal 5 (f) Block 9

Figure 5.14: Subsets of neighbouring antenna positions used to perform factorisation of a matrix $\mathbf{M}$ with $\mathbf{s}_{a,h}$ signals. The dots represent each antenna position, the dashed line represents the selection of the (a,h) antenna position and the dotted line represents the selection of neighbouring antenna positions.

reconstructed in three planes - axial (xy), coronal (xz) and sagittal (yz) - while considering the body compartment filled with adipose mimicking liquid. The performance of this setup and algorithms is evaluated using the metrics as presented in Section 2.2.4: Signal-to-Clutter Ratio (SCR), Signal-to-Mean Ratio (SMR), Full Width Half Maximum (FWHM) and Localisation Error (LE).

5.2.4.3 Spatial Filter

As mentioned in Section 5.1.3, the region of interest to be imaged is a limited part of the torso. Selecting that region is important in order to remove potential artefacts created by other structures. To that end, a spatial filter (**SF**) is used to analytically select the sub-volume of the phantom which is relevant for ALN detection. This sub-volume corresponds to the superficial region where the ALNs are more likely to be located, as represented in Figure 5.15.

The **SF** is a volume where each voxel is assigned to a weight ranging from 0 to 1, assigning higher weight to the voxels of the Volume of Interest (VOI) of the axillary region. The final microwave image results from the multiplication between the **SF** and the reconstructed image obtained from the wave migration algorithm.

The **SF** is defined as a skewed Gaussian function (Figure 5.16), which results from the multiplication of a power function of exponent γ ($\mathbf{SF_1}$) and a piece-wise function

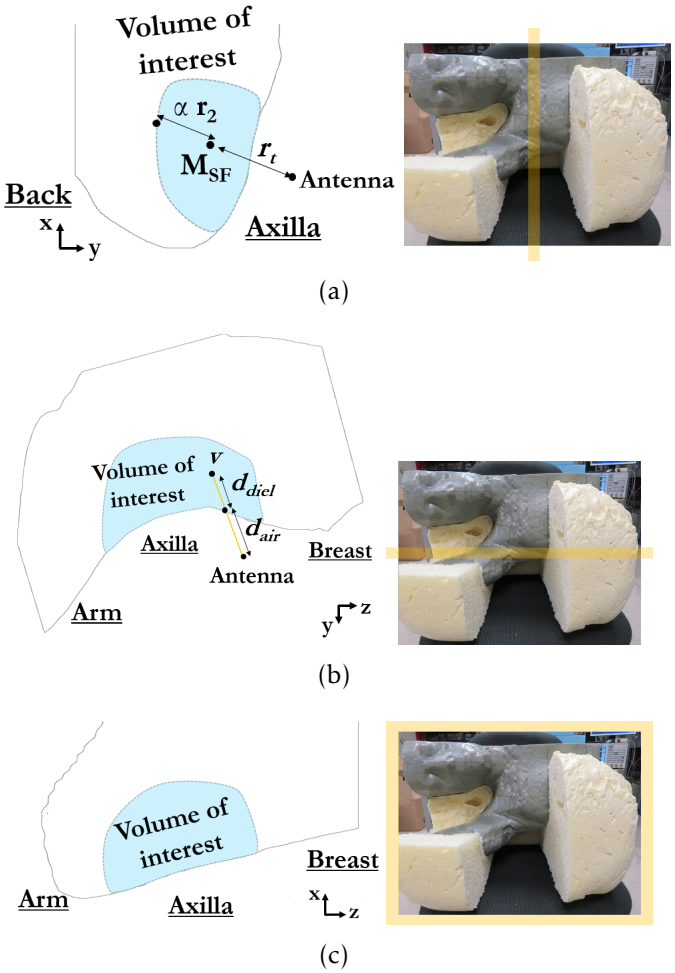

Figure 5.15: Representation of the VOI for (a) axial, (b) sagittal and (c) coronal planes. The light blue shade represents the sub-volume of the axillary region where ALNs are more likely to be located. The yellow shade represents each plane in the phantom .

with a Gaussian decay ($\mathbf{SF_2}$):

$$\mathbf{SF}_1 = \left(\frac{d_{diel,ahv}}{r_1}\right)^{\gamma} \tag{5.1}$$

$$\mathbf{SF}_2 = \begin{cases} 1, & \text{if } d_{\mathrm{SF},ahv} < r_t \\ \exp\left(-\left(\frac{d_{\mathrm{SF},ahv}-r_t}{r_2}\right)^2\right), & \text{otherwise} \end{cases} \tag{5.2}$$

$$d_{\mathrm{SF},ahv} = d_{air,ahv} + 2 \cdot d_{diel,ahv} \tag{5.3}$$

where $d_{air,ahv}$ and $d_{diel,ahv}$ are the distances between each antenna position (a,h) (considered for creating the **SF**) and each voxel v travelled in air and in the phantom medium, respectively. $d_{SF,ahv}$ is a weighted distance (neither physical nor electrical distance) to give a higher weight to $d_{diel,ahv}$ since the region of interest is close to the phantom surface. Parameter r_1 is proportional to the magnitude of function $\mathbf{SF_1}$, γ defines the growth rate of function $\mathbf{SF_1}$, and r_t and r_2 determine the threshold and the rate of the Gaussian decay of function $\mathbf{SF_2}$, respectively. The parameters r_1, r_t, γ, and r_2 can be

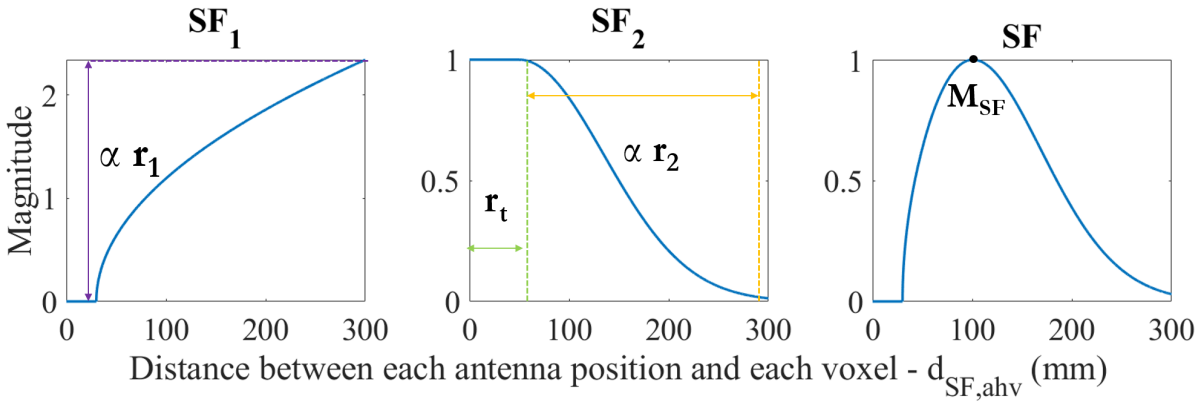

Figure 5.16: Graphical representation of each function of the spatial filter (**SF**) over the distance between each antenna position and a voxel ($d_{SF,ahv}$) for an arbitrary combination of parameters. $\mathbf{M_{SF}}$ represents the point of maximum magnitude.

adjusted according to the region one aims to select and can be defined differently for each antenna position.

The **SF** is created independently of the antenna positions used for image reconstruction ($\mathbf{G_I}$). To that end, a specific subset of antenna positions $\mathbf{G_{SF}}$ is used to create the **SF**, comprising the 30% of the horizontal antenna positions centred at the region of interest and the angular antenna positions that are closer to and surrounding the VOI. Therefore, the selected subset of antenna positions depends on the volume of the axillary region under study.

As shown in previous studies [75], [218], [219] and in a study conducted by my research group [220], the region where ALNs are located varies from patient to patient. The **SF** can be designed considering patient-specific information of the patient to preselect the VOI. At the time of the measurements, the ALN positioning was determined as an approximation and independently of the BMI of the patient. The study that defines the relationship between the BMI and the VOI [220] was performed at a later stage. As a result, the ALNs were placed in a deeper position that is often observed for this patient's BMI (19 kg/m^2) as reported in [220]. Therefore, the **SF** for this phantom comprises parameters which are defined iteratively by visual inspection of the resulting **SF**. In Section 5.3 an automatic method to define the **SF** parameters is presented.

5.2.4.4 Antenna Position Selection

The image reconstruction algorithm considers only a subset of antenna positions for image reconstruction ($\mathbf{G_I}$), since the original grid of antenna positions ($\mathbf{G_M}$) covers a larger volume in front of the phantom than the volume where ALNs can be located. Some antenna positions may be far or provide unfavourable contributions to the ALN detection, penalising the quality of the reconstructed images. Thus, the size and the subset of antenna positions that provide better ALN identification with less artefacts should be identified.

$\mathbf{G_I}$ is found by evaluating the imaging results by visual inspection and by analysing the corresponding performance metrics using 25 subsets of antenna positions. Each subset results from the translation of a 5×4 grid with 1 displacement unit over $\mathbf{G_M}$. Future work should include improving this methodology. In a clinical application, the location of the ALNs is not known and therefore, an automatic test should be run to successively test different subsets $\mathbf{G_I}$ to maximise SCR and SMR.

5.2.5 Results and Discussion

In this section, the results of the optimisation of the parameters of the algorithms and the reconstructed images are presented. Four experimental tests were performed with the experimental prototype.

One level I ALN was embedded in adipose mimicking liquid in three different locations, named ALN-1, ALN-2 and ALN-3, and one level I ALN and a muscle phantom were embedded in adipose mimicking liquid named ALNM-1. The projections of each ALN location in the phantom are represented in Figure 5.17. ALN-1 is at a central position between the breast and the arm, ALN-2 and ALNM-1 are closer to the arm, and ALN-3 is closer to the breast. The distance between ALN-2 and ALN-3 is 48 mm. ALN-1, ALN-3, ALNM-1 are placed at an average depth from the phantom surface of approximately 30 mm, while ALN-2 is closer to the surface at approximately 20 mm depth.

5.2.5.1 Spatial Filter Parameters

The $\mathbf{G_{SF}}$ used for **SF** is defined considering the dimensions of the used physical phantom. The subset of antenna positions $\mathbf{G_{SF}}$ comprises the horizontal positions 4 to 5 (corresponding to 30% of the horizontal antenna positions) and the angular antenna positions C to I.

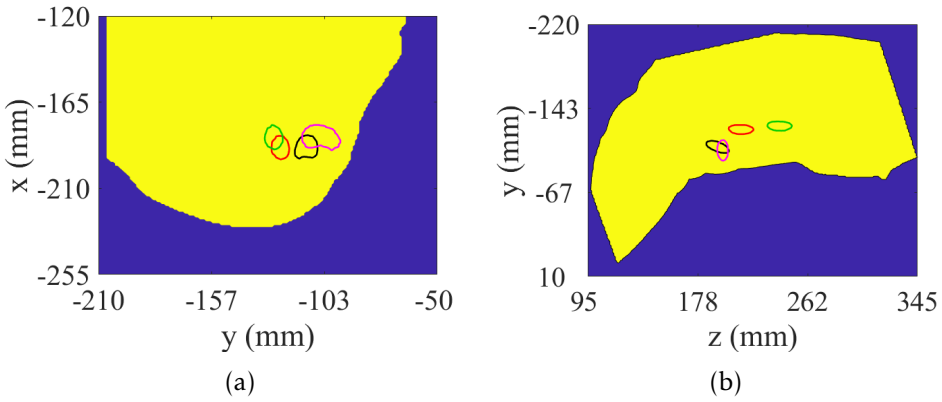

Figure 5.17: Projection of the axillary region phantom and lymph nodes positions on (a) axial and (b) sagittal planes. Average contours of the axillary phantom are represented in yellow, ALN-1 in red, ALN-2 in magenta, ALN-3 in green and ALNM-1 in black.

The **SF** parameters are defined as $r_1 = 75$ mm, $\gamma = 0.5$, $r_t = 0$ mm, and $r_2 = 120$ mm. Since a large volume is considered, parameters r_1 and r_t are increased for angular positions G to I since they are farther away from the region of interest than the others: $r_1 = 400$ mm and $r_t = 50$ mm. This combination of parameters highlights a VOI extending from the phantom surface to a depth of approximately 50 mm in the phantom, as shown in Figure 5.18. These parameters ensure most of the ALN positions (Figure 5.17) are included in the VOI.

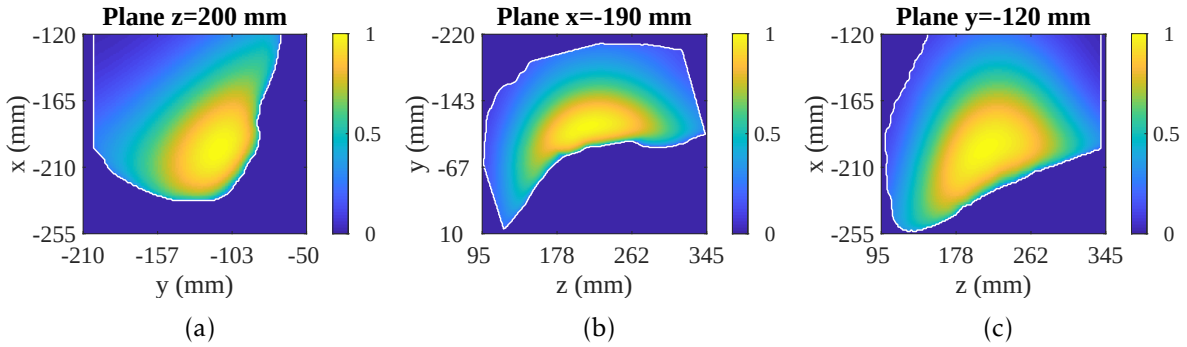

Figure 5.18: Spatial filter of the axillary region phantom with hand-picked parameters in (a) axial, (b) sagittal and (c) coronal planes. Yellow colours represent voxels with higher weight. The white solid contour represents the phantom contour.

5.2.5.2 Image Reconstruction Parameters

The optimal subset of antenna positions ($\mathbf{G_I}$) used to image the axillary region phantom comprises the angular antenna positions E to I and the horizontal antenna positions 3 to 6 as shown in Figure 5.12(a). In a clinical scenario, the $\mathbf{G_I}$ would need to be adjusted according to patient-specific information.

5.2.5.3 Artefact Removal Parameters

Figures 5.19 and 5.20 show the performance metrics of the experimental tests over the number of singular vectors removed (n_{sv}) using SVD and considering the different subsets of neighbouring antenna positions showed in Figure 5.14.

In all four tests, when the patterns Vertical 3, Horizontal 3 and Diagonal 3 are considered, either SCR is too low or LE is too high when the singular vectors are removed. When using only 3 antenna positions, the number of singular vectors which can be removed is limited to 1 or 2 and the number of signals (3) is not enough to successfully separate the air-phantom interface response from the ALN response, thus, ALN detection is not possible.

When considering more antenna positions for the artefact removal, namely Cross 5, Diagonal 5 and Block 9, the signals can be decomposed in a higher number of singular vectors. As observed in Figures 5.19 and 5.20, when three or more singular vectors

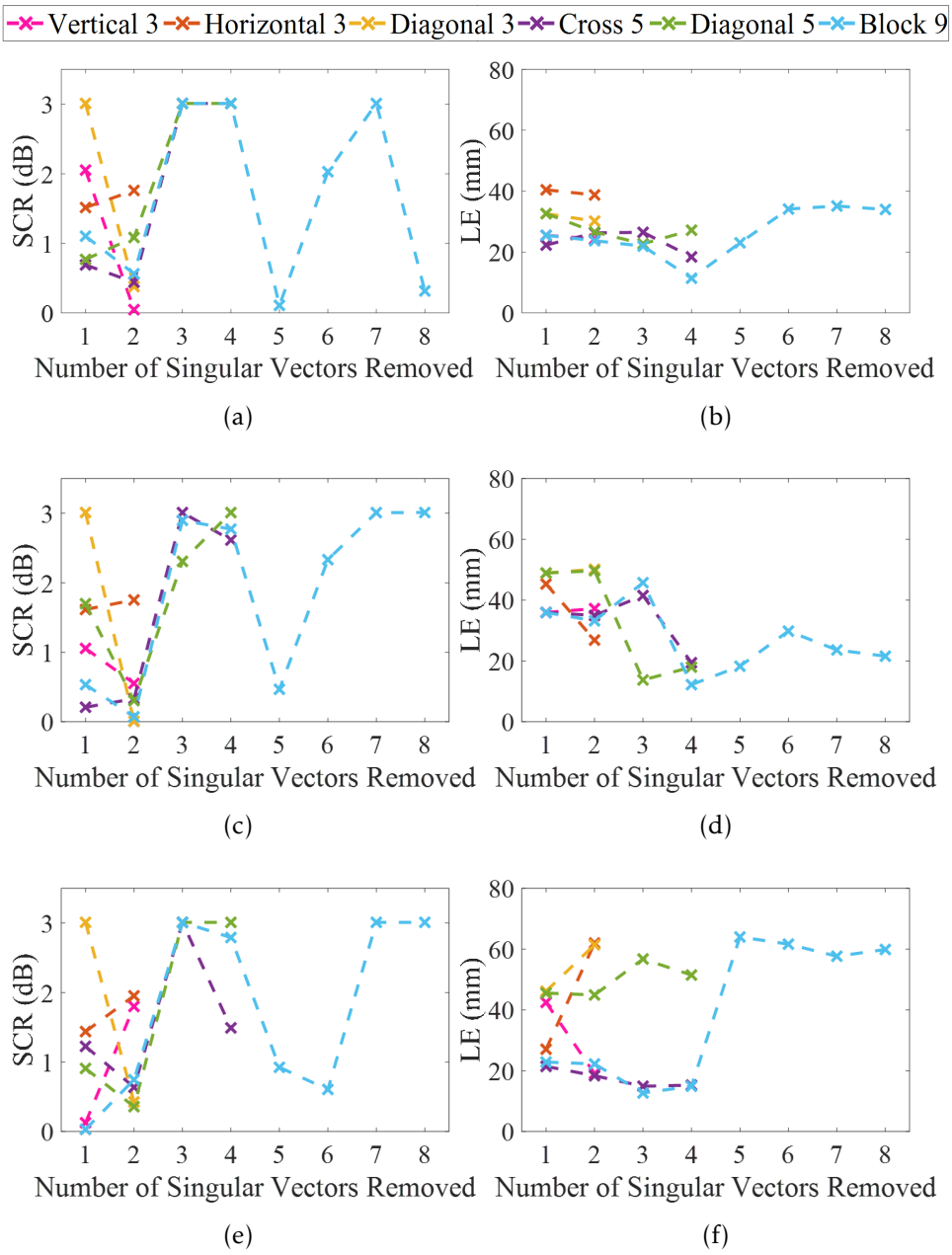

Figure 5.19: Performance metrics over the number of singular vectors removed for each subset of neighbouring antenna positions and the three experimental tests with a single ALN inside the axillary region phantom. Signal-to-Clutter Ratio and Location Error are shown on the left and right columns, respectively. The first, second, third and fourth rows correspond to imaging results of ALN-1, ALN-2, and ALN-3, respectively.

are removed, the performance of the artefact removal algorithm improves, i.e. SCR is higher and LE is lower. Nonetheless, Diagonal 5 still shows a high LE for ALN-2. Both Cross 5 and Block 9 subsets show similar performance behaviour considering the experimental tests. When more than 4 singular vectors are removed, Cross 5 cannot be used while the performance of Block 9 subset shows an increase of LE, except in the case of ALNM-1. When considering ALNM-1, SCR and LE are still acceptable up to 6 singular vectors are removed.

The minimum value of LE is obtained for ALN-1, ALN-2 and ALN-3 when 4 singular

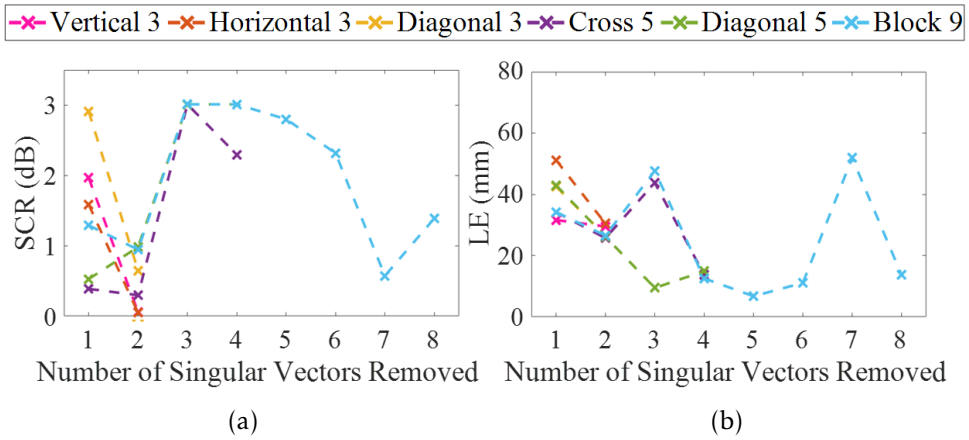

Figure 5.20: Performance metrics over the number of singular vectors removed for each subset of neighbouring antenna positions and the experimental test with a single ALN and muscle models inside the axillary region phantom (ALNM-1). Signal-to-Clutter Ratio and Location Error are shown in the left and right columns, respectively.

vectors (n_{sv}) are removed considering Block 9 subset. For ALNM-1, the minimum value of LE is obtained when $n_{sv} = 5$ and considering Block 9. When $n_{sv} = 4$, LE is also acceptable, i.e. it is within the size of the ALN. LE is 11.4, 14.9, 12.2 and 12.5 mm for ALN-1, ALN-2, ALN-3, and ALNM-1, respectively. SCR is higher than 2.78 dB in all tests, which is above the minimum 1.5 dB.

There are three reasons which might explain why considering all the neighbouring antenna positions (Block 9) and removing four singular vectors is the optimal combination. Firstly, due to its non-uniform shape, the response of the phantom surface is present in more than one singular vector. Secondly, the air-phantom response is only successfully separated from the ALN response when a high number of singular vectors is obtained with SVD. Lastly, when a higher number of antenna positions is considered for the SVD algorithm, which is the case of Block 9, the probability that the majority of the antenna positions have similar air-phantom response is also higher, ultimately improving the decomposition performance.

The first singular vector resulting from applying Block 9 contains the main reflection from the surface of the phantom with an average magnitude of 22 for each antenna position. The remaining singular vectors present residual reflections with average magnitudes of 1.3, 0.9 and 0.7. The singular vectors preserving the ALN response have average magnitudes below 0.5 for each antenna position. This means SVD is able to remove components with magnitudes up to 44 times higher than the ALN response, which is encouraging to the feasibility of an air-operated setup.

5.2.5.4 Imaging Results

Table 5.1 shows a summary of the resulting metrics for all the experimental tests. Figure 5.21(a-c) shows the reconstructed images on the planes of the voxel with maximum intensity with ALN-1, obtained using **SF**. The ALN is correctly detected, with an

SCR of 3.01 dB and an LE of 11.40 mm, which is within the range of its dimensions ($23.6 \times 17.6 \times 12$ mm^3). FWHM is larger than the average dimensions of the ALN, specially in the yz-plane. This is explained by the shape of the axillary region in that plane, which results in a lower cross-range resolution. Figure 5.21(d-f) shows the same reconstructed images before the **SF** is applied. Firstly, no substantial impact on the

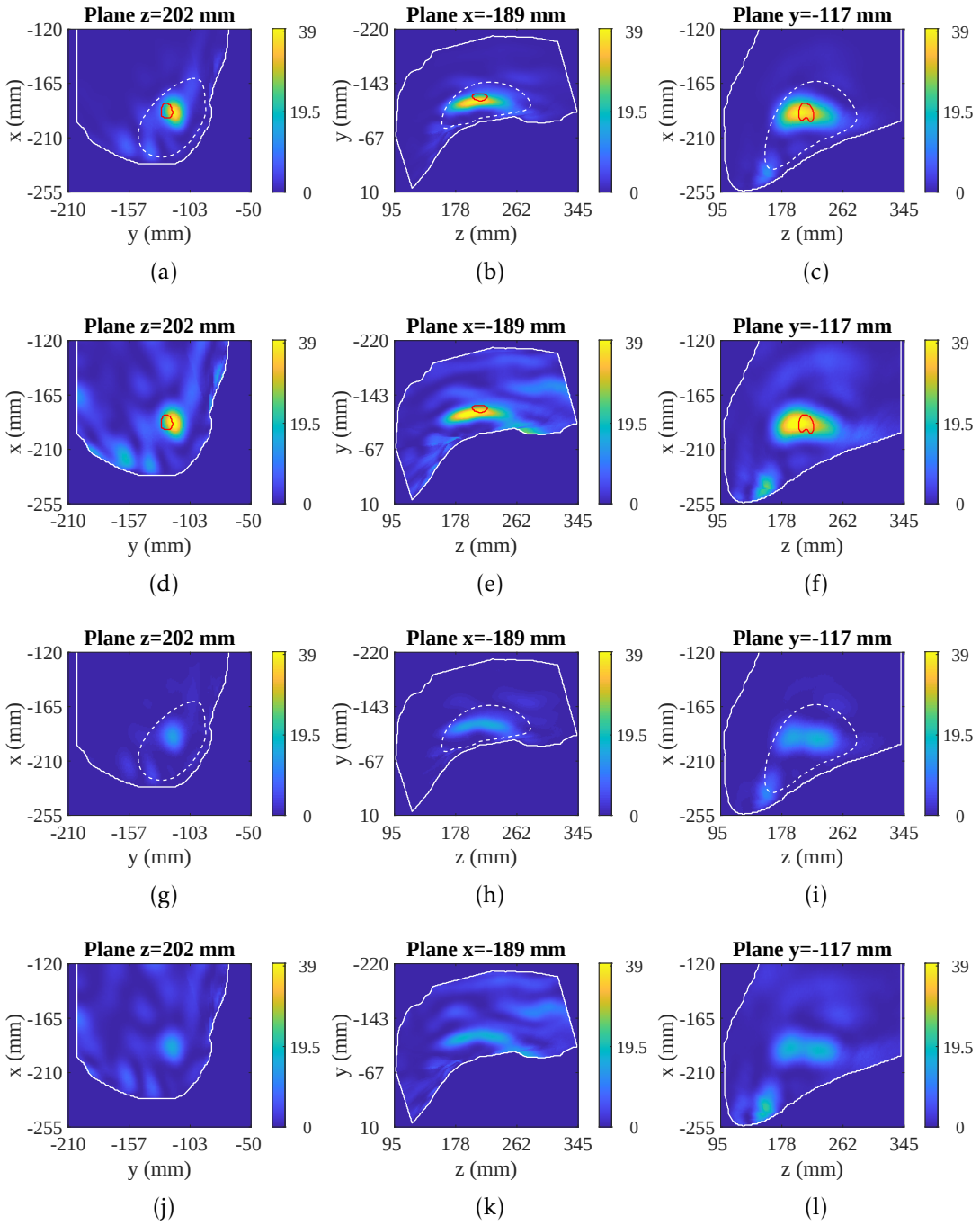

Figure 5.21: Reconstructed images of the axillary region phantom in the experimental test ALN-1. The first and second rows show the images with the ALN inside, when applying and not applying the spatial filter, respectively. The third and fourth rows show the images of the axillary region without ALN and when applying and not applying the spatial filter, respectively. The left, centre and right images show the axial, sagittal and coronal planes, respectively. The approximate location and shape of the ALN is represented as a red contour. The white solid and dashed contours represent the phantom contour and the volume of interest selected by the spatial filter, respectively.

Table 5.1: Performance metrics of the reconstructed images from the experimental tests with the prototype. "Ref" corresponds to the experimental test without target performed at the same day as the corresponding experimental test with target.

	Maximum Intensity	**SCR (dB)**	**SMR (dB)**	**FWHM (mm)**	**LE (mm)**
ALN-1	39.6	3.01	8.95	33	11.4
ALN-1 Ref	17.7	2.76	8.70	35	17.5
ALN-2	16.6	2.78	8.69	35	12.2
ALN-2 Ref	12.1	2.40	8.04	34	24.9
ALN-3	10.9	2.89	8.73	35	14.9
ALN-3 Ref	9.4	2.01	9.18	23	14.9
ALNM-1	27.9	3.01	8.97	19	12.5
ALNM-1 Ref	17.8	2.76	8.70	35	34.8

maximum intensity of the image is observed, as the maximum of the filter is 1. However, voxel intensities may change slightly as the filter is not binary and shows a Gaussian behaviour. Secondly, the existent clutter in the back, arm and breast regions is removed after applying the filter. Thirdly, the position of the ALN detection does not change when the **SF** is applied. Finally, the major artefacts at the air-phantom interface are entirely removed with SVD and without the help of the spatial filter **SF**.

Moreover, Figure 5.21(j-l) shows the reconstructed images when no ALN is placed inside the axillary region phantom and when **SF** is not used. The images show the effect of the challenging shape of the axillary region on microwave images. The irregularity of this shape causes some artefacts which are the major challenge for this MWI application. Independently whether **SF** is applied [Figure 5.21(g-i)] or not [Figure 5.21(j-l)] when no ALN is placed inside the phantom, the maximum intensity point is in the centre of the VOI which matches the location of the ALN. As explained in Section 5.1.3, this may correspond to a focusing region within the phantom that is not related to the existence of targets. This focusing region is a result of the effect of concavities and convexities of the axillary region phantom and SVD performance. In fact, this image has an SCR higher than 1.5 dB when the ALN is not placed inside the phantom (marked with "Ref" in Table 5.1). However, SCR and SMR decrease when compared to the test with the ALN. Also, the maximum intensity of the reconstructed image with ALN [Figure 5.21(a-f)] is 39.6, whereas without the ALN it is 17.7 [Figure 5.21(g-l)]. This shows that MWI is sufficiently sensitive to the presence of an ALN. Nonetheless, this means that in a real situation, besides the usual performance metrics, a threshold of intensity should be used to identify whether a detection is associated to a detected ALN or to a region

that has higher response due to the shape of the axillary region. In order to define a reliable threshold, more experimental tests would need to be performed, which were not possible during the course of this thesis.

The reconstructed images of the experimental tests with ALN-2 and ALN-3 are shown in Figure 5.22 and 5.23, respectively. Both present a correct detection of the

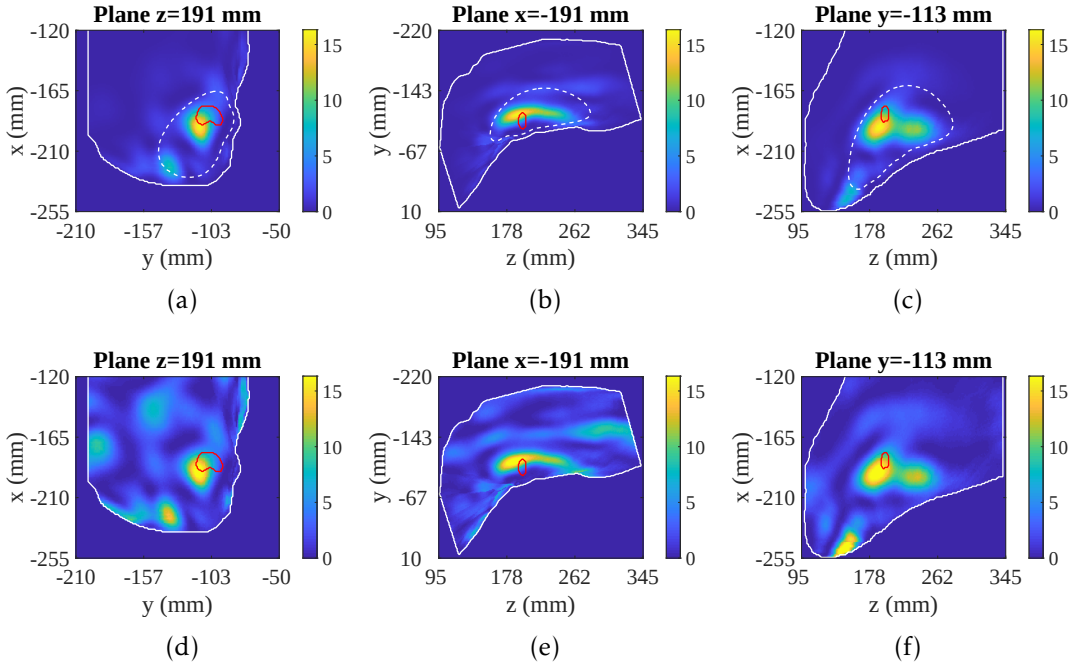

Figure 5.22: Reconstructed images of the axillary region phantom in the experimental test ALN-2. The first and second rows show the images with the ALN inside, when applying and not applying the spatial filter, respectively, in (a,d) axial, (b,e) sagittal and (c,f) coronal planes. The approximate location and shape of the ALN is represented as a red contour. The white solid and dashed contours represent the phantom contour and the volume of interest selected by the spatial filter, respectively.

ALN, having an SCR higher than 2.78 dB. As can also be observed by the performance metrics in Table 5.1, the imaging results with ALN-3 are slightly worse in terms of LE, even though it is still within the range of ALN dimensions. FWHM is slightly higher for both ALN-2 and ALN-3 when compared to the corresponding metric of ALN-1 and larger than the ALN dimensions. This can be explained by their positioning in the axillary region phantom, which are farther from the selected $\mathbf{G_I}$ when compared to ALN-1 position. Additionally, with both ALN-2 and ALN-3, more artefacts are observed when the **SF** is not applied, and some of the artefacts present higher intensity when compared to the ALN response. The intensity of detection of both ALN-2 and ALN-3 is lower compared to ALN-1. Firstly, both ALN positions are farther away from the grid of antenna positions used for image reconstruction ($\mathbf{G}_I$), which means a more attenuated response is being used to reconstruct the image. Secondly, all experiments were performed in different days, some months apart, and some of the properties of the ALN phantom may have changed. However, the measurement without the ALN, i.e. "Ref", was performed in the same day of the measurement with the ALN in each

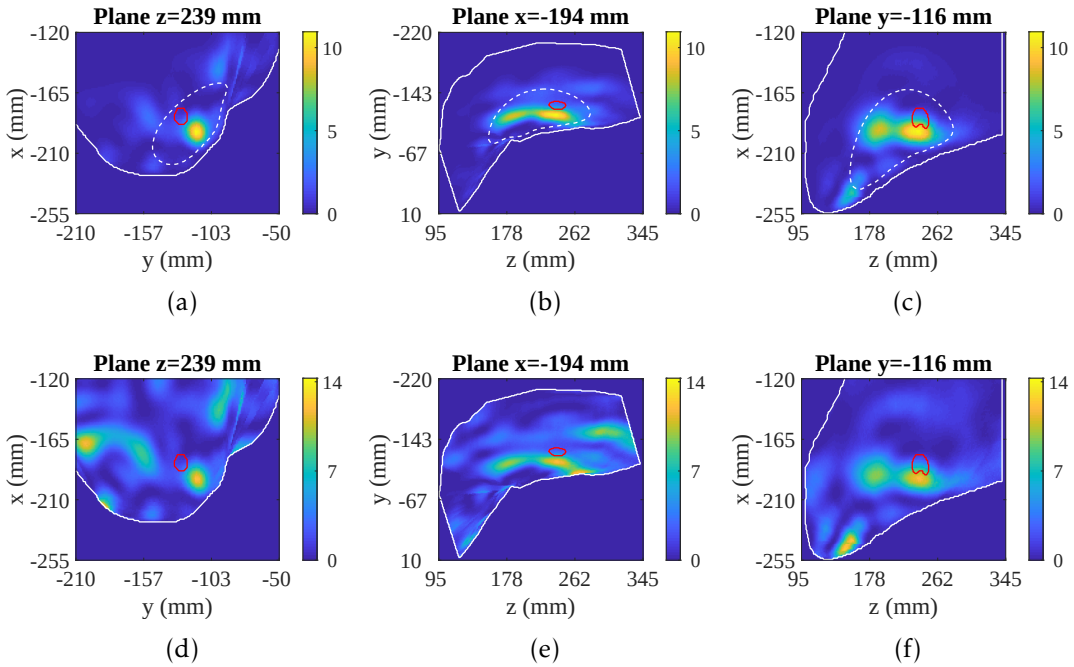

Figure 5.23: Reconstructed images of the axillary region phantom in the experimental test ALN-3. The first and second rows show the images with the ALN inside, when applying and not applying the spatial filter, respectively, in (a,d) axial, (b,e) sagittal and (c,f) coronal planes. The approximate location and shape of the ALN is represented as a red contour. The white solid and dashed contours represent the phantom contour and the volume of interest selected by the spatial filter, respectively.

position. In ALN-2 "Ref" and ALN-3 "Ref", SCR and SMR are also lower than when the ALN is placed inside the phantom. Conversely, the LE in the ALN-3 measurements is the same whether the ALN is placed inside the phantom or not, which may indicate the artefacts are located in the same position as the ALN.

Figure 5.24 shows the reconstructed images of the experimental test ALNM-1, where both ALN and muscle phantoms are embedded in the adipose mimicking liquid. The resulting images are very similar to the images obtained with the remaining experimental tests when the muscle phantom was not used. The muscle response is successfully removed by the combination of the selected grid of antennas ($\mathbf{G_I}$), which is farther away from the location of the muscle model, and the artefact removal algorithm performance. In this experimental test, the **SF** does not have an impact on the muscle response removal, as shown in Figure 5.24(d-f). However, one must note that this muscle phantom is a very simplified version of the *pectoralis minor* muscle and that ALNs are usually surrounded by multiple muscles. The ALN is detected with an SCR of 3.01 dB and an LE of 12.9 mm. The corresponding experimental test without the ALN has lower SCR, SMR and intensity, and higher LE, as expected, but SCR is still higher than 1.5 dB due to the presence of the focusing region [Figure 5.24(g-i)].

The average response in the four experimental tests is very similar, with SMR ranging from 8.69 to 8.97 dB. In all cases, the FWHM metric shows that the overall spatial resolution of the ALN detection is low, which is common in MWI systems. In this

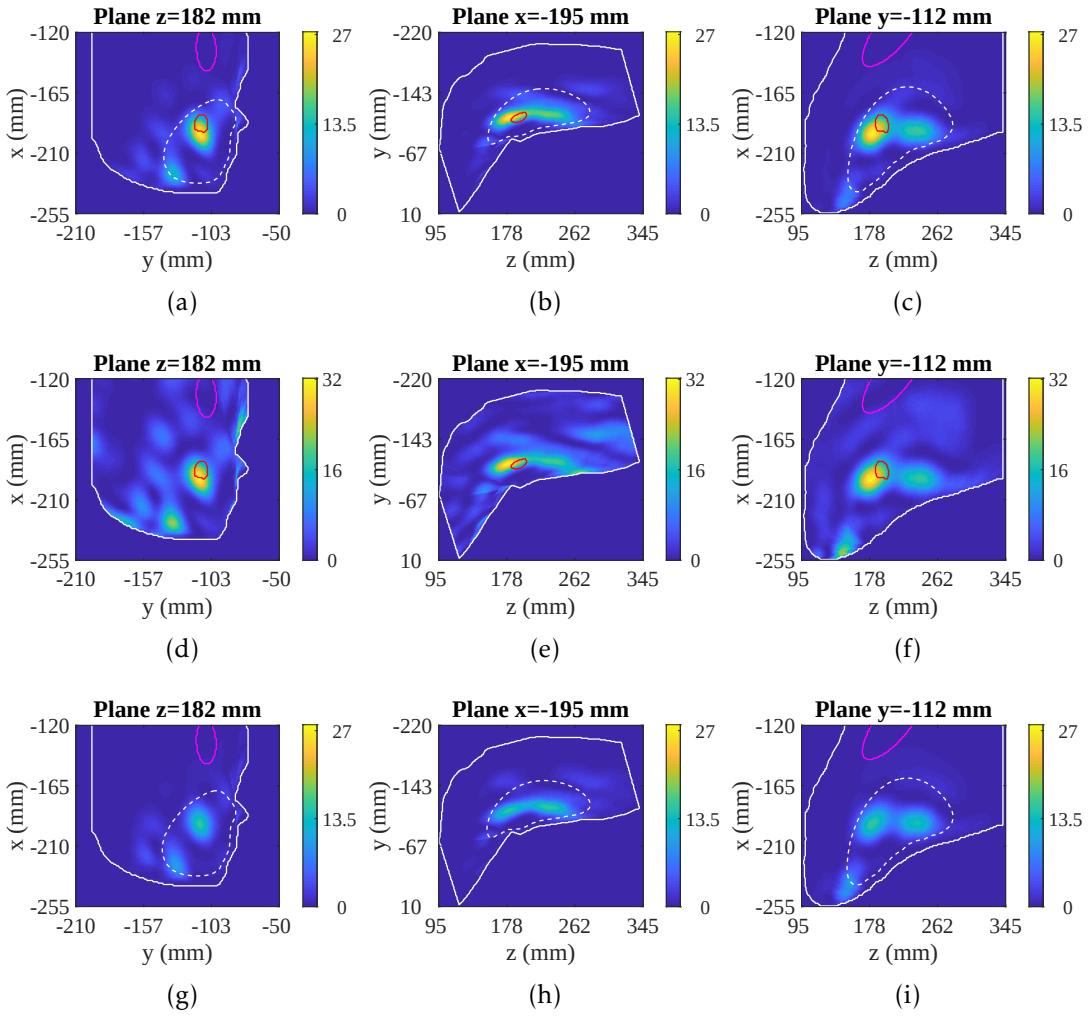

Figure 5.24: Reconstructed images of the axillary region phantom in the experimental test ALNM-1. The first and second rows show the images with the ALN and the muscle inside when applying and not applying the spatial filter, respectively. The third row shows the images of the axillary region without ALN and when applying the spatial filter. The left, centre and right images show the axial, sagittal and coronal planes, respectively. The approximate locations and shapes of the ALN and the muscle are represented as red and pink contours, respectively. The white solid and dashed contours represent the phantom contour and the volume of interest selected by the spatial filter, respectively.

particular application, this is very likely affected by the limited angular range imposed by the shape of the torso. Nonetheless, ALNs in different positions are detected in their correct location which are promising results to the detection of ALNs with MWI technology.

SVD yields good results for ALNs positioned at depths varying between 20 to 30 mm. However, the detection of shallower ALNs can be more challenging, since the ALN and the phantom surface response can be factorised in the same singular vector, which can hamper the removal of the surface response and consequent ALN detection. Conversely, deeper ALNs can have a weaker response. These cases still need to be evaluated, despite the fact that ALNs shallower than 15 mm are only observed in very few cases of breast cancer patients [75]. The spatial filter should accommodate these difference depths of ALNs and should be designed according to patient-specific information, as further

detailed in the following section. Additionally, the best combination of parameters (n_{sv} and subset of neighbouring antenna positions) needs to be tested for more axillary region phantoms in order to find representative parameters which can be applied in a clinical scenario.

5.3 Selection of Volume of Interest with Patient-specific Information

In order to develop an automatic method to define **SF** parameters, information collected in [220], which relates BMI to the depth of ALNs, is used to define the relationship between BMI and the size of the VOI and, consequently, the **SF** parameters.

The relationship between BMI (between 15 and 39) and the depth where level I ALNs are likely to be located can be written as follows [220]:

$$min_w = \max(0, -58.54 + 4.28\ \text{BMI} - 0.056\ \text{BMI}^2)\ [\text{mm}] \tag{5.4}$$

$$w = 13.02 + 1.75\ \text{BMI} - 0.021\ \text{BMI}^2\ [\text{mm}] \tag{5.5}$$

where min_w is the distance between the surface and the start of the VOI and w is the width of the VOI in the axial plane, as represented in Figure 5.25.

The axillary region phantom used in the experimental tests in Section 5.2 is used as a reference to find this relationship, by measuring the size of the VOI (Figure 5.25) for several combination of parameters. Parameters r_1 and γ are fixed to 400 mm and 0.5, respectively, as no substantial influence in the **SF** size was observed. Parameters r_t and r_2 are varied from 0 to 100 mm, and from 30 to 130 mm, respectively. The resulting data is then fitted to Polynomial Linear Regression Models (PLRMs). The parameter r_t can be defined as a function of min_w. The parameter r_2 can be defined as a function of r_t and w.

The PLRMs fitted to the measured data of depth (min_w) and width (w) of the VOI, while changing r_t and r_2, allow to infer equations that represent the relationship between the parameters. A PLRM, fitted to the measured min_w and r_t, shows that parameter r_t has a quadratic relationship with min_w ($R^2 = 0.91$) as follows:

$$r_t = max(0, 0.7 + 7.9 * min_w - 0.1322 * min_w^2)\ [\text{mm}] \tag{5.6}$$

A PLRM, fitted to the measured w and r_2 for several values of r_t, shows parameter r_2 has a linear relationship with both parameters ($R^2 = 0.94$), as follows:

$$r_2 = 1.69 * w - 0.27 * r_t + 25\ [\text{mm}] \tag{5.7}$$

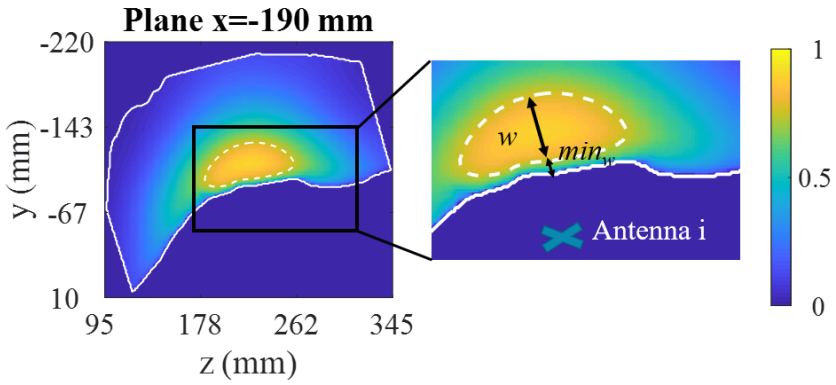

Figure 5.25: Example of the spatial filter (**SF**) representing the volume of interest inside the entire volume of axillary region phantom (left) and measurements taken from the **SF** (right), shown in a sagittal slice. The region in yellow is defined as VOI. min_w is the distance between the surface and the start of the VOI and w is the width of the VOI. The blue cross represents an example of an antenna position.

Combining equations 5.4, 5.5, 5.6, 5.7 and considering a BMI= 19, the parameters for a patient with BMI of 19 kg/m^2 are defined as $r_1 = 400$ mm, $\gamma = 0.5$, $r_t = 20$ mm, and $r_2 = 85$ mm. The subset of antenna positions $\mathbf{G_{SF}}$ is defined as 30% of the horizontal antenna positions centred at the axillary region and the closest angular antenna positions to the VOI. The VOI highlighted by this combination of parameters in the presented axillary region phantom is shown in Figure 5.26. The obtained VOI corresponds to a region extending from the phantom surface to a depth of approximately 40 mm in the phantom, which is smaller than the one considered for the experimental tests (Figure 5.18). If the **SF** presented in Figure 5.26 was applied to the images from the experimental tests with the phantom, the ALNs would be outside the VOI, and therefore their detection would be compromised.

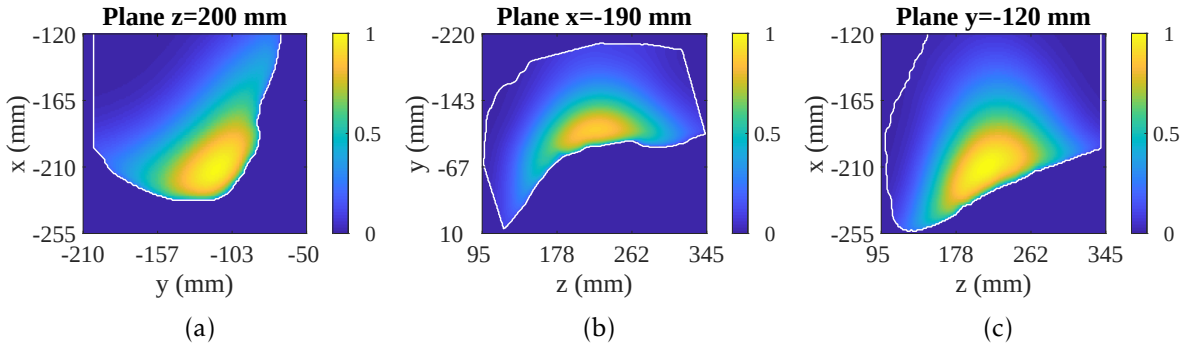

Figure 5.26: Reconstructed images of the spatial filter of the axillary region phantom with parameters optimised for the patient BMI in (a) axial, (b) sagittal, and (c) coronal planes. The white solid contour represents the phantom contour.

The same procedure can be applied to the 2D slices presented in Section 5.1 which were obtained from breast exams of patients with BMI of 19, 21 and 31 kg/m^2. Figure 5.27 shows the resulting microwave images after the corresponding **SF** is applied. Shapes A and B are obtained from the same patient exam (BMI = 19 kg/m^2). The artefacts located in the regions of reduced interest (e.g. the posterior part of the body) are

removed from the images when **SF** is applied. In fact, in the case of shape B, the detection of the ALN improves as those artefacts are removed. In shapes A and D the ALN is slightly outside the VOI. While in the case of shape D, only artefacts are detected as SVD did not show a good performance (as shown in Section 5.1.3), the detection of the ALN in shape A is not affected. The VOI is defined as the voxels with intensity higher than 0.75. Nonetheless, **SF** shows a Gaussian behaviour, and therefore, the transition of the **SF** between the inside and the outside of the VOI is smooth and so the ALN can still be detected.

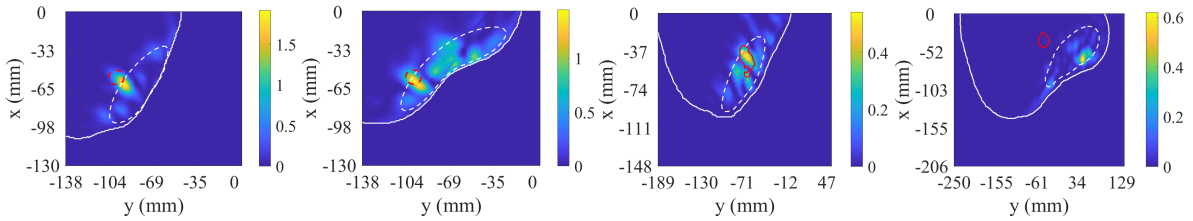

(a) Shape A (b) Shape B (c) Shape C (d) Shape D

Figure 5.27: Reconstructed images of 2D slices of axillary region phantoms when applying the spatial filter with parameters optimised for the patient BMI and using SVD with a fixed n_{sv} for all source points. The white solid and dashed contours represent the phantom contour and the volume of interest selected by the spatial filter, respectively. The red contour represents the true location and shape of the target.

5.4 Assessment of Electromagnetic Exposure Risk

In this section, an assessment of the electromagnetic exposure risk is performed for the proposed MWI system. The calculation of Specific Absorption Rate (SAR) has to be performed in a simulated environment using CST [189]. To this end, the numerical axillary region phantom developed within my research group [55] is used. The phantom was created from the same CT exam as the phantom presented in Section 5.2.1, but the CT images were further processed in order to obtain a smoother surface of the air-body interface and to create models of the internal tissues and organs.

Although it is expected that the maximum value of SAR is obtained in a superficial region, the numerical phantom includes all the segmented tissues (more than its surface): a skin layer, adipose tissue, muscle, bone and lung. A Vivaldi antenna identical to the one used in the experimental tests (described in Section 5.2.3) is used in the simulations. The antenna is placed at different distances from the skin surface (1.5, 35 and 55 mm) in order to represent a similar scenario to the experimental setup, where that distance varies along the phantom (Figure 5.13). The radiated power is 1 W and the SAR calculation is computed in an average volume of 10 g. Each tissue is modelled considering the Debye models reported in the literature by Gabriel *et al.* [116] and considering density values reported in the IT'IS Foundation dataset [221], as shown in Table 5.2.

Table 5.2: Dielectric properties and density of the tissues considered in the simulation for SAR calculation.

Tissue	ϵ_r **at 4 GHz**	σ **at 4 GHz (S/m)**	**Density** ρ (kg/m^3)
Adipose	5.12	0.84	911
Bone	16.76	6.46	1908
Lung	19.62	5.86	394
Skin	36.69	10.42	1109
Muscle	51.12	13.56	1090

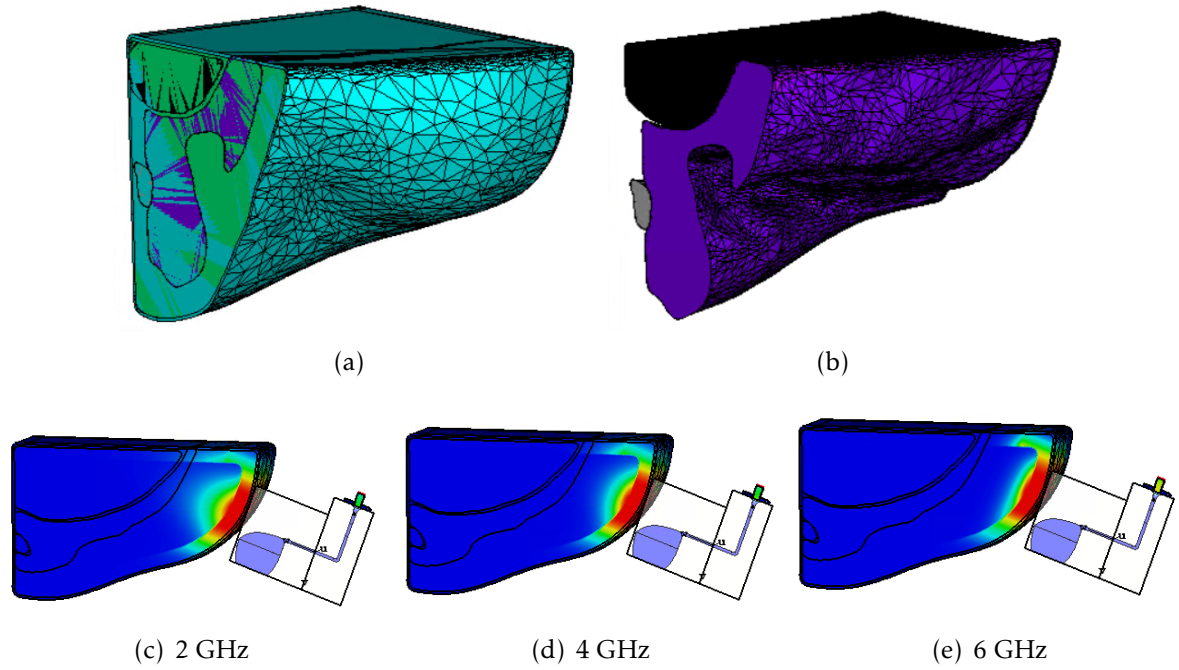

(a) (b)

(c) 2 GHz (d) 4 GHz (e) 6 GHz

Figure 5.28: (a,b) Numerical axillary region phantom used for SAR calculation, and (c-e) SAR maps in an average volume of 10 g using a Vivaldi antenna placed 15 mm away from the phantom surface at different frequencies. Red colours correspond to higher values of SAR, while blue colours correspond to lower values.

Figure 5.28 shows the simulated numerical phantom and the corresponding SAR maps for the closest position of the antenna to the phantom surface. The resulting SAR values are shown in Table 5.3. Higher frequencies result in a lower penetration into the axillary region tissues, thus the maximum value of SAR is also higher. As expected, the SAR decreases as the distance between the antenna and the phantom increases. The three calculated SAR values for the lower distance between the antenna and the phantom are higher than the limits recommended by International Commission on Non Ionizing Radiation Protection (ICNIRP), namely 2 W/kg. The ICNIRP limit is also exceeded for higher frequencies when the distance between the antenna and the skin surface is 35 mm. The remaining values are below the ICNIRP limit. Considering a

linear relationship between the radiated power and the SAR, SAR will be below the limits if the radiated power is lower than 0.07 W. In an MWI experimental prototype, this power can be as low as 0.01 W, so the current system can be made safe in terms of exposure.

Table 5.3: Maximum SAR values (W/kg) in three frequencies for the axillary region MWI prototype.

Distance between the antenna and the phantom	**2 GHz**	**4 GHz**	**6 GHz**
1.5 mm	14.93	22.89	28.13
35 mm	1.06	1.99	3.66
50 mm	0.53	1.08	1.59

5.5 Chapter Conclusions

This chapter presented the development of a radar MWI system aiming to detect ALNs. Firstly, the challenges of this type of system were analysed in a simulated scenario. The 3D shape of the torso limits the antenna positioning around the region of interest. Also, the concavities and convexities inherent to the axillary region shape may create artefacts that match the ALNs locations, which, combined with the limited antenna positioning, affect the quality of imaging results.

Then, a full pre-clinical system is presented, comprising: the mechanical setup, the axillary realistic phantom and algorithms specially designed for the ALN-MWI application. The results of four experimental tests were also presented, addressing the challenges in a 3D scenario. The current methodology showed promising results in the detection of a single level I ALN embedded in adipose mimicking liquid, with SCR higher than 2.77 dB and LE lower than 14.7 mm. The shape of the axillary region is the major challenge when applying an artefact removal algorithm. To that end, a thorough methodology was proposed to evaluate several combinations of parameters to optimise this algorithm for the axillary region phantom under consideration. However, further validation is needed with other axillary region phantoms in order to either define parameters that can be used for any phantom or a more robust methodology able to find the optimal parameters depending on the phantom. The importance of the selection of a subset of antenna positions to image the axillary region was also shown. Likewise, further evaluation is needed to find an automated methodology to define the optimal subset. Then, clinical information was included in the algorithms through the implementation of patient-specific information, specifically BMI, in the design of a spatial filter to select the volume where ALNs are more likely to be located. Finally,

an exposure assessment was performed, which showed the electromagnetic exposure of the current setup is below the limits and is safe for clinical practice.

Furthermore, future work should include the performance of more experimental tests. The evaluation of the spatial resolution of the system in detecting and differentiating multiple ALNs, as well as the ability to detect the contrast between healthy and metastasised ALNs, are crucial for the ultimate goal of the system (i.e. diagnose ALNs). The influence of the muscles should also be evaluated, by replacing the simplified version considered in this thesis with a more realistic one. The presence of muscles can deteriorate the quality of the microwave images, compromising the feasibility of this type of system. Although the frequency band of 2 to 5 GHz provided good results in the presented experimental tests, the frequency band of the system may need to be tailored depending on future results.

In the following chapter, a study to evaluate whether Machine Learning (ML) algorithms can distinguish between healthy and metastasised ALNs using MWI signals is performed. Ultimately, this type of algorithms can be incorporated in an experimental ALN-MWI prototype as the one presented in this chapter to aid the interpretation of the imaging results.

6 Classification of Axillary Lymph Nodes using Microwave Imaging Signals

This chapter presents a study of classification of Axillary Lymph Nodes (ALNs) to be used as a complementary tool to Microwave Imaging (MWI) of the axillary region. The resulting microwave images of the axillary region may have low spatial resolution and artefacts that hinder a correct interpretation of the images. Therefore, providing more objective information is important to aid this interpretation in a clinical scenario. Different morphological characteristics from healthy and metastasised ALNs are reported in the literature [80]–[83]. Similarly to other studies where microwave signals are used to classify between benign and malignant breast tumours [172]–[174] or between healthy and diseased breasts [182], Machine Learning (ML) algorithms can be used to classify healthy and metastasised ALNs based on their size and shape.

The classification of ALNs in a real situation presents some challenges. Although differences in size and shape of healthy and metastasised ALNs have been observed, ALNs of similar size and shape may have different pathology results. This can be observed either due to micro-metastases, which are difficult to detect using imaging modalities, or due to changes in the hilum, which - as seen in Chapter 4 - can affect dielectric properties. Although dielectric contrast between healthy and metastasised ALNs was observed in Chapter 4, this topic needs to be further studied. Small changes in ALN morphology can have a low impact on dielectric properties and, consequently, the dielectric contrast between healthy and metastasised ALNs may not be substantial. Additionally, contrarily to what is often assessed in classification of breast tumours, the axillary region usually has multiple ALNs, which can be either healthy or metastasised. This means the recorded microwave signals will contain signatures of different ALNs and the classification might be more challenging. Finally, the muscle and the skin response can also mask the ALN response. However, classification methods are worth studying to complement imaging results and could be advantageous to highlight characteristics of ALNs which are not detected in the images, and potentially contribute to ALNs diagnosis. To the best of my knowledge, no lymph node classification using

MWI signals was ever performed.

In the following sections, the simulated setup and classification methods used in this study are described. The first objective of this study is to evaluate whether the microwave signature of healthy and metastasised lymph nodes is different, independently of the surrounding medium. Then, the complexity of the surrounding medium is increased in order to evaluate its impact on the classification of ALNs. The microwave signals were recorded using Computer Simulation Technology (CST) Studio Suite® software [189] in several distinct scenarios.

6.1 Simulated Setup

This section presents the developed methodology to create the ALN models in the different simulated scenarios considered to evaluate the performance of algorithms in classifying healthy and metastasised ALNs.

6.1.1 Axillary Lymph Nodes Modelling

The ALN models used in this study were created using mathematical formulations. This methodology allows creating several models with variable size and shapes, whereas extracting this type of variability from medical exams (as shown in Chapter 4) is more limited as it would require a larger dataset, and it is time-consuming as those models would require additional processing.

Firstly, the following mathematical formulations using spherical coordinates were used to create 20 models with distinct shapes of healthy and metastasised ALNs:

$$r_1(\theta) = 1 - a \cdot [\sin\theta]^b \tag{6.1}$$

$$r_2(\theta) = 1 - c \cdot \exp\left(-\left(\frac{\theta - \theta_0}{d} \right)^2 \right) \tag{6.2}$$

$$r(\theta, \phi) = \begin{cases} r_1(\theta), & \text{if } \frac{\pi}{2} < \phi < \frac{3\pi}{2} \\ r_1(\theta)[\sin\phi]^2 + r_2(\theta)[\cos\phi]^2, & \text{otherwise} \end{cases} \tag{6.3}$$

where parameters a, b, c, d and θ_0 define the shape of the model. Parameters a and b define the concavity of the model, which is mainly observed in the negative x-axis shown in Figure 6.1. Parameters c, d and θ_0 reflect the depth, shape and location of convexity observed in the positive x-axis, respectively. This convexity is an approximate representation of the hilum.

Then, a total of 60 ALNs models (30 healthy and 30 metastasised) were obtained after resizing each one of the original 20 models, based on the morphological characteristics of healthy and metastasised ALNs, and rotating them along their centre.

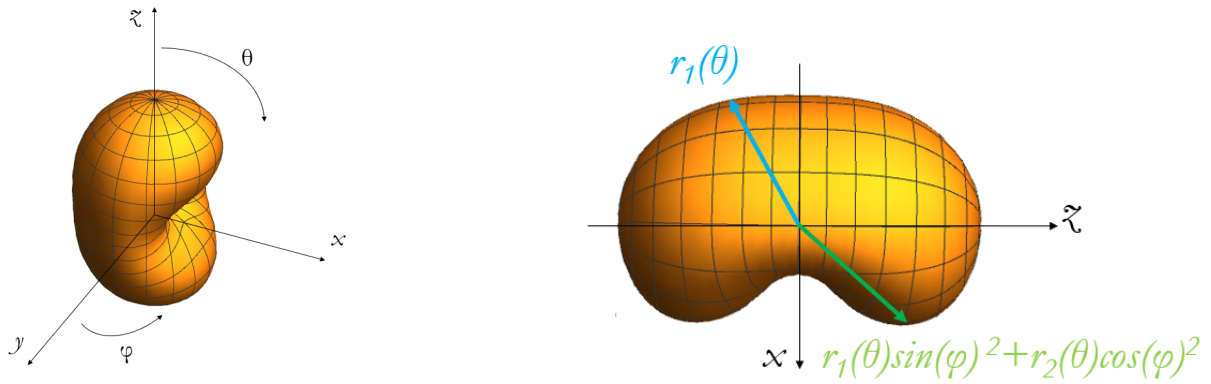

(a) (b)

Figure 6.1: Representation of the numerical ALN model created using mathematical formulations in equation 6.3. (a) represents the model in a 3D view and the spherical coordinates and (b) represents the model in the *xz*-plane and the equations used to calculate the shape in each quadrant.

The resulting models respect the criteria previously reported in Section 2.1.3: the ratio between the longest-axis (L) and the shortest-axis (S) - L/S - is equal or greater than 1.7 and $S < 9$ mm for healthy ALNs; healthy ALNs have a concavity which represents the hilum, while it may be absent in metastasised ALNs. One should note this methodology is limited by the fact that not all lymph nodes respect these criteria (as seen in Section 2.1.3). Also, the effect of hilum presence in the dielectric properties is not considered in the models, since the same dielectric properties are considered for both healthy and metastasised ALNs, assuming the worst-case scenario. As seen in Chapter 4, a larger hilum (observed in healthy ALNs) results in overall lower dielectric properties. Figure 6.2 shows examples of 5 ALN models of each type. The full dataset of ALN models is shown in Appendix G and the corresponding dimensions basic statistics are shown in Table 6.1.

Table 6.1: Dimensions of ALN models created with mathematical formulations.

	Healthy ALNs (n=30)		**Metastasised ALNs (n=30)**	
	Mean	**Range**	**Mean**	**Range**
L (mm)	14.6	9.0 to 20.0	15.0	10.0 to 20.0
S (mm)	4.9	3.0 to 9.0	11.8	10.0 to 18.0
L/S (mm)	3.2	1.8 to 6.7	1.3	1.0 to 1.6

ALNs: Axillary Lymph Nodes; L: Longest-Axis; S: Shortest-Axis

6.1.2 Scenarios

Four scenarios with increased complexity in a monostatic configuration were simulated with the modelled ALNs. In all simulated scenarios, no dielectric contrast between

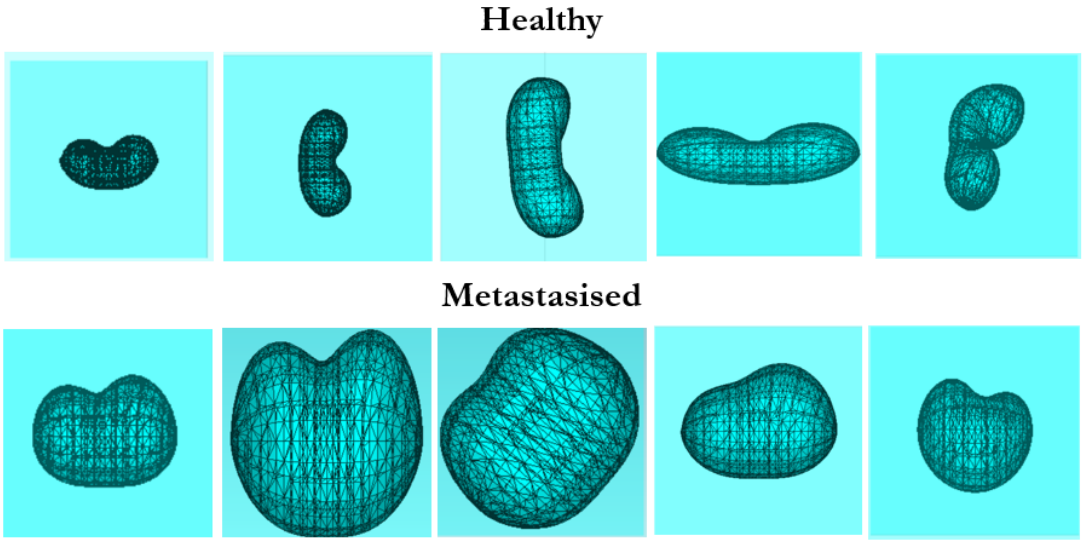

Figure 6.2: Examples of ALN models created using mathematical formulations and resize operations.

healthy and metastasised ALNs is considered, which corresponds to a worst-case scenario. Hence, the classification methods distinguish ALNs based only on their shape and sizes. The ALN models are defined with a relative permittivity of $\epsilon_r = 40$ and a dissipation factor $\tan(\delta) = 0.1$. The ALN models are restricted to a $20 \times 20 \times 20$ mm^3 size cube placed in a dielectric phantom of relative permittivity $\epsilon_r = 8$ and a dissipation factor $\tan(\delta) = 0.1$, which is meant to mimic adipose tissue.

Table 6.2 summarises the details for each scenario. In all scenarios, the antenna is calibrated by performing the subtraction between the simulated monostatic signals with all components (antenna, phantom and ALN models) and the signals obtained from the corresponding simulation without the phantom and ALN models.

In the first and less complex scenario (Scenario A), the antenna and the ALN are placed in the same medium with properties mimicking adipose tissue [Figure 6.4(a)]. Since the antenna is no longer placed in air, the antenna needs to be tailored to the

Table 6.2: Summary of scenarios considered in this study.

	Scenarios			
	A	**B**	**C**	**D**
Dielectric interface	None	Cylindrical shape	Pseudo--Realistic	Pseudo--Realistic
Number of ALNs per simulation	1	1	1	2
Number of simulations	60	60	60	30
Number of antenna positions	7	7	28	28
Number of scanned planes	1	1	4	4

medium under consideration. Hence, a Crossed Exponential Tapered Slot Antenna (XETS) antenna, similar to the one presented in Chapter 3, designed by my research group, is used to record the simulated signals. It has the dimensions of 17 mm radius and 0.25 mm thickness and it is impedance-matched from 2 to 6 GHz (Figure 6.3). However, higher frequencies might provide a weaker response of the target due to the lossy medium.

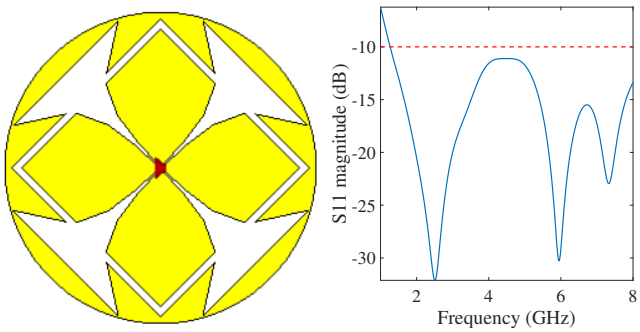

(a) (b)

Figure 6.3: (a) Schematic of XETS and (b) plot of the corresponding S-Parameter (magnitude in dB).

The antenna is swept in 7 antenna positions in a quarter of a circumference of radius 140 mm at the same plane as the ALN [Figure 6.4(a)]. The ALN model is always centred in the $20 \times 20 \times 20$ mm^3 cube to minimise confounders affecting the recorded signals. The average distance between the centre of the ALN and the antenna positions is 74.5 mm, ranging from 46 to 120 mm. Each simulation considers one of the 60 ALNs at a time, resulting in a total of 60 simulations.

In the second scenario (Scenario B), the antenna is placed in air and the dielectric is a simplified axillary region phantom represented by a pseudo-quarter of a cylinder [Figure 6.4(b)]. The cylinder has a radius of 140 mm and 120 mm height. The antenna is swept in 7 positions across a quarter of circumference 35 mm away from the dielectric surface. As the antenna is placed in air, the XETS antenna presented in Chapter 3 is used to record the simulated signals. This antenna is impedance-matched from 2 to 6 GHz. In this scenario, the reflection in the air-dielectric interface is expected to have higher response than the ALN response and potentially mask it. The ALN model is also always placed in the same position. The average distance between the position of the ALN and the antenna positions is 105 mm, ranging from 80 to 120 mm. Sixty simulations, i.e. one per ALN, are also performed.

In the third scenario (Scenario C), the dielectric has a more complex shape, closer to a realistic axillary region phantom, with concavities and convexities. This shape is created in CST using modelling tools (using an anatomically realistic shape would substantially increase the computational time of the simulations). The phantom has 220 mm height and a varying radius that ranges from 120 mm to 260 mm. The antenna is swept across a quarter of circumference of 155 mm radius. Four different planes of

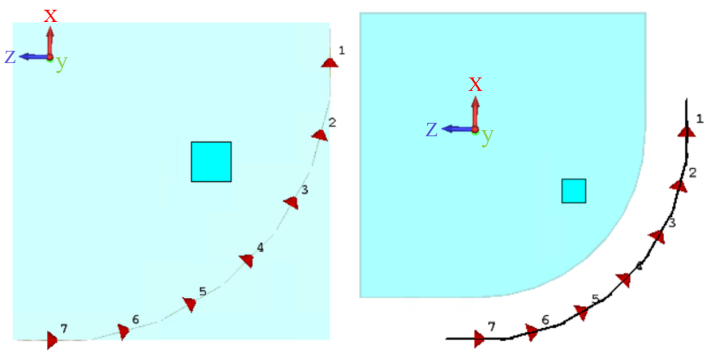

(a) (b)

Figure 6.4: Simulated scenarios with (a) no change in medium and (b) a cylindrical dielectric phantom.

the axillary region phantom are simulated. For each plane, the 7 antenna positions and the ALNs are placed in that plane. Figure 6.5 shows the four considered planes and Table 6.3 shows the variability of distances 1) between the ALN position and the dielectric surface, and 2) between the surface and the first and last antenna positions. This procedure allows to artificially represent different axillary region phantoms, while increasing the variability of air-phantom interface and position of ALNs in relation to the surface. The same antenna of setup B is used to transmit and record the signals.

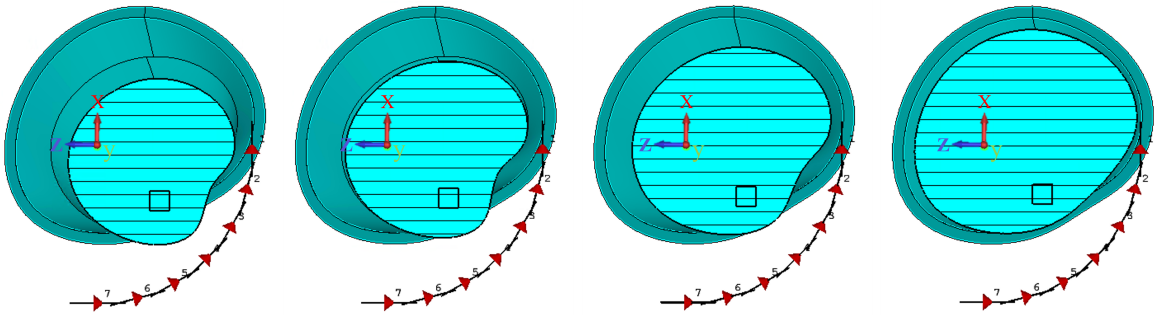

(a) $\Delta y = -20$ mm (b) $\Delta y = 0$ mm (c) $\Delta y = 20$ mm (d) $\Delta y = 40$ mm

Figure 6.5: Screenshots from CST simulation of four different xz-planes of the axillary region phantom with one ALN. The planes are separated from each other by 20 mm in the y-axis.

In the fourth scenario (Scenario D), multiple ALNs are placed inside the realistic-shaped axillary region phantom. This scenario aims to evaluate whether the classifiers are able to distinguish signals acquired in healthy axillary regions from axillary regions with metastasised ALNs. Three positions are pre-defined to place the ALNs, as shown in Figure 6.6, but only two ALNs are considered in each simulation. The two of the three positions where ALNs are placed are chosen randomly, but each of the 3 combinations is chosen the same number of times. The distance between the ALNs will depend on which 2 pre-defined locations have ALNs, on their orientation within each location and the size of each ALN. The distance between the centre of the adjacent pre-defined positions of the ALN is 25 mm. This means the distance between the surfaces of ALNs

Table 6.3: Relative approximate distances between the ALN position, antenna position and phantom surface in the four planes of the axillary region phantom in scenario C.

	Planes			
Distances	$\Delta y = -20$ mm	$\Delta y = 0$ mm	$\Delta y = 20$ mm	$\Delta y = 40$ mm
ALN to nearest phantom surface (mm)	46	41	35	29
First antenna position to phantom surface (mm)	18	23	21	13
Last antenna position to phantom surface (mm)	82	80	75	76

can vary from 0 to 50 mm. Each axillary region simulation includes a combination of different ALNs, either 0, 1 or 2 metastasised ALNs. The same ALN model is not used in more than one simulation. This means the 60 ALN models are distributed as follows: 10 simulations with 2 healthy ALNs; 10 simulations with 1 healthy and 1 metastasised ALNs; 10 simulations with 2 metastasised ALNs. No dielectric contrast is considered between healthy and metastasised ALNs. The antenna is swept in 7 positions around

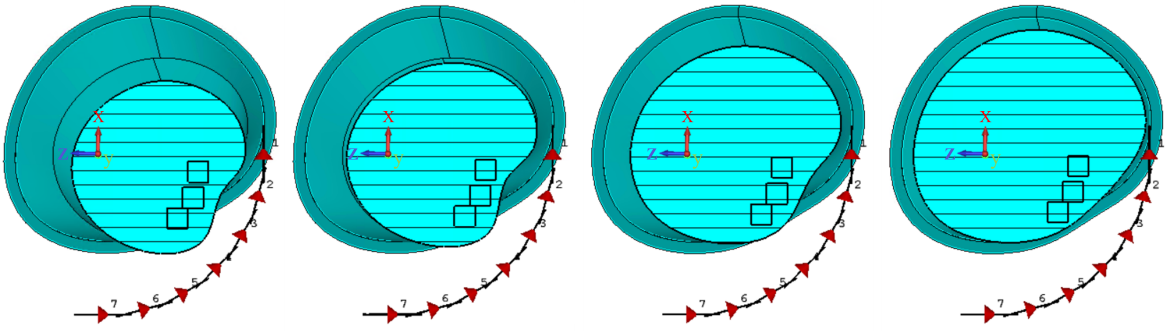

(a) $\Delta y = -20$ mm (b) $\Delta y = 0$ mm (c) $\Delta y = 20$ mm (d) $\Delta y = 40$ mm

Figure 6.6: Screenshots from CST simulation of four different xz-planes of the axillary region phantom with multiple ALNs. The planes are separated from each other by 20 mm in the y-axis.

the axillary region in four different planes. Similarly to Scenario C, this procedure aims to artificially represent variability of the air-phantom interface and the positions of the ALNs relatively to the air-phantom interface. Figure 6.6 shows the four considered planes and the three pre-determined positions for the ALNs, and Table 6.4 shows the variability of distances between each ALN position and the nearest phantom surface.

Table 6.4: Relative approximate distances between each ALN position and phantom surface in the four planes of the axillary region phantom in scenario D. Positions 1 to 3 are defined in top-down order.

	Planes			
Distances	$\Delta y = -20$ mm	$\Delta y = 0$ mm	$\Delta y = 20$ mm	$\Delta y = 40$ mm
ALN (position 1) to nearest phantom surface (mm)	13	9	17	25
ALN (position 2) to nearest phantom surface (mm)	12	8	9	10
ALN (position 3) to nearest phantom surface (mm)	18	14	8	4

6.2 Classification Pipeline

The classification pipeline was fully implemented in MATLAB® 2018b using the Statistics and Machine Learning Toolbox. An extensive combination of type of signals, Feature Extraction Methods (FEMs) and classifiers is used to create models able to classify healthy and metastasised ALN models using microwave signals. Each microwave signal is processed with a FEM, then used as an input to the classification models. In the scenarios with only one ALN, the output classes are defined as healthy and metastasised. In scenario D, where multiples ALNs are used, three binary models are built where the output classes are: 1) axillary regions with only healthy ALNs and axillary regions with at least 1 metastasised ALN; 2) axillary regions with only healthy ALNs and axillary regions with exactly 1 metastasised ALN; and 3) axillary regions with only healthy ALNs and axillary regions with exactly 2 metastasised ALNs. Figure 6.7 shows the adopted ML pipeline. The classifiers are trained using a cross-validation methodology, ensuring that all signals acquired for one specific ALN are all included in the same set (training or testing sets).

6.2.1 Type of signals

Four different types of signals were considered before applying FEMs: reflection coefficients $\mathbf{s}_{i,i}$ in Frequency Domain (FD) - absolute, real and imaginary parts - and reflection coefficients $\mathbf{S}_{i,i}$ in Time Domain (TD). Each type of signals is used, one at once, for the remaining steps of the ML processing, as represented in Figure 6.7.

The FD signals are extracted from the CST simulations and originally have 1001

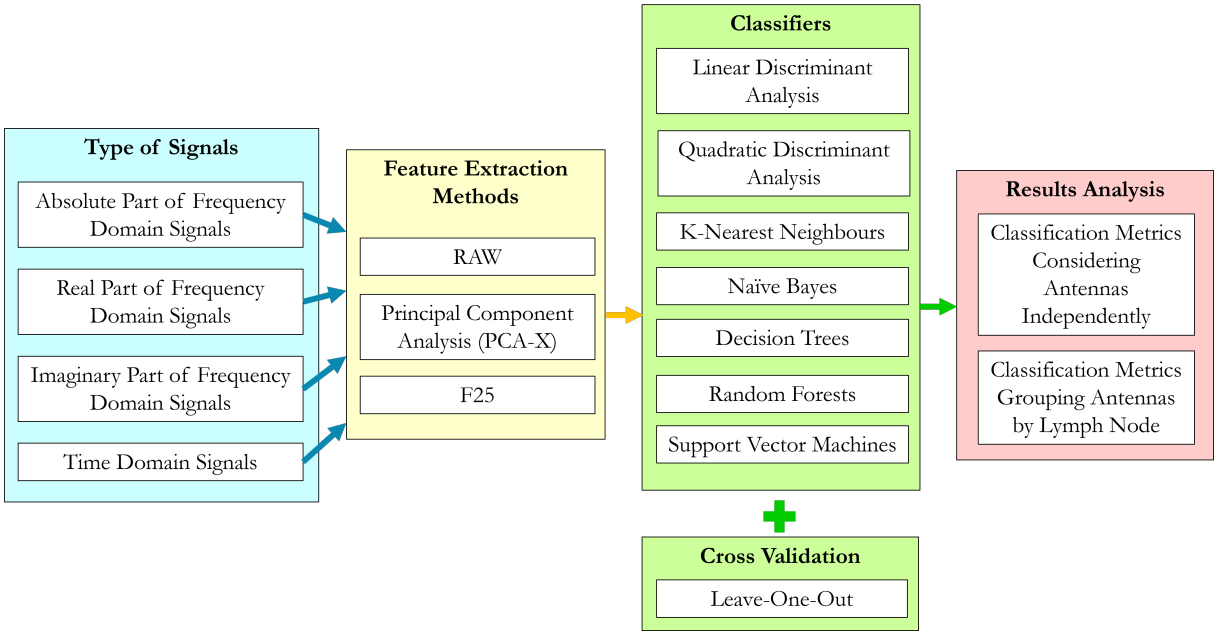

Figure 6.7: Machine Learning pipeline divided in four steps: type of signals, feature extraction methods, classifiers and results analysis.

frequency samples, from 1 to 8 GHz. Then, the signals are restricted to a 2 to 6 GHz frequency band, resulting in 572 frequency samples. The TD signals are obtained after applying an Inverse Fast Fourier Transform (IFFT) to the FD signals and also have 572 time samples.

6.2.2 Feature Extraction Methods

Three FEMs are used to select the features used to classify the microwave signals:

- **RAW:** No feature extraction is applied. Each frequency or time sample is considered as a feature.
- **F25:** Twenty-five customised features are extracted from the FD or TD microwave signals.
- **PCA-X:** Principal Component Analysis (PCA) is applied to the signals and X components are used as features. X ranges from 1 to 20.

The features extracted with the F25 method were designed by my research group in previous studies [173], [222] inspired by morphological features of TD signals. In this study, they are also extracted from FD signals. The 25 features are defined as follows:

1. Amplitude of the absolute maximum peak
2. Location of the absolute maximum peak
3. Amplitude of the absolute minimum peak

4. Location of the absolute minimum peak
5. Variance
6. Standard deviation
7. Root-mean-squared error
8. Number of positive peaks
9. Number of negative peaks
10. Mean amplitude of the positive peaks
11. Mean amplitude of the negative peaks
12. Mean Full Width Half Maximum (FWHM) of the positive peaks (when exist)
13. Mean FWHM of the negative peaks (when exist)
14. Mean separation between positive peaks (when exist)
15. Mean separation between negative peaks (when exist)
16. Number of zero crossings (when exist)
17. Integral of the signal
18. Integral of the absolute of the signal
19. Positive percentage area of the signal (when exist)
20. Negative percentage area of the signal (when exist)
21. Mean value of the autocorrelation signal
22. Number of peaks of the autocorrelation signal
23. Mean amplitude of the peaks of the autocorrelation signal
24. Mean FWHM of the peaks of the autocorrelation signal
25. Mean separation between peaks of the autocorrelation signal

6.2.3 Classifiers

As presented in Section 2.4.2, several classifiers, with different characteristics, have been widely used in the literature to classify microwave signals. Although some are known to provide promising results using microwave signals for breast tumour classification, such as Support Vector Machines (SVM) [171], k-Nearest Neighbours (kNN) [174] and Random Forests (RFO) [173], in this study a larger range of classifiers is used to evaluate the classification of ALNs in an axillary region. To this end, seven classifiers are used: Linear Discriminant Analysis (LDA), Quadratic Discriminant Analysis (QDA), kNN, Naïve Bayes (NB), Decision Trees (DT), RFO and SVM. The corresponding hyperparameters are optimised as per Table 6.5. The values were chosen in order to keep a good compromise between the coverage of a wide range of values and a moderate computational time of the training process.

6.2.4 Cross-Validation and Result Analysis

A Leave-One-Out cross-validation strategy is used to test the performance of the classifiers, since the dataset is relatively small and to avoid over-fitting. In scenarios A to C, the data is divided into 60 groups, where each group comprises the signals of one single ALN. In scenario D, the data is divided into 30 groups or 20 groups (depending on the binary model considered), where each group comprises the signals of one axillary region with a combination of two ALNs. The training set has $N_a * (N_g - 1)$ microwave signals, while the testing set has N_a signals, where N_a is the number of antennas and N_g is the total number of groups.

When considering PCA as FEM, PCA is applied to each training set and the resulting transformation is applied to the corresponding testing set, ensuring there is no data contamination. The classifiers hyperparameters are optimised globally, i.e. considering the results of the final metrics and not for each testing set, in order to avoid over-fitting.

The resulting performance metrics (namely, accuracy, sensitivity and specificity) are calculated considering the predictions of all testing sets. For unbalanced datasets, accuracy is not the best metric. Therefore, the Matthews Correlation Coefficient (MCC) (detailed in Section 2.4) is calculated, as it considers the weight of positive and negative cases. A value of 1 means a perfect classification and 0 means a random classification. Sensitivity and specificity are indicated for completeness but only the accuracy metric or MCC are thoroughly discussed. The analysis of the results is performed by considering the predictions of the signals from each antenna position treated as independent observations (independent signals), and the majority vote of the predictions of the signals of all antenna positions per ALN (grouped signals).

Table 6.5: Hyperparameters optimised for each classifier.

Classifier	Hyperparameter name	Hyperparameter values
LDA	γ	10 linearly-spaced values: $0,\ldots,1$
	δ	10 logarithmically-spaced values: $10^{-2},\ldots,10^{2}$
QDA	γ	10 linearly-spaced values: $0,\ldots,1$
kNN	Number of neighbours (k)	$1,2,\ldots,10$
	Type of distance (d)	• cityblock ($d = \sum_{i=1}^{n} \|A_i - B_i\|$) • chebyshev ($d = \max_i(\|A_i - B_i\|)$) • euclidean ($d = \sum_{i=1}^{n} \sqrt{(A_i - B_i)^2}$) • hamming (where d is defined as the fraction of number of different coordinates A_i and B_i)
NB	Data distribution	• normal (Gaussian) • multivariate multinomial distribution • kernel smoothing density estimate
DT	Pruning criterion	• error ($1 - p(j)$) • impurity
	Split criterion (if impurity is chosen as pruning criterion)	• Gini's diversity index ($1 - \sum_i p^2(i)$) • twoing rule (which considers the fractions of observations of each left and right child nodes) • cross entropy ($-\sum_i p(i)\log_2 p(i)$)
RFO	Number of trees	12 linearly-spaced values $25,\ldots,300$
	Pruning criterion	(same as for Decision Trees)
	Split criterion	(same as for Decision Trees)
SVM	Type of kernel	• linear • polynomial of order 3 • Radial Basis Function (RBF)
	C	7 logarithmically-spaced values $2^{-16}, 2^{-11},\ldots, 2^{9}, 2^{14}$
	γ	7 logarithmically-spaced values $2^{-16}, 2^{-11},\ldots, 2^{9}, 2^{14}$

- A_i and B_i are the coordinates of two points A and B
- $p(i)$ is the fraction of class i in the node; j is the class with the largest number of samples in a node

6.3 Results and Discussion

The classification results of the four scenarios are presented in the following sections.

6.3.1 Single Axillary Lymph Node in the Same Medium as the Antennas (scenario A)

This section presents the results with the simulated signals with each of the 60 ALNs embedded in the same medium as the antenna. This scenario comprises 7 antenna positions per ALN, which makes a total of 420 observations to be classified.

Figure 6.8 shows an example of the first samples of TD signals collected by antenna 1 of one healthy and one metastasised ALNs. The plot shows there is a difference between the response from each of the ALNs for this antenna position. Depending on the antenna position and the orientation of the ALN, the microwave signature of each ALN may vary.

Figure 6.9 shows the box plots of the distribution of the samples of each type of signal (absolute FD signals, real part of FD signals, imaginary part of FD signals, and TD signals) used for classification before applying any FEM over each class (healthy and metastasised). These plots allow to compare the variability of magnitude values of the response of healthy and metastasised ALNs but this comparison is not performed comparing the magnitude sample by sample (either time or frequency samples). The performance of ML algorithms indicate whether the microwave responses of healthy and metastasised ALNs can be classified. For each type of signal, box plots per each of the 7 antenna positions are shown, as well as considering all antenna positions. For each antenna position, each box plot is created using the magnitude values of 17,160 samples resulting from the 572 signal samples of the 30 simulated ALNs per class. For the plot that considers all antenna positions, a total of 7×17,160 samples are considered.

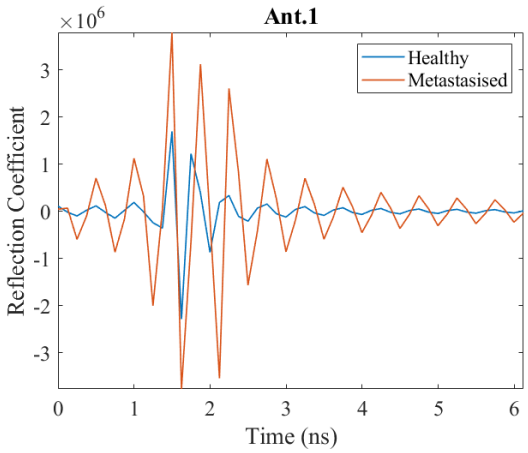

Figure 6.8: Plots of reflection coefficient signal in time-domain of one healthy and one metastasised ALN in scenario A with antenna position 1.

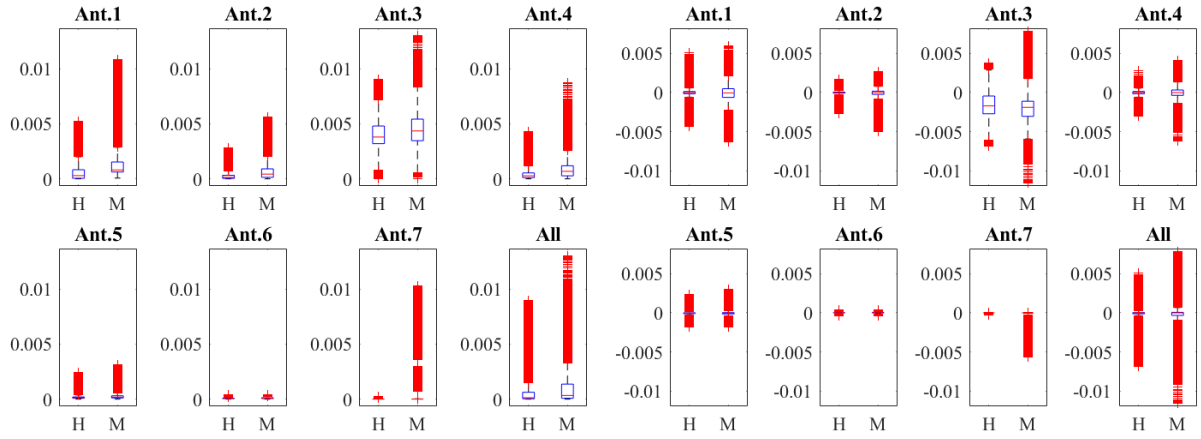

(a) Absolute FD

(b) Real Part FD

(c) Imaginary Part FD

(d) TD

Figure 6.9: Box plots of magnitude distribution of each type of signals over each class (H: Healthy and M: Metastasised) in scenario A and for the antenna positions. The red line represents the median, the boxes represent the first and third quartile of the distribution, and the red crosses represent the outliers of the distribution.

The red crosses shown in the box plots represent outliers of the distribution. An outlier is a value that is more than 1.5 times the interquartile range away from the bottom or top of the box. In this case, these outliers are values that represent the variability of the magnitude values within the class (healthy or metastasised). In general, independently of the type of signal, microwave signals present some differences regarding the variability of the magnitude values between healthy and metastasised ALNs, but the differences are not substantial. The responses recorded at different antenna positions are different both regarding the maximum of magnitude and regarding the variability in magnitude values. This is explained by the fact that each antenna position is placed at a different distance from the target. In the TD signals, most of the magnitude values are around 0, which means part of the signal has no response, and the box plots mostly indicate high magnitude samples as outliers.

Table 6.6 shows the accuracy results of scenario A for each classifier after optimising the hyperparameters. The accuracy values are obtained considering the signal from

Table 6.6: Accuracy (%) of classification models considering independent signals of scenario A after optimising classifiers hyperparameters. The PCA-X rows show the best results between 1 and 20 principal components. N/A means the classifier was not able to converge.

Type of signals	FEM	LDA	QDA	kNN	NB	DT	RFO	SVM
Absolute FD	RAW	71.2	50.0	**95.7**	69.1	88.3	92.4	84.5
	F25	N/A	N/A	90.7	71.9	83.3	88.3	82.4
	PCA-X	74.8	73.6	95.5	74.3	85.5	91.7	86.2
Real Part FD	RAW	65.2	52.9	94.5	70.5	84.8	92.6	86.7
	F25	78.8	61.9	92.4	74.1	83.1	89.3	84.0
	PCA-X	72.9	75.2	**95.2**	75.2	86.9	91.4	85.2
Imag. Part FD	RAW	64.8	46.9	**95.2**	68.8	85.0	93.1	85.2
	F25	75.0	57.1	94.0	74.0	89.1	89.5	83.8
	PCA-X	68.1	75.5	**95.2**	75.2	87.1	92.9	86.2
TD	RAW	62.6	55.5	92.9	74.5	85.0	87.4	84.3
	F25	N/A	N/A	92.1	70.0	81.2	87.4	84.3
	PCA-X	71.9	73.8	**94.5**	74.3	88.8	92.1	85.0

each antenna as an independent observation (independent signals). When using LDA and QDA, the accuracy results vary up to 10% for different type of signals or FEM. kNN is the classifier yielding better results, followed by RFO. When considering an X number of PCA components as features, the accuracy results outperform the results with F25 and RAW in the majority of the cases. In other cases, RAW may outperform PCA but the computational time of the training process is higher as the number of features is considerably higher. The accuracy between the four types of signals are different but differences are not substantial.

Optimal accuracy results for each type of signals correspond to different classifier hyperparameters and X number of PCA components, and result in different accuracies when grouping the antennas per ALN. The parameters of the models with highest accuracy values, per type of signals, are as follows:

- **Absolute FD signals:** kNN, cityblock distance, k=2 (neighbours) and RAW signals; 95.7% accuracy, 98.6% sensitivity and 93.9% specificity when considering independent signals; 98.3% accuracy, 100% sensitivity and 96.7% specificity when grouping the antenna signals per ALN (1 false positive)

- **Real Part FD signals:** kNN, euclidean distance, k=2 (neighbours) and 20 PCA

components; 95.2% accuracy, 97.6% sensitivity and 92.9% specificity when considering independent signals; 98.3% accuracy, 100% sensitivity and 96.7% specificity when grouping the antenna signals per ALN (1 false positive)

- **Imaginary Part FD signals:** kNN, cityblock distance, k=2 (neighbours) and 20 PCA components; 95.2% accuracy, 98.1% sensitivity and 92.4% specificity when considering independent signals; 98.3% accuracy, 100% sensitivity and 96.7% specificity when grouping the antenna signals per ALN (1 false positive)
- **TD signals:** kNN, cityblock distance, k=2 (neighbours) and 16 PCA components; 94.5% accuracy, 98.6% sensitivity and 90.5% specificity when considering independent signals; 98.3% accuracy, 100% sensitivity and 96.7% specificity when grouping the antenna signals per ALN (1 false positive)

The ALN which is misclassified when grouping the antenna signals is the healthy ALN 11 (see Appendix G). This ALN is one of the ALNs with the largest L (20 mm) and, within those with the largest L, it is the one that has the lowest L/S ratio (2.5). These dimensions might explain why the algorithm is not able to classify correctly this ALN. Nonetheless, the high accuracy encourages the adoption of these algorithms to classify ALNs using microwave signals.

A high number of PCA components and a low number of neighbours in kNN yield the best accuracy results. Figure 6.10(a) shows how accuracy values vary over the number of PCA components for a fixed combination of hyperparameters when considering TD signals. Figure 6.10(b) shows how the accuracy varies with the number of K neighbours used in kNN for a fixed FEM (PCA-16) and remaining hyperparameters also when considering TD signals. The changes of accuracy values are more evident when considering independent signals versus considering grouped signals, i.e. the majority vote of the predictions of all antenna signals grouped per ALN is less affected

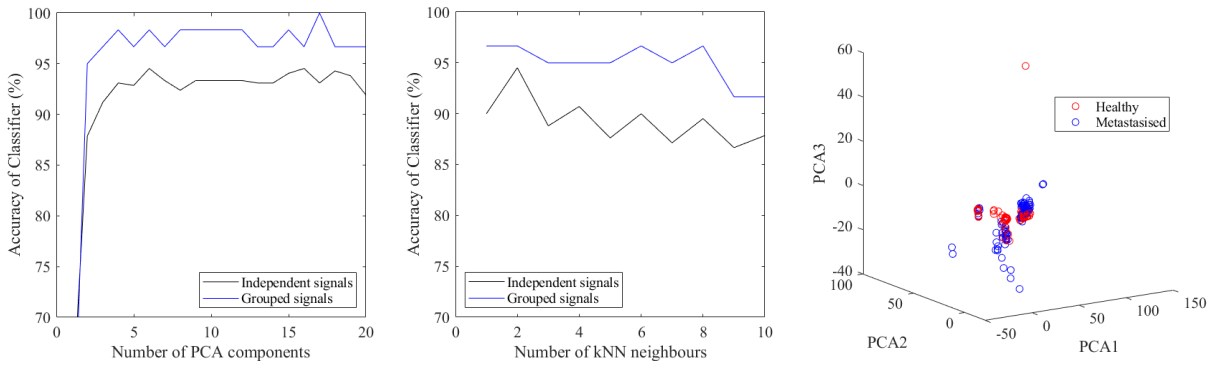

(a) (b) (c)

Figure 6.10: Plots of (a, b) accuracy values over the number of PCA components as features and number of kNN neighbours, respectively, and (c) PCA components in 3D view. Accuracy values in (a) are obtained with TD signals, kNN using Cityblock distance and $k = 2$, while in (b) are obtained with TD signals, 16 PCA components as features and kNN using Cityblock distance.

by changing hyperparameters. The accuracy increases when more PCA components are used and decreases when more neighbours are considered for kNN. Figure 6.10(c) shows a 3D plot of the first 3 PCA components of signals of each class, which are represented in red and blue. There are no well-defined clusters for each class, while there are several sub-clusters within the range of values. This may explain why kNN and a low number of neighbours yields good results: each point is classified as the majority of the closest neighbours in the closest sub-cluster. Considering a higher number of PCA components, a better separation into these sub-clusters may be observed and, therefore, the classification is improved. Similar conclusions can be drawn when using the three other types of signals.

6.3.2 Single Axillary Lymph Node in a Cylindrical Phantom (scenario B)

This section shows the results with the simulated signals obtained with a simplified cylindrical dielectric mimicking the axillary region. Measurements are taken at 7 antenna positions per ALN in a total of 60 ALNs, yielding 420 observations to be classified.

Figure 6.11 shows the box plots of the distribution of each type of signal used for classification before applying a FEM over each class (healthy and metastasised). In contrast with scenario A, when considering FD signals, there are less outliers (represented by red crosses) in the distributions and there is less variability of magnitude values among the antenna positions. This means that the magnitude values of each signal are similar within the class and among antennas, caused by the air-phantom interface response. When considering TD signals, the box plots show the high magnitude values as outliers, and no substantial difference is observed between healthy and metastasised ALNs. One must note that the magnitude values cannot be directly compared to scenario A because in that scenario the antenna positions were closer to the ALN and embedded in a different medium, and in scenario B the response of the cylindrical dielectric is higher than the ALNs.

Table 6.7 shows the accuracy results of scenario B for each classifier with optimised hyperparameters. Similarly to the case of scenario A, kNN yields better results, also followed by RFO. In most cases, using PCA improves the accuracy results in comparison to when F25 or RAW are used as FEM. Moreover, no relevant changes are observed between the types of signals.

The optimal accuracy results with kNN for the four type of signals correspond to different classifier hyperparameters, X number of PCA components and accuracy values, as follows:

- **Absolute FD signals:** kNN, cityblock distance, k=2 (neighbours) and 14 PCA

components; 97.1% accuracy, 99.1% sensitivity and 95.2% specificity when considering independent signals; 98.3% accuracy, 100% sensitivity and 96.7% specificity when grouping the antenna signals per ALN (1 false positive)

- **Real Part FD signals:** kNN, cityblock distance, k=2 (neighbours) and 16 PCA components; 97.1% accuracy, 99.5% sensitivity and 94.8% specificity when considering independent signals; 98.3% accuracy, 100% sensitivity and 96.7% specificity when grouping the antenna signals per ALN (1 false positive)

- **Imaginary Part FD signals:** kNN, cityblock distance, k=2 (neighbours) and 14 PCA components; 97.4% accuracy, 99.1% sensitivity and 95.7% specificity when considering independent signals; 98.3% accuracy, 100% sensitivity and 96.7% specificity when grouping the antenna signals per ALN (1 false positive)

- **TD signals:** kNN, euclidean distance, k=2 (neighbours) and 17 PCA components;

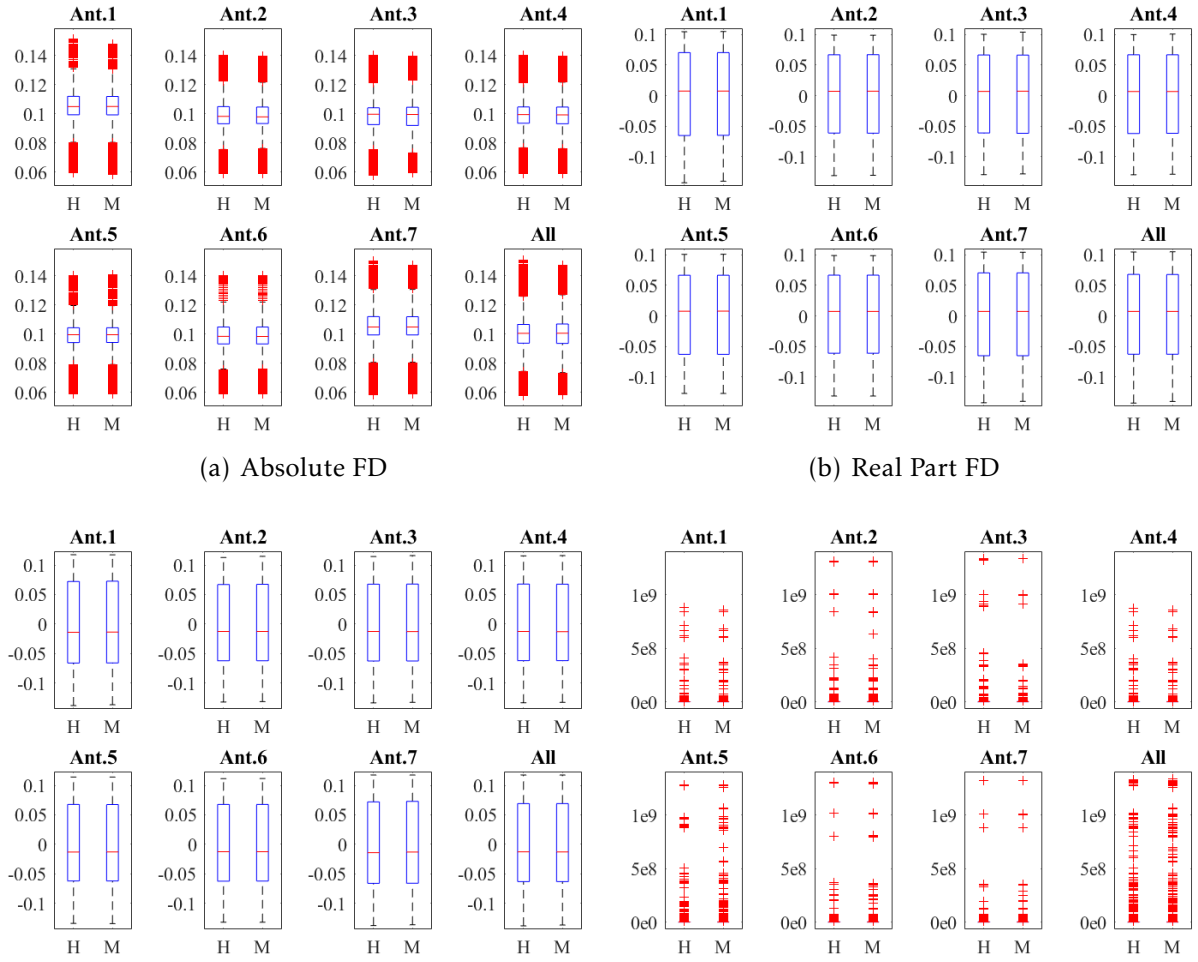

(a) Absolute FD (b) Real Part FD

(c) Imaginary Part FD (d) TD

Figure 6.11: Box plots of magnitude distribution of each type of signals over each class (H: Healthy and M: Metastasised) in scenario B and for the antenna positions. The red line represents the median, the boxes represent the first and third quartile of the distribution, and the red crosses represent the outliers of the distribution

96.0% accuracy, 97.1% sensitivity and 94.8% specificity when considering independent signals; 98.3% accuracy, 100% sensitivity and 96.7% specificity when grouping the antenna signals per ALN (1 false positive)

The optimal combination of hyperparameters in scenario B is similar to the one observed in scenario A (low number of neighbours and high number of PCA components yield better results). Contrarily to what was expected due to the high air-dielectric interface response, the accuracy results of the independent signals are better when compared to scenario A. Similarly to scenario A, the healthy ALN 11 is the only misclassified ALN when grouping the antenna signals per ALN independently of the type of signal used. The presented results show the air-dielectric interface response does not hamper the classification results.

6.3.3 Single Axillary Lymph Node in a Pseudo-realistic Axillary Phantom (scenario C)

This section shows the results with the simulated signals obtained with a more complex axillary region phantom, and antenna positions and ALNs in four different planes. It comprises 7 angular antenna positions in each plane, i.e. 28 antenna positions per ALN, and 60 simulated ALNs, which results in a total of 1680 observations to be classified.

Table 6.7: Accuracy (%) of classification models considering independent signals of scenario B after optimising classifiers hyperparameters. The PCA-X rows show the best results between 1 and 20 principal components. N/A means the classifier was not able to converge.

Type of signals	FEM	LDA	QDA	kNN	NB	DT	RFO	SVM
Absolute FD	RAW	63.8	57.9	96.9	64.5	85.7	94.3	89.3
	F25	N/A	N/A	93.1	65.7	85.7	89.8	83.1
	PCA-X	71.4	80.7	**97.1**	72.4	87.1	94.0	87.6
Real Part FD	RAW	65.9	60.5	**97.1**	68.6	88.3	93.8	89.1
	F25	N/A	N/A	94.3	66.2	88.3	91.7	85.0
	PCA-X	73.1	80.9	**97.1**	71.7	88.3	94.0	88.3
Imag. Part FD	RAW	64.8	55.7	**97.4**	66.9	88.8	94.5	89.3
	F25	N/A	N/A	96.2	66.9	86.7	90.2	84.1
	PCA-X	68.1	81.7	**97.4**	71.4	86.7	93.8	89.5
TD	RAW	65.2	55.5	95.2	59.3	88.3	88.8	85.0
	F25	N/A	N/A	88.8	51.7	84.0	86.9	84.1
	PCA-X	68.1	76.2	**96.0**	73.8	88.3	91.4	87.4

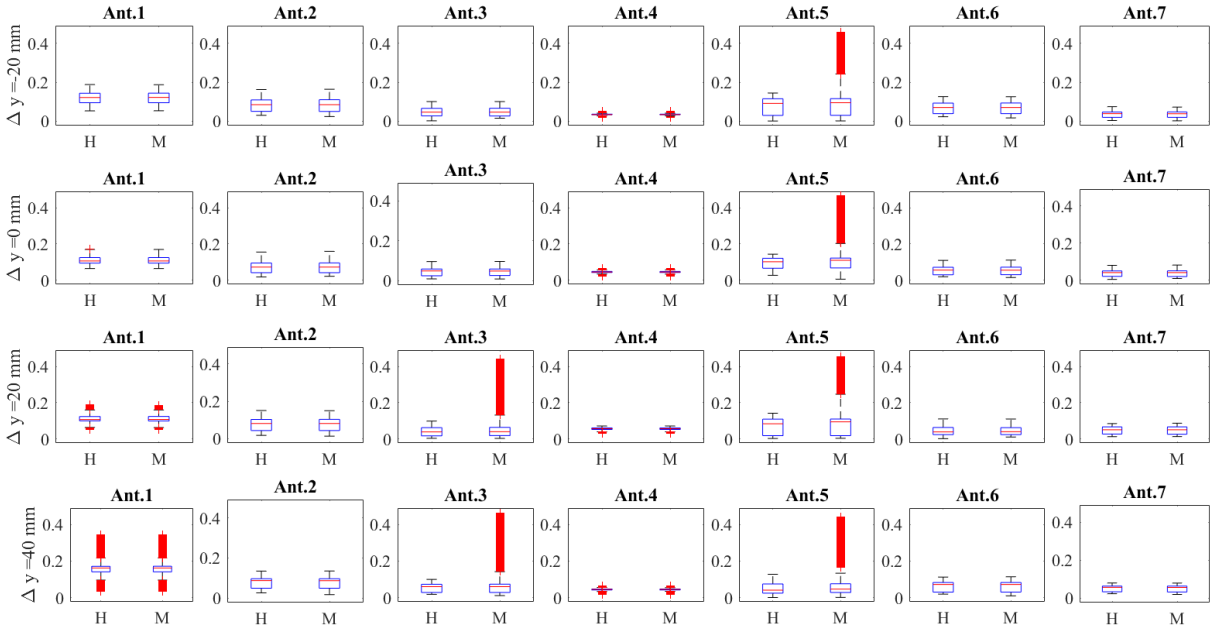

Figure 6.12: Box plots of magnitude distribution of absolute FD signals over each class (H: Healthy and M: Metastasised) in scenario C, for each antenna position and each plane. The red line represents the median, the boxes represent the first and third quartile of the distribution, and the red crosses represent the outliers of the distribution

Figure 6.12 presents the box plots of the distribution of the absolute FD signals samples used for classification before applying any FEM over each class (healthy and metastasised). These box plots are shown for each antenna position in each plane (each row of Figure 6.12). There are variable magnitude values across the same antenna position in different planes. The differences of magnitude values may result from the fact that the antenna is placed at different distances from the phantom surface at each of the four planes, as shown in Table 6.3. Similarly to the previous scenarios, different antenna positions also have distinct ranges of magnitude responses. Furthermore, the box plots of antenna positions 3 and 5 in some planes show some outliers in magnitude of signals from metastasised ALNs. Despite that, the differences between healthy and metastasised ALNs are not substantial in most antenna positions.

Table 6.8 shows the accuracy results of scenario C for each classifier after optimising the hyperparameters. kNN yields higher accuracy results when compared to other classifiers independently of the type of signals or the FEM. The maximum accuracy values are comparable to scenario B.

The different classifier hyperparameters, X number of PCA components and accuracy values which provide the optimal models are as follows:

- **Absolute FD signals:** kNN, cityblock distance, k=2 (neighbours) and 18 PCA components; 96.0% accuracy, 97.6% sensitivity and 94.3% specificity when considering independent signals; 98.3% accuracy, 100% sensitivity and 96.7% specificity when grouping the antenna signals per ALN (1 false positive)

- **Real Part FD signals:** kNN, cityblock distance, k=2 (neighbours) and 20 PCA

Table 6.8: Accuracy (%) of classification models considering independent signals of scenario C after optimising classifiers hyperparameters. The PCA-X rows show the best results between 1 and 20 principal components. N/A means the classifier was not able to converge.

Type of signals	FEM	LDA	QDA	kNN	NB	DT	RFO	SVM
Absolute FD	RAW	58.3	50.2	95.5	50.2	82.9	91.5	91.0
	F25	N/A	N/A	88.5	45.3	81.0	87.9	81.0
	PCA-X	56.3	57.2	**96.0**	61.4	85.4	92.7	91.6
Real Part FD	RAW	61.8	49.6	95.3	49.6	82.6	91.1	90.0
	F25	44.6	44.6	82.6	49.9	83.2	88.7	77.3
	PCA-X	61.1	56.8	**96.4**	63.8	83.8	91.8	92.5
Imag. Part FD	RAW	60.4	50.0	95.5	50.0	83.7	92.3	90.5
	F25	49.6	50.1	93.0	50.0	84.3	89.3	86.3
	PCA-X	61.5	59.2	**96.7**	60.2	85.7	93.0	95.0
TD	RAW	55.6	50.5	95.0	50.5	85.7	87.5	90.5
	F25	N/A	N/A	90.3	51.8	82.7	86.8	84.9
	PCA-X	45.2	60.7	**95.6**	64.7	85.1	92.1	91.9

components; 96.4% accuracy, 98.2% sensitivity and 94.6% specificity when considering independent signals; 98.3% accuracy, 100% sensitivity and 96.7% specificity when grouping the antenna signals per ALN (1 false positive)

- **Imaginary Part FD signals:** kNN, cityblock distance, k=2 (neighbours) and 20 PCA components; 96.7% accuracy, 98.4% sensitivity and 95.0% specificity when considering independent signals; 98.3% accuracy, 100% sensitivity and 96.7% specificity when grouping the antenna signals per ALN (1 false positive)

- **TD signals:** kNN, euclidean distance, k=2 (neighbours) and 20 PCA components; 95.6% accuracy, 97.1% sensitivity and 94.1% specificity when considering independent signals; 98.3% accuracy, 100% sensitivity and 96.7% specificity when grouping the antenna signals per ALN (1 false positive)

The only misclassified ALN was the healthy ALN 11. These results indicate that the complexity of scenario C does not substantially affect the microwave signals and, ultimately, the classification performance. However, these performance results may be influenced by the fact that signals from the same plane are present in both training and testing set. This means the training set may have information of the reflections at the air-dielectric surface, and, as a result, the overall classification is slightly compromised. Alternatively, the model could be trained with signals acquired in three planes and

tested with the remaining plane. However, this procedure would require a different implementation of the cross-validation step.

6.3.4 Multiple Axillary Lymph Nodes in a pseudo-realistic axillary phantom (scenario D)

This section shows the results with the simulated signals obtained with the pseudo-realistic axillary region phantom with 2 ALNs. The antenna positions and ALNs are placed in four different planes. Seven angular antenna positions are considered in each plane, i.e. 28 antenna positions per ALN, and 30 simulated groups of ALNs. Three different models are created to perform the analysis with this dataset: 1) healthy axillary regions are compared to axillary regions with metastasised ALNs (H-M), independently of the number of healthy or metastasised ALNs, which means the dataset is unbalanced; 2) healthy axillary regions are compared to axillary regions with only one metastasised ALN (H-M1); 3) healthy axillary regions are compared to axillary regions with only metastasised ALNs (H-M2). A total of 840 observations are classified in model H-M, while 560 observations are classified in models H-M1 and H-M2. For conciseness and because using PCA has outperformed the other FEMs in previous results, only the results with PCA-X are presented.

Table 6.9 shows the accuracy results of scenario D for each classifier with optimised hyperparameters. The results show that when more than one ALN is included in the axillary region, the classification between healthy and diseased axillary regions is more challenging. The accuracy values decrease almost 20% when compared to scenario C. Besides the increase of complexity in the phantom, the lower number of observations used for training when compared to the scenarios A, B and C can also have an influence in the results.

For the H-M model, the best accuracy results are obtained with RFO or SVM, outperforming kNN. As H-M model is created with an unbalanced dataset, MCC is calculated. The optimal models are as follows:

- **Absolute FD signals:** SVM, linear kernel, $\gamma = 2^{-16}$, $C = 2^{-1}$, and 3 PCA components; 77.6% accuracy, 82.5% sensitivity, 67.9% specificity and 0.50 of MCC when considering independent signals; 73.3% accuracy, 75.0% sensitivity, 70.0% specificity and 0.43 of MCC when grouping the antenna signals per ALN (5 false negatives and 3 false positives)

- **Real Part FD signals:** RFO, 200 trees, error as prune criterion, Gini as split criterion, and 20 PCA components; 78.4% accuracy, 93.0% sensitivity, 49.3% specificity and 0.49 of MCC when considering independent signals; 83.3% accuracy, 100% sensitivity, 50.0% specificity and 0.63 of MCC when grouping the antenna signals per ALN (5 false positives)

- **Imaginary Part FD signals:** RFO, 50 trees, impurity as prune criterion, Twoing as split criterion, and 20 PCA components; 79.2% accuracy, 92.7% sensitivity, 52.1% specificity and 0.51 of MCC when considering independent signals; 86.7% accuracy, 100% sensitivity, 60.0% specificity and 0.71 of MCC when grouping the antenna signals per ALN (4 false positives)

- **TD signals:** RFO, SVM, RBF kernel, $\gamma = 2^{-1}$, $C = 2^{4}$, and 15 PCA components; 82.3% accuracy, 94.6% sensitivity, 57.5% specificity and 0.59 of MCC when considering independent signals; 83.3% accuracy, 100% sensitivity, 50.0% specificity and 0.63 of MCC when grouping the antenna signals per ALN (5 false positives)

Although the model with TD signals provides a higher accuracy value when considering the independent signals, the performance of the classification when grouping the signals is better when using the imaginary part of FD signals. MCC is lower than 0.71 in all cases. A high number of false positives is observed, which means the model tends to classify the data into the most frequent class in the training set. No pattern is observed between the positions or sizes of the considered ALNs in the misclassified cases.

As the dataset is balanced for the H-M1 models, accuracy is a good metric but MCC is also presented for comparison with H-M models. The H-M1 models present the worse accuracy values but they have similar MCC results to H-M. The classifiers

Table 6.9: Accuracy (%) of classification models considering independent signals of scenario D after optimising classifiers hyperparameters when using PCA-X as FEM. N/A means the classifier was not able to converge.

Comparison	Type of signals	LDA	QDA	kNN	NB	DT	RFO	SVM
H-M	Absolute FD	66.9	54.6	73.8	66.8	66.6	76.6	**77.6**
	Real Part FD	66.7	53.7	74.2	66.7	66.8	**78.4**	77.7
	Imag. Part FD	70.8	54.8	74.6	66.7	69.4	**79.2**	78.0
	TD	66.7	61.1	78.3	68.0	72.9	81.7	**82.3**
H-M1	Absolute FD	54.5	64.8	66.4	64.6	61.4	69.1	**71.8**
	Real Part FD	49.8	63.0	67.0	62.7	59.5	72.5	**73.4**
	Imag. Part FD	51.3	64.8	68.2	62.1	65.5	73.2	**77.5**
	TD	32.5	68.0	72.9	65.7	68.6	**76.6**	74.3
H-M2	Absolute FD	52.5	64.1	71.6	66.3	61.3	68.2	**72.7**
	Real Part FD	50.4	61.4	**78.6**	61.3	64.3	72.1	71.8
	Imag. Part FD	53.4	61.6	**77.5**	62.3	67.1	74.6	71.8
	TD	49.1	66.8	**77.0**	65.0	67.5	**77.0**	75.4

obtaining best results are also RFO or SVM. The optimal models are as follows:

- **Absolute FD signals:** SVM, linear kernel, $\gamma = 2^{-16}$, $C = 2^{-16}$, and 4 PCA components; 71.8% accuracy, 47.5% sensitivity, 96.1% specificity and 0.50 of MCC when considering independent signals; 75.0% accuracy, 50.0% sensitivity, 100% specificity and 0.58 of MCC when grouping the antenna signals per ALN (5 false negatives)

- **Real Part FD signals:** SVM, RBF kernel, $\gamma = 2^{4}$, $C = 2^{14}$, and 20 PCA components; 73.4% accuracy, 67.5% sensitivity, 79.3% specificity and 0.47 of MCC when considering independent signals; 80.0% accuracy, 70.0% sensitivity, 90.0% specificity and 0.61 of MCC when grouping the antenna signals per ALN (1 false positive and 3 false negatives)

- **Imaginary Part FD signals:** SVM, polynomial kernel, $\gamma = 2^{-1}$, $C = 2^{14}$, and 2 PCA components; 77.5% accuracy, 84.6% sensitivity, 70.4% specificity and 0.56 of MCC when considering independent signals; 80.0% accuracy, 90.0% sensitivity, 70.0% specificity and 0.61 of MCC when grouping the antenna signals per ALN (3 false positives and 1 false negative)

- **TD signals:** RFO, 225 trees, error as prune criterion, Gini as split criterion, and 19 PCA components; 76.6% accuracy, 84.6% sensitivity, 68.6% specificity and 0.54 of MCC when considering independent signals; 85.0% accuracy, 90.0% sensitivity, 80.0% specificity and 0.70 of MCC when grouping the antenna signals per ALN (2 false positives and 1 false negative)

Contrarily to what was observed in scenarios A to C, different combinations of type of signals, classifiers and corresponding hyperparameters values resulted in different performances both when analysing each antenna signal independently and when grouping the antenna signals. The most common false positive is one case where the ALNs are placed in positions 1 and 2, 25 mm away from each other, and one ALN is larger than the other. The most common false negative consists of one case where the ALNs are also placed in positions 1 and 2, and the longest-axis of the healthy ALN is larger than the metastasised ALN.

As expected, the best accuracy results are obtained in H-M2 models as the axillary regions exclusively have only one type of ALNs. In this case, kNN, SVM and RFO provide the best results. The optimal models are defined as follows:

- **Absolute FD signals:** SVM, linear kernel, $\gamma = 2^{-11}$, $C = 2^{-6}$, and 4 PCA components; 72.7% accuracy, 71.4% sensitivity, 73.9% specificity and 0.45 of MCC when considering independent signals; 70.0% accuracy, 70.0% sensitivity, 70.0% specificity and 0.40 of MCC when grouping the antenna signals per ALN (3 false positives and 3 false negatives)

- **Real Part FD signals:** kNN, cityblock distance, k=1 (neighbours), and 20 PCA components; 78.6% accuracy, 77.1% sensitivity, 80.0% specificity and 0.57 of MCC when considering independent signals; 95.0% accuracy, 100% sensitivity, 90.0% specificity and 0.90 of MCC when grouping the antenna signals per ALN (1 false positive)

- **Imaginary Part FD signals:** kNN, euclidean distance, k=1 (neighbours), and 20 PCA components; 77.5% accuracy, 71.4% sensitivity, 83.6% specificity and 0.55 of MCC when considering independent signals; 95.0% accuracy, 90.0% sensitivity, 100% specificity and 0.90 of MCC when grouping the antenna signals per ALN (1 false negative)

- **TD signals:** kNN, euclidean distance, k=1 (neighbours), and 19 PCA components; 77.0% accuracy, 71.8% sensitivity, 82.1% specificity and 0.55 of MCC when considering independent signals; 95.0% accuracy, 90.0% sensitivity, 100% specificity and 0.90 of MCC when grouping the antenna signals per ALN (1 false negative)

In the three last models, only one axillary region is misclassified. The accuracy results, as well as the misclassified cases, vary depending on the type of signals used. In general, the absolute FD signals yield the worse classification results. There is also no pattern observed among the misclassified cases. These results show that, when multiple ALNs are inside the axillary region, more factors affect the classification of the axillary region (healthy or diseased).

The results are encouraging but more realistic scenarios should be tested to evaluate the feasibility of using this type of models to give more objective information in a clinical scenario. This methodology is limited to infer the presence or the absence of metastasised ALNs but no information is provided regarding which ALN may be affected. Reconstructed images should be able to indicate that type of information. Thus, reconstructed images and ML models would be complementing each other in order to provide useful information to clinicians regarding the diagnosis of ALNs. The next steps to assess the classification of ALNs should include the consideration of muscles inside the model. In future work, anthropomorphic phantoms of the axillary region of different dimensions should also be considered, as well as placing the ALNs at different depths and considering realistic models of ALNs with their dielectric properties. Ultimately, the combination of imaging results with ML classification should be evaluated, by identifying in which scenarios they complement each other.

6.4 Chapter Conclusions

This chapter presented the first study of classification of healthy and metastasised ALNs of different sizes and shapes using microwave signals, which were acquired in

simulation. Sixty ALNs models were created and used in four different scenarios with increasing complexity. The scenarios comprised a scenario where single ALNs and the antennas were placed in the same medium, a scenario with single ALNs inside a cylindrical dielectric phantom and antennas placed in air, a scenario with single ALNs inside a more realistic phantom of the axillary region and antennas placed in air, and a scenario with multiple ALNs inside the same pseudo-realistic phantom and antennas placed in air. Several combinations of types of signals, FEMs and classifiers were considered. The results were analysed considering the signals recorded by each antenna individually and grouping the results of all antennas per ALN.

The maximum accuracy values ranged from 94.5% to 97.4% when considering only one single ALN per simulation, obtained with kNN and PCA, when considering each antenna individually. When grouping the antenna signals per ALN, the accuracy values were as high as 98.3% with kNN for several scenarios and combination of parameters. PCA often outperforms the use of RAW or F25 features. No substantial difference of classification was observed when considering different types of signals. The classification of axillary region phantoms with multiple ALNs posed new challenges. The accuracy values ranged from 71.8% to 82.3% when considering each antenna individually and performances varied with the type of signals and classifiers used. When comparing axillary regions with only healthy ALNs and axillary regions with only metastasised ALNs (when grouping the antennas per axilla) only one observation was misclassified. PCA, together with kNN, SVM or RFO, yield the best results.

The results show there is potential to use models created with ML algorithms to aid the assessment of presence of metastasised ALNs inside the axillary region and complement imaging results. More tests should be performed in order to consider more realistic scenarios, such as different axillary region phantoms with muscle, and perform experimental tests.

7 Dielectric Lens in Breast Microwave Imaging

In this chapter, Microwave Imaging (MWI) is applied to breast cancer detection. There are several approaches in the literature to address this problem using MWI prototypes, from monostatic to multistatic systems and with different antenna configurations. This chapter presents a feasibility study of a new approach using an air-operated MWI system. The proposed setup comprises the use of a shaped-beam dielectric lens assembled with a feed to focus the energy in specific parts of the body, thus reducing the artefacts caused by undesired body structures. In multistatic air-operated systems, since the antennas are operating in air, the measured signals from antennas close to each other may suffer from antenna coupling effects and affect the quality of imaging results. Focusing the energy in the breast with a Bessel beam should minimise antenna coupling effects and maximise the signal reflected by the breast tissues and, consequently, improve the detection of targets in the reconstructed images.

This approach of using a Bessel lens to focus the energy is different from the state-of-the-art antennas used for MWI. Authors in [223], [224] have used dielectric lenses incorporated in the antenna to increase the directivity of the antennas immersed in a coupling medium for MWI. However, these type of lenses are not suitable for air-operated systems as the size of the lens increases for low permittivity media. In other research areas, Wang *et al.* [225] used a flat left-handed metamaterial lens (i.e. has negative permittivity and permeability) to study the focusing properties in microwave detection and imaging of targets in free space. Later, the proposed lens was used for breast cancer hyperthermia [226]. Akhter *et al.* [227] presented a Vivaldi antenna and a hemispheric dielectric lens in a monostatic setup to improve the detection of metallic targets, which could be applied to illegal imports detection. In contrast to these studies, the Bessel lens proposed in this thesis has the advantage of creating a beam with constant width along the axis, which allows a stable focusing region across the different media and target detection in the near-field. Additionally, to the best of my knowledge, applying lenses in air-operated MWI systems for medical applications has never been attempted before.

The impact in image reconstruction when using a lens is evaluated with different

approaches. Firstly, a monostatic and a multistatic approach are investigated when applied to simplified phantoms, via simulations created and run in Computer Simulation Technology (CST) Studio Suite® software [189]. Secondly, a detailed evaluation with an anthropomorphic phantom using the multistatic approach is performed, comprising the implementation of realistic artefact removal algorithms with two breast tumours mimicking models. The ability of selecting different targets with one radiating antenna is evaluated. Then, the safety of a system using a dielectric lens is assessed in terms of electromagnetic exposure. Finally, the experimental evaluation of the proposed multistatic system with a lens is presented using both homogeneous and heterogeneous anthropomorphic breast phantoms.

7.1 Focal System

The considered focal system includes a feed placed behind a lens in its focus, which radiates through the lens, which in turn will focus the energy into the body. The considered feed is the Crossed Exponential Tapered Slot Antenna (XETS), the antenna already presented in Section 3.2 [190], [191] (Figure 3.2). The antenna is impedance matched from 2 to 6 GHz and this study was carried in that frequency band.

A Gaussian or a Bessel lenses could be considered for the setup. The main difference between them is that Gaussian lenses focus the energy in a small region defined by a beam waist along the lens axis, while Bessel lenses focus the energy in an elongated region along the lens axis. This work considered the Bessel lens, which is represented in Figure 7.1, because its beam is more stable across the tissues. The lens can be designed with a dielectric material such as Polylactic Acid (PLA) or Polypropylene (PP). Either material allows to create a lens with a focus beam and its dimensions can be adapted according to the adopted material. The lens is designed using Geometric Optics to have a continuous focus along the axis and a focal point (where the feed is placed) of 180 mm, following the methodology in [106], [228].

The initial tests in simulation were performed with PLA material, which has real permittivity of $\epsilon_r = 2.9$ and a dissipation factor $\tan(\delta) = 0.013$. The PLA lens used in simulations has a radius of 126.85 mm and a thickness of 95.3 mm. For experimental purposes, the lens could be fabricated either by 3D-printing or using a Computer Numerical Controlled (CNC) machine. For technical reasons, the better choice was to fabricate the lens in PP using CNC. The PP lens has real permittivity of $\epsilon_r = 2.3$ and a dissipation factor $\tan(\delta) = 0.001$. It has a radius of 121.8 mm and a thickness of 118.1 mm. Both lenses were designed by my supervisor Carlos Fernandes [228].

Figure 7.2 shows the maps of the electric fields in the near-field produced by the XETS at 2, 4, and 6 GHz in free-space. XETS has a main lobe in the Z direction, radiating more energy at the central frequency (4 GHz). In contrast, Figure 7.3 shows the electric

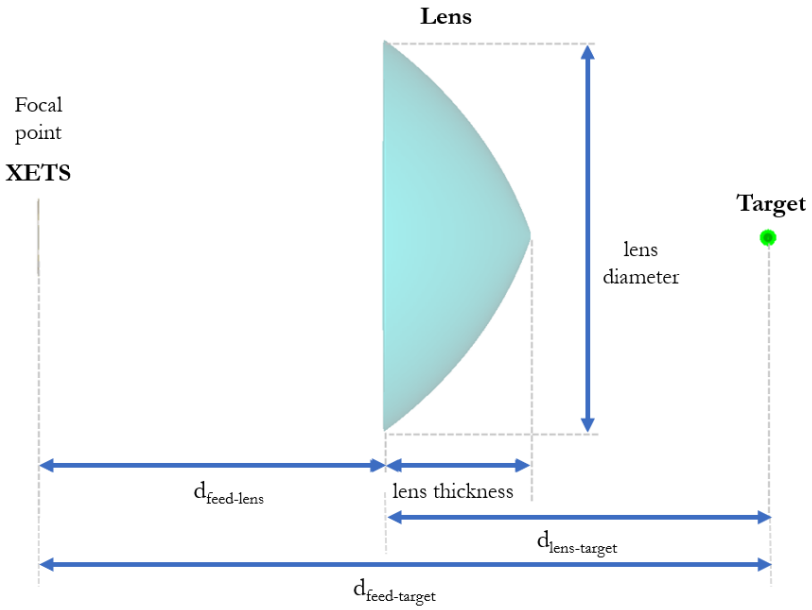

Figure 7.1: Schematic with Bessel lens dimensions and focus distances.

fields with both XETS and the PLA lens where the distance between the feed and the lens ($d_{feed-lens}$) is 110 mm. The lens allows to redirect the energy into a narrower beam. The beam width is larger for lower frequencies than for higher frequencies (approximately 150 mm compared to approximately 100 mm), and it depends on the wavelength and the lens dimensions. The waves generated by the XETS alone or the combination of XETS+Lens are different, as shown in the phase maps of Figure 7.4. The XETS generates spherical waves, i.e. radial from the antenna source point, while the waves generated by the XETS+Lens are plane waves, i.e. perpendicular to the xy-plane. This can be a limitation in cross-range resolution when attempting to detect targets in the same xy-plane.

7.2 Numerical Evaluation in Simulation

This section presents the numerical evaluations performed with the dielectric lens and the comparison with an equivalent setup without lens (i.e. XETS as a stand-alone antenna). Firstly, the focal distances of the Bessel lens are optimised. Then, preliminary tests with a monostatic configuration are presented. Finally, a multistatic configuration is proposed and validated with breast phantoms.

7.2.1 Optimisation of Distances

The design of the lens for a certain focal point is based on Geometrical Optics, which uses the assumption that the size of the lens is much larger than the wavelength. As it is not true in this application, the first tests consisted of finding the optimal focal distances for the PLA lens, i.e., the optimal distance between the feed and the lens

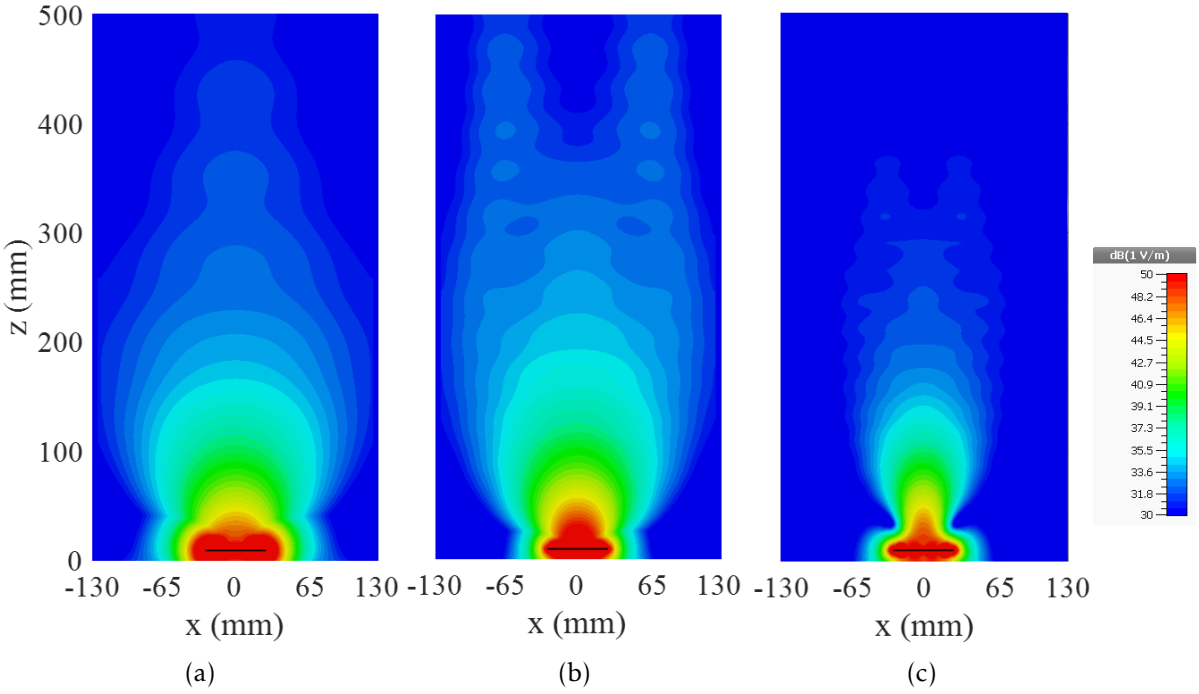

Figure 7.2: Representation of the electric field in the near-field of the XETS at (a) 2 GHz, (b) 4 GHz, and (c) 6 GHz. The selected plane is at $y = 0$ and the magnitude of the absolute value of the electric field is represented with a scale from 30 to 50 dB.

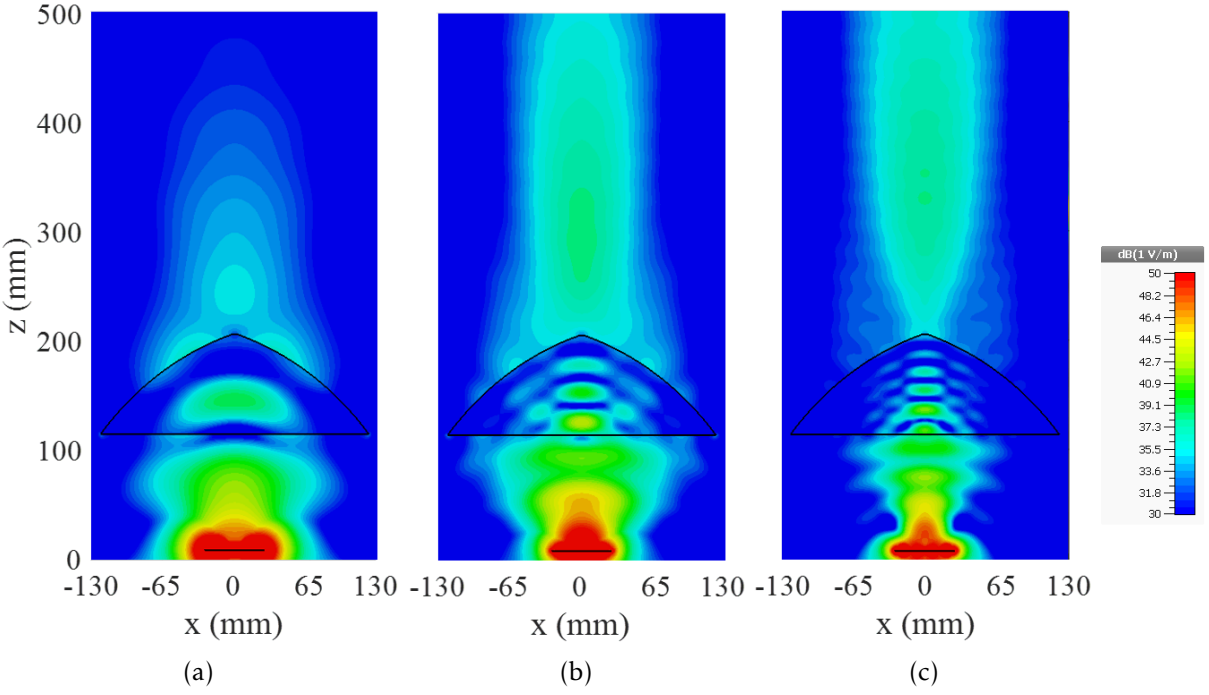

Figure 7.3: Representation of the electric field in the near-field of the XETS and the Bessel lens at (a) 2 GHz, (b) 4 GHz, and (c) 6 GHz. The selected plane is at $y = 0$ and the magnitude of the absolute value of the electric field is represented with a scale from 30 to 50 dB.

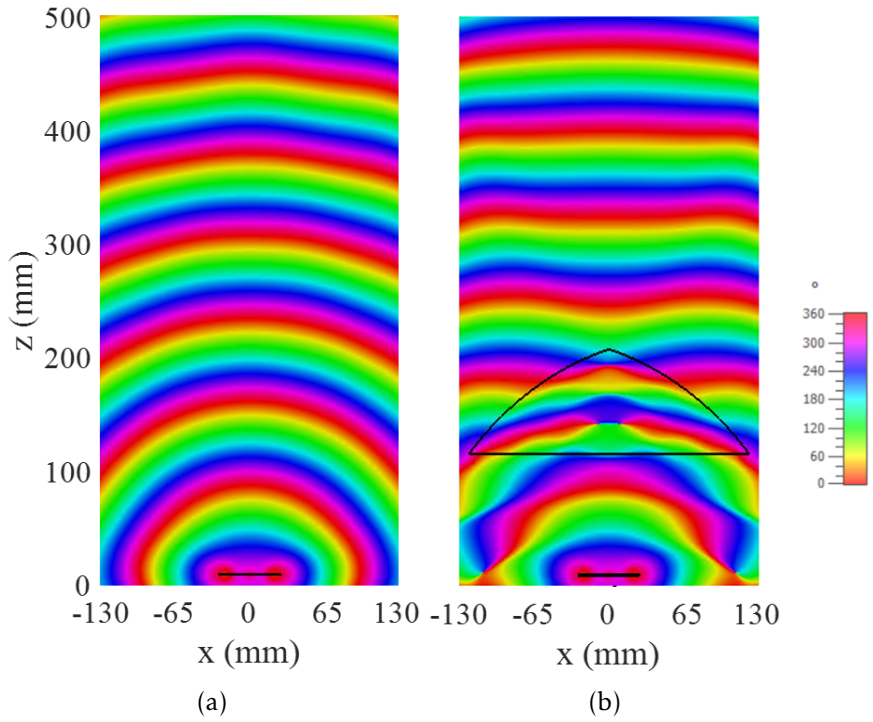

Figure 7.4: Representation of the phase in the near-field with (a) a XETS as a stand-alone antenna and (b) a XETS and the Bessel lens at 4 GHz. (a) shows the XETS radiating radially, the waves are spherical and becoming planar at farther distances. (b) shows the waves becoming planar after the Bessel lens.

($d_{feed-lens}$), and between the feed and the target ($d_{feed-target}$), in order to maximise the transmitted signal. Several combinations of distances were simulated, and the maximum of magnitude of the signal at $x = 0$ mm and the beam width were calculated. The beam width is defined as the width between the points where the magnitude of the beam drops to half of the maximum. One of the optimal combinations found was $d_{feed-lens} = 110$ mm and $d_{feed-target} = 305$ mm and those were the distances used in the setups represented in the following subsections. However, other combinations can also present satisfactory results. Figure 7.5 shows how the beam width and the maximum magnitude behaves while changing the distance of the target ($d_{feed-target}$) for a fixed distance between the feed and the lens ($d_{feed-lens}$). For the chosen distances, the beam width varies between 66 and 103 mm and the maximum between 34 and 38 dB in the three frequencies (2, 4, and 6 GHz). These distances ensure a narrow beam width in the region of interest with a satisfactory magnitude of the transmitted signal.

The electrical distance of the XETS+Lens was calculated using the same procedure used for the XETS as a stand-alone antenna, presented in Section 3.2.1, and is 96 mm.

7.2.2 Monostatic Configuration

In this section, the performance of a monostatic focal system with a XETS and a Bessel lens is evaluated. The XETS is placed in the xy-plane, with a discrete port at coordinates $(0, 0, 0)$ mm.

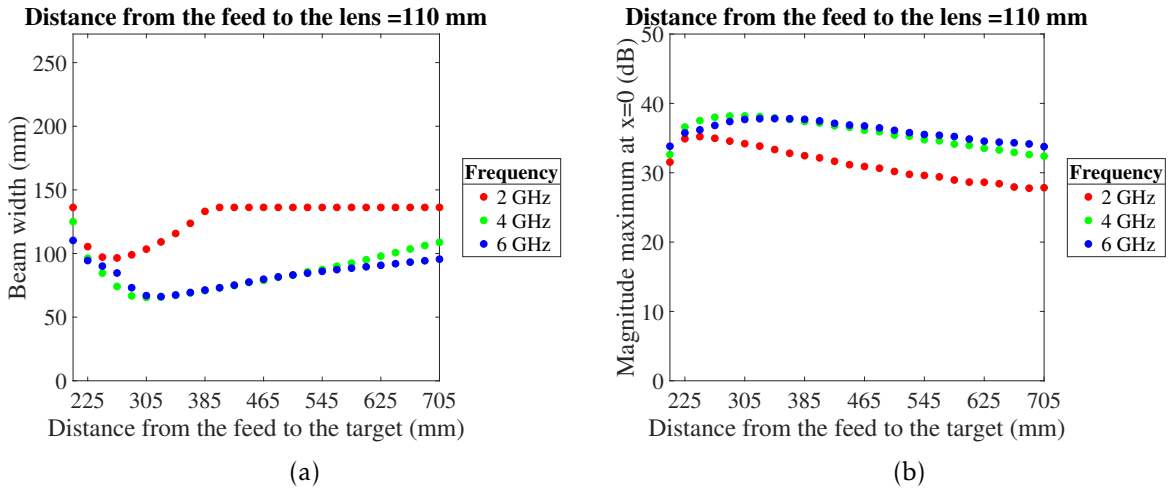

Figure 7.5: Variation of (a) beam width and (b) maximum magnitude obtained with the Bessel lens over the distance between the feed to the target ($d_{feed-target}$) for a fixed distance between the feed and the lens ($d_{feed-lens}$).

7.2.2.1 Signal Processing Algorithms

The analysed signals correspond to the input reflection coefficients $\mathbf{s}_{i,i}$ after applying an ideal artefact removal. This means $\mathbf{s}_{i,i}$ results from the difference between the simulated response from all components (i.e. antenna, phantom and targets) and the simulated response of the same setup without the considered targets.

The wave-migration algorithm is used to reconstruct the images (as presented in Section 2.2.3.1). Refraction effects are not considered in the image reconstruction algorithm since, as concluded in Chapter 3, refraction computation can be disregarded when phantoms have average low average permittivity values. The results are processed in a frequency band from 2 to 6 GHz.

7.2.2.2 Dielectric Parallelepiped Phantom and Target

A dielectric parallelepiped phantom, with a Perfect Electric Conductor (PEC) target inside, was placed in front of the assembly XETS+Lens (Figure 7.6) in order to evaluate the target detection with this assembly. The dielectric has 150 mm width, 150 mm length and 200 mm height, a relative permittivity $\epsilon_r = 4$, and dissipation factor $\tan(\delta) = 0.1$. The PEC target is also a parallelepiped (with 60 mm width, 10 mm length and 60 mm height). The distances between the feed, the lens and the target were the ones defined in the Section 7.1: $d_{feed-lens} = 110$ mm and $d_{feed-target} = 305$ mm.

Figure 7.7 shows the reconstructed images with this setup. The target is successfully detected, with the maximum intensity approximately at the location of the surface of the target. However, the shape is not well detected since only one antenna position is used to reconstruct the image.

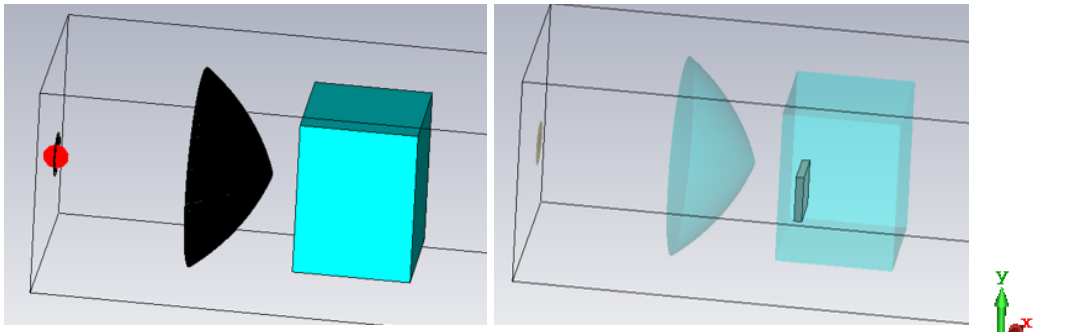

(a) (b)

Figure 7.6: Screenshots from CST simulation with a dielectric parallelepiped and a target in front of the XETS and Bessel lens.

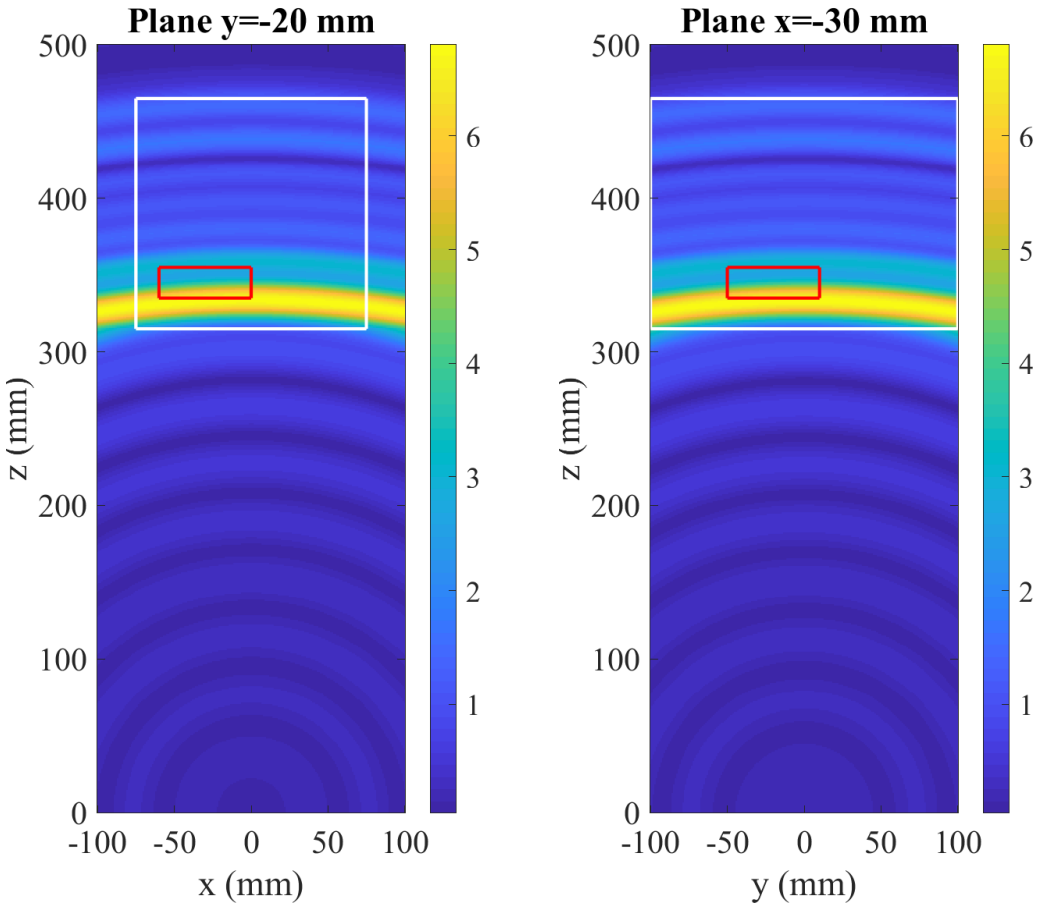

(a) (b)

Figure 7.7: Reconstructed images of a PEC target inside a dielectric parallelepiped using monostatic signals and the assembly XETS+Lens in (a) xz-plane and (b) yz-plane. The red contour represents the true location and shape of the target. The parallelepiped contour is represented in white.

7.2.2.3 Two Targets in Free-space

To test the resolution of the assembly XETS+Lens with a monostatic system, two targets were placed in free-space in front of a XETS at $z = 100$ mm and in front of the XETS+Lens at $z = 305$ mm (i.e. 100 mm from the tip of the lens) for comparison, as shown in Figure 7.8. The targets are two 10 mm radius PEC spheres separated by 20 mm in the x-axis. In both cases, XETS and the lens were shifted together in a range of $[-100, 100]$ mm in the x-axis, with a step of 10 mm, in a total of 21 positions.

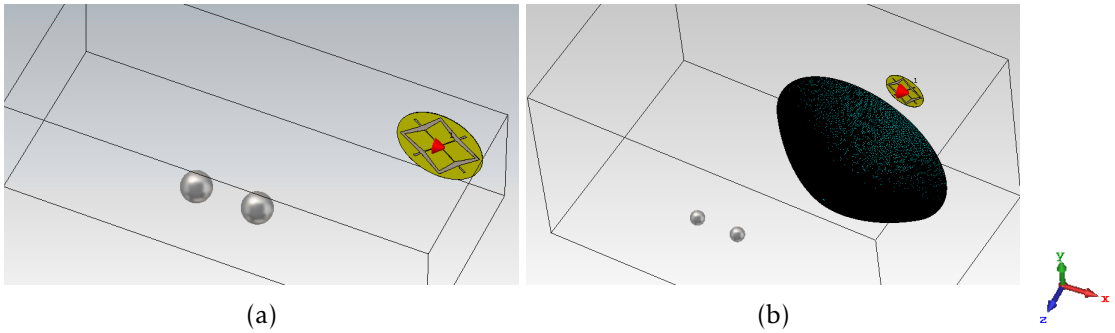

Figure 7.8: Screenshots from the CST simulation of resolution tests for a monostatic setup with (a) XETS and with (b) XETS and Bessel lens.

Figure 7.9 shows the reconstructed images of these two setups. The XETS, as a stand-alone antenna, has higher cross-range resolution than the XETS+Lens, which is expected due to the different shape of waves created by both antennas (Figure 7.4). When using the assembly XETS+Lens, the two targets are detected together, as a consequence of the plane waves in that region. The magnitude of the images is not comparable as the targets are placed at different distances from the feed, but the resolution of the assembly XETS+Lens would not improve significantly if the distance from the feed was reduced or increased. This result shows that a monostatic setup with the lens in a planar configuration is not a reasonable solution for target detection due to its low cross-range resolution. Nonetheless, using the assembly XETS+Lens in a multistatic setup may improve the resolution and the feasibility of a system with a dielectric lens.

7.2.3 Multistatic Configuration

In this section, a multistatic system with a dielectric lens is presented. This system is designed for a scenario in which the patient lies in the prone position, with the breast extending through an opening on the table (Figure 7.10). It is a bistatic configuration where a ring of antennas, or a single antenna rotating around the breast, is positioned in the z-plane. The lens with the respective feed is placed under the breast, using its pencil beam to focus the breast. This positioning allows to improve the resolution along the z-axis and it is the most feasible position in a real case due to the large size of the lens. The antenna (XETS+Lens) can be translated to change the location of its

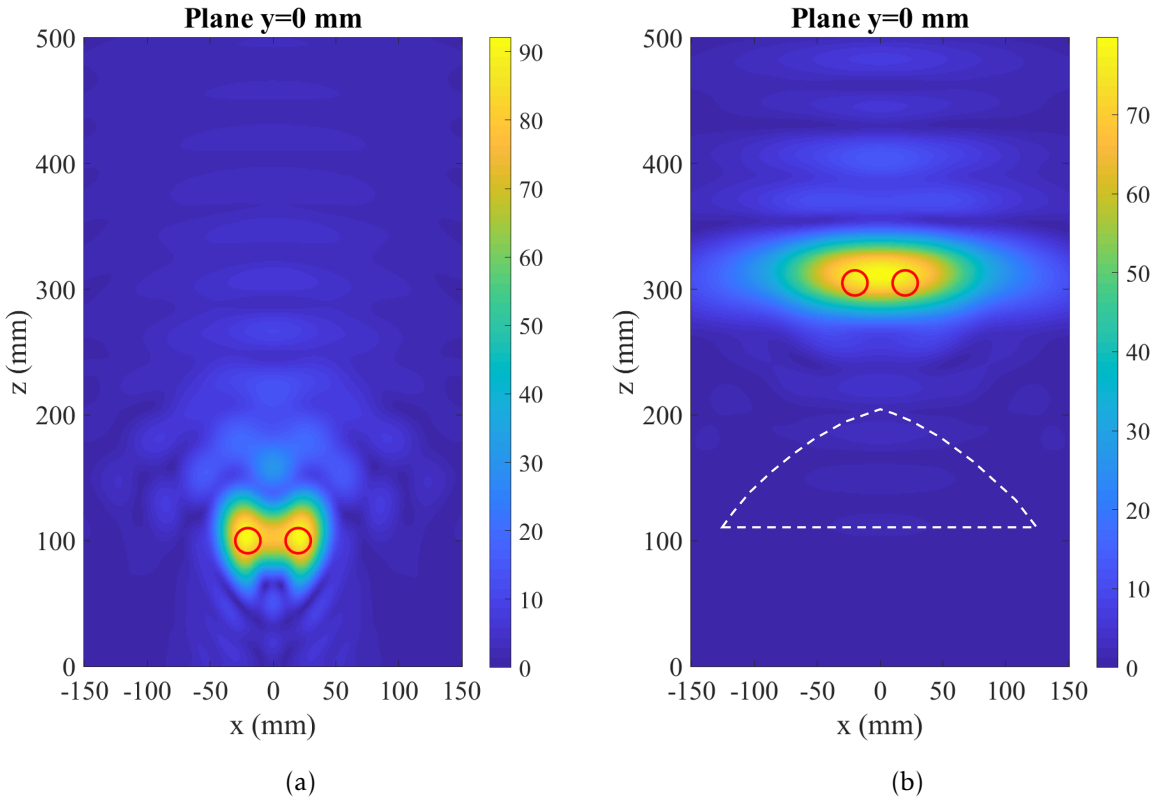

Figure 7.9: Reconstructed images of two PEC targets in free-space in the *xz*-plane using monostatic signals and (a) the XETS as stand-alone antenna, and (b) the assemble XETS+Lens. The red contours represent the true location and shape of the targets. The white dashed contour represents the lens contour.

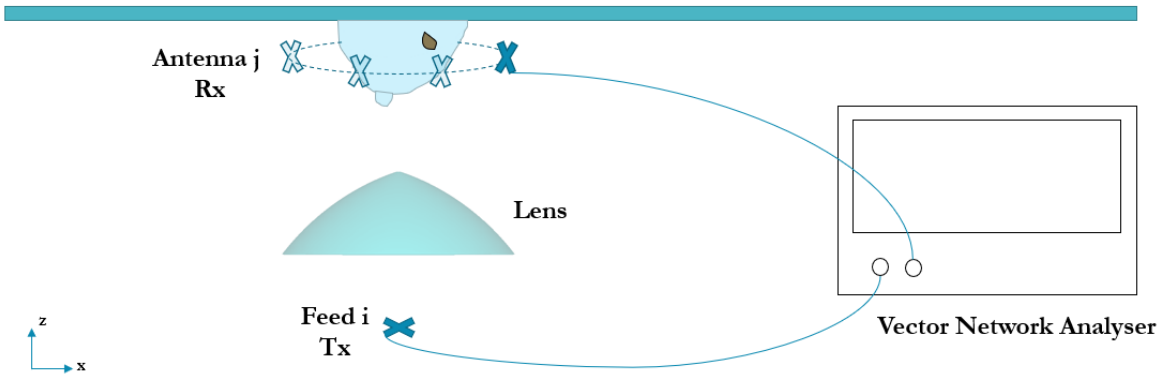

Figure 7.10: Schematic of the setup with the feed below the lens. Tx is the transmit antenna coupled with the lens and Rx is the receive antenna.

axis with respect to the breast, or, alternatively, the feed position can be slightly shifted off-axis to change the direction of the pencil beam and thus scan different parts of the breast.

In this type of setup, the analysed signals correspond to both reflection coefficients $\mathbf{s}_{i,j}$ when $i = j$, and transmission coefficients $\mathbf{s}_{i,j}$ when $i \neq j$. In both cases, i and j represent the number of the antenna position. In transmission coefficients, the transmit (Tx) antenna is always the feed below the lens and the receive (Rx) antenna represents

each antenna position around the breast.

In the following sections, the proposed setup comprises a single Rx antenna that rotates in twelve positions circularly distributed around a breast phantom with 30° step in the z-plane with an 80 mm radius. The distance between the dielectric surface of the breast and the Rx antenna in the z-plane is around 30 mm. In order to ensure polarisation match between each Tx and Rx antennas, the Tx antenna is synchronously rotated as the Rx antenna sweeps the breast phantom. Several phantoms, antennas and two different lenses were considered for simulations. For conciseness, only a subset of these tests, which were found to be the best choices, are presented.

Firstly, the tests are performed with a dielectric spherical phantom to evaluate the lens capability to focus on specific regions using an ideal artefact removal algorithm. Then, the performance of this multistatic system is evaluated in a realistic scenario, while considering a realistic breast phantom and a Singular Value Decomposition (SVD)-based artefact removal algorithm (see Section 2.2.3.3). Refraction effects are not considered in the image reconstruction algorithm following the conclusions of Chapter 3.

In both cases, the setup with the lens is compared to a setup without it, in order to evaluate whether increasing the distance between the antenna and the phantom affects the target detection. To do this comparison, the XETS as a stand-alone antenna is placed at a distance from the breast phantom equivalent to the distance considered in the setup XETS+Lens. This distance is found by calculating the point where the electric field intensity at the breast surface is the same in both cases. Finally, an exposure assessment is performed calculating the Specific Absorption Rate (SAR) for both setups with and without the lens, to evaluate the safety of this system.

7.2.3.1 Spherical Breast Phantom

A dielectric spherical phantom of 50 mm radius was considered for the first tests with the multistatic system. The phantom is homogeneous with relative permittivity $\epsilon_r = 8$ and dissipation factor $\tan(\delta) = 0.1$, which corresponds approximately to the upper limit of adipose tissue permittivity [126]. Two PEC targets were placed inside the sphere at $(x, y) = (\pm 30, 0)$ mm and at the same z plane (50 mm from the surface). The same setup with and without the lens is compared (Figure 7.11). The distance between the feed behind the lens and the surface of the sphere is 255 mm ($d_{feed-target} = 305$ mm), while the distance between the XETS (as stand-alone antenna) and the surface is 115 mm ($d_{feed-target} = 165$ mm). In both cases, both the XETS and the assembly XETS+Lens were placed in two positions $x = [0; 30]$ mm, in order to evaluate if this setup allows to select only one target and the differences between XETS and XETS+Lens.

Figure 7.12 shows the transmission signals $\mathbf{s}_{i,j}$ between the feed below the spherical breast phantom at $(x, y, z) = (0, 0, 0)$ mm and each of the antenna positions around

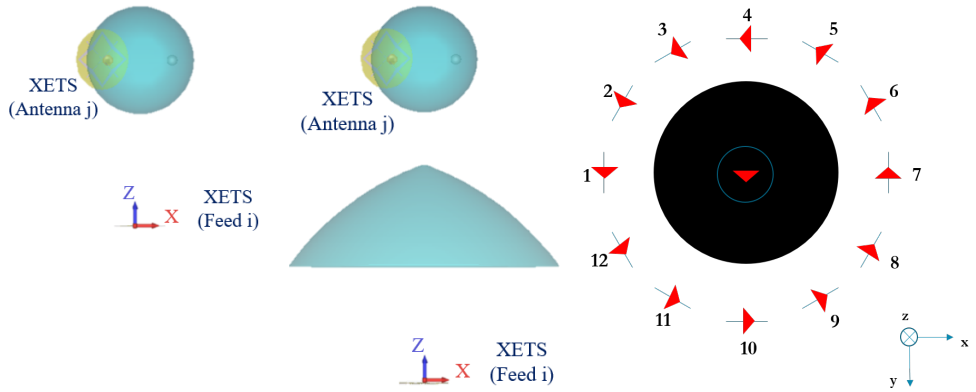

Figure 7.11: Screenshots from the CST simulation of a multistatic setup with a dielectric spherical phantom above (a) the XETS as a stand-alone antenna, and (b) XETS and Bessel lens. (c) shows the representation of antennas polarisation, where the antenna behind the lens is located at the centre of the image and its polarisation matches the 1st antenna position polarisation and rotates for the remaining positions.

the phantom. The signals correspond to the targets detection after applying an ideal

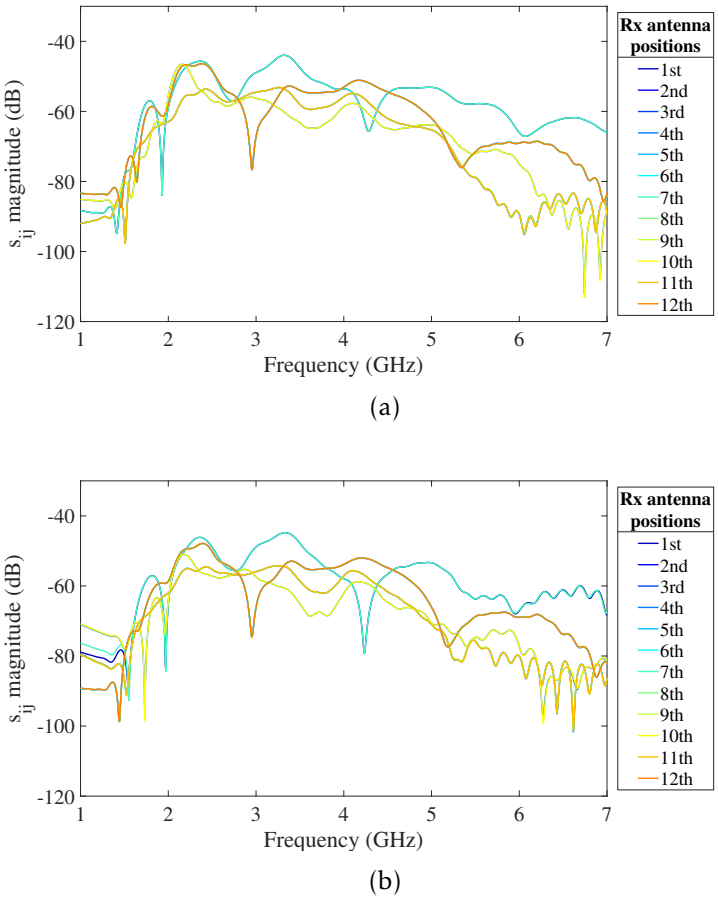

Figure 7.12: Transmission signals $\mathbf{s}_{i,j}$ of the setup (a) without and (b) with the lens. i is the feed behind the lens at $x = 0$ mm and j is each antenna position around the spherical phantom.

artefact removal algorithm, i.e. the signals correspond to the difference between the simulated response from all components and the simulated response of the same setup

without the targets. Figure 7.12(a,b) shows the signals in a setup without and with the lens, respectively. In both cases, some $\mathbf{s}_{i,j}$ signals overlap due to the setup symmetries. The level of targets response is similar to one another, below −40 dB, and all received signals are above −80 dB within the frequency band of interest (2 to 6 GHz). This means that 1) adding a lens and increasing the distance between the feed and the target does not substantially reduce the targets response, and 2) the targets response is above the noise level of our equipment which is −110 dBm [49].

Figure 7.13 shows the reconstructed images when both stand-alone XETS and XETS+Lens are located at $(x, y, z) = (0, 0, 0)$ mm. Both targets are successfully detected and there are no substantial differences in the setup with and without the lens. The intensity of the detection with XETS as a stand-alone antenna (43.7) is slightly higher than with XETS+Lens (33.7). This bistatic setup increases the resolution in the xz-plane, when compared to a case where only the monostatic signals collected by the XETS rotating around the sphere are used (Figure 7.14). The detection in the xy-plane is also closer to the true shape and size of the targets.

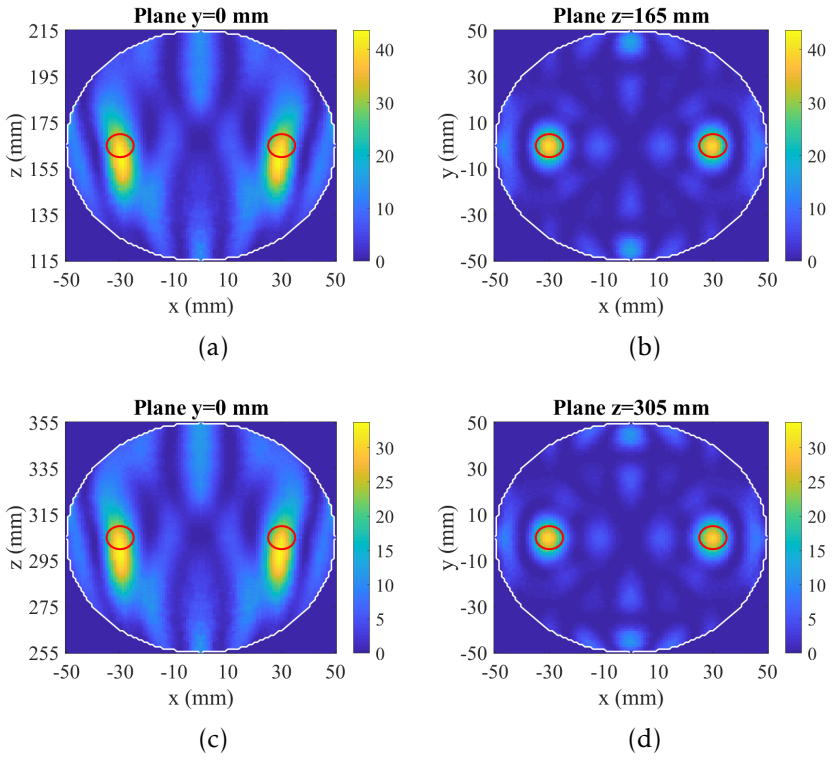

Figure 7.13: Reconstructed images of two PEC targets inside a dielectric sphere using multistatic signals, (a,b) XETS as a stand-alone antenna, and (c,d) XETS+Lens placed at $x = 0$ mm. The images on the left (a,c) and on the right (b,d) show the reconstructed images in the xz and the xy-planes, respectively. The red contours represent the true location and shape of the targets. The spherical breast contour is represented in white.

Figure 7.15 shows the reconstructed images when the position of the XETS and XETS+Lens is shifted to $(x, y, z) = (30, 0, 0)$ mm, centred with only one of the targets. In this case, only that target is detected. In the considered scenario, no significant changes are observed between the setups with and without the lens. These results are promising

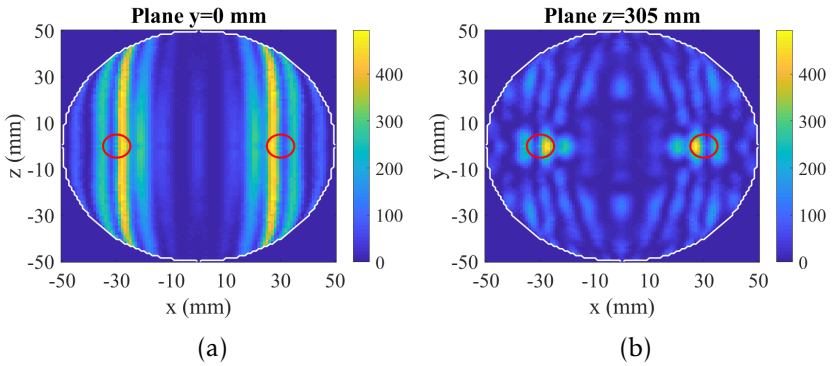

Figure 7.14: Reconstructed images of two PEC targets inside a dielectric sphere using monostatic signals recorded from the XETS around the phantom. The left and right images show the reconstructed images on the xz and the xy-planes, respectively. The red contours represent the true location and shape of the targets. The spherical breast contour is represented in white.

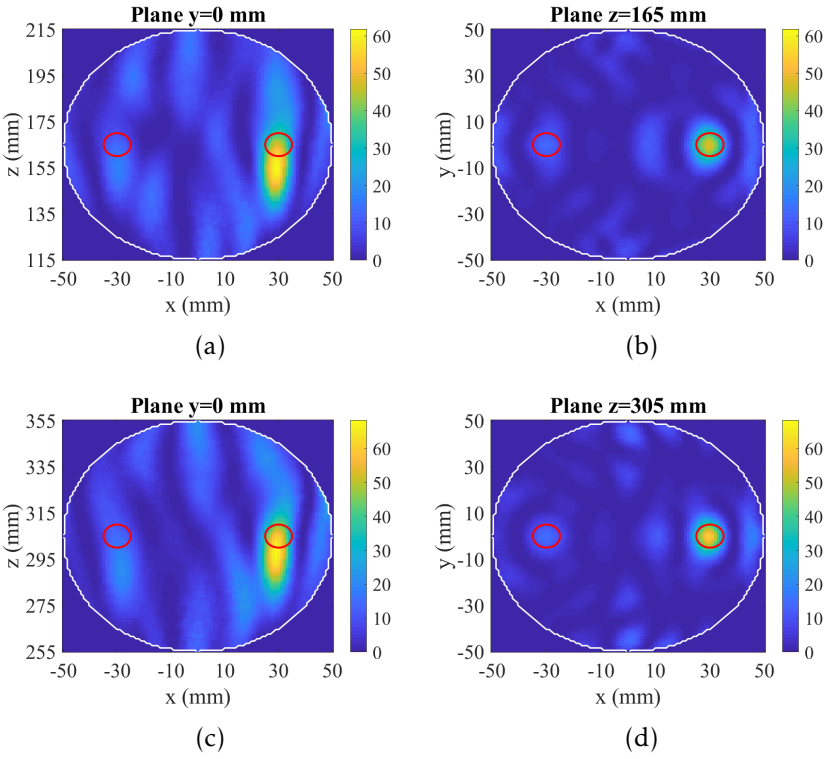

Figure 7.15: Reconstructed images of two PEC targets inside the dielectric sphere using multistatic signals and (a,b) XETS as a stand-alone antenna, and (c,d) XETS+Lens placed at $x = 30$ mm. The images on the left (a,c) and on the right (b,d) show the reconstructed images in the xz and the xy-planes, respectively. The red contours represent the true location and shape of the targets. The spherical breast contour is represented in white.

in the sense that this setup can be used to illuminate the area to image, allowing to focus only on some parts of the breast at each time. In a clinical perspective, this feature can be useful to analyse smaller parts of the breast at each time, avoiding structures that can potentially hamper the imaging results, such as fibroglandular tissue or cysts.

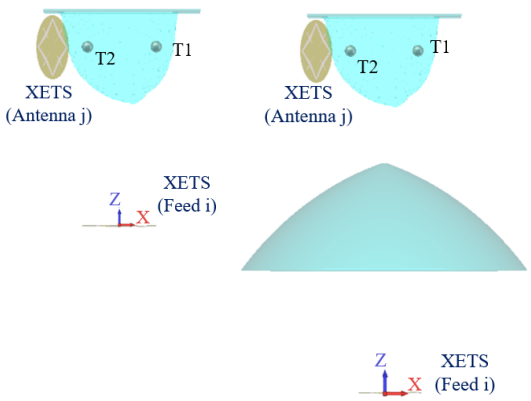

Figure 7.16: Screenshots from CST simulation of a multistatic setup with a dielectric anthropomorphic breast phantom above (a) the XETS as a stand-alone antenna, and (b) XETS and Bessel lens.

7.2.3.2 Anthropomorphic Breast Phantom

The realistic breast phantom was obtained from the repository available online [147] for MWI validation. The Magnetic Resonance Imaging (MRI)-derived phantom with ID 062204 was considered. Similarly to the dielectric spherical phantom, the realistic breast was considered homogeneous with a real permittivity $\epsilon_r = 8$ and dissipation factor $\tan(\delta) = 0.1$. Several tests were completed, including placing one single target or two targets in different positions within the breast phantom. For conciseness, only the results with two spherical PEC targets with 5 mm radius are shown. They were placed asymmetrically, at coordinates $(x, y) = (30, 0)$ mm and $(x, y) = (-30, 10)$ mm at the same z plane (50 mm from the surface). These targets will be called T1 and T2 from now on, as shown in Figure 7.16.

Shifting the XETS+Lens to one position yields a similar result if only the XETS below the lens is shifted in the opposite direction. Hence, three positions of the XETS below the lens were considered $x = [-30, 0, 30]$ mm, while y and z coordinates remain the same (0 mm). Figure 7.17 shows the three equivalent positions for each setup with and without the lens.

Artefact Removal Algorithm The results with the anthropomorphic breast phantom are obtained after applying an artefact removal algorithm to the input transmission coefficients $\mathbf{s}_{i,j}$ (with $i \neq j$, where i is always the same antenna). The original $\mathbf{s}_{i,j}$ are obtained from the difference between the simulated response from all components (i.e. antennas, breast and targets) and the simulated response of the same setup without the breast and the targets (i.e. only the antennas). The air-breast interface response is removed using the SVD algorithm.

In this study, an automated procedure was implemented in order to find the optimal number of singular vectors which should to be removed (n_{sv}) to successfully remove

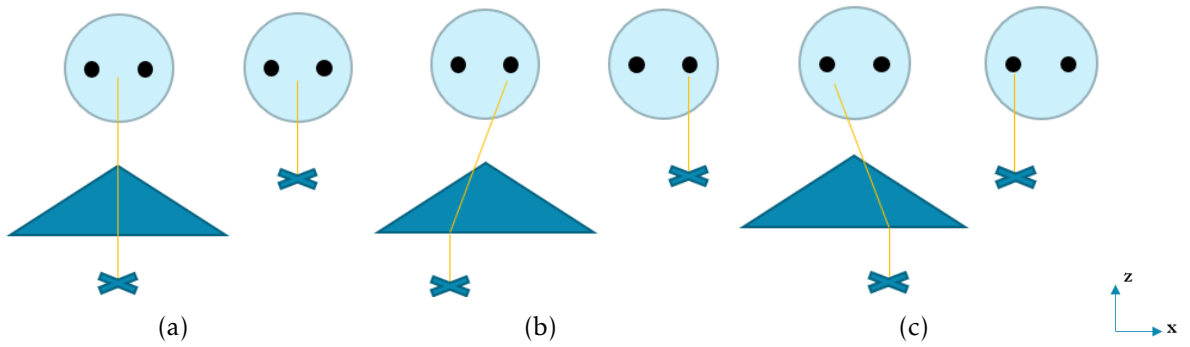

Figure 7.17: Representation of the XETS positions for the setup with and without the lens (a) in a centred position, (b) focusing T1, and (c) focusing T2. The light blue circle corresponds to the breast phantom, the black circles correspond to the targets, the dark blue triangle corresponds to the lens, the blue cross corresponds to the antenna, and the orange line corresponds to the direction of the beam.

the artefacts and maintain the target response. Contrarily to the case of the axillary region phantom, a constant number of n_{sv} does not provide good results in the majority of the tests performed with the breast phantom using multistatic signals. Hence, the algorithm proposed by Felício *et al.* [49], where n_{sv} is found for each antenna position by minimising the response at air-phantom interface, was adapted for a multistatic imaging setup. The matrix $\mathbf{M}$ is a $N_f \times N_s$ matrix where each column corresponds to the input transmission coefficient $\mathbf{s}_{i,j}$, where i corresponds to the XETS below the breast and j corresponds to the XETS that rotates around the breast. N_f is the number of frequency points and N_s is the number of antenna positions considered for the matrix factorisation.

The artefact response is removed from each $\mathbf{s}_{i,j}$ signal considering the signals of the three neighbouring antennas of each side of the antenna position i,j: $\mathbf{s}_{i,j-3}, \mathbf{s}_{i,j-2}, \mathbf{s}_{i,j-1}$, $\mathbf{s}_{i,j}, \mathbf{s}_{i,j+1}, \mathbf{s}_{i,j+2}, \mathbf{s}_{i,j+3}$. The signals after removing 1 to $N_s - 1$ singular vectors are automatically analysed, where N_s corresponds to the maximum number of singular vectors. Two electrical distances are considered in this analysis, as shown in Figure 7.18: the sum of the distance between antenna j and the closest entry point in the phantom and the distance between that entry point and feed i (d_{min}); the sum of the distance between antenna j and the farthest entry point in the phantom and the distance between that entry point and the feed i (d_{max}). The optimal n_{sv} for each antenna position is determined considering the ratio between the magnitudes of the singular vector at the minimum ($m_{\mathrm{d}_{min}}$) and maximum ($m_{\mathrm{d}_{max}}$) distances to the air-phantom interface and the maximum magnitude of each singular vector (m_{sv}), ensuring the following criteria is verified: $m_{\mathrm{d}_{min}}/m_{sv} \leq 0.5$ and $m_{\mathrm{d}_{min}}/m_{sv} + m_{\mathrm{d}_{max}}/m_{sv} \leq 1$. This ensures the response of the air-phantom interface is minimised, even when multiple reflections are recorded by the receiving antenna j.

Results and Discussion Table 7.1 shows the performance metrics of each 3D reconstructed image for all the considered scenarios.

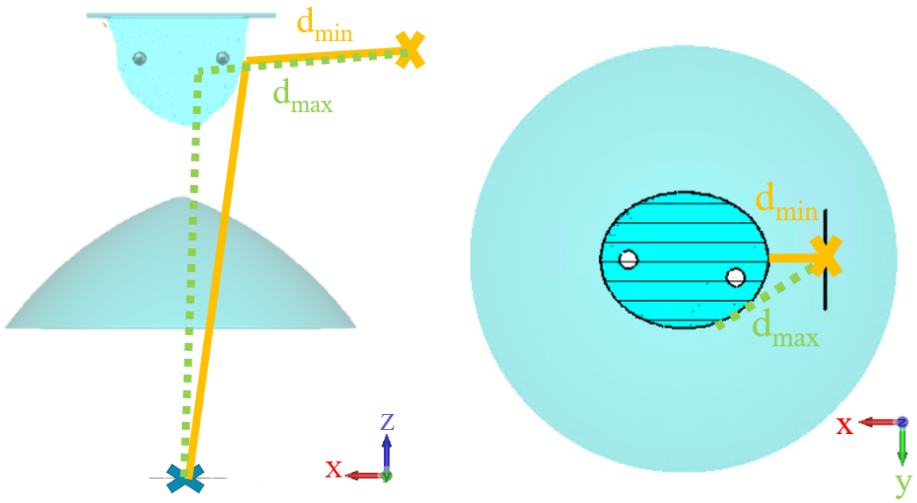

(a) (b)

Figure 7.18: Schematic of the minimum and maximum distances to the air-phantom interface for one pair of antennas in (a) xz and (b) xy planes. The orange and green lines represent the minimum (d_{min}) and the maximum (d_{max}) distances between the two antenna positions to the air-phantom interface, respectively.

Figures 7.19 and 7.20 show the reconstructed images in the same planes as the targets using a realistic calibration of a setup with and without a Bessel lens, respectively, when the XETS was placed at $(x, y, z) = (0, 0, 0)$ mm [Figure 7.17(a)]. The intensity scale of the images are normalised to the highest intensity value of the 3D-volume, while the images are reconstructed in the planes of the targets. In both cases, SVD is not able to successfully remove the artefacts, as the highest intensity value of the 3D-volume is not located close to the targets and the artefacts have a much higher intensity than the target intensity. However, the intensity near the true location of the targets is about half of the maximum intensity, and higher than the surrounding voxels. Although the targets are detected, they cannot be observed in the presented images.

Table 7.1: Performance metrics of the reconstructed images with the anthropomorphic breast phantom using SVD as the artefact removal algorithm.

	Focus region					
	XETS + Lens			***XETS***		
Metrics	***-30***	***0***	***30***	***-30***	***0***	***30***
SCR (dB)	0.8	1.4	1.9	0.5	1.5	1.3
SMR (dB)	8.9	9.7	11.2	8.9	9.9	9.3
FWHM T1 (mm)	18.0	13.3	14.3	6.3	5.3	7.7
FWHM T2 (mm)	16.3	7.3	4.7	2.3	9.3	13.7
LE T1 (mm)	41.2	35.4	**7.0**	47.9	51.0	57.8
LE T2 (mm)	**15.9**	43.9	61.2	53.0	55.0	31.0

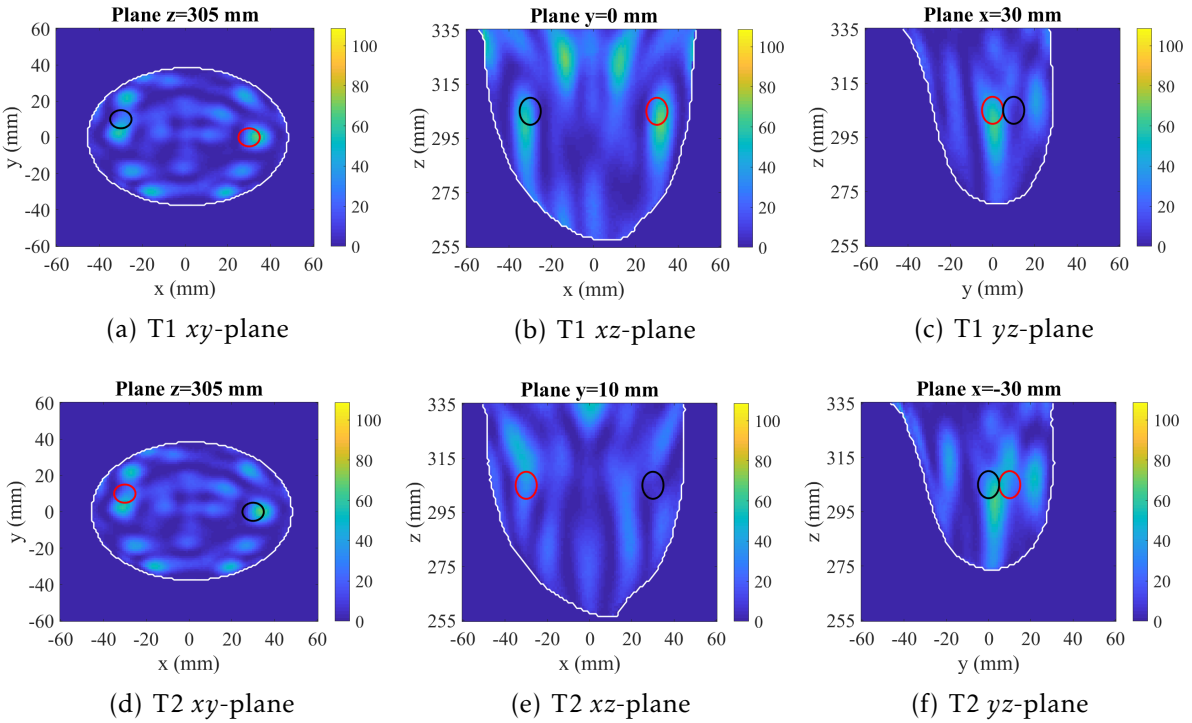

(a) T1 xy-plane (b) T1 xz-plane (c) T1 yz-plane

(d) T2 xy-plane (e) T2 xz-plane (f) T2 yz-plane

Figure 7.19: Reconstructed images of two PEC targets inside an anthropomorphic breast phantom using multistatic signals and the XETS and Bessel lens, where XETS is placed at $x = 0$ mm, when applying SVD as the artefact removal algorithm. (a-c) show the images in the planes of the true location of T1, and (d-f) T2. The left, centre and right images show the coronal, sagittal and axial planes, respectively. The red contour represents the true location and shape of the target in the selected planes and the black contour represents the projection of the true location and shape of the other target, which is located in at least one different plane. The breast contour is represented in white.

Figures 7.21 and 7.22 show the reconstructed images in the same planes as the targets using a realistic calibration of a setup with and without a Bessel lens, respectively, where the region of T1 ($x = 30$ mm) is illuminated. The XETS was placed at $x = -30$ mm when the Bessel lens was used, and placed at $x = 30$ mm when it worked as a standalone antenna [Figure 7.17(b)]. When using a Bessel lens, T1 is well-detected with an Localisation Error (LE) of 7 mm, while T2 is not detected. Signal-to-Clutter Ratio (SCR) and Signal-to-Mean Ratio (SMR) are 1.9 dB and 11.2 dB, respectively, which are satisfactory values for a positive detection. Full Width Half Maximum (FWHM) is 14.3 mm, which means the detection is slightly larger than the true size of the target (10 mm diameter). This is due to the fact that only one plane of antennas is considered in the z-axis, which limits the resolution. Nonetheless, the resolution is better compared to when no antenna was placed below the breast, which would result in a similar result to Figure 7.14. Furthermore, when removing the lens from the setup, the XETS is not able to focus the target and there are several artefacts spread over the whole volume.

Figures 7.23 and 7.24 show the reconstructed images using a realistic calibration of a setup with and without a Bessel lens, respectively, where the region of T2 ($x = -30$ mm) is illuminated. Unlike the previous example, the XETS was placed at $x = 30$ mm when combined with the Bessel lens and placed at $x = -30$ mm when it operated as a standalone antenna [Figure 7.17(c)]. When the Bessel lens is used, T2 is detected, with an LE

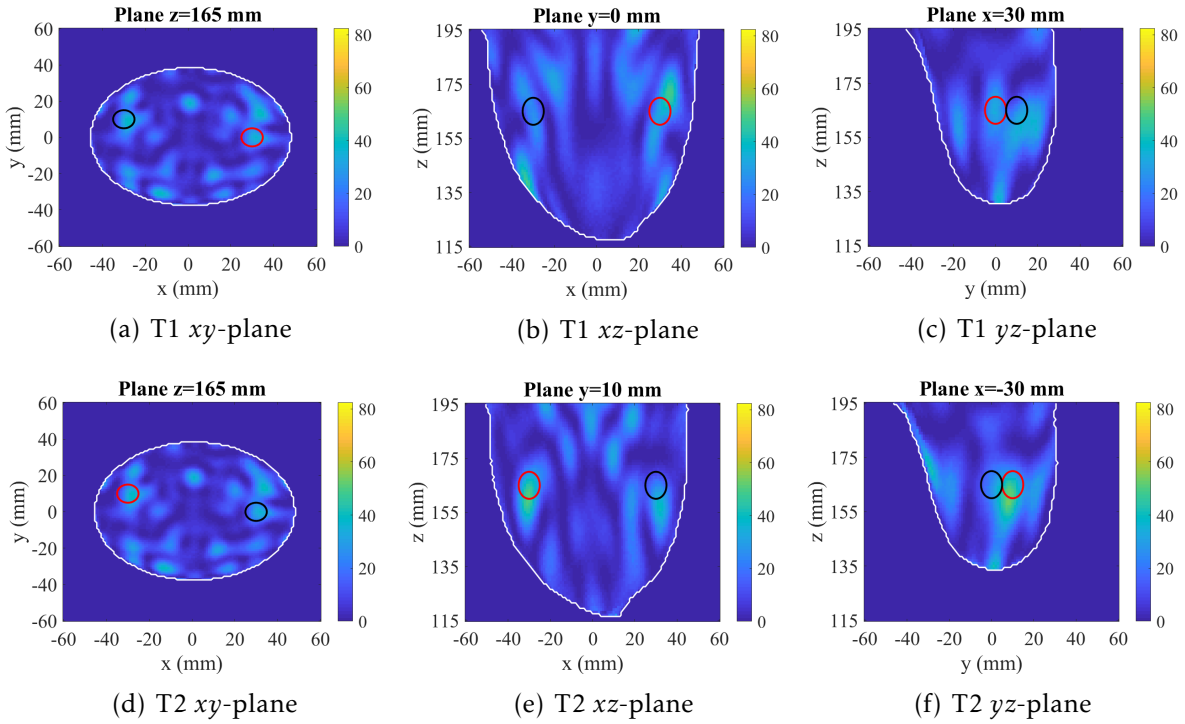

(a) T1 xy-plane (b) T1 xz-plane (c) T1 yz-plane

(d) T2 xy-plane (e) T2 xz-plane (f) T2 yz-plane

Figure 7.20: Reconstructed images of two PEC targets inside an anthropomorphic breast phantom using multistatic signals and the XETS at $x = 0$ mm, when applying SVD as the artefact removal algorithm. (a-c) show the images in the planes of the true location of T1, and (d-f) of T2. The left, centre and right images show the coronal, sagittal and axial planes, respectively. The red contour represents the true location and shape of the target in the selected planes and the black contour represents the projection of the true location and shape of the other target, which is located in at least one different plane. The breast contour is represented in white.

of 15.9 mm (observed both in y and z axes), but with some clutter in the images. This can be explained by the fact that T2 is not centred in the y-axis and the XETS was only shifted in the x-axis, and therefore, T2 was not fully illuminated by the Bessel beam. When considering the XETS as a stand-alone antenna, no high intensity regions can be associated with T2. The highest intensity voxel of the 3D volume is not located in the 2D planes shown in the figure, which explains the LE higher than 47 mm for both targets. Because this position of the XETS did not directly illuminate the region of T1, the detection of this target using this position was not expected. The positive detection of T1 and the non-detection of T2 may be a result of the higher coupling between the transmitting antenna and the receiving antenna positions closest to T2, and lower coupling between the transmitting antenna and the receiving antenna positions closest to T1. The large beam of the XETS, in contrast to the Bessel beam, still illuminates the region of T1, and, therefore, the receiving antenna positions closest to T1 can still record the response of the target.

An electromagnetic exposure safety assessment is performed in the following section in order to evaluate the compliance in terms of SAR of the proposed prototype. Although the results are promising for the use of the lens, experimental evaluation is required, as presented in Section 7.3.

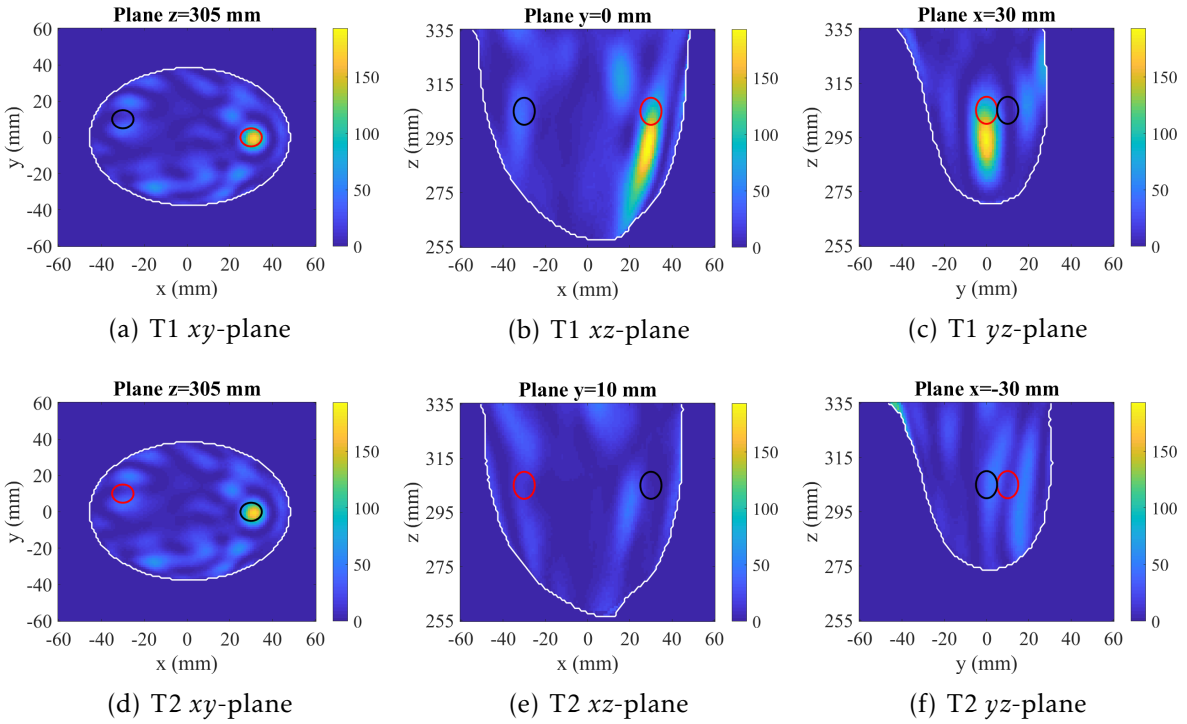

(a) T1 xy-plane (b) T1 xz-plane (c) T1 yz-plane

(d) T2 xy-plane (e) T2 xz-plane (f) T2 yz-plane

Figure 7.21: Reconstructed images of two PEC targets inside an anthropomorphic breast phantom using multistatic signals and the XETS and Bessel lens, where XETS is placed at $x = -30$ mm, when applying SVD as the artefact removal algorithm. (a-c) show the images in the planes of the true location of T1, and (d-f) of T2. The left, centre and right images show the coronal, sagittal and axial planes, respectively. The red contour represents the true location and shape of the target in the selected planes and the black contour represents the projection of the true location and shape of the other target, which is located in at least one different plane. The breast contour is represented in white.

7.2.3.3 Assessment of Electromagnetic Exposure Risk

A realistic breast phantom with skin, fibroglandular and fat tissue was considered to calculate the SAR and study the effect of adding a Bessel lens to the prototype in terms of electromagnetic exposure. To this end, SAR was calculated for the antenna below the breast in both prototypes with and without the lens. The radiated power by the XETS was 1 W.

Table 7.2 shows the SAR values for three frequencies and Figure 7.25 shows the SAR maps at 4 GHz. The maximum value of SAR is located in the first illuminated region. At lower frequencies, it tends to be deeper in the breast than at higher frequencies. In the case of the lens, a deeper maximum value of SAR is more evident which can be explained by the focusing feature the lens has. The maximum value of SAR is similar in both setups with or without the lens, which is expected since the simulated scenarios had the same electric field at the breast surface. All calculated values are below International Commission on Non Ionizing Radiation Protection (ICNIRP) limits (2 W/kg up to 6 GHz), which means the presence of the lens does not substantially increase the SAR. The results also indicate that the radiated power by the XETS under the breast can be increased at least 3 times using a power amplifier, and therefore increase the signal-to-noise ratio. These values are calculated for 1 W of radiated

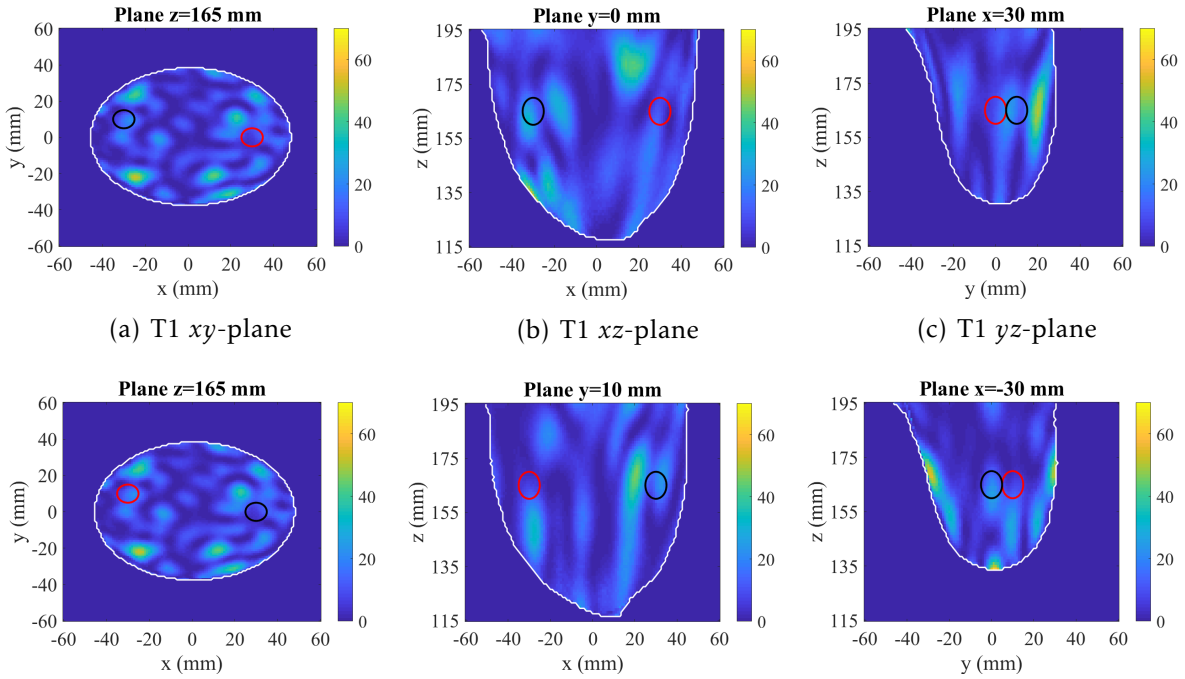

(a) T1 xy-plane (b) T1 xz-plane (c) T1 yz-plane

(d) T2 xy-plane (e) T2 xz-plane (f) T2 yz-plane

Figure 7.22: Reconstructed images of two PEC targets inside an anthropomorphic breast phantom using multistatic signals and the XETS at x = 30 mm, when applying SVD as the artefact removal algorithm. (a-c) show the images in the planes of the true location of T1, and (d-f) of T2. The left, centre and right images show the coronal, sagittal and axial planes, respectively. The red contour represents the true location and shape of the target in the selected planes and the black contour represents the projection of the true location and shape of the other target, which is located in at least one different plane. The breast contour is represented in white.

power. In an experimental setup, this power can be as low as 0.01 W, which means the SAR values would be even lower.

Table 7.2: Maximum SAR values and location for each simulated setup in three frequencies.

	XETS + Lens			**XETS**		
	2 GHz	**4 GHz**	**6 GHz**	**2 GHz**	**4 GHz**	**6 GHz**
Max. SAR (W/kg)	0.62	0.64	0.37	0.61	0.54	0.38
x (mm)	11.86	4.51	13.26	6.71	11.98	12.75
y (mm)	10.91	7.59	8.29	11.27	8.57	8.66
z (mm)	314.42	267.44	255.30	143.74	115.21	115.06

7.3 Experimental Evaluation

This section presents the experimental evaluation of the multistatic prototype with the lens and its comparison with an equivalent setup without the lens. Firstly, a preliminary experimental prototype was built to define the best distances between each component of the setup that provide the ideal focusing beam. Secondly, the final experimental

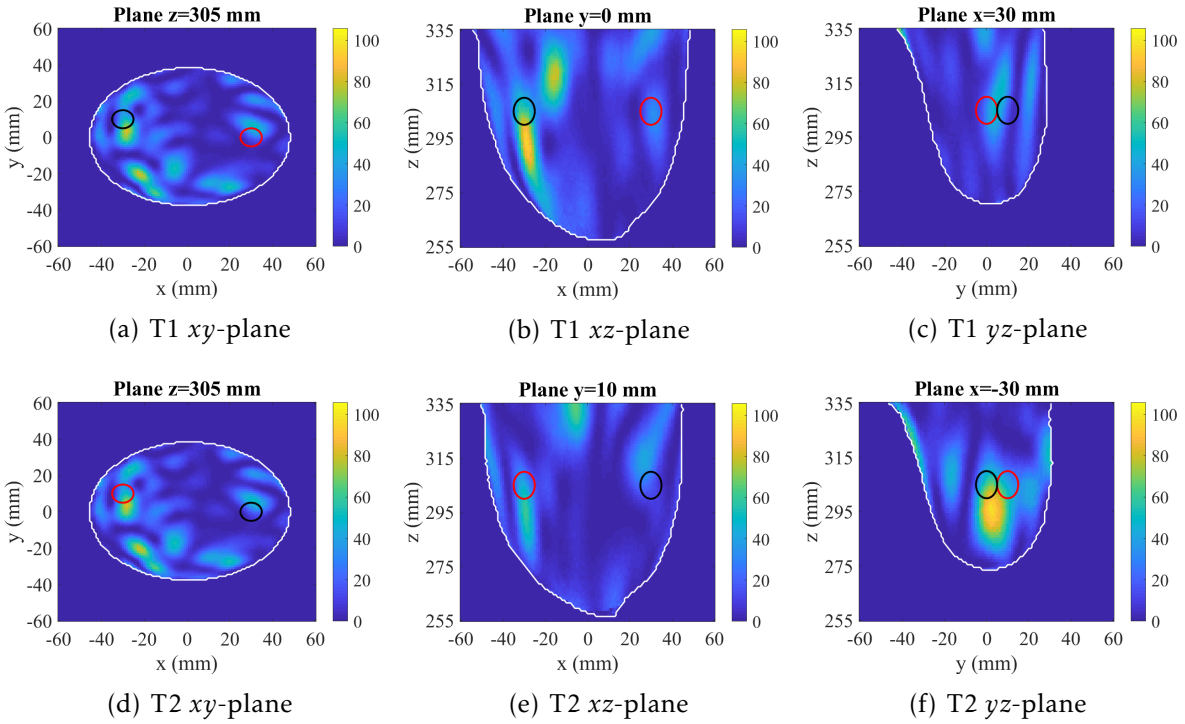

(a) T1 xy-plane (b) T1 xz-plane (c) T1 yz-plane

(d) T2 xy-plane (e) T2 xz-plane (f) T2 yz-plane

Figure 7.23: Reconstructed images of two PEC targets inside an anthropomorphic breast phantom using multistatic signals and the XETS and Bessel lens, where XETS is placed at $x = 30$ mm, when applying SVD as the artefact removal algorithm. (a-c) show the images in the planes of the true location of T1, and (d-f) of T2. The left, centre and right images show the coronal, sagittal and axial planes, respectively. The red contour represents the true location and shape of the target in the selected planes and the black contour represents the projection of the true location and shape of the other target, which is located in at least one different plane. The breast contour is represented in white.

prototype was used to image an anthropomorphic breast phantom. The first tests were performed with a homogeneous medium with single and multiple targets. Then, heterogeneity was included with a fibroglandular tissue phantom.

7.3.1 Optimisation of Distances

A monostatic experimental prototype was used to find the distances between the feed (XETS) and the PP Bessel lens ($d_{feed-lens}$), between the lens and the target ($d_{lens-target}$), and, consequently, between the feed and the target ($d_{feed-target}$). The prototype comprises a linear positioner where the lens is fixed and the position of the XETS and the target are changed in several combinations of distances (Figure 7.26). The XETS is impedance-matched in the frequency band of 2 to 6 GHz. The signals are acquired in the frequency band of 1 to 7 GHz, but only the bandwidth 2 to 6 GHz is considered for analysis. A 40×40 mm^2 aluminium square is used as target, as shown in Figure 7.26(c).

The distance $d_{feed-lens}$ was varied from 50 to 350 mm, with a spacing of 25 mm, and $d_{lens-target}$ was varied from 177 to 447 mm, with a spacing of 25 mm. The target was moved in the x-axis from the centre of the lens ($x = 0$ mm) to a distance of 104 mm, with a spacing of 13 mm. The target position was only varied for the subset of values of

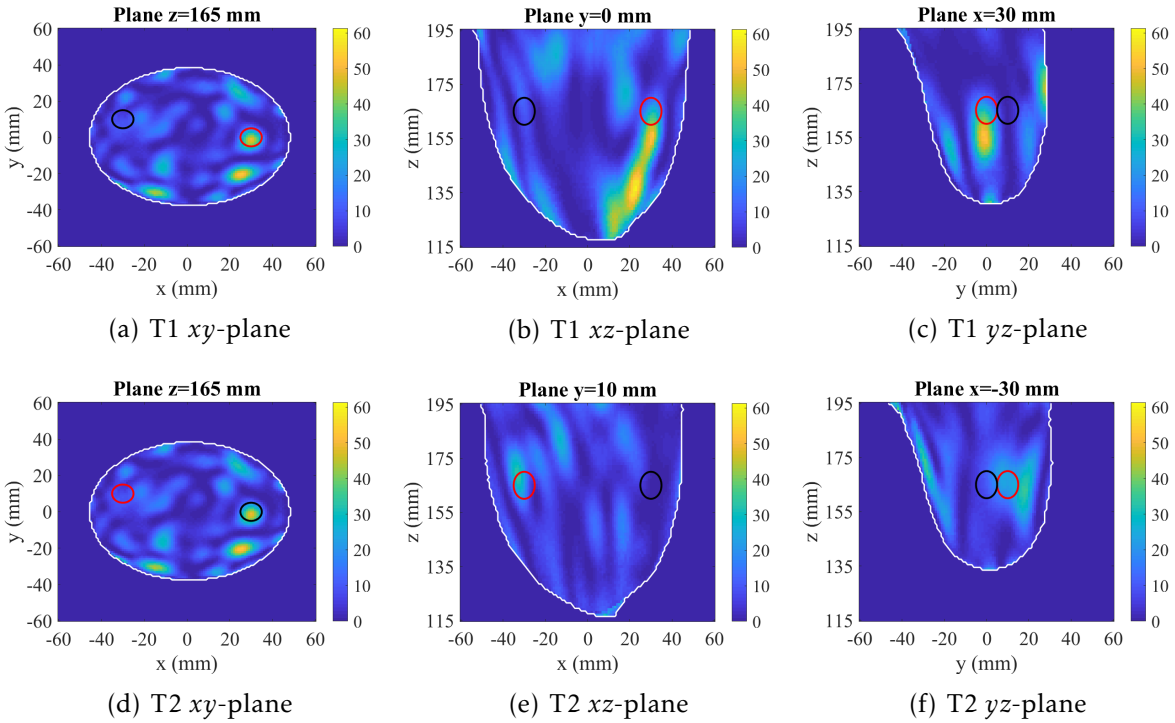

(a) T1 xy-plane (b) T1 xz-plane (c) T1 yz-plane

(d) T2 xy-plane (e) T2 xz-plane (f) T2 yz-plane

Figure 7.24: Reconstructed images of two PEC targets inside an anthropomorphic breast phantom using multistatic signals and the XETS at $x = -30$ mm, when applying SVD as the artefact removal algorithm. (a-c) show the images in the planes of the true location of T1, and (d-f) of T2. The left, centre and right images show the coronal, sagittal and axial planes, respectively. The red contour represents the true location and shape of the target in the selected planes and the black contour represents the projection of the true location and shape of the other target, which is located in at least one different plane. The breast contour is represented in white.

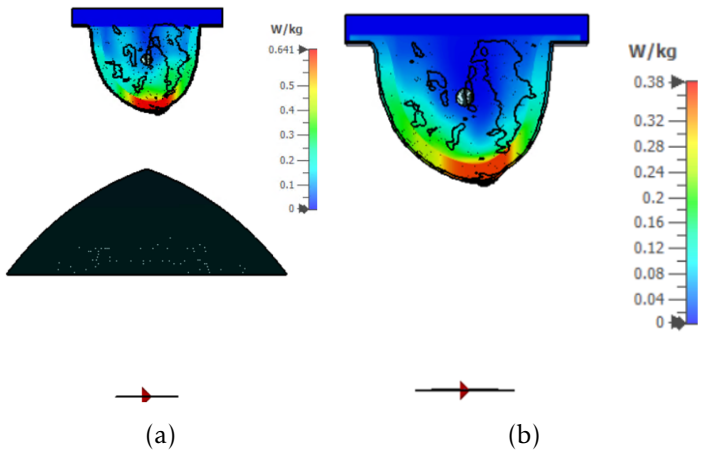

(a) (b)

Figure 7.25: SAR maps in an average volume of 10 g at 4 GHz of a numerical breast phantom when considering (a) the assembly XETS+Lens and (b) the XETS as a stand-alone antenna. Red colours correspond to higher values of SAR, while blue colours correspond to lower values of SAR in each reference scale.

$d_{feed-lens}$ that provide a beam with higher and more stable magnitude over its depth.

The beam is evaluated measuring the magnitude of the signal reconstructed with the imaging algorithm in 1D. The beam width is defined as the distance in the x-axis at which the magnitude of the signal drops to half of the magnitude at $x = 0$ mm. Figure 7.27 shows the maximum magnitude of the signal and the beam width over the

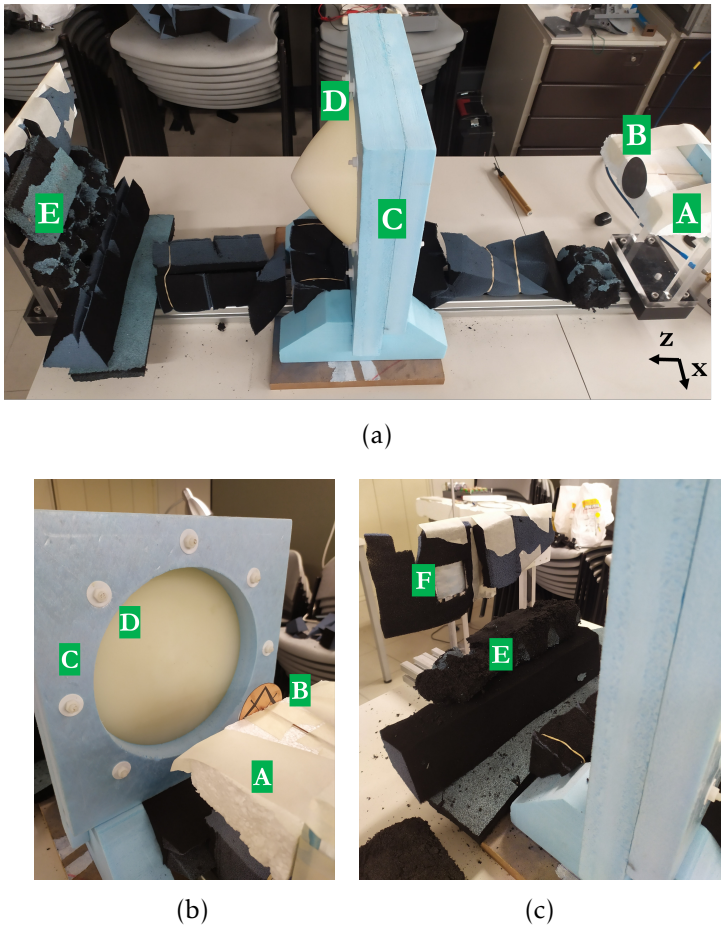

(a)

(b) (c)

Figure 7.26: Experimental prototype with a linear positioner used to find the optimal distances between the feed, the lens and the target. (a) shows the all components ([A] styrofoam support for the feed, [B] feed, [C] styrofoam support for the lens, and [D] lens). (b) shows a closer picture of [B] the feed behind the [D] dielectric lens, and (c) shows the [F] aluminium target. The metallic parts of the linear positioner are covered with [E] electromagnetic absorbers.

$d_{lens-target}$ for fixed values of $d_{feed-lens}$. The beam width is mostly constant for the evaluated values of $d_{lens-target}$ when $d_{feed-lens} = 175$ mm, over a depth of at least 175 mm. The beam width is around 110 mm, one of the narrowest beams for a combination of distances, which corresponds approximately to the size of a small breast. The higher magnitude of the beam for $d_{feed-lens} = 175$ mm is at $d_{lens-target} = 227$ mm.

Hence, the optimal distances are the following: $d_{feed-lens} = 175$ mm, $d_{lens-target} = 227$ mm, and consequently $d_{feed-target} = 402$ mm. These distances are higher than the ones considered in Section 7.2.

7.3.2 Breast Phantoms

The experimental tests were performed with the physical phantom of the numerical anthropomorphic breast phantom presented in Section 7.2.3.2 [147]. All elements of the phantoms used in this work are made of compartments and had been already designed and 3D-printed for the work of Felício *et al.* [49] (Figure 7.28).

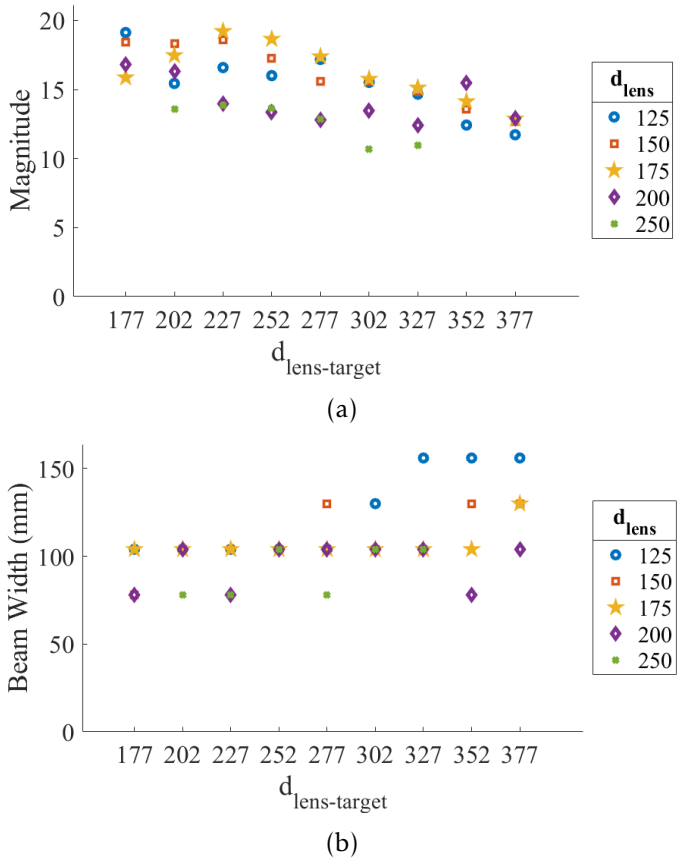

Figure 7.27: Plots of the (a) maximum magnitude and (b) total width of the beam created with the Bessel lens in the experimental prototype, considering a frequency band from 2 to 6 GHz.

The breast phantom was 3D-printed using an Ultimaker 3 Extended 3D-printer (Ultimaker [213]), with a 1.2 mm-thickness wall in PLA, which has a relative permittivity ranging from 2.75 and 2.9 and dissipation factor $\tan(\delta) = 0.01$ [214]. The tumour models are positioned inside the breast phantom by inserting them in pre-determined openings through the cover. Two tumour phantoms were used. They are ellipsoids with dimensions $20 \times 10 \times 10$ mm^3 connected to a tube with varying length that defines the depth of the tumour within the breast. The tumour denominated T1 is connected to a tube with length of 32 mm, while the tumour denominated T2 is connected to a tube with length of 50 mm. The fibroglandular phantom, adapted from the original phantom [147] by Felício *et al.* [49], is attached to another cover with new openings for the tumour models. No skin layer was considered at this stage.

The phantoms were filled with the tissue mimicking liquids proposed by Joachimowicz *et al.* [145]. The G3, G1 and T mixtures were considered to mimic adipose tissue, fibroglandular tissue, and the tumour, respectively. Figure 5.10 of Chapter 5 shows the curves of these liquids, which were also used for the axillary imaging experiments.

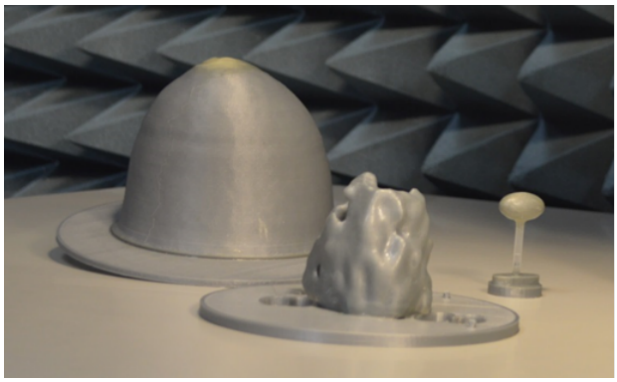

Figure 7.28: Anthropomorphic breast phantom including the fibroglandular and tumour compartments [49].

7.3.3 Measurement Setup

The Radio Frequency (RF) measurements were acquired with an Agilent E5071C Vector Network Analyser (VNA). Similarly to the simulation setup, two XETS antennas impedance-matched from 2 to 6 GHz were used as transmitting and receiving antennas. The measurements were performed in the frequency domain between 1 and 7 GHz, but only the bandwidth 2 to 6 GHz is used for image reconstruction. As mentioned in Section 2.2.1, one advantage of using a bistatic configuration is the possibility to use an amplifier to increase the dynamic range of the measurements. Hence, the transmitting antenna is placed below the breast connected to an amplifier, which is then connected to port 1 of the VNA [Figure 7.29(a)]. The amplifier is a Mini-Circuits® ZVA-183-S+, which works in the frequency band of 0.7-18 GHz, with a gain of 26 dB, output power of 24 dBm, and noise figure of 3 dB. These specifications allow the setup to be compliant with the SAR limits presented in Section 7.2.3.3. The receiving antenna is placed at a radius of 80 mm, which corresponds approximately to a 30 mm distance to the breast wall, and connected to the port 2 of the VNA.

The rotation of the antenna is emulated by rotating the breast phantom in a total of twelve positions using the circular grid shown in Figure 7.29(b) as reference, while keeping the antenna fixed. When the XETS below the breast is centred, it is equivalent to rotate the breast while the antennas are fixed or rotate both antennas while the breast is fixed. However, this is not true when the XETS is moved below the lens, as the region focused by the Bessel beam changes as the breast rotates. Hence, the experimental tests presented with this prototype are limited to the case where the XETS is centred at the breast.

In the setup with the lens, the distances were defined as $d_{feed-lens}$ = 170 mm and $d_{lens-target}$ = 233 mm, and therefore, $d_{feed-target}$ = 403 mm. These are a few millimetres different from the distances defined in Section 7.3.1, due to technical constraints. However, such small differences do not have an impact on the beam shape. In the setup without the lens, the XETS was placed at an equivalent distance from the target, ensuring the electric field intensity at the breast surface is the same in both cases. This

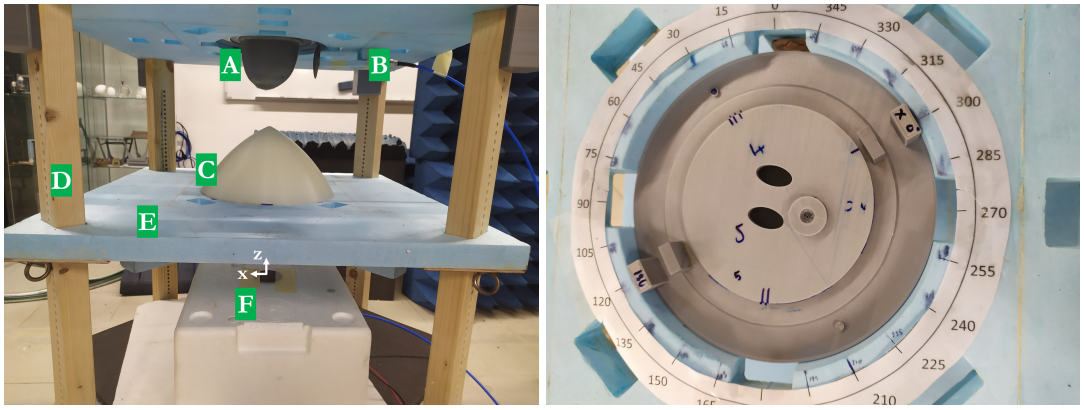

(a) (b)

Figure 7.29: Measurement setup with (a) all components ([A] breast phantom, [B] antenna, [C] lens, [D] wood supports, [E] styrofoam support, and [F] feed). (b) shows a picture of the phantom and the reference grid setup for rotation from a top view.

distance was found by simulating the electric field of both setups in CST and is defined as $d_{feed-target} = 120$ mm. In both cases, the $d_{feed-target}$ corresponds to the z coordinate of the receiving antenna positions.

The electrical distance offsets of all antennas were calculated using a similar procedure to the one presented in Section 3.2.1. It is 281 mm for the assembly XETS+Lens connected to the amplifier, 231 mm for the XETS as a stand-alone antenna below the breast connected to the amplifier, and 192 mm for the XETS connected to port 2.

7.3.3.1 Signal processing

The algorithms presented in Section 7.2.3.2 are applied to the experimental signals. In these experimental tests, the artefact response is successfully removed considering only one neighbouring antenna of each side of the antenna position under analysis. The shape of the breast is assumed to be known for the image reconstruction algorithm. As mentioned before, in a clinical scenario, the retrieval of this shape can be performed using low-cost optical devices [49] or laser systems [217].

7.3.4 Results and Discussion

Three experimental tests were completed with the prototype using both the XETS as a stand-alone antenna, and the assembly XETS+Lens. The first test consisted of a single target T1 placed on the same plane of the receiving antenna, at position $(x, y) = (20, -15)$ in a homogeneous phantom. The second test, called T1T2, consisted of two targets, T1, and T2 placed at position $(x, y) = (5, 15)$ and 20 mm below the plane of the receiving antenna, in a homogeneous phantom. The third test, called T1-FG, was performed with a heterogeneous phantom, by inserting fibroglandular tissue compartment inside the phantom and T1 at position $(x, y) = (30, 20)$.

Table 7.3: Performance metrics of the reconstructed images with the homogeneous phantom using the experimental prototype. "Ref" corresponds to the reference experimental test without target.

		Maximum Intensity	SCR (dB)	SMR (dB)	FWHM T1 (mm)	FWHM T2 (mm)	LE T1 (mm)	LE T2 (mm)
XETS	T1	1171	2.81	8.71	23.7	-	15.7	-
+	T1T2	2107	1.95	7.84	21.7	23.0	33.6	18.1
Lens	Ref	638	0.64	7.71	23.0	22.7	11.9	42.5
	T1	2721	0.38	8.93	19.0	-	23.5	-
XETS	T1T2	4169	2.67	9.30	20.3	18.7	11.2	54.2
	Ref	659	1.96	8.64	20.0	20.0	12.7	23.8

Table 7.3 summarises the performance metrics of the reconstructed images of the experimental tests with the homogeneous breast phantom using both the XETS as a stand-alone antenna and the assembly XETS+Lens.

Figures 7.30 and 7.31 show the reconstructed images of the experimental tests with target T1 for both XETS+Lens and XETS, respectively. The images are reconstructed on the planes of the voxel with maximum intensity of the whole reconstructed 3D image. When the Bessel lens is used, a single target in the same z-plane of the antennas is well detected. SCR is higher than 1.5 dB and SMR is satisfactory, as the target is distinguishable from the surrounding medium. LE is 15.7 mm and FWHM is 23.7 mm, mainly due to the oval effect observed in the z-axis. As mentioned before, this is a consequence of using just one plane of antenna positions around the breast, instead of using multiple planes. When only the XETS is used below the breast, an artefact with higher intensity is detected near the air-phantom interface, resulting in an LE of 23.5 mm and a low SCR (0.38 dB).

Figures 7.32 and 7.33 show the reconstructed images of the experimental tests with target T1 and T2 for both XETS+Lens and XETS, respectively. In both cases, only one target is detected. When the XETS+Bessel lens is used, only T2 is detected in the correct position (LE of 18.1 mm, with a higher contribution from the z-axis). A second high intensity spot, a false positive, is detected in a location that does not match the location of any of the targets, resulting in an LE of 33.6 mm. SCR and SMR are sufficiently high to indicate a positive detection. When the XETS is used as a stand-alone antenna, only T1 is detected, with an LE of 11.9 mm. The second detected high intensity region has approximately half the maximum intensity of the whole image (Figure 7.33(d-f)) and it is in a location that also does not match the location of any of the targets. Similarly to what happens in simulation (Section 7.2.3.2), when the feed is centred at the breast, the detection of multiple targets is more challenging.

The reference measurements (i.e. where no target was inside the phantom) are

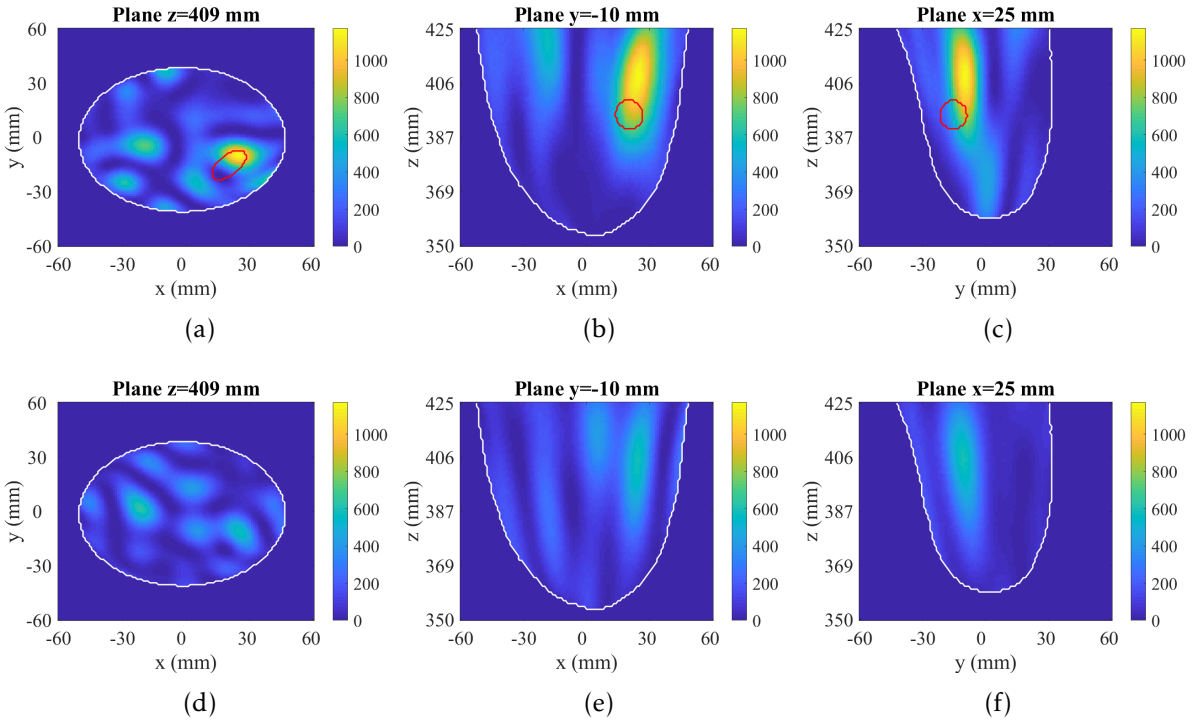

Figure 7.30: Reconstructed images of experimental tests with XETS and Bessel Lens and with target T1 inside a homogeneous breast phantom. (a-c) show the reconstructed images with the target in the planes of the voxel with maximum intensity, and (d-f) show the reconstructed images when there is no target. The left, centre and right images show the coronal, sagittal and axial planes, respectively. The red contour represents the projection of the approximate location and shape of the target in each plane. The breast contour is represented in white.

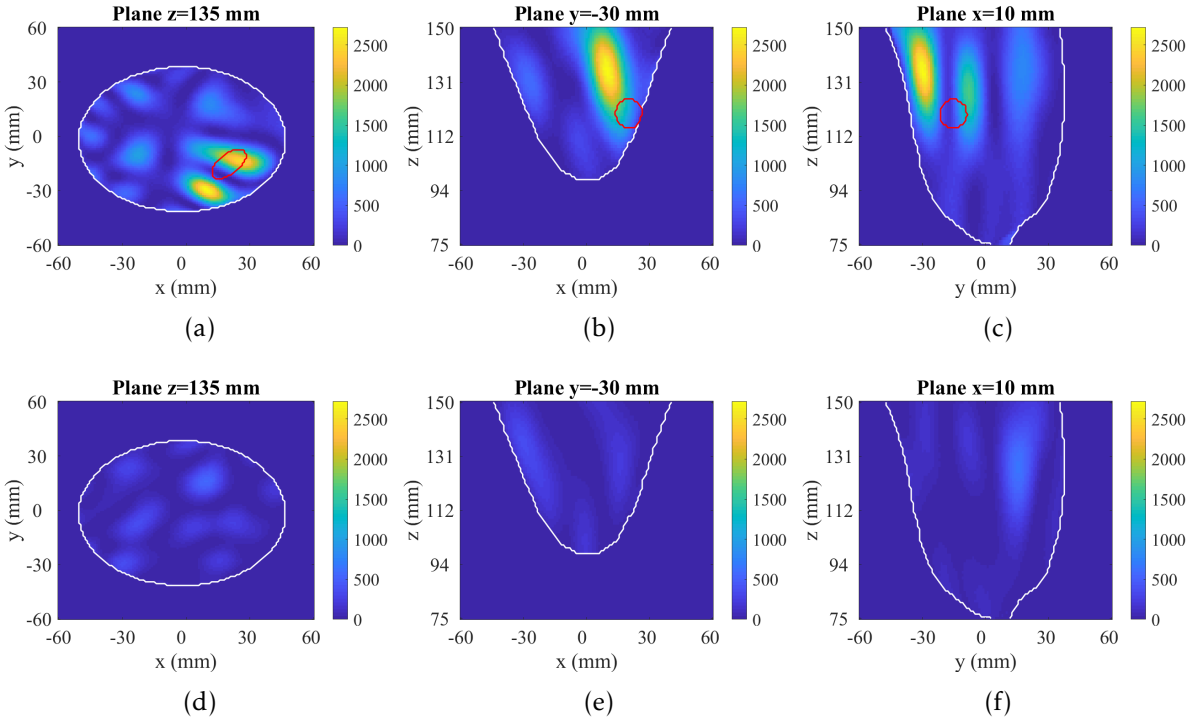

Figure 7.31: Reconstructed images of experimental tests with XETS as stand-alone antenna and with target T1 inside a homogeneous breast phantom. (a-c) show the reconstructed images with the target in the planes of the voxel with maximum intensity, and (d-f) show the reconstructed images when there is no target. The left, centre and right images show the coronal, sagittal and axial planes, respectively. The red contour represents the projection of the approximate location and shape of the target in each plane. The breast contour is represented in white.

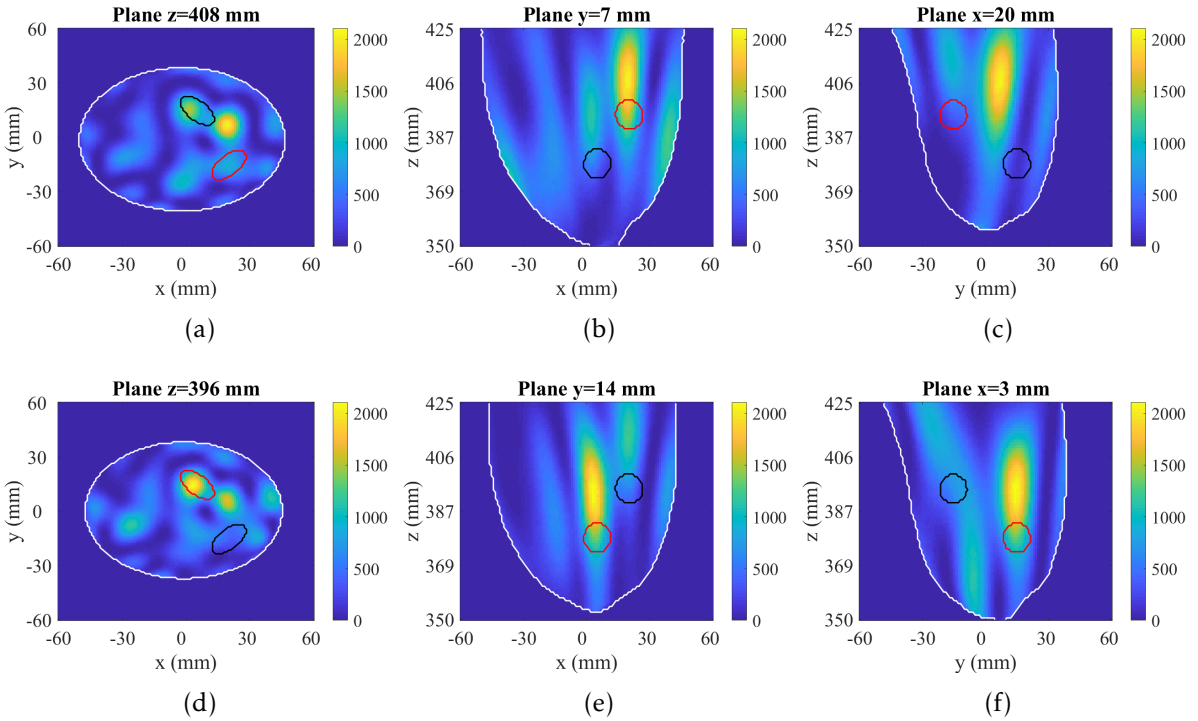

Figure 7.32: Reconstructed images of experimental tests with XETS and Bessel Lens and two targets inside a homogeneous breast phantom. (a-c) show the images of the breast with the targets in the planes of maximum intensity closest to T1, and (d-f) show the images of the breast with the targets in the planes of maximum intensity closest to T2. The left, centre and right images show the coronal, sagittal and axial planes, respectively. The red and black contours represent the projection of the approximate location and shape of the targets. The red contour corresponds to the target closest to the selected planes and the black contour corresponds to the other target. The breast contour is represented in white.

important to understand how well a target is detected. As discussed in Chapter 5, using only SCR as a metric for positive detection may not be sufficient. In the experimental tests with the homogeneous breast phantom, when the lens is considered, SCR is below 1.5 dB in the reference measurement, and the maximum intensity is approximately less than half of the maximum intensity when a target is inside the phantom. However, in the measurement without the lens, SCR is 1.96 dB, although the maximum intensity of the image is one quarter of the maximum when a target is considered. More tests would be needed to define the intensity threshold to complement the SCR in the definition of a positive detection.

Table 7.4 shows the performance metrics of the reconstructed images of the experimental tests with the heterogeneous breast phantom. The maximum intensity of these images are higher than the intensity verified with the homogeneous phantom (Table 7.3). Although the measurements with the homogeneous and heterogeneous phantoms were performed in different days and the amount of tissue mimicking liquid inside the target may have varied, this might not be the reason for such intensity differences. Firstly, the intensity values when applying an ideal artefact removal (results not shown) are in the same order of magnitude when comparing T1 and T1-FG. Nonetheless, the maximum intensity of T1-FG when applying an ideal artefact removal is 5 times higher

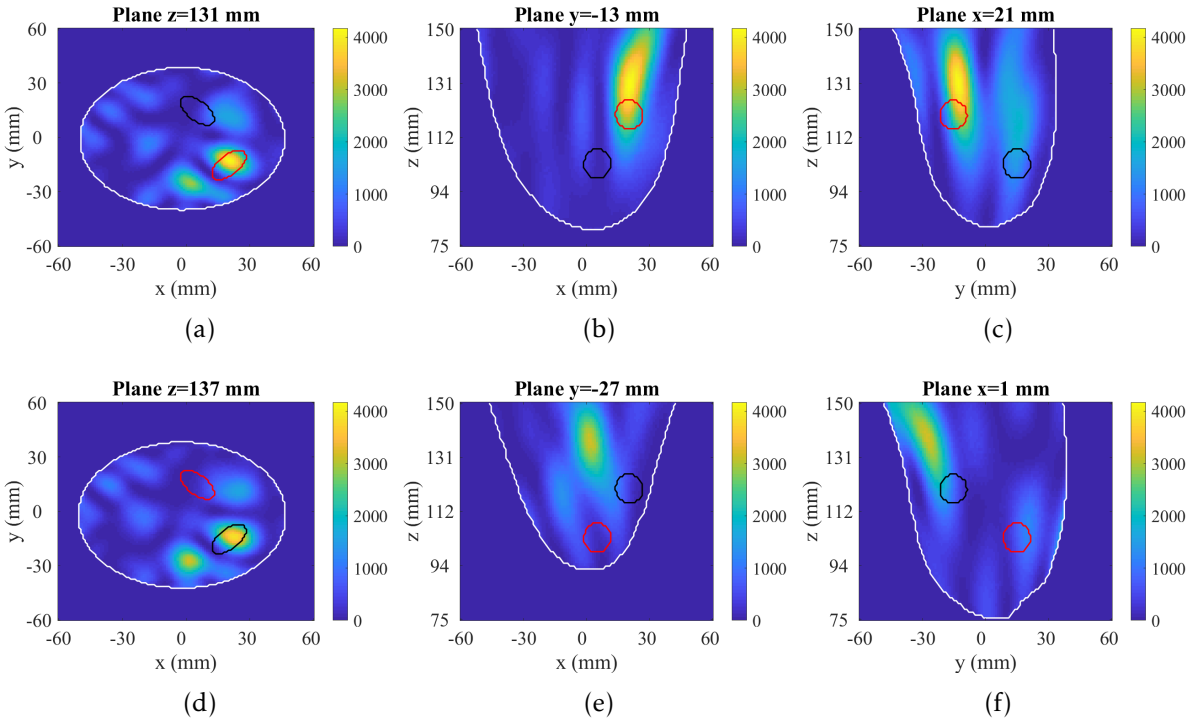

Figure 7.33: Reconstructed images of experimental tests with XETS as stand-alone antenna and two targets inside a homogeneous breast phantom. (a-c) show the images of the breast with the targets in the planes of maximum intensity closest to T1, and (d-f) show the images of the breast with the targets in the planes of maximum intensity closest to T2. The left, centre and right images show the coronal, sagittal and axial planes, respectively. The red and black contours represent the projection of the approximate location and shape of the targets. The red contour corresponds to the target closest to the selected planes and the black contour corresponds to the other target. The breast contour is represented in white.

than the intensity of T1. Secondly, the targets in the heterogeneous phantom are shallower than in the homogeneous breast phantom, which may explain the higher intensity of T1-FG. This can also influence the results with SVD, as less singular vectors may have been removed in order to detect the target. Thirdly, the presence of the fibroglandular tissue in the phantom may influence the reflections inside the breast and how the signals coherently add between them, creating high intensity regions.

Whether the lens is used or not, the target T1 is successfully detected in the correct location with an LE lower than 8.2 mm. FWHM is larger than the dimensions of the target, also due to the z-axis resolution. SMR is satisfactory in both cases. When the lens is considered, SCR is lower than 1.5 dB due to some clutter in the air-phantom interface. When the lens is not used, SCR is 1.63 dB. Visually, the images do not present substantial differences. The reference measurements with the breast and fibroglandular phantoms show a substantial decrease in both maximum intensity and SCR when compared to the tests with target.

In all experimental tests, SVD has a satisfactory performance. Since the breast has a more regular shape, no focusing region is observed unlike was observed in the axillary region application (see Section 5.2.5.4).

The advantages of using a Bessel lens in the proposed bistatic system are promising

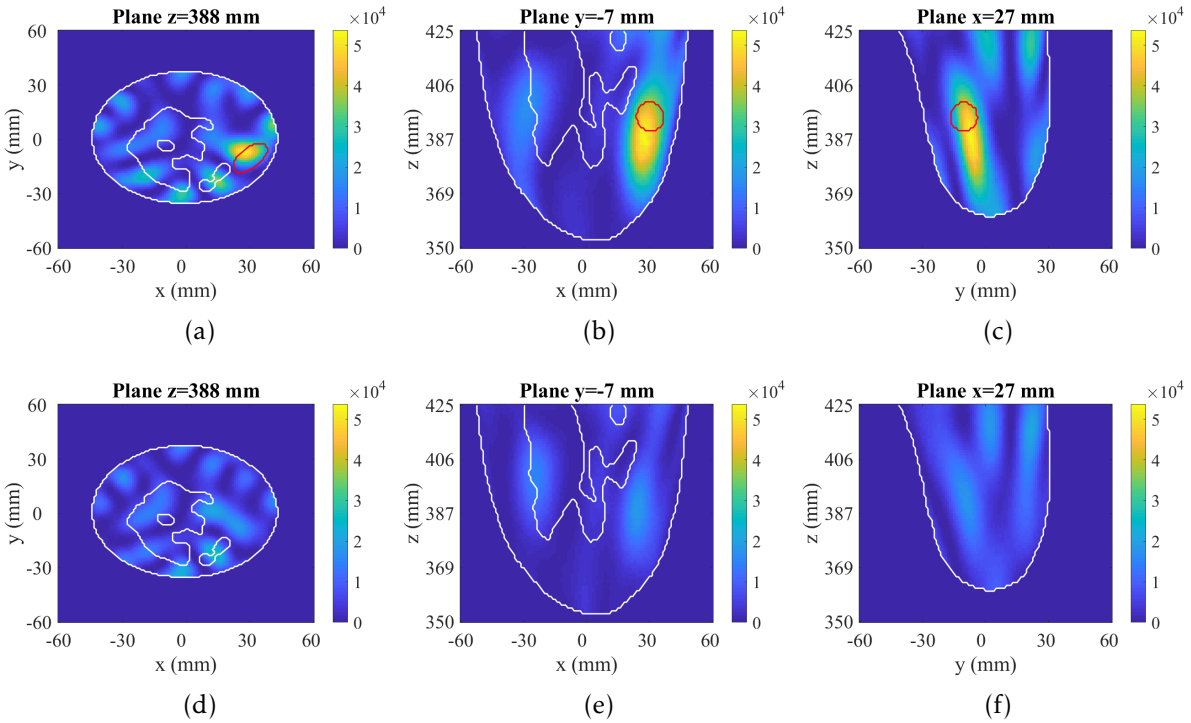

Figure 7.34: Reconstructed images of experimental tests with XETS and Bessel Lens and a heterogeneous breast phantom. (a-c) show the images with the target in the planes of the voxel with maximum intensity, and (d-f) show the images without the target. The left, centre and right images show the coronal, sagittal and axial planes, respectively. The red contour represents the projection of the approximate location and shape of the target in each plane. The breast and fibroglandular contours are represented in white.

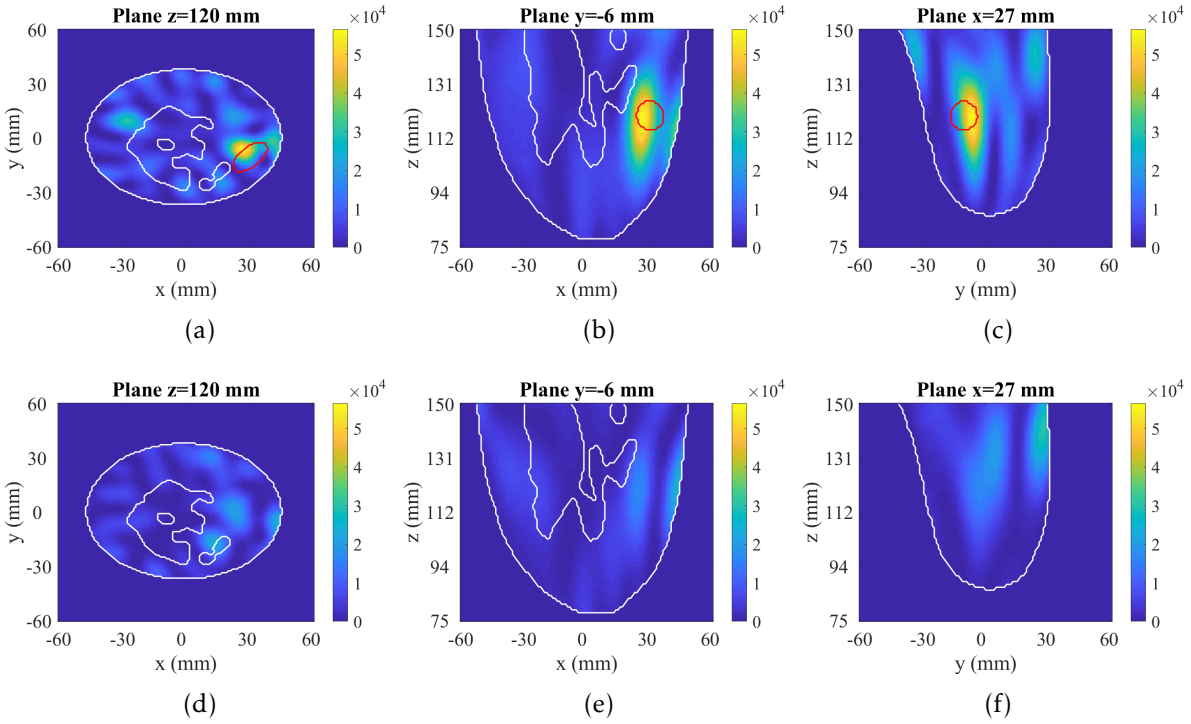

Figure 7.35: Reconstructed images of experimental tests with XETS as stand-alone antenna and a heterogeneous breast phantom. (a-c) show the images with the target in the planes of the voxel with maximum intensity, and (d-f) show the images without the target. The left, centre and right images show the coronal, sagittal and axial planes, respectively. The red contour represents the projection of the approximate location and shape of the target in each plane. The breast and fibroglandular contours are represented in white.

Table 7.4: Performance metrics of the reconstructed images with the heterogeneous phantom using the experimental prototype. "FG Ref" corresponds to the reference experimental test without target and with fibroglandular tissue phantom.

		Maximum Intensity	SCR (dB)	SMR (dB)	FWHM (mm)	LE (mm)
XETS + Lens	T1-FG	53681	1.16	8.31	20.3	8.2
	FG Ref	28521	0.38	7.05	24.0	21.0
XETS	T1-FG	56484	1.63	9.35	18.7	5.0
	FG Ref	31169	0.71	8.99	14.3	42.1

but still inconclusive. In the first experimental test with a single target in a homogenous breast, the assembly XETS+Lens presents better imaging results than when only the XETS is used. In the second test, when two targets are considered, the imaging results are different but none of the two setups (stand-alone XETS or XETS+Lens) successfully detect both targets, only one target is detected. Nonetheless, this experimental test outperforms the test performed in the simulated test where none of the two targets were detected. In the third test, the results with a heterogeneous breast are similar between both configurations but the XETS as stand-alone antenna slightly outperforms the assembly XETS+Lens. This test is an important milestone towards the feasibility of this prototype as it uses a more realistic phantom. However, these experimental tests were limited to the case where the feed is centred at the breast. More evidences may be found when shifting the XETS, as performed in simulation in Section 7.2.3.2, and considering larger breast phantoms.

7.4 Chapter Conclusions

This chapter proposed the use of a Bessel lens for focusing targets in the breast and, consequently, improve their detection. Two configurations to include the Bessel lens in an MWI prototype were tested. In a monostatic approach, the use of the Bessel lens was not able to provide a satisfactory cross-range resolution and ultimately, this approach was discarded. However, promising results were obtained when considering a multistatic approach using a Bessel lens in a static position below the breast and a ring of antennas around the breast. This also gives the possibility to include power amplifiers in the system in order to increase the dynamic range and improve target detection.

The proposed multistatic prototype was tested in simulation and in experimental work. Two comparable setups with and without the lens were evaluated. Firstly, the configuration was tested using a spherical and a realistic-shaped breast phantoms. SVD was presented as an option for artefact removal algorithm and an adaptation from the

previously proposed automated methods was presented. The imaging results showed the use of the lens and this type of multistatic setup is able to increase the resolution in the coronal axis of the patient without moving the ring of antennas. Nonetheless, an elongated shape was still observed in the coronal axis. The results also showed the ability of selecting targets inside the breast when moving the antenna below the breast. The safety in terms of electromagnetic exposure of the prototype was assessed by calculating its SAR. The results showed the SAR is below the defined limits and power amplifiers can be used to increase SCR. Experimental results allowed to confirm the feasibility of the prototype and the proposed algorithms to detect breast tumour phantoms. The validation of the selection of targets observed with the simulated setup was not possible due to technical and time constraints. The proposed setup allows to increase the resolution in the coronal axis without the need of a large number of antennas, which allows to decrease the acquisition time. It also allows the use of power amplifiers with the transmitting antenna, potentially improving target detection. The size and weight of the lens can be a limitation but most pre-clinical prototypes already include a bed table, where the lens could be placed. Preliminary experimental tests did not provide an explicit advantage of adding the lens to the multistatic setup but further testing is advised.

Future work should include experimental validation with larger and more complex phantoms, with different Breast Imaging-Reporting and Data System (BI-RADS) categories. In these cases, using the beam of the dielectric lens to focus the energy into the region of interest can be more beneficial. Using higher frequencies, in order to reduce the beam width, can also be considered. The selection of targets by moving the feed below the breast should also be tested experimentally in the proposed scenarios, which would require modifications in the prototype.

8 | Conclusions and Future Work

This chapter summarises the work developed in this thesis and presents suggestions for future work. Section 8.1 summarises the work developed per chapter and the drawn conclusions. Finally, Section 8.2 presents the relevant steps that should be explored in the future to further extend and/or validate the findings of this thesis.

8.1 Summary and Conclusions

Many advances have been conducted in the last few decades towards the development and implementation of Microwave Imaging (MWI) systems in clinical practice, namely as an alternative imaging modality for early breast cancer detection. This thesis presented the first complete study to aid both breast cancer detection and staging using MWI systems. Many studies have addressed breast cancer detection, but cancer staging through detection of Axillary Lymph Nodes (ALNs) with MWI has never been attempted before. Simulated and experimental work was conducted to study the feasibility of such systems, and further explore air-operated MWI systems.

The development of the MWI prototype aimed to diagnose ALNs included a complete research of several aspects that are crucial to evaluate the feasibility of such a system. These included anatomically realistic phantoms, which resulted in the creation of an open-access repository, dielectric properties information, experimental assessment with realistic conditions in the first developed prototype for this application, and complementary classification of ALN signatures, which were still a gap in the literature. Moreover, an analysis of refraction effects in air-operated MWI systems was performed, showing how they can affect MWI results and when a real-time image reconstruction is not compromised. A preliminary study towards the development of a prototype with novel features for breast cancer detection was also performed, presenting a possible solution for a selective scanning of breast tumours.

Overall, the work yielded promising results in the areas of electromagnetic simulations, experimental work with Radio Frequency (RF) acquisition, implementation and optimisation of signal processing algorithms, development of image processing pipelines, model creation and 3D-printing, dielectric properties assessment, and Machine Learning (ML) for classification of microwave signals.

Chapter 3 presented a study of refraction effects in air-operated MWI systems. Air-operated MWI setups have been recently introduced by several authors to avoid the limitations of using a coupling liquid between antennas and the body. While reconstructing the images, researchers consider a direct path between the antenna and each voxel (corresponding to a point in the body), without considering refraction at the interface between air and the body. However, a quantification of refraction effects on imaging results using this type of setups had never been performed before this thesis.

Numerical simulations and experimental tests were used to qualitatively and quantitatively study the effects of refraction by varying several conditions: spherical or planar waves, regular or irregular shapes, permittivity values of the medium, size of targets and number of antennas. The results showed for the first time that blind regions can occur for certain antenna positions due to refraction by the curved surface of the body. These blind regions can affect target detection when considering planar waves or spherical waves for high permittivity values (e.g. $\epsilon_r = 40$). The differences between imaging results for low to moderate permittivity values ($\epsilon_r <= 8$) were negligible, while for high permittivity values, the detection of targets can be affected if refraction is not taken into account. The size of targets and number of antennas affected the imaging results but there was no substantial change when refraction was considered or not. This means there are conditions where discarding refraction does not substantially improve the imaging results and an unnecessary increase of computational cost can be avoided, allowing real-time image reconstruction. The results from this study can be used as a reference for other researchers to decide whether to consider refraction in their calculations or not when using air-operated systems. This work was published in a conference and a journal publications.

In **Chapter 4**, a Magnetic Resonance Imaging (MRI) processing pipeline was presented to create numerical phantoms of the axillary region with realistic representations of ALNs and infer information about the dielectric properties of ALNs. The pipeline comprised pre-processing steps to remove noise and effects of MRI inhomogeneities and different segmentation steps to segment the main tissues in the axillary region. Ten numerical phantoms were made available in an open-access repository, the first of its kind for the axillary region, comprising different file formats and with information of dielectric properties mapping. The phantoms presented variability in terms of number of healthy and metastasised ALNs and Body Mass Index (BMI) of the patient.

Moreover, Magnetic Resonance (MR) images were used to estimate the dielectric properties of ALNs by associating state-of-the-art dielectric properties of known tissues to the images. A large study with 50 patients, and a total of 100 ALNs, showed there is a dielectric contrast of 32% between healthy and metastasised ALNs. A large variability of property values among healthy ALNs, as reported in the literature, was

also observed. As there are many factors that may affect MRI voxel intensities, a 3D-printed phantom filled with liquids with known dielectric properties was tested in an MRI scanner and used to validate the methodology of estimating dielectric properties. This study showed the error of the method can range from 2 to 17.2 of points of permittivity. Nonetheless, the results indicated the methodology produced underestimated contrasts between dielectric properties of tissues. The dielectric properties of only a very limited number of metastasised ALNs had been assessed before this study and the heterogeneity of ALNs had compromised the measurements in some of the state-of-the-art studies. This study complemented the knowledge about dielectric properties of ALNs, by confirming a large variability of values of healthy ALNs and indicating a high dielectric contrast between healthy and metastasised ALNs. These findings are encouraging to the feasibility of the diagnosis of ALNs using MWI, since the underestimated contrast is still large enough to allow MWI-based diagnosis. This work was published in a conference and a journal publication.

Chapter 5 presented the evaluation of an air-operated radar MWI prototype to image the axillary region. Firstly, a preliminary study was performed with 2D simulated slices of anthropomorphic axillary region phantoms. The results with different shapes showed the shape of the axillary region presents some challenges in the design of an MWI prototype: the antenna positioning is limited by the size of the torso and the irregularities of the axillary region; the scanning range is limited because a 360° scanning would include structures outside the region of interest, and so the scanning range was limited to 90°; the concavities and convexities of the axillary region may hamper the performance of the artefact removal algorithms and consequently hinder the ALN detection.

Then, an experimental evaluation of an MWI prototype was performed tackling the above challenges. This work comprised the definition of the antenna positioning, the creation of the ALN models that were placed inside a previously created axillary region phantom, and the development of signal processing algorithms dedicated to the axillary region imaging application. In a 3D configuration, it was more difficult to remove the air-phantom response because of the irregularity of the axillary region. The results allowed to conclude that the target detection can be improved by finding an optimal combination of parameters for artefact removal, by implementing a spatial filter to select the region where ALNs are usually located inside the axillary region, and by considering a pre-selection of antenna positions for image reconstruction. The resulting images presented a focusing region, i.e. a region with higher intensity voxels in the centre of the phantom, as a consequence of the shape of the axillary region, which is not observed in breast MWI. Despite the challenges, the performance metrics of the considered experimental tests showed a Signal-to-Clutter Ratio (SCR) higher than 2.77 dB and a Localisation Error (LE) lower than 14.7 mm. Although these results were promising for ALN detection, the implemented methodology still needs to be tested in

other realistic phantoms. The findings in this chapter were a valuable contribution to the development of a radar MWI system to address the detection of ALNs by giving a first overview of the challenges and a first proposal of a pre-clinical system. This work was published in a conference and a journal publications, and a second journal publication is currently under review.

Several authors have shown that machine learning algorithms have the potential to complement MWI results by classifying microwave signals. In this context, **Chapter 6** presented a study of classification between healthy and metastasised ALNs using microwave signals. Sixty ALN models were created using mathematical formulations according to the state-of-the-art characteristics of healthy and metastasised ALNs. Backscattered signals of these ALN models were acquired in simulation considering four scenarios of different complexity. The first three scenarios considered one single ALN inside a dielectric and the fourth scenario comprised two ALNs placed inside a pseudo-realistic axillary region phantom. Several combinations between type of signals, Feature Extraction Methods (FEMs) and classifiers were considered.

The classification performance in the first three scenarios was similar. The maximum accuracy values of the classification were 95.7% in the first scenario and approximately 97% in the second and third scenarios, all obtained with k-Nearest Neighbours (kNN). The classification with multiple ALNs inside an axillary region was more challenging. The accuracy results ranged from 73.4% to 82.3%, with different combinations of classifiers and type of signals. The development of classification models for the axillary region presented a more challenging problem than the classification of breast tumours, as multiple ALNs are always present in a heterogeneous medium with muscles surrounding them. Overall, these preliminary results indicate classification algorithms were able to differentiate healthy from metastasised ALNs based on their shape and size, and potentially will be able to distinguish healthy from diseased axillary regions. Hence, there is potential in using classification models to aid the interpretation of reconstructed images of an axillary MWI system. One journal publication is in preparation regarding this part of the work.

The work presented in **Chapter 7** focused on the study of some aspects which have not yet been fully addressed in air-operated systems for breast cancer detection. To this end, a novel setup with a dielectric lens was proposed, which aimed to increase the energy coupling to the breast, while minimising the coupling between antennas in multistatic systems. It comprised an assembly of a feed and a dielectric lens which illuminate the breast, while one antenna sweeps one coronal plane of the breast and records the backscattered signals. This prototype allows the use of power amplifiers to increase the dynamic range, which are important to potentially increase the target response.

Firstly, the prototypes with and without dielectric lens were compared in 3D simulation. The use of the lens provided better results in the detection of the targets and

in focusing targets inside the breast region, while being compliant with the Specific Absorption Rate (SAR) limits. When the beam created by the lens was centred at one of the targets, the LE was 7 mm, and SCR and Signal-to-Mean Ratio (SMR) were 1.9 and 11.2 dB, respectively. Additionally, results showed this type of setup allowed to increase the resolution in the coronal axis without requiring a higher number of antennas. Finally, an experimental validation of the setup was performed using both homogeneous and heterogeneous anthropomorphic breast phantoms, with single and multiple targets, when the feed and the lens were centred with the breast. Multiple targets were not successfully detected but the detection of a single target in the heterogeneous phantom was satisfactory with an LE below 8.2 mm. Nonetheless, there was no consistency across all the results regarding the advantage of using the dielectric lens when compared to the same prototype with only a feed radiating from below. Further evaluation is still needed with this prototype in order to draw final conclusions. This work was published in two conference publications.

8.2 Future Work

The work developed in this thesis showed promising results in air-operated systems for the detection of ALNs and breast cancer. However, there are several aspects that need further investigation in order to create suitable MWI systems for clinical implementation in the breast cancer screening process.

The study of refraction effects covered some of the main aspects that can vary in an MWI scan, namely the permittivity of the body/phantom under evaluation. The major refraction effect in air-operated systems happens in the transition between air and the body/phantom, which was analysed in this study. However, other effects may affect other transitions between tissues when imaging a part of the body and may be worth studying. Heterogeneous phantoms may be considered. The skin layer may be included in the phantoms. In this study skin was not considered as no major effects were expected, considering that the used wavelength is much higher than the skin thickness. In the case of breast imaging, fibroglandular tissue can also be considered. Due to the extreme irregularity of the fibroglandular tissue, other effects such as diffraction may occur and these are more challenging to account for in the calculations of ray paths.

The work towards the development of an MWI system to detect the ALNs can still be deepened and several research possibilities should be explored. Firstly, although the study presented in Chapter 4 contributes to a better understanding of the dielectric properties of ALNs with different morphologies, complementary studies should be performed. A large-scale study of measurements of dielectric properties of ALNs with traditional methods is still encouraged. Factors such as the heterogeneity and dehydration of the samples should be considered during such measurements.

Secondly, from an anatomical perspective, there are two main characteristics of the axillary region which were not evaluated during the evaluation of the radar prototype: the effect of the muscle response and the detection of multiple ALNs. Although an experimental test was performed with a muscle phantom, the phantom was simple and did not represent the large volume of muscles that surround the region where ALNs are often located. The detection of ALNs is expected to be more challenging in patients with lower BMI, where the muscles are closer to the skin and closer to the ALNs, which may create higher reflections than the ALNs. In fact, Savazzi *et al.* [56] performed a preliminary radar imaging study with a 2D slice of an axillary region phantom of a patient with low BMI and showed the muscle response was strong and comparable to ALN response. The spatial filter designed in this thesis can be a useful tool to attenuate this response when combined with suitable artefact removal algorithms.

Moreover, the correct detection of multiple ALNs is crucial to implement an MWI system to diagnose the ALNs in clinical practice. The study presented in this thesis showed the feasibility of detecting ALNs in a 3D configuration but the feasibility of the diagnosis is yet to be explored. The evaluation of the resolution of the system, i.e. how well can two or more ALNs can be detected as different structures, and the ability of the system to differentiate between healthy and metastasised ALNs should be further assessed. Numerical phantoms, such as those presented in Chapter 4, can be used for this purpose as they include ALNs of different depths within the axillary region and of different sizes and shapes. The contrast between healthy and metastasised ALNs in imaging results can also be compared to the estimated properties and contrast reported in Chapter 4. Additionally, a skin layer should also be included in the evaluated phantoms.

Thirdly, the performance of the proposed artefact removal and imaging algorithms should be tested with more axillary region phantoms, ensuring representativeness of sizes and shapes. The numerical models presented in Chapter 4 can also be used for these experimental tests once optimised for 3D-printing. The repeatability of the measurements should also be ensured, in order to find a magnitude threshold that defines the presence of an ALN and can be used to complement the performance metric SCR, commonly used to define the presence of targets. These tests can also contribute to the definition of the parameters for artefact removal and the selection of the optimal antenna position grid used for image reconstruction.

New antenna positioning to image the axillary region can also be investigated. In this thesis, a semi-cylindrical antenna positioning was considered, based on the most frequent state-of-the-art prototypes that use fixed antennas in circular configurations. However, as observed in Chapter 5, the large range of distance values between each antenna position and the axillary region may hinder the performance of the artefact removal algorithm. One alternative that can be explored is to use a mechanical arm that changes the positions of the antenna while scanning the axillary region in order to

maintain a constant distance between the antenna and the body. However, the prototyping of this type of configuration poses technical challenges, and therefore, the viability of such configuration should be first evaluated in 3D simulations. Another possible antenna configuration is a planar configuration, similar to what Eleutério *et. al* [52] proposed. As mentioned before, the number of antennas that can be used are limited by the antenna dimensions for the microwave frequencies used (2 to 6 GHz). An alternative to this would be to place the antennas inside a conformable water-tight pillow that would adapt to the shape of the axillary region and contain a coupling medium. This type of solution would reduce the antenna dimensions (since the properties of the medium are higher), allowing more antennas, and does not pose sanitation issues as immersing the axillary region would do. Additionally, other frequency ranges can also be explored. The frequency range from 2 to 6 GHz was chosen due to the similarity of the axillary region to the breast imaging case, and other frequency ranges were briefly investigated, but no definitive conclusions could be drawn.

The classification of ALNs with ML algorithms have also an important role to potentially give additional and more objective information to clinicians when analysing microwave images. Several tests still need to be performed to extend the study presented in this thesis. The feasibility of ML models rely on the representativeness of the training data. Hence, more complex and real scenarios should be used to train the ML models, such as including varying axillary region phantoms, realistic-shaped ALNs at different depths, inclusion of realistic-shaped muscles, and improving the ALN modelling with realistic shapes and assigned corresponding dielectric properties. The data collection in experimental conditions is also important in order to consider more realistic data. However, these tests should be performed step-by-step as proposed in this thesis, so the effects of each new feature of the evaluated phantoms in the classification can be analysed. Depending on the results, more complex algorithms such as neural networks or deep learning algorithms may be tested to improve the classification performance. Complementing imaging results with the results from ML models is important to provide an easier interpretation of the MWI results by clinicians. Therefore, the combination of the two methods should be evaluated. In a clinical scenario, this type of models could give an indication of the probability of the examined axillary region to have metastasised ALNs.

During the course of my PhD, I received training towards the translation of the technology developed in my research to the market. There are a few points that should be considered when developing this system so it can be viable from a commercial point-of-view. After evaluating the feasibility of the system, the sensitivity and specificity of the system should be determined and compared to other imaging techniques for proper benchmarking. To this end, patient studies should be performed where the same patient undergoes an MWI exam and at least one of the other standard medical imaging exams (e.g. MRI). The beneficiaries of this type of system are women with breast cancer

in more advanced stages (reported to be around 0.5 million every year worldwide [1], [2]), radiology technicians and radiologists will use the system but the medical centres are the ones who will buy the technology. For the adoption of this technique, MWI should be advantageous for all these beneficiaries: an MWI exam should be comfortable and accessible to the patients; it should not require a complex training of the medical professionals, by ensuring it is user-friendly for radiology technicians and allows an easy interpretation of imaging results by the radiologists; and the cost/benefit ratio of the acquisition of these systems should be advantageous for the medical centres.

The current most accurate method to diagnose lymph nodes, Sentinel Lymph Node Biopsy (SLNB), is invasive, time-consuming and has high costs for the health care system. This procedure can cost more than 1000€ [229], while costs for MWI are comparable to an ultrasound exam, which costs around 60€ per exam (excluding the cost of the machine) [230]. The use of MWI could be accepted by the medical community if it can replace or reduce the need for SLNB. Although many women may have ALNs affected by breast cancer and a dedicated screening might be important, the current incidence may not justify the acquisition of such a system by most medical centres. As significant progress has been made in the development of breast MWI systems, the most viable solution would be to incorporate this setup to a breast MWI prototype, addressing two problems at once. To this end, in more advanced stages of development, the prototype to aid axillary imaging should be designed in such a way that can be combined with a breast MWI prototype. Considering the most advanced breast MWI prototypes [35], [94], [231], the design seems compatible with attaching the axillary imaging prototype to one of the sides of the examination table.

A novel prototype for breast cancer detection with a focal system was also proposed in this thesis. Many breast MWI prototype designs have been proposed in the literature. Hence, the adoption of a new proposed system requires a clear definition of the advantages of using a dielectric lens to focus the energy in the breast. To this end, more experimental studies with breast phantoms of different sizes and densities need to be performed. Using larger breasts combined with an increase of frequency band can show new advantages of the narrow beam created by the Bessel lens. The ability of focusing targets inside the breast should also be evaluated experimentally while considering situations where only a region of the breast is meant to be illuminated.

Overall, the results of this thesis suggest that MWI, together with the use of ML, has the potential to be a complementary medical imaging technique for breast cancer detection and staging, through ALN diagnosis, and can have a real impact on patient outcome.

References

[1] The Global Cancer Observatory - World Health Organization, *Breast Cancer Fact Sheets*, 2020. [Online]. Available: http://gco.iarc.fr/today (accessed on 24/05/2021).

[2] C. E. DeSantis, J. Ma, M. M. Gaudet, L. A. Newman, K. D. Miller, A. G. Sauer, A. Jemal and R. L. Siegel, "Breast Cancer Statistics , 2019", *CA: A Cancer Journal for Clinicians*, vol. 69, no. 6, pp. 438–451, 2019. DOI: 10.3322/caac.21583.

[3] American Cancer Society, *Breast Cancer Facts & Figures 2019-2020*, 2019. [Online]. Available: https://www.cancer.org/content/dam/cancer-org/research/cancer-facts-and-statistics/breast-cancer-facts-and-figures/breast-cancer-facts-and-figures-2019-2020.pdf (accessed on 24/05/2021).

[4] V. Dialani, B. Dogan, K. Dodelzon, B. N. Dontchos, N. Modi and L. Grimm, "Axillary Imaging Following a New Invasive Breast Cancer Diagnosis - A Radiologist's Dilemma", *Journal of Breast Imaging*, vol. 3, no. 6, pp. 645–658, 2021. DOI: 10.1093/jbi/wbab082.

[5] T. M. Kolb, J. Lichy and J. H. Newhouse, "Comparison of the Performance of Screening Mammography, Physical Examination, and Breast US and Evaluation of Factors that Influence Them: An Analysis of 27,825 Patient Evaluations", *Radiology*, vol. 225, no. 1, pp. 165–175, 2002. DOI: 10.1148/radiol.2251011667.

[6] H. Zhao, L. Zou, X. Geng and S. Zheng, "Limitations of mammography in the diagnosis of breast diseases compared with ultrasonography: A single-center retrospective analysis of 274 cases", *European Journal of Medical Research*, vol. 20, no. 49, pp. 1–7, 2015. DOI: 10.1186/s40001-015-0140-6.

[7] M. Pamilo, M. Soiva and E.-M. Lavast, "Real-time Ultrasound, Axillary Mammography, and Clinical Examination in the Detection of Axillary Lymph Node Metastases in Breast Cancer Patients", *Journal of Ultrasound in Medicine*, vol. 8, pp. 115–120, 1989. DOI: 10.7863/jum.1989.8.3.115.

[8] S. A. Valente, G. M. Levine, M. J. Silverstein, J. A. Rayhanabad, J. G. Weng-Grumley, L. Ji, D. R. Holmes, R. Sposto and S. F. Sener, "Accuracy of predicting

axillary lymph node positivity by physical examination, mammography, ultrasonography, and magnetic resonance imaging", *Annals of Surgical Oncology*, vol. 19, no. 6, pp. 1825–1830, 2012. DOI: 10.1245/s10434-011-2200-7.

[9] V. Giuliano and C. Giuliano, "Improved breast cancer detection in asymptomatic women using 3D-automated breast ultrasound in mammographically dense breasts", *Clinical Imaging*, vol. 37, no. 3, pp. 480–486, 2013. DOI: 10.1016/j.clinimag.2012.09.018.

[10] S. M. Dudea, M. Lenghel, C. Botar-Jid, D. Vasilescu and M. Duma, "Ultrasonography of superficial lymph nodes: Benign vs. malignant", *Medical Ultrasonography*, vol. 14, no. 4, pp. 294–306, 2012.

[11] D. M. Holwitt, M. E. Swatske, W. E. Gillanders, B. S. Monsees, F. Gao, R. L. Aft, T. J. Eberlein and J. A. Margenthaler, "The combination of axillary ultrasound and ultrasound-guided biopsy is an accurate predictor of axillary stage in clinically node-negative breast cancer patients", *American Journal of Surgery*, vol. 196, no. 4, pp. 477–482, 2008. DOI: 10.1016/j.amjsurg.2008.06.006.

[12] S. Alvarez, E. Añorbe, P. Alcorta, F. López, I. Alonso and J. Cortés, "Role of sonography in the diagnosis of axillary lymph node metastases in breast cancer: A systematic review", *American Journal of Roentgenology*, vol. 186, no. 5, pp. 1342–1348, 2006. DOI: 10.2214/AJR.05.0936.

[13] A. Aktaş, M. G. Gürleyik, S. Aydın Aksu, F. Aker and S. Güngör, "Diagnostic Value of Axillary Ultrasound, MRI, and 18F-FDG-PET/ CT in Determining Axillary Lymph Node Status in Breast Cancer Patients", *European Journal of Breast Health*, vol. 18, no. 1, pp. 37–47, 2022. DOI: 10.4274/ejbh.galenos.2021.2021-3-10.

[14] V. Altomare, G. Guerriero, R. Carino, C. Battista, A. Primavera, A. Altomare, D. Vaccaro, A. Esposito, A. M. Ferri and C. Rabitti, "Axillary lymph node echo-guided fine-needle aspiration cytology enables breast cancer patients to avoid a sentinel lymph node biopsy. Preliminary experience and a review of the literature", *Surgery Today*, vol. 37, no. 9, pp. 735–739, 2007. DOI: 10.1007/s00595-006-3366-7.

[15] S. G. Orel and M. D. Schnall, "MR imaging of the breast for the detection, diagnosis, and staging of breast cancer", *Radiology*, vol. 220, no. 1, pp. 13–30, 2001. DOI: 10.1148/radiology.220.1.r01jl3113.

[16] M. Van Goethem, W. Tjalma, K. Schelfout, I. Verslegers, I. Biltjes and P. Parizel, "Magnetic resonance imaging in breast cancer", *European Journal of Surgical Oncology*, vol. 32, no. 9, pp. 901–910, 2006. DOI: 10.1016/j.ejso.2006.06.009.

[17] V. E. Mortellaro, J. Marshall, L. Singer, S. N. Hochwald, M. Chang, E. M. Copeland and S. R. Grobmyer, "Magnetic Resonance Imaging for Axillary Staging in Patients With Breast Cancer", *Journal of Magnetic Resonance Imaging*, vol. 30, pp. 309–312, 2009. DOI: 10.1002/jmri.21802.

[18] P. A. Baltzer, M. Dietzel, H. P. Burmeister, R. Zoubi, M. Gajda, O. Camara and W. A. Kaiser, "Application of MR mammography beyond local staging: Is there a potential to accurately assess axillary lymph nodes? Evaluation of an extended protocol in an initial prospective study", *American Journal of Roentgenology*, vol. 196, no. 5, pp. 641–647, 2011. DOI: 10.2214/AJR.10.4889.

[19] R. L. Wahl, B. A. Siegel, R. E. Coleman and C. G. Gatsonis, "Prospective Multicenter Study of Axillary Nodal Staging by Positron Emission Tomography in Breast Cancer: A Report of the Staging Breast Cancer With PET Study Group", *Journal of Clinical Oncology*, vol. 22, no. 2, pp. 277–285, 2004. DOI: 10.1200/JCO.2004.04.148.

[20] R. E. Mansel, L. Fallow, M. Kissin, A. Goyal, R. G. Newcombe, J. M. Dixon, C. Yiangou, K. Horgan, N. Bundred, I. Monypenny, D. England, M. Sibbering, T. I. Abdullah, L. Barr, U. Chetty, D. H. Sinnett, A. Fleissig, D. Clarke and P. J. Ell, "Randomized Multicenter Trial of Sentinel Node Biopsy Versus Standard Axillary Treatment in Operable Breast Cancer: The ALMANAC Trial", *Journal of the National Cancer Institute*, vol. 98, no. 9, pp. 599–609, 2006. DOI: 10.1093/jnci/djj158.

[21] U. Veronesi, G. Paganelli, G. Viale, A. Luini, S. Zurrida, V. Galimberti, M. Intra, P. Veronesi, C. Robertson, P. Maisonneuve, G. Renne, C. De Cicco, F. De Lucia and R. Gennari, "A Randomized Comparison of Sentinel-Node Biopsy with Routine Axillary Dissection in Breast Cancer", *New England Journal of Medicine*, vol. 349, no. 6, pp. 546–553, 2003. DOI: 10.1056/NEJMoa012782.

[22] D. N. Krag, S. J. Anderson, T. B. Julian, A. M. Brown, S. P. Harlow, T. Ashikaga, D. L. Weaver, B. J. Miller, L. M. Jalovec, T. G. Frazier, R. D. Noyes, A. Robidoux, H. M. C. Scarth, D. M. Mammolito, D. R. Mccready and P Eleftherios, "Technical outcomes of sentinel-lymph-node resection and conventional axillary-lymph-node dissection in patients with clinically node-negative breast cancer: results from the NSABP B-32 randomised phase III trial", *The Lancet Oncology*, vol. 8, no. 10, pp. 881–888, 2007. DOI: 10.1016/S1470-2045(07)70278-4.

[23] M. B. Mainiero, C. M. Cinelli, S. L. Koelliker, T. A. Graves and M. A. Chung, "Axillary Ultrasound and Fine-Needle Aspiration in the Preoperative Evaluation of the Breast Cancer Patient: An Algorithm Based on Tumor Size and Lymph Node Appearance", *American Journal of Roentgenology*, vol. 195, no. 5, pp. 1261–1267, 2010. DOI: 10.2214/AJR.10.4414.

[24] H. Rahbar, J. L. Conlin, S. Parsian, W. B. DeMartini, S. Peacock, C. D. Lehman and S. C. Partridge, "Suspicious Axillary Lymph Nodes Identified on Clinical Breast MRI in Patients Newly Diagnosed with Breast Cancer: Can Quantitative Features Improve Discrimination of Malignant from Benign?", *Academic Radiology*, vol. 22, no. 4, pp. 430–438, 2015. DOI: 10.1016/j.acra.2014.10.010.

[25] A. Lucci, L. M. McCall, P. D. Beitsch, P. W. Whitworth, D. S. Reintgen, P. W. Blumencranz, A. M. Leitch, S. Saha, K. K. Hunt and A. E. Giuliano, "Surgical Complications Associated With Sentinel Lymph Node Dissection (SLND) Plus Axillary Lymph Node Dissection Compared With SLND Alone in the American College of Surgeons Oncology Group Trial Z0011", *Journal of Clinical Oncology*, vol. 25, no. 24, pp. 3657–3663, 2007. DOI: 10.1200/JCO.2006.07.4062.

[26] G. H. Sakorafas, G. Peros, L. Cataliotti and G. Vlastos, "Lymphedema following axillary lymph node dissection for breast cancer", *Surgical Oncology*, vol. 15, no. 3, pp. 153–165, 2006. DOI: 10.1016/j.suronc.2006.11.003.

[27] G. Gill, "Sentinel-lymph-node-based management or routine axillary clearance? One-year outcomes of sentinel node biopsy versus axillary clearance (SNAC): A randomized controlled surgical trial", *Annals of Surgical Oncology*, vol. 16, no. 2, pp. 266–275, 2009. DOI: 10.1245/s10434-008-0229-z.

[28] G. R. Kim, J. S. Choi, B. K. Han, J. E. Lee, S. J. Nam, E. Y. Ko, E. S. Ko and S. K. Lee, "Preoperative axillary US in early-stage breast cancer: Potential to prevent unnecessary axillary lymph node dissection", *Radiology*, vol. 288, no. 1, pp. 55–63, 2018.

[29] G. Viale, S. Zurrida, E. Maiorano, G. Mazzarol, G. Pruneri, G. Paganelli, P. Maisonneuve and U. Veronesi, "Predicting the status of axillary sentinel lymph nodes in 4351 patients with invasive breast carcinoma treated in a single institution", *Cancer*, vol. 103, no. 3, pp. 492–500, 2005. DOI: 10.1002/cncr.20809.

[30] S. Zahoor, A. Haji, A. Battoo, M. Qurieshi, W. Mir and M. Shah, "Sentinel Lymph Node Biopsy in Breast Cancer: A Clinical Review and Update", *Journal of Breast Cancer*, vol. 20, no. 3, pp. 217–227, 2017. DOI: 10.4048/jbc.2017.20.3.217.

[31] A. E. Giuliano, L. McCall, P. D. Beitsch, P. W. Whitworth, P. W. Blumencranz, A. M. Leitch, S. Saha, K. K. Hunt, M. Morrow and K. Ballman, "Locoregional Recurrence after Sentinel Lymph Node Dissection with or without Axillary Dissection in Patients with Sentinel Lymph Node Metastases: The American College of Surgeons Oncology Group Z0011 Randomized Trial", *Annals of Surgery*, vol. 252, no. 3, pp. 426–433, 2010. DOI: 10.1097/SLA.0b013e3181f08f32.

[32] F. Magnoni, V. Galimberti, G. Corso, M. Intra, V. Sacchini and P. Veronesi, "Axillary surgery in breast cancer: An updated historical perspective", *Seminars in Oncology*, vol. 47, no. 6, pp. 341–352, 2020. DOI: 10.1053/j.seminoncol.2020.09.001.

[33] S. C. Hagness, A. Taflove, J. E. Bridges and L. Fellow, "Two-Dimensional FDTD Analysis of a Pulsed Microwave Confocal System for Breast Cancer Detection: Fixed-Focus and Antenna-Array Sensors", *IEEE Transactions on Biomedical Engineering*, vol. 45, no. 12, pp. 1470–1480, 1998. DOI: 10.1109/10.730440.

[34] A. Fasoula, L. Duchesne, J. D. G. Cano, P. Lawrence, G. Robin and J.-G. Bernard, "On-Site Validation of a Microwave Breast Imaging System, before First Patient Study", *Diagnostics*, vol. 8, no. 53, pp. 1–38, 2018. DOI: 10.3390/diagnostics8030053.

[35] M. Shere, I. Lyburn, R. Sidebottom, H. Massey, C. Gillett and L. Jones, "MARIA® M5: A multicentre clinical study to evaluate the ability of the Micrima radiowave radar breast imaging system (MARIA®) to detect lesions in the symptomatic breast", *European Journal of Radiology*, vol. 116, pp. 61–67, 2019. DOI: 10.1016/j.ejrad.2019.04.017.

[36] J. A. Vasquez, R. Scapaticci, G. Turvani, G. Bellizzi, D. O. Rodriguez-Duarte, N. Joachimowicz, B. Duchêne, E. Tedeschi, M. R. Casu, L. Crocco and F. Vipiana, "A Prototype Microwave System for 3D Brain Stroke Imaging", *Sensors*, vol. 20, no. 9, pp. 1–16, 2020. DOI: 10.3390/s20092607.

[37] B. Amin, A. Shahzad, M. O'Halloran and M. A. Elahi, "Microwave bone imaging: A preliminary investigation on numerical bone phantoms for bone health monitoring", *Sensors*, vol. 20, no. 21, 2020. DOI: 10.3390/s20216320.

[38] R. C. Conceição, M. O'Halloran, M. Glavin and E. Jones, "Comparison of Planar and Circular Antenna Configurations for Breast Cancer Detection Using Microwave Imaging", *Progress In Electromagnetics Research*, vol. 99, pp. 1–20, 2009. DOI: 10.2528/PIER09100204.

[39] R. C. Conceição, J. J. Mohr, M. O'Halloran, T. Rubæk, D. Byrne, M. A. Elahi, E. Jones, M. Glavin, M. Jones, P. Kosmas and Y. Chen, *An Introduction to Microwave Imaging for Breast Cancer Detection*, R. C. Conceição, J. J. Mohr and M. O'Halloran, Eds., ser. Biological and Medical Physics, Biomedical Engineering. Switzerland: Springer, 2016. DOI: 10.1007/978-3-319-27866-7.

[40] F. Hillen and A. W. Griffioen, "Tumour vascularization: Sprouting angiogenesis and beyond", *Cancer and Metastasis Reviews*, vol. 26, no. 3-4, pp. 489–502, 2007. DOI: 10.1007/s10555-007-9094-7.

[41] N. K. Nikolova, "Microwave imaging for breast cancer", *IEEE Microwave Magazine*, vol. 12, no. 7, pp. 78–94, 2011. DOI: 10.1109/MMM.2011.942702.

[42] H. B. Lim, N. Thi, T. Nhung, E.-p. Li and N. D. Thang, "Confocal Microwave Imaging for Breast Cancer Detection : Delay-Multiply-and-Sum Image", *IEEE Transactions on Biomedical Engineering*, vol. 55, no. 6, pp. 1697–1704, 2008. DOI: 10.1109/TBME.2008.919716.

[43] E. C. Fear, J. Bourqui, C. Curtis, D. Mew, B. Docktor and C. Romano, "Microwave breast imaging with a monostatic radar-based system: A study of application to patients", *IEEE Transactions on Microwave Theory and Techniques*, vol. 61, no. 5, pp. 2119–2128, 2013. DOI: 10.1109/TMTT.2013.2255884.

[44] D. O'Loughlin, B. L. Oliveira, A. Santorelli, E. Porter, M. Glavin, E. Jones, M. Popovic and M. O'Halloran, "Sensitivity and Specificity Estimation using Patient-Specific Microwave Imaging in Diverse Experimental Breast Phantoms", *IEEE Transactions on Medical Imaging*, vol. 38, no. 1, pp. 303–311, 2019. DOI: 10.1109/TMI.2018.2864150.

[45] A. Vispa, L. Sani, M. Paoli, A. Bigotti, G. Raspa, N. Ghavami, S. Caschera, M. Ghavami, M. Duranti and G. Tiberi, "UWB device for breast microwave imaging: phantom and clinical validations", *Measurement*, vol. 146, pp. 582–589, 2019. DOI: 10.1016/j.measurement.2019.05.109.

[46] E. Porter, H. Bahrami, A. Santorelli, B. Gosselin, L. A. Rusch and M. Popović, "A Wearable Microwave Antenna Array for Time-Domain Breast Tumor Screening", *IEEE Transactions on Medical Imaging*, vol. 35, no. 6, pp. 1501–1509, 2016. DOI: 10.1109/TMI.2016.2518489.

[47] M. Adachi, T. Nakagawa, T. Fujioka, M. Mori, K. Kubota, G. Oda and T. Kikkawa, "Feasibility of Portable Microwave Imaging Device for Breast Cancer Detection", *Sensors*, vol. 12, no. 1, 2021. DOI: 10.1109/TMI.2016.2518489.

[48] M. T. Islam, M. Z. Mahmud, M. T. Islam, S. Kibria and M. Samsuzzaman, "A Low Cost and Portable Microwave Imaging System for Breast Tumor Detection Using UWB Directional Antenna array", *Scientific Reports*, vol. 9, no. 15491, pp. 1–13, 2019. DOI: 10.1038/s41598-019-51620-z.

[49] J. M. Felício, J. M. Bioucas-Dias, J. R. Costa and C. A. Fernandes, "Microwave Breast Imaging using a Dry Setup", *IEEE Transactions on Computational Imaging*, vol. 6, pp. 167–180, 2020. DOI: 10.1109/TCI.2019.2931079.

[50] M. Solis-Nepote, T. Reimer and S. Pistorius, "An Air-Operated Bistatic System for Breast Microwave Radar Imaging: Pre-Clinical Validation", in *41st Annual International Conference of the IEEE Engineering in Medicine and Biology Society (EMBC)*, Berlin, Germany, 2019, pp. 1859–1862. DOI: 10.1109/EMBC.2019.8857646.

[51] T. Reimer, M. Solis-Nepote and S. Pistorius, "The Application of an Iterative Structure to the Delay-and-Sum and the Delay-Multiply-and-Sum Beamformers in Breast Microwave Imaging", *Diagnostics*, vol. 10, no. 6, pp. 411–426, 2020. DOI: 10.3390/diagnostics10060411.

[52] R. J. N. Eleutério, "Microwave Imaging of the Axilla to Aid Breast Cancer Diagnosis", Master, Faculdade de Ciências e Tecnologia, Universidade Nova de Lisboa, Portugal, 2014.

[53] R. Eleutério and R. C. Conceição, "Initial Study for Detection of Multiple Lymph Nodes in the Axillary Region Using Microwave Imaging", in *11th European Conference on Antennas and Propagation (EuCAP)*, Lisbon, Portugal, 2015, pp. 1–3.

[54] J. Liu and S. G. Hay, "Prospects for Microwave Imaging of the Lymphatic System in the Axillary", in *Antennas and Propagation in Wireless Communications (APWC)*, Cairns, QLD, Australia, 2016, pp. 183–186. DOI: 10.1109/APWC.2016.7738152.

[55] M. Savazzi, S. Abedi, N. Ištuk, N. Joachimowicz, H. Roussel, E. Porter, M. O' Halloran, J. R. Costa, C. A. Fernandes, J. M. Felício and R. C. Conceição, "Development of an anthropomorphic phantom of the axillary region for microwave imaging assessment", *Sensors*, vol. 20, no. 17, p. 4968, 2020. DOI: https://doi.org/10.3390/s20174968.

[56] M. Savazzi, J. R. Costa, C. A. Fernandes, J. M. Felicio and R. C. Conceicao, "Numerical Assessment of Microwave Imaging for Axillary Lymph Nodes Screening Using Anthropomorphic Phantom", in *15th European Conference on Antennas and Propagation (EuCAP)*, Düssoldorf, Germany, 2021. DOI: 10.23919/EuCAP51087.2021.9410925.

[57] J. W. Choi, J. Cho, Y. Lee, J. Yim, B. Kang, K. O. Ki, H. J. Woo, J. K. Hee, C. Cheon, H. D. Lee and Y. Kwon, "Microwave detection of metastasized breast cancer cells in the lymph node; potential application for sentinel lymphadenectomy", *Breast Cancer Research and Treatment*, vol. 86, no. 2, pp. 107–115, 2004. DOI: 10.1023/b:brea.0000032979.52773.fb.

[58] T. R. Cameron, M. Okoniewski and E. C. Fear, "A Preliminary Study of the Electrical Properties of Healthy and Diseased Lymph Nodes", in *International Symposium on Antenna Technology and Applied Electromagnetics & the American Electromagnetics Conference (ANTEM-AMEREM)*, Ottawa, Canada, 2010. DOI: 10.1109/ANTEM.2010.5552566.

[59] D. B. Kopans, "Breast Anatomy and Basic Histology Physiology", in *Breast Imaging*, 3rd Ed., Philadelphia, USA: Lippincott Williams & Wilkins, 2007, ch. 2A, pp. 7–42.

[60] S. Standring, "Chest Wall and Breast", in *Gray's Anatomy: The Anatomical Basis of Clinical Practice*, 41st Ed., Elsevier Limited, 2016, ch. 7, pp. 931–952.

[61] E. Sickles, D. CJ, B. LW and E. Al, "ACR BI-RADS® Mammography", in *ACR BI-RADS® Atlas, Breast Imaging Reporting and Data System*, Reston, VA: American College of Radiology, 2013, pp. 121–140.

[62] I. Schreer, "Dense breast tissue as an important risk factor for breast cancer and implications for early detection", *Breast Care*, vol. 4, no. 2, pp. 89–92, 2009. DOI: 10.1159/000211954.

[63] Division of Cancer Prevention and Control, *What Is Breast Cancer?*, 2021. [Online]. Available: https://www.cdc.gov/cancer/breast/basic{_}info/what-is-breast-cancer.htm (accessed on 24/05/2021).

[64] National Cancer Institute (U.S.) Office of Cancer Communications, "The Development of Breast Cancer", in *The Breast Cancer Digest: A Guide to Medical Care, Emotional Support, Educational Programs, and Resources*, ser. DHHS publication, 2nd ed., Bethesda, Maryland: National Cancer Institute, 1984, pp. 4–12.

[65] American Joint Committee on Cancer, "Breast Cancer", in *AJCC Cancer Staging Manual*, 8th Ed., New York, NY, USA: Springer, 2018.

[66] American Cancer Society, *Non-cancerous Breast Conditions*, 2018. [Online]. Available: https://www.cancer.org/cancer/breast-cancer/non-cancerous-breast-conditions.html (accessed on 06/12/2020).

[67] J. M. Castañeda-Gill and J. K. Vishwanatha, "Antiangiogenic mechanisms and factors in breast cancer treatment", *Journal of Carcinogenesis*, vol. 15, no. 1, pp. 1–11, 2016. DOI: 10.4103/1477-3163.176223.

[68] Medical Art Library, *Breast Cancer*, 2021. [Online]. Available: https://medicalartlibrary.com/breast-cancer/ (accessed on 24/05/2021).

[69] Breast 360 - Program of The American Society of Breast Surgeons Foundation, *Clinical Staging of Breast Cancer*, 2017. [Online]. Available: https://breast360.org/topics/2017/01/01/clinical-staging-breast-cancer/ (accessed on 24/05/2021).

[70] S. Standring, "Blood, lymphoid tissues and haemopoiesis", in *Gray's Anatomy: The Anatomical Basis of Clinical Practice*, 41st Ed., Elsevier Limited, 2016, pp. 68–80.

[71] P. P. Rosen, M. L. Lesser, D. W. Kinne and E. J. Beattie, "Discontinuous or 'skip' metastases in breast carcinoma: Analysis of 1228 axillary dissections", *Annals of Surgery*, vol. 197, no. 3, pp. 276–283, 1983.

[72] U. Veronesi, F. Rilke, A. Luini, V. Sacchini, V. Galimberti, T. Campa, E. D. Bei, M. Greco, A. Magni, M. Merson and V. Quagliuolo, "Distribution of axillary node metastases by level of invasion: An analysis of 539 cases", *Cancer*, vol. 59, no. 4, pp. 682–687, 1987.

[73] M. Khafagy, A. Mostafa and I. Fakhr, "Distribution of axillary lymph node metastases in different levels and groups in breast cancer, a pathological study", *Journal of the Egyptian National Cancer Institute*, vol. 23, no. 1, pp. 25–30, 2011. DOI: 10.1016/j.jnci.2011.07.004.

[74] R. L. Goodman, A. Grann, P. Saracco and M. F. Needham, "The relationship between radiation fields and regional lymph nodes in carcinoma of the breast", *International Journal of Radiation Oncology Biology Physics*, vol. 50, no. 1, pp. 99–105, 2001. DOI: 10.1016/S0360-3016(00)01581-9.

[75] G. C. Bentel, L. B. Marks, P. H. Hardenbergh and L. R. Prosnitz, "Variability of the depth of supraclavicular and axillary lymph nodes in patients with breast cancer: Is a posterior axillary boost field necessary?", *International Journal of Radiation Oncology Biology Physics*, vol. 47, no. 3, pp. 755–758, 2000. DOI: 10.1016/s0360-3016(00)00485-5.

[76] H. Rahbar, S. C. Partridge, S. H. Javid and C. D. Lehman, "Imaging Axillary Lymph Nodes in Patients with Newly Diagnosed Breast Cancer", *Current Problems in Diagnostic Radiology*, vol. 41, no. 5, pp. 149–158, 2012. DOI: 10.1067/j.cpradiol.2011.08.002.

[77] National Cancer Institute, *Lymph Nodes*, 2018. [Online]. Available: https://training.seer.cancer.gov/anatomy/lymphatic/components/nodes.html (accessed on 05/02/2019).

[78] C. E. Edmonds, S. P. Zuckerman and E. F. Conant, "Management of Unilateral Axillary Lymphadenopathy Detected on Breast MRI in the Era of COVID-19 Vaccination", *American Journal of Roentgenology*, vol. 217, no. 4, pp. 831–834, 2021. DOI: doi.org/10.2214/AJR.21.25604.

[79] C. Özütemiz, L. A. Krystosek, A. L. Church, A. Chauhan, J. M. Ellermann, E. Domingo-Musibay and D. Steinberger, "Lymphadenopathy in COVID-19 Vaccine Recipients: Diagnostic Dilemma in Oncologic Patients", *Radiology*, vol. 300, no. 1, E290–E294, 2021. DOI: 10.1148/radiol.2021210275.

[80] V. Sathyanarayan and S. Bharani, "Enlarged lymph nodes in head and neck cancer: Analysis with triplex ultrasonography", *Annals of Maxillofacial Surgery*, vol. 3, no. 1, p. 35, 2013. DOI: 10.4103/2231-0746.110077.

[81] A. T. Ahuja, M Ying, S. Y. Ho, G Antonio, Y. P. Lee, A. D. King and K. T. Wong, "Ultrasound of malignant cervical lymph nodes", *Cancer Imaging*, vol. 8, pp. 48–56, 2008. DOI: 10.1102/1470-7330.2008.0006.

[82] C. F. Chen, Y. L. Zhang, Z. L. Cai, S. M. Sun, X. F. Lu, H. Y. Lin, W. Q. Liang, M. H. Yuan and D. Zeng, "Predictive Value of Preoperative Multidetector-Row Computed Tomography for Axillary Lymph Nodes Metastasis in Patients With Breast Cancer", *Frontiers in Oncology*, vol. 8, no. 666, pp. 1–10, 2019. DOI: 10.3389/fonc.2018.00666.

[83] Y. Mao, S. Hedgire and M. Harisinghani, "Radiologic Assessment of Lymph Nodes in Oncologic Patients", *Current Radiology Reports*, vol. 2, no. 36, pp. 1–13, 2014. DOI: 10.1007/s40134-013-0036-6ESSENTIALS.

[84] Y. Liu, M. Bellomi, G. Gatti and X. Ping, "Accuracy of computed tomography perfusion in assessing metastatic involvement of enlarged axillary lymph nodes in patients with breast cancer", *Breast Cancer Research*, vol. 9, no. R40, 2007. DOI: 10.1186/bcr1738.

[85] N. Mori, S. Mugikura, M. Miyashita, Y. Kudo, M. Suzuki, L. Li, Y. Mori, S. Takahashi and K. Takase, "Perfusion contrast-enhanced ultrasound to predict early lymph-node metastasis in breast cancer", *Japanese Journal of Radiology*, vol. 37, no. 2, pp. 145–153, 2019. DOI: 10.1007/s11604-018-0792-6.

[86] G. Unal, G. Slabaugh, A. Ess, A. Yezzi, T. Fang, J. Tyan, M. Requardt, R. Krieg, R. Seethamraju, M. Harisinghani and R. Weissleder, "Semi-automatic lymph node segmentation in LN-MRI", in *International Conference on Image Processing*, Atlanta, GA, USA, 2006, pp. 77–80. DOI: 10.1109/ICIP.2006.312366.

[87] A. Barbu, M. Suehling, X. Xu, D. Liu, S. K. Zhou and D. Comaniciu, "Automatic detection and segmentation of lymph nodes from CT data", *IEEE Transactions on Medical Imaging*, vol. 31, no. 2, pp. 240–250, 2012. DOI: 10.1109/TMI.2011.2168234.

[88] A. Barbu, M. Suehling, X. J. Xu, D. Liu, S. K. Zhou and D. Comaniciu, *Method and System for Automatic Detection and Segmentation of Axillary Lymph Nodes*, *U.S. Patent 8391579 B2*, 2013.

[89] R. Ha, P. Chang, J. Karcich, S. Mutasa, R. Fardanesh, R. T. Wynn, M. Z. Liu and S. Jambawalikar, "Axillary Lymph Node Evaluation Utilizing Convolutional Neural Networks Using MRI Dataset", *Journal of Digital Imaging*, vol. 31, pp. 851–856, 2018. DOI: 10.1007/s10278-018-0086-7.

[90] Z. Liu, S. Ni, C. Yang, W. Sun, D. Huang, H. Su, J. Shu and N. Qin, "Axillary lymph node metastasis prediction by contrast-enhanced computed tomography images for breast cancer patients based on deep learning", *Computers in Biology and Medicine*, vol. 136, no. 104715, 2021. DOI: 10.1016/j.compbiomed.2021.104715.

[91] Y. Xie, B. Guo, L. Xu, J. Li and P. Stoica, "Multistatic Adaptive Microwave Imaging for Early Breast Cancer Detection", *IEEE Transactions on Biomedical Engineering*, vol. 53, no. 8, pp. 1647–1657, 2006. DOI: 10.1109/TBME.2006.878058.

[92] M. Klemm, D. Gibbins, J. Leendertz, T. Horseman, A. Preece, R. Benjamin and I. Craddock, "Development and Testing of a 60-Element UWB Conformal Array for Breast Cancer Imaging", in *5th European Conference on Antennas and Propagation (EUCAP)*, Rome, Italy, 2011, pp. 3077–3079.

[93] A. W. Preece, I. Craddock, M. Shere, L. Jones and H. L. Winton, "MARIA M4: clinical evaluation of a prototype ultrawideband radar scanner for breast cancer detection", *Journal of Medical Imaging*, vol. 3, no. 3, p. 033 502, 2016. DOI: 10.1117/1.JMI.3.3.033502.

[94] B. M. Moloney, P. F. Mcanena, S. M. Elwahab, A. Fasoula, L. Duchesne, J. D. Cano, C. Glynn, A. O'connell, R. Ennis, A. J. Lowery and M. J. Kerin, "The Wavelia Microwave Breast Imaging system-tumour discriminating features and their clinical usefulness", *British Journal of Radiology*, vol. 94, no. 1128, 2021. DOI: 10.1259/bjr.20210907.

[95] J. M. Felício, J. M. Bioucas-Dias, J. R. Costa and C. A. Fernandes, "Antenna Design and Near-Field Characterization for Medical Microwave Imaging Applications", *IEEE Transactions on Antennas and Propagation*, vol. 67, no. 7, pp. 4811–4824, 2019. DOI: 10.1109/TAP.2019.2905742.

[96] International Commission of Non-Ionizing Radiation Protection (ICNIRP), "ICNIRP Guidelines for limiting exposure to electromagnetic fields (100 kHz to 300 GHz)", *Health Physics*, vol. 118, no. 5, pp. 483–524, 2020. DOI: 10.1097/HP.0000000000001210.

[97] A. G. Dagheyan, A. Molaei, R. Obermeier and J. Martinez-Lorenzo, "Preliminary imaging results and SAR analysis of a microwave imaging system for early breast cancer detection", in *38th Annual International Conference of the IEEE Engineering in Medicine and Biology Society (EMBC)*, Orlando, USA, 2016, pp. 1066–1069. DOI: 10.1109/EMBC.2016.7590887.

[98] R. Yahya, M. R. Kamarudin and N. Seman, "New wideband textile antenna for SAR investigation in head microwave imaging", in *IEEE MTT-S International Microwave Workshop Series on RF and Wireless Technologies for Biomedical and Healthcare Applications (IMWS-Bio)*, London, UK, 2015. DOI: 10.1109/IMWS-BIO.2014.7032443.

[99] X. Li and S. Hagness, "A confocal microwave imaging algorithm for breast cancer detection", *IEEE Microwave and Wireless Components Letters*, vol. 11, no. 3, pp. 130–132, 2001. DOI: 10.1109/7260.915627.

[100] E. J. Bond, S. Member, X. Li, S. Member, S. C. Hagness and B. D. V. Veen, "Microwave Imaging via Space-Time Beamforming for Early Detection of Breast Cancer", *IEEE Transactions on Antennas and Propagation*, vol. 51, no. 8, pp. 1690–1705, 2003. DOI: 10.1109/TAP.2003.815446.

[101] M. A. Elahi, M. Glavin, E. Jones and M. O'Halloran, "Adaptive artifact removal for selective multistatic microwave breast imaging signals", *Biomedical Signal Processing and Control*, vol. 34, pp. 93–100, 2017. DOI: 10.1016/j.bspc.2017.01.006.

[102] M. Klemm, I. J. Craddock, J. A. Leendertz, A. Preece and R. Benjamin, "Improved Delay-and-Sum Beamforming Algorithm for Breast Cancer Detection", *International Journal of Antennas and Propagation*, vol. 2008, pp. 1–9, 2008. DOI: 10.1155/2008/761402.

[103] M. Klemm, J. A. Leendertz, D. Gibbins, I. J. Craddock, A. Preece and R. Benjamin, "Microwave radar-based breast cancer detection: Imaging in inhomogeneous breast phantoms", *IEEE Antennas and Wireless Propagation Letters*, vol. 8, pp. 1349–1352, 2009. DOI: 10.1109/LAWP.2009.2036748.

[104] M. O'Halloran, M. Glavin and E. Jones, "Channel-ranked beamformer for the early detection of breast cancer", *Progress In Electromagnetics Research*, vol. 103, no. 4, pp. 153–168, 2010. DOI: 10.2528/PIER10030902.

[105] J. M. Lopez-Sanchez and J. Fortuny-Guasch, "3-D Radar Imaging Using Range Migration Techniques", *IEEE Transactions on Antennas and Propagation*, vol. 48, no. 5, pp. 728–737, 2000. DOI: 10.1109/8.855491.

[106] C. A. Fernandes, E. B. Lima and J. R. Costa, "Dielectric lens antennas", in *Handbook of Antenna Technologies*, Z. N. Chen, Ed., Singapore: Springer, 2016, pp. 1001–1064. DOI: 10.1007/978-981-4560-75-7.

[107] Y. Wang and A. Abbosh, "Three-dimensional Microwave Breast Imaging Using Least Electrical Path Method", in *Asia-Pacific Microwave Conference Proceedings (APMC)*, Seoul, South Korea, 2013, pp. 1021–1023. DOI: 10.1109/APMC.2013.6695011.

[108] W. Shao, S. Member, T. R. Mccollough and W. J. Mccollough, "A Phase Shift and Sum Method for UWB Radar Imaging in Dispersive Media", *IEEE Transactions on Microwave Theory and Techniques*, vol. 67, no. 5, pp. 2018–2027, 2019. DOI: 10.1109/TMTT.2019.2891539.

[109] M. Klemm, I. J. Craddock, A. Preece, J. Leendertz and R. Benjamin, "Evaluation of a hemi-spherical wideband antenna array for breast cancer imaging", *Radio Science*, vol. 43, no. 6, pp. 1–15, 2008. DOI: 10.1029/2007RS003807.

[110] J. M. Sill and E. C. Fear, "Tissue sensing adaptive radar for breast cancer detection-experimental investigation of simple tumor models", *IEEE Transactions on Microwave Theory and Techniques*, vol. 53, no. 11, pp. 3312–3319, 2005. DOI: 10.1109/TMTT.2005.857330.

[111] M. O'Halloran, M. Glavin and E. Jones, "Quasi-Multistatic MIST Beamforming for the Early Detection of Breast Cancer", *IEEE Transactions on Biomedical Engineering*, vol. 57, no. 4, pp. 830–840, 2010. DOI: 10.1109/TBME.2009.2016392.

[112] B. Maklad, C. Curtis, E. Fear and G. Messier, "Neighborhood-based algorithm to facilitate the reduction of skin reflections in radar-based microwave imaging", *Progress In Electromagnetics Research B*, vol. 39, no. 39, pp. 115–139, 2012. DOI: 10.2528/PIERB11122208.

[113] G. Ruvio, R. Solimene, A. Cuccaro, D. Gaetano, J. E. Browne and M. J. Ammann, "Breast cancer detection using interferometric MUSIC: Experimental and numerical assessment", *Medical Physics*, vol. 41, no. 10, 2014. DOI: 10.1118/1.4892067.

[114] D. O'Loughlin, "Improving the Sensitivity of Radar-based Breast Imaging Algorithms in Diverse Patient Populations", Ph.D. dissertation, National University of Ireland Galway, Ireland, 2018.

[115] Keysight Technologies, *Basics of Measuring the Dielectric Properties of Materials*, 2019. [Online]. Available: http://literature.cdn.keysight.com/litweb/pdf/5989-2589EN.pdf (accessed on 24/05/2021).

[116] S. Gabriel, R. W. Lau and C. Gabriel, "The dielectric properties of biological tissues: III Parametric models for the dielectric spectrum of tissues", *Physics in Medicine and Biology*, vol. 41, no. 11, pp. 2271–2293, 1996. DOI: 10.1088/0031-9155/41/11/003.

[117] C. Gabriel and A. Peyman, "Dielectric measurement: Error analysis and assessment of uncertainty", *Physics in Medicine and Biology*, vol. 51, no. 23, pp. 6033–6046, 2006. DOI: 10.1088/0031-9155/51/23/006.

[118] A. La Gioia, E. Porter, I. Merunka, A. Shahzad, S. Salahuddin, M. Jones and M. O'Halloran, "Open-Ended Coaxial Probe Technique for Dielectric Measurement of Biological Tissues: Challenges and Common Practices", *Diagnostics*, vol. 8, no. 2, 2018. DOI: 10.3390/diagnostics8020040.

[119] E. Porter, A. La Gioia, S. Salahuddin, S. Decker, A. Shahzad, M. A. Elahi, M. O'Halloran and O. Beyan, "Minimum information for dielectric measurements of biological tissues (MINDER): A framework for repeatable and reusable data", *International Journal of RF and Microwave Computer-Aided Engineering*, vol. 28, no. e21201, pp. 1–27, 2018. DOI: 10.1002/mmce.21201.

[120] R. J. Halter, T. Zhou, P. M. Meaney, A. Hartov, R. J. Barth, K. M. Rosenkranz, W. A. Wells, C. A. Kogel, A. Borsic, E. J. Rizzo and K. D. Paulsen, "The correlation of in vivo and ex vivo tissue dielectric properties to validate electromagnetic breast imaging: Initial clinical experience", *Physiological Measurement*, vol. 30, no. 6, 2009. DOI: 10.1088/0967-3334/30/6/S08.

[121] D. Haemmerich, O. R. Ozkan, J. Z. Tsai, S. T. Staelin, S. Tungjitkusolmun, D. M. Mahvi and J. G. Webster, "Changes in electrical resistivity of swine liver after occlusion and postmortem", *Medical and Biological Engineering and Computing*, vol. 40, pp. 29–33, 2002. DOI: 10.1007/BF02347692.

[122] L. Farrugia, P. S. Wismayer, L. Z. Mangion and C. V. Sammut, "Accurate in vivo dielectric properties of liver from 500 MHz to 40 GHz and their correlation to ex vivo measurements", *Electromagnetic Biology and Medicine*, vol. 35, no. 4, pp. 365–373, 2016. DOI: 10.3109/15368378.2015.1120221.

[123] T. Athey, M. Stuchly and S. Stuchly, "Measurement of Radio Frequency Permittivity of Biological Tissues with an Open-Ended Coaxial Line: Part I", *IEEE Transactions on Microwave Theory and Techniques*, vol. 30, no. 1, pp. 82 –86, 1982. DOI: 10.1109/TMTT.1982.1131021.

[124] T. Sugitani, S. I. Kubota, S. I. Kuroki, K. Sogo, K. Arihiro, M. Okada, T. Kadoya, M. Hide, M. Oda and T. Kikkawa, "Complex permittivities of breast tumor tissues obtained from cancer surgeries", *Applied Physics Letters*, vol. 104, no. 25, p. 253 702, 2014. DOI: 10.1063/1.4885087.

[125] M. Lazebnik, L. McCartney, D. Popovic, C. B. Watkins, M. J. Lindstrom, J. Harter, S. Sewall, A. Magliocco, J. H. Booske, M. Okoniewski and S. C. Hagness, "A large-scale study of the ultrawideband microwave dielectric properties of normal breast tissue obtained from reduction surgeries", *Physics in Medicine and Biology*, vol. 52, no. 10, pp. 2637–3656, 2007. DOI: 10.1088/0031-9155/52/10/001.

[126] M. Lazebnik, D. Popovic, L. McCartney, C. B. Watkins, M. J. Lindstrom, J. Harter, S. Sewall, T. Ogilvie, A. Magliocco, T. M. Breslin, W. Temple, D. Mew, J. H. Booske, M. Okoniewski and S. C. Hagness, "A large-scale study of the ultrawideband microwave dielectric properties of normal, benign and malignant breast tissues obtained from cancer surgeries", *Physics in Medicine and Biology*, vol. 52, no. 20, pp. 6093–6115, 2007. DOI: 10.1088/0031-9155/52/20/002.

[127] E. Porter, A. L. Gioia, M. A. Elahi and M. O'Halloran, "Significance of heterogeneities in accurate dielectric measurements of biological tissues", in 32^{nd} *General Assembly and Scientific Symposium of the International Union of Radio Science (URSI GASS)*, Montreal, Canada, 2017. DOI: 10.23919/URSIGASS.2017.8104989.

[128] A. La Gioia, M. O'Halloran and E. Porter, "Challenges of Post-measurement Histology for the Dielectric Characterisation of Heterogeneous Biological Tissues", *Sensors*, vol. 20, no. 11, pp. 3290–3304, 2020. DOI: 10.3390/s20113290.

[129] A. Martellosio, M. Pasian, M. Bozzi, L. Perregrini, A. Mazzanti, F. Svelto, P. E. Summers, G. Renne, L. Preda and M. Bellomi, "Dielectric properties characterization from 0.5 to 50 GHz of breast cancer tissues", *IEEE Transactions on Microwave Theory and Techniques*, vol. 65, no. 3, pp. 998–1011, 2017. DOI: 10.1109/TMTT.2016.2631162.

[130] W. T. Joines, Y. Zhang, C. Li and R. L. Jirtle, "The measured electrical properties of normal and malignant human tissues from 50 to 900 MHz", *Medical Physics*, vol. 21, no. 4, pp. 547–550, 1994. DOI: 10.1118/1.597312.

[131] X. Yu, Y Sun, K. Cai, H. Yu, D. Zhou, D. Lu and S. X. Xin, "Dielectric Properties of Normal and Metastatic Lymph Nodes Ex Vivo From Lung Cancer Surgeries", *Bioelectromagnetics*, vol. 41, no. 2, pp. 148–155, 2020. DOI: 10.1002/bem.22246.

[132] M. Klemm, I. J. Craddock, J. A. Leendertz, A. Preece and R. Benjamin, "Radar-Based Breast Cancer Detection Using a Hemispherical Antenna Array - Experimental Results", *IEEE Transactions on Antennas and Propagation*, vol. 57, no. 6, pp. 1692–1704, 2009.

[133] E. Zastrow, S. K. Davis, M. Lazebnik, F. Kelcz, B. D. V. Veen and S. C. Hagness, "Development of anatomically realistic numerical breast phantoms with accurate dielectric properties for modeling microwave interactions with the human breast", *IEEE Transactions on Biomedical Engineering*, vol. 55, no. 12, pp. 2792–2800, 2008. DOI: 10.1109/TBME.2008.2002130.

[134] G. Zhu, B. Oreshkin, E. Porter, M. Coates and M. Popović, "Numerical breast models for commercial FDTD simulators", in 3^{rd} *European Conference on Antennas and Propagation (EuCAP)*, Berlin, Germany, 2009, pp. 263–267.

[135] A. H. Tunçay and I. Akduman, "Realistic microwave breast models through T1-weighted 3-D MRI data", *IEEE Transactions on Biomedical Engineering*, vol. 62, no. 2, pp. 688–698, 2015. DOI: 10.1109/TBME.2014.2364015.

[136] M. Omer and E. C. Fear, "Automated 3D method for the construction of flexible and reconfigurable numerical breast models from MRI scans", *Medical and Biological Engineering and Computing*, vol. 56, no. 6, pp. 1027–1040, 2018. DOI: 10.1007/s11517-017-1740-9.

[137] M. Lu, X. Xiao, H. Song, G. Liu, H. Lu and T. Kikkawa, "Accurate construction of 3-D numerical breast models with anatomical information through MRI scans", *Computers in Biology and Medicine*, vol. 130, p. 104 205, 2021. DOI: 10.1016/j.compbiomed.2020.104205.

[138] A. C. Pelicano, M. C. T. Gonçalves, D. M. Godinho, T. Castela, M. L. Orvalho, N. A. M. Araújo, E. Porter and R. C. Conceição, "Development of 3D MRI-Based Anatomically Realistic Models of Breast Tissues and Tumours for Microwave Imaging Diagnosis", *Sensors*, vol. 21, p. 8265, 2021. DOI: 10.3390/s21248265.

[139] M. Omer and E. Fear, "Anthropomorphic breast model repository for research and development of microwave breast imaging technologies", *Scientific Data*, vol. 5, 2018. DOI: 10.1038/sdata.2018.257.

[140] R. C. Conceição, L. G. Oliveira, B. Banks and E. Fear, "Development of Axilla Phantoms to Aid Breast Cancer Staging Via Sentinel Lymph Node Detection", in *8th European Conference on Antennas and Propagation (EuCAP)*, The Hague, Netherlands, 2014, pp. 522–524. DOI: 10.1109/EuCAP.2014.6901808.

[141] M. C. Gosselin, E. Neufeld, H. Moser, E. Huber, S. Farcito, L. Gerber, M. Jedensjo, I. Hilber, F. D. Gennaro, B. Lloyd, E. Cherubini, D. Szczerba, W. Kainz and N. Kuster, "Development of a new generation of high-resolution anatomical models for medical device evaluation: The Virtual Population 3.0", *Physics in Medicine and Biology*, vol. 59, no. 18, pp. 5287–5303, 2014.

[142] E. Porter, J. Fakhoury, R. Oprisor, M. Coates and M. Popovic, "Improved tissue phantoms for experimental validation of microwave breast cancer detection", in *4th European Conference on Antennas and Propagation (EuCAP)*, Barcelona, Spain, 2010.

[143] J. Garrett and E. Fear, "A New Breast Phantom With a Durable Skin Layer for Microwave Breast Imaging", *IEEE Transactions on Antennas and Propagation*, vol. 63, no. 4, pp. 1693–1700, 2015. DOI: 10.1109/TAP.2015.2393854.

[144] A. Santorelli, O. Laforest, E. Porter and M. Popović, "Image classification for a time-domain microwave radar system: Experiments with stable modular breast phantoms", in *9th European Conference on Antennas and Propagation (EuCAP)*, Lisbon, Portugal, 2015.

[145] N. Joachimowicz, C. Conessa, T. Henriksson and B. Duchêne, "Breast Phantoms for Microwave Imaging", *IEEE Antennas and Wireless Propagation Letters*, vol. 13, pp. 1333–1336, 2014. DOI: 10.1109/LAWP.2014.2336373.

[146] B. L. Oliveira, D. O'Loughlin, M. O'Halloran, E. Porter, M. Glavin and E. Jones, "Microwave Breast Imaging: Experimental tumour phantoms for the evaluation of new breast cancer diagnosis systems", *Biomedical Physics and Engineering Express*, vol. 4, no. 2, 2018. DOI: 10.1088/2057-1976/aaaaff.

[147] M. J. Burfeindt, T. J. Colgan, R. O. Mays, J. D. Shea, N. Behdad, B. D. V. Veen and S. C. Hagness, "MRI-Derived 3-D-Printed Breast Phantom for Microwave Breast Imaging Validation", *IEEE Antennas and Wireless Propagation Letters*, vol. 11, pp. 1610–1613, 2012. DOI: 10.1109/LAWP.2012.2236293.

[148] N. Joachimowicz, B. Duchêne, C. Conessa and O. Meyer, "Easy-to-produce adjustable realistic breast phantoms for microwave imaging", in *10th European Conference on Antennas and Propagation (EuCAP)*, Davos, Switzerland, 2016. DOI: 10.1109/EuCAP.2016.7481715.

[149] T. Rydholm, A. Fhager, M. Persson, S. Geimer and P. Meaney, "Effects of the Plastic of the Realistic GeePS-L2S-Breast Phantom", *Diagnostics*, vol. 8, no. 3, p. 61, 2018. DOI: 10.3390/diagnostics8030061.

[150] T. Reimer, J. Krenkevich and S. Pistorius, "An Open-Access Experimental Dataset for Breast Microwave Imaging", in *14th European Conference on Antennas and Propagation (EuCAP)*, Copenhagen, Denmark, 2020. DOI: 10.23919/EuCAP48036.2020.9135659.

[151] C. Westbrook, C. Kaut Roth and J. Talbot, *MRI in Practice*, 4th. New Jersey, USA: Wiley-Blackwell, 2011.

[152] D. Weishaupt, V. D. Köchli and B. Marincek, *How does MRI work?*, 2nd Ed., D. U. Heilmann, Ed. Heidelberg: Springer-Verlag Berlin Heidelberg, 2003.

[153] W. T. Dixon, "Simple proton spectroscopic imaging", *Radiology*, vol. 153, no. 1, pp. 189–194, 1984. DOI: doi.org/10.1148/radiology.153.1.6089263.

[154] U. Vovk, F. Pernuš and B. Likar, "A review of methods for correction of intensity inhomogeneity in MRI", *IEEE Transactions on Medical Imaging*, vol. 26, no. 3, pp. 405–421, 2007. DOI: 10.1109/TMI.2006.891486.

[155] C. Li, C. Xu, A. W. Anderson and J. C. Gore, "MRI Tissue Classification and Bias Field Estimation Based on Coherent Local Intensity Clustering: A Unified Energy Minimization Framework", in *International Conference on Information Processing in Medical Imaging*, vol. LNCS 5636, Philadelphia, USA, 2009, pp. 288–299. DOI: 10.1007/978-3-642-02498-6_24.

[156] N. J. Tustison, B. B. Avants, P. A. Cook, Y. Zheng, A. Egan, P. A. Yushkevich and J. C. Gee, "N4ITK: Improved N3 bias correction", *IEEE Transactions on Medical Imaging*, vol. 29, no. 6, pp. 1310–1320, 2010. DOI: 10.1109/TMI.2010.2046908.

[157] C. A. Glasbey and G. W. Horgan, "Mathematical Morphology", in *Image Analysis for the Biological Sciences*, Wiley, 1995, ch. 5.

[158] N. Otsu, "A Threshold Selection Method from Gray-Level Histograms", *IEEE Transactions on Systems, Man, and Cybernetics*, vol. 9, no. 1, pp. 62–66, 1979. DOI: 10.1109/TSMC.1979.4310076.

[159] Y. Feng, H. Zhao, X. Li, X. Zhang and H. Li, "A multi-scale 3D Otsu thresholding algorithm for medical image segmentation", *Digital Signal Processing*, vol. 60, pp. 186–199, 2017. DOI: 10.1016/j.dsp.2016.08.003.

[160] A. Rosenfeld and J. L. Pfaltz, "Sequential Operations in Digital Picture Processing", *Journal of the Association for Computing Machinery*, vol. 13, no. 4, pp. 471–494, 1966. DOI: 10.1145/321356.321357.

[161] J. C. Rajapakse and F. Kruggel, "Segmentation of MR images with intensity inhomogeneities", *Image and Vision Computing*, vol. 16, no. 3, pp. 165–180, 1998.

[162] J. Selvakumar, A. Lakshmi and T. Arivoli, "Brain tumor segmentation and its area calculation in brain MR images using K-mean clustering and Fuzzy C-mean algorithm", in *IEEE-International Conference on Advances in Engineering, Science and Management (ICAESM)*, Nagapattinam, India, 2012, pp. 186–190.

[163] K. Nie, J.-H. Chen, S. Chan, M.-K. I. Chau, H. J. Yu, S. Bahri, T. Tseng, O. Nalcioglu and M.-Y. Su, "Development of a quantitative method for analysis of breast density based on three-dimensional breast MRI", *Medical Physics*, vol. 35, no. 12, pp. 5253–5262, 2008. DOI: 10.1118/1.3002306.

[164] C. Dachena, A. Fedeli, A. Fanti, M. B. Lodi, G. Fumera, A. Randazzo and M. Pastorino, "Microwave Imaging of the Neck by Means of Artificial Neural Networks for Tumor Detection", *IEEE Open Journal of Antennas and Propagation*, vol. 2, pp. 1044–1056, 2021. DOI: 10.1109/OJAP.2021.3121177.

[165] M. Lu, X. Xiao, G. Liu and H. Lu, "Microwave breast tumor localization using wavelet feature extraction and genetic algorithm-neural network", *Medical Physics*, vol. 48, no. 10, pp. 6080–6093, 2021. DOI: 10.1002/mp.15198.

[166] A. Santorelli, E. Porter, E. Kirshin, Y. J. Liu and M. Popovic, "Investigation of Classifiers for Tumor Detection with an Experimental Time-Domain Breast Screening System", *Progress in Electromagnetics Research*, vol. 144, pp. 45–57, 2014. DOI: 10.2528/PIER13110709.

[167] D. Byrne, M. O'Halloran, M. Glavin and E. Jones, "Breast cancer detection based on differential ultrawideband microwave radar", *Progress In Electromagnetics Research M*, vol. 20, pp. 231–242, 2011.

[168] T. Reimer and S. Pistorius, "The Diagnostic Performance of Machine Learning in Breast Microwave Sensing on an Experimental Dataset", *IEEE Journal of Electromagnetics, RF and Microwaves in Medicine and Biology*, pp. 1–7, 2021. DOI: 10.1109/JERM.2021.3076100.

[169] R. A. Martins, J. M. Felicio, J. R. Costa and C. A. Fernandes, "Comparison of Slot-based and Vivaldi Antennas for Breast Tumor Detection using Machine Learning and Microwave Imaging Algorithms", in *15th European Conference on Antennas and Propagation (EuCAP)*, Düssoldorf, Germany, 2021. DOI: 10.23919/EuCAP51087.2021.9411128.

[170] S. K. Davis, B. D. Van Veen, S. C. Hagness and F. Kelcz, "Breast tumor characterization based on ultrawideband microwave backscatter", *IEEE Transactions on Biomedical Engineering*, vol. 55, no. 1, pp. 237–246, 2008. DOI: 10.1109/TBME.2007.900564.

[171] R. C. Conceição, M. O'Halloran, M. Glavin and E. Jones, "Support Vector Machines for the Classification of Early-Stage Breast Cancer Based on Radar Target Signatures", *Progress In Electromagnetics Research B*, vol. 23, no. 23, pp. 311–327, 2010. DOI: 10.2528/PIERB10062407.

[172] B. McGinley, M. O'Halloran, R. C. Conceicao, F. Morgan, M. Glavin and E. Jones, "Spiking Neural Networks for Breast Cancer Classification Using Radar Target Signatures", *Progress In Electromagnetics Research C*, vol. 17, pp. 79–94, 2010. DOI: 10.2528/PIERC10100202.

[173] B. L. Oliveira, D. Godinho, M. O'Halloran, M. Glavin, E. Jones and R. C. Conceição, "Diagnosing Breast Cancer with Microwave Technology: remaining challenges and potential solutions with machine learning", *Diagnostics*, vol. 8, no. 2, 2018. DOI: 10.3390/diagnostics8020036.

[174] R. C. Conceição, H. Medeiros, D. M. Godinho, M. O'Halloran, D. Rodriguez-Herrera, D. Flores-Tapia and S. Pistorius, "Classification of breast tumor models with a prototype microwave imaging system", *Medical Physics*, vol. 47, no. 4, pp. 1860–1870, 2020. DOI: 10.1002/mp.14064.

[175] J. Teo, Y. Chen, C. B. Soh, E. Gunawan, K. S. Low, T. C. Putti and S. C. Wang, "Breast lesion classification using ultrawideband early time breast lesion response", *IEEE Transactions on Antennas and Propagation*, vol. 58, no. 8, pp. 2604–2613, 2010. DOI: 10.1109/TAP.2010.2050423.

[176] Y. Chen, I. J. Craddock and P. Kosmas, "Feasibility study of lesion classification via contrast-agent-aided UWB breast imaging", *IEEE Transactions on Biomedical Engineering*, vol. 57, no. 5, pp. 1003–1007, 2010. DOI: 10.1109/TBME.2009.2038788.

[177] A. Fasoula, L. Duchesne, J. D. G. Cano, B. M. Moloney, S. M. Elwahab and M. J. Kerin, "Automated breast lesion detection and characterization with the wavelia microwave breast imaging system: Methodological proof-of-concept on first-in-human patient data", *Applied Sciences*, vol. 11, no. 21, 2021. DOI: 10.3390/app11219998.

[178] D. Chicco and G. Jurman, "The advantages of the Matthews correlation coefficient (MCC) over F1 score and accuracy in binary classification evaluation", *BMC Genomics*, vol. 21, pp. 1–13, 2020, ISSN: 14712164. DOI: 10.1186/s12864-019-6413-7.

[179] R. C. Conceição, M. O'Halloran, M. Glavin and E. Jones, "Evaluation of features and classifiers for classification of early-stage breast cancer", *Journal of Electromagnetic Waves and Applications*, vol. 25, no. 1, 2011. DOI: 10.1163/156939311793898350.

[180] U. Hirose and S. Kidera, "Breast Tumor Characterization with Raw Data Based Machine Learning for Microwave Ultra-wideband Mammography", in *International Symposium on Antennas and Propagation (ISAP)*, Xi'an, China, 2019.

[181] B. Gerazov and R. C. Conceicao, "Deep learning for tumour classification in homogeneous breast tissue in medical microwave imaging", in *17th IEEE International Conference on Smart Technologies (EUROCON)*, Ohrid, Macedonia, 2017, pp. 564–569. DOI: 10.1109/EUROCON.2017.8011175.

[182] T. A. Reimer, "Improving Image Reconstruction and Machine Learning Methods in Breast Microwave Sensing", Master, The University of Manitoba, Canada, 2020.

[183] R. Nisbet, J. Elder and G. Miner, *Handbook of statistical analysis and data mining applications*. Boston, MA: Academic Press, 2009. DOI: 10.1016/B978-0-12-374765-5.X0001-0.

[184] C. Campbell, *Introduction to Support Vector Machines*, 2008. [Online]. Available: http://videolectures.net/epsrcws08{_}campbell{_}isvm/ (accessed on 12/02/2021).

[185] K. P. Bennett and C. Campbell, "Support vector machines: hype or hallelujah?", *ACM SIGKDD Explorations Newsletter*, vol. 2, no. 2, pp. 1–13, 2000.

[186] I. D. Dinov, "Decision Tree Divide and Conquer Classification", in *Data Science and Predictive Analytics: Biomedical and Health Applications using R*, Switzerland: Springer, 2018, ch. 9, pp. 307–343. DOI: 10.1007/978-3-319-72347-1.

[187] L. Breiman, "Random Forests", *Machine Learning*, vol. 45, pp. 5–32, 2001. DOI: 10.1023/A:1010933404324.

[188] T. M. Oshiro, P. S. Perez and J. A. Baranauskas, "How many trees in a random forest?", in *Machine Learning and Data Mining in Pattern Recognition*, P. Perner, Ed., Berlin, Heidelberg: Springer, 2012. DOI: 10.1007/978-3-642-31537-4_13.

[189] Dassault Systèmes, *CST – Computer Simulation Technology*. [Online]. Available: https://www.3ds.com/products-services/simulia/products/cst-studio-suite/ (accessed on 15/02/2021).

[190] J. R. Costa and C. A. Fernandes, "Broadband slot feed for integrated lens antennas", *IEEE Antennas and Wireless Propagation Letters*, vol. 6, pp. 396–400, 2007. DOI: 10.1109/LAWP.2007.900954.

[191] J. R. Costa, C. R. Medeiros and C. A. Fernandes, "Performance of a crossed exponentially tapered slot antenna for UWB systems", *IEEE Transactions on Antennas and Propagation*, vol. 57, no. 5, pp. 1345–1352, 2009. DOI: 10.1109/TAP.2009.2016727.

[192] A. S. Alqadami, N. Nguyen-Trong, B. Mohammed, A. E. Stancombe, M. T. Heitzmann and A. Abbosh, "Compact Unidirectional Conformal Antenna Based on Flexible High-Permittivity Custom-Made Substrate for Wearable Wideband Electromagnetic Head Imaging System", *IEEE Transactions on Antennas and Propagation*, vol. 68, no. 1, pp. 183–194, 2020. DOI: 10.1109/TAP.2019.2938849.

[193] N. Mori, K. Tsuchiya, D. Sheth, S. Mugikura, K. Takase, U. Katscher and H. Abe, "Diagnostic value of electric properties tomography (EPT) for differentiating benign from malignant breast lesions: comparison with standard dynamic contrast-enhanced MRI", *European Radiology*, vol. 29, no. 4, pp. 1778–1786, 2019. DOI: 10.1007/s00330-018-5708-4.

[194] R. Leijsen, C. van den Berg, A. Webb, R. Remis and S. Mandija, "Combining deep learning and 3D contrast source inversion in MR-based electrical properties tomography", *NMR in Biomedicine*, vol. e4211, pp. 1–7, 2019. DOI: 10.1002/nbm.4211.

[195] D. M. Godinho, J. M. Felício, T. Castela, N. A. Silva, M. d. L. Orvalho, C. A. Fernandes and R. C. Conceição, "Development of MRI-based axillary numerical models and estimation of axillary lymph node dielectric properties for microwave imaging", *Medical Physics*, vol. 48, no. 10, pp. 5974–5990, 2021. DOI: 10.1002/mp.15143.

[196] H. Q. Woodard and D. R. White, "The composition of body tissues", *The British Journal of Radiology*, vol. 59, no. 708, pp. 1209–1219, 1986. DOI: g/10.1259/0007-1285-59-708-1209.

[197] L. W. Thomas, "The chemical composition of adipose tissue of man and mice", *Quarterly Journal of Experimental Physiology and Cognate Medical Sciences*, vol. 47, pp. 179–188, 1962. DOI: 10.1113/expphysiol.1962.sp001589.

[198] E. Askew, "Water", in *Present Knowledge in Nutrition*, E. Ziegler and L. Filer, Eds., Washington, DC: ILSI Press, 1996, pp. 98–108. DOI: 10.1002/9781119946045.

[199] L. W. Huwe, W. E. Brown, J. C. Hu and K. A. Athanasiou, "Characterization of costal cartilage and its suitability as a cell source for articular cartilage tissue engineering", *Journal of Tissue Engineering and Regenerative Medicine*, vol. 12, no. 5, pp. 1163–1176, 2018. DOI: 10.1002/term.2630.

[200] Z. Yaniv, B. C. Lowekamp, H. J. Johnson and R. Beare, "SimpleITK Image-Analysis Notebooks: a Collaborative Environment for Education and Reproducible Research", *Journal of Digital Imaging*, vol. 31, no. 3, pp. 290–303, 2018. DOI: 10.1007/s10278-017-0037-8.

[201] A. Gubern-Mérida, M. Kallenberg, R. M. Mann, R. Martí and N. Karssemeijer, "Breast segmentation and density estimation in breast MRI: A fully automatic framework", *IEEE Journal of Biomedical and Health Informatics*, vol. 19, no. 1, pp. 349–357, 2015. DOI: 10.1109/JBHI.2014.2311163.

[202] A. Bazhin, *Ellipsoid fit python*, 2020. [Online]. Available: https://github.com/aleksandrbazhin/ellipsoid{_}fit{_}python (accessed on 06/04/2021).

[203] X. Ying, L. Yang, J. Kong, Y. Hou, S. Guan and H. Zha, "Direct least square fitting of ellipsoids", in *21st International Conference on Pattern Recognition (ICPR)*, Tsukuba, Japan, 2012, pp. 3228–3231.

[204] D. A. Turner, I. J. Anderson, J. C. Mason and M. G. Cox, "An Algorithm for Fitting an Ellipsoid to Data", National Physical Laboratory, Middlesex, England, Tech. Rep. RR9803, 1999.

[205] D. M. Godinho, J. M. Felício, T. Castela, N. A. Silva, M. L. Orvalho, C. A. Fernandes and R. C. Conceição, *Axillary Region Models Repository*, 2021. [Online]. Available: https://github.com/dmgodinho/axillary-region-models-repository (accessed on 29/01/2022).

[206] FormLabs, *Form 3*, 2021. [Online]. Available: https://formlabs.com/3d-printers/form-3/ (accessed on 28/01/2022).

[207] N. Joachimowicz, B. Duchêne, C. Conessa and O. Meyer, "Anthropomorphic Breast and Head Phantoms for Microwave Imaging", *Diagnostics*, vol. 8, no. 4, pp. 85–97, 2018. DOI: 10.3390/diagnostics8040085.

[208] Keysight Technologies, *N1501A Dielectric Probe Kit 10 MHz to 50 GHz*, 2020. [Online]. Available: https://www.keysight.com/zz/en/assets/7018-04631/technical-overviews/5992-0264.pdf (accessed on 20/01/2022).

[209] M. J. Lee, S. Kim, S. A. Lee, H. T. Song, Y. M. Huh, D. H. Kim, H. H. Seung and J. S. Suh, "Overcoming artifacts from metallic orthopedic implants at high-field-strength MR imaging and multidetector CT", *Radiographics*, vol. 27, no. 3, pp. 791–803, 2007. DOI: 10.1148/rg.273065087.

[210] M. C. Wapler, J. Leupold, I. Dragonu, D. Von Elverfeld, M. Zaitsev and U. Wallrabe, "Magnetic properties of materials for MR engineering, micro-MR and beyond", *Journal of Magnetic Resonance*, vol. 242, pp. 233–242, 2014. DOI: 10.1016/j.jmr.2014.02.005.

[211] P. Esquinazi and R. Höhne, "Magnetism in carbon structures", *Journal of Magnetism and Magnetic Materials*, vol. 37, no. 12, pp. 20–27, 2005. DOI: 10.1016/j.jmmm.2004.11.154.

[212] C. A. Fernandes, "mamaGen Simulator", Instituto de Telecomunicações, Instituto Superior Técnico, Universidade de Lisboa, Tech. Rep., 2021.

[213] Ultimaker, *Ultimaker 3*, 2021. [Online]. Available: https://ultimaker.com/3d-printers/ultimaker-3 (accessed on 06/04/2021).

[214] J. M. Felício, C. A. Fernandes and J. R. Costa, "Complex Permittivity and Anisotropy Measurement of 3D-Printed PLA at Microwaves and Millimeter-waves", in *22nd International Conference on Applied Electromagnetics and Communications (ICECOM)*, Dubrovnik, Croatia, 2017. DOI: 10.1109/ICECom.2016.7843900.

[215] O. Karadima, M. Rahman, I. Sotiriou, N. Ghavami, P. Lu, S. Ahsan and P. Kosmas, "Experimental Validation of Microwave Tomography with the DBIM-TwIST Algorithm for Brain Stroke Detection and Classification", *Sensors*, vol. 20, no. 3, pp. 840–856, 2020. DOI: 10.3390/s20030840.

[216] Embodi3D, *Kidney 3D STL*, 2019. [Online]. Available: https://www.embodi3d.com/files/file/23187-kidney-3d-stl-file/ (accessed on 24/05/2021).

[217] D. Kurrant, J. Bourqui and E. Fear, "Surface Estimation for Microwave Imaging", *Sensors*, vol. 17, no. 7, pp. 1658–1678, 2017. DOI: 10.3390/s17071658.

[218] M. Houshyari, A. S. Y. Kashi, S. S. Varaki, A. Rakhsha and E. R. Blookat, "Regional lymph node radiotherapy in breast cancer: single anterior supraclavicular field vs. two anterior and posterior opposed supraclavicular fields", *Electronic Physician*, vol. 7, no. 2, pp. 1032–1038, 2015. DOI: 10.14661/2015.1032-1038.

[219] R. Liengsawangwong, T. K. Yu, T. L. Sun, J. J. Erasmus, G. H. Perkins, W. Tereffe, J. L. Oh, W. A. Woodward, E. A. Strom, M. Salephour and T. A. Buchholz, "Treatment Optimization Using Computed Tomography-Delineated Targets Should be Used for Supraclavicular Irradiation for Breast Cancer", *International Journal of Radiation Oncology Biology Physics*, vol. 69, no. 3, pp. 711–715, 2007. DOI: 10.1016/j.ijrobp.2007.05.075.

[220] D. M. Godinho, C. Silva, C. Baleia, J. M. Felício, T. Castela, N. A. Silva, M. L. Orvalho, C. A. Fernandes and R. C. Conceição, "Modelling Level I Axillary Lymph Nodes Depth for Diagnostic Imaging Technologies", *(under review in Physica Medica)*, 2022.

[221] P. Hasgall, F. Di Gennaro, C. Baumgartner, E. Neufeld, B. Lloyd, M. Gosselin, D. Payne, A. Klingenböck and N. Kuster, *IT'IS Database for thermal and electromagnetic parameters of biological tissues*, 2018. [Online]. Available: itis.swiss/database (accessed on 24/05/2021).

[222] R. C. Conceição and D. M. Godinho, "Extracting Features from Multistatic Signals in a Radar Microwave Imaging System for Breast Cancer Detection", in *2nd URSI AT-RASC*, Gran Canaria, 2018.

[223] J. Bourqui, M. Okoniewski and E. C. Fear, "Balanced antipodal vivaldi antenna with dielectric director for near-field microwave imaging", *IEEE Transactions on Antennas and Propagation*, vol. 58, no. 7, pp. 2318–2326, 2010. DOI: 10.1109/TAP.2010.2048844.

[224] M. Wang, L. Crocco and M. Cavagnaro, "Antipodal Vivaldi Antenna with Ceramic Cone Lens for Biomedical Microwave Imaging Systems", in *15th European Conference on Antennas and Propagation (EuCAP)*, Düssoldorf, Germany, 2021. DOI: 10.23919/EuCAP51087.2021.9411294.

[225] G. Wang, J. Fang and X. Dong, "Resolution of Near-Field Microwave Target Detection and Imaging by Using Flat LHM Lens", *IEEE Transactions on Antennas and Propagation*, vol. 55, no. 12, pp. 3534–3541, 2007. DOI: 10.1109/TAP.2007.910365.

[226] G. Wang and Y. Gong, "Metamaterial lens applicator for microwave hyperthermia of breast cancer", *International Journal of Hyperthermia*, vol. 25, no. 6, pp. 434–445, 2009. DOI: 10.1080/02656730903061609.

[227] Z. Akhter, B. N. Abhijith and M. J. Akhtar, "Hemisphere lens-loaded Vivaldi antenna for time domain microwave imaging of concealed objects", *Journal of Electromagnetic Waves and Applications*, vol. 30, no. 9, pp. 1183–1197, 2016. DOI: 10.1080/09205071.2016.1186574.

[228] C. A. Fernandes, "Design of a Bessel lens", Instituto de Telecomunicações, Instituto Superior Técnico, Universidade de Lisboa, Tech. Rep., 2018.

[229] L. Perrier, K. Nessah, M. Morelle, H. Mignotte, M.-O. Carrère and A. Brémond, "Cost comparison of two surgical strategies in the treatment of breast cancer: Sentinel lymph node biopsy versus axillary lymph node dissection", *International Journal of Technology Assessment in Health Care*, vol. 20, no. 4, pp. 449–454, 2004. DOI: 10.1017/s0266462304001345.

[230] Department of Health, *National schedule of NHS costs 2019/20*, 2020. DOI: https://www.england.nhs.uk/wp-content/uploads/2021/06/National_Schedule_of_NHS_Costs_FY1920.xlsx. (accessed on 13/02/2022).

[231] L. Sani, A. Vispa, R. Loretoni, M. Duranti, N. Ghavami, D. A. Sánchez-Bayuela, S. Caschera, M. Paoli, A. Bigotti, M. Badia, M. Scorsipa, G. Raspa, M. Ghavami and G. Tiberi, "Breast lesion detection through MammoWave device: Empirical detection capability assessment of microwave images' parameters", *PLoS ONE*, vol. 16, no. 4, 2021. DOI: 10.1371/journal.pone.0250005.

Appendices

A Analytical Form of Refraction Calculation

This appendix extends the implementation of the analytical form of refraction calculation briefly described in Sections 2.2.3.2 and 3.1.

Refraction is a change in direction of a wave passing between two media and it follows the Snell's law:

$$n_1 \sin(\theta_i) = n_2 \sin(\theta_t) \tag{A.1}$$

where n_1 and n_2 are the refraction indexes of each medium and θ_i and θ_t are the angles of the incident and transmission rays with respect to the interface normal.

Considering a transition between air and a dielectric, $n_1 = 1$ and $n_2 = \sqrt{\epsilon_{diel}}$, where ϵ_{diel} is the relative permittivity of the dielectric, and the equation can be simplified to a vector form:

$$\hat{i} \times \hat{N} = \sqrt{\epsilon_{diel}}\hat{t} \times \hat{N} \Leftrightarrow \left(\frac{1}{\sqrt{\epsilon_{diel}}}\hat{i} - \hat{t}\right) \times \hat{N} = 0 \tag{A.2}$$

where $\hat{i}$ is the unit vector in the incident direction, $\hat{N}$ is the unit normal vector to the surface, and $\hat{t}$ is the unit vector in the direction of the refracted ray.

For a spherical surface, the $\hat{N}$ vector is radial to the surface and is easily determined. Given the source point of the incident ray of coordinates (x_a, y_a, z_a) and the destination point of coordinates (x_p, y_p, z_p), the entry point at the interface of coordinates (x_c, y_c, z_c) that follows Snell's law can be analytically calculated using the implicit equation A.2, considering:

$$\hat{i} = \frac{(x_c - x_a, y_c - y_a, z_c - z_a)}{\sqrt{(x_c - x_a)^2 + (y_c - y_a)^2 + (z_c - z_a)^2}} \tag{A.3}$$

$$\hat{t} = \frac{(x_p - x_c, y_p - y_c, z_p - z_c)}{\sqrt{(x_p - x_c)^2 + (y_p - y_c)^2 + (z_p - z_c)^2}} \tag{A.4}$$

$$\hat{N} = \frac{(x_0 - x_c, y_0 - y_c, z_0 - z_c)}{R} \tag{A.5}$$

where R and (x_0, y_0, z_0) are the radius and coordinates of the centre of the sphere.

Although multiple solutions for (x_c, y_c, z_c) can be sometimes found, the correct solution can be singled-out, by excluding imaginary or physically impossible solutions.

B | Model AR_001

This appendix shows the details of the axillary region models AR_001 developed using the methodology presented in Chapter 4.

B.1 Patient Details

- Body Mass Index: 22
- Age: 57
- Approximate Skin Thickness: 3 mm

B.2 Left Axillary Region Model

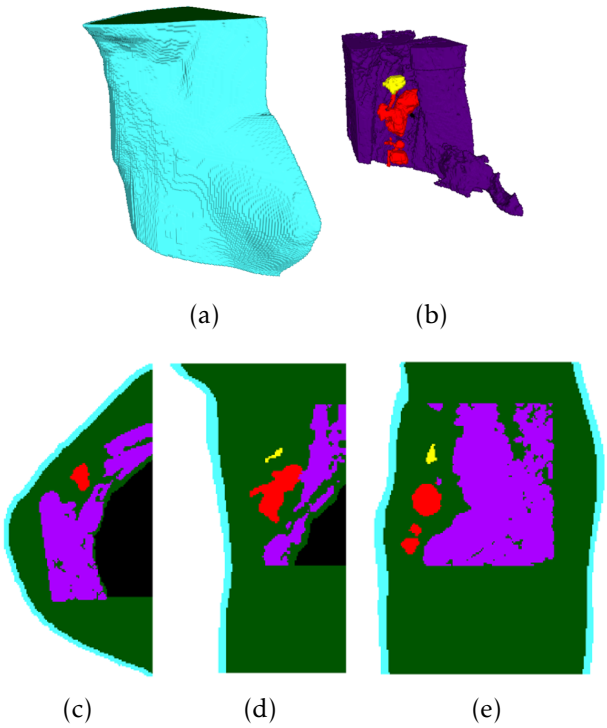

Figure B.1: Left axillary region model of AR_001 in: (a) 3D with all tissues, (b) 3D without skin nor adipose tissue, (c) axial, (d) coronal, and (e) sagittal planes. Blue represents the skin, green represents the adipose tissue, purple represents the muscle and fibroglandular tissue, black represents the lung cavity, yellow represents the healthy ALNs and red represents the metastasised ALNs.

- Available Files:
  1. AR_001_R_skin (.mat/.raw/.stl)
  2. AR_001_R_skin_filled (.stl)
  3. AR_001_R_adipose (.mat/.raw/.stl)
  4. AR_001_R_adipose_filled (.stl)
  5. AR_001_R_lung (.mat/.raw/.stl)
  6. AR_001_R_muscle (.mat/.raw/.stl)
  7. AR_001_R_h_aln (.mat/.raw/.stl)
  8. AR_001_R_m_aln (.mat/.raw/.stl)
  9. AR_001_R_label_map (.mat/.raw)
  10. AR_001_R_weight_map (.mat/.raw)
- Grid Size: $190 \times 298 \times 121$ (Axial × Coronal × Sagittal)
- Voxel Size: $0.9965 \times 0.9965 \times 1$ mm^3 (Axial × Coronal × Sagittal)
- Number of Healthy Lymph Nodes: 1
- Number of Metastasised Lymph Nodes: 2 + 1 Matted

B.2.1 Volume Ratios

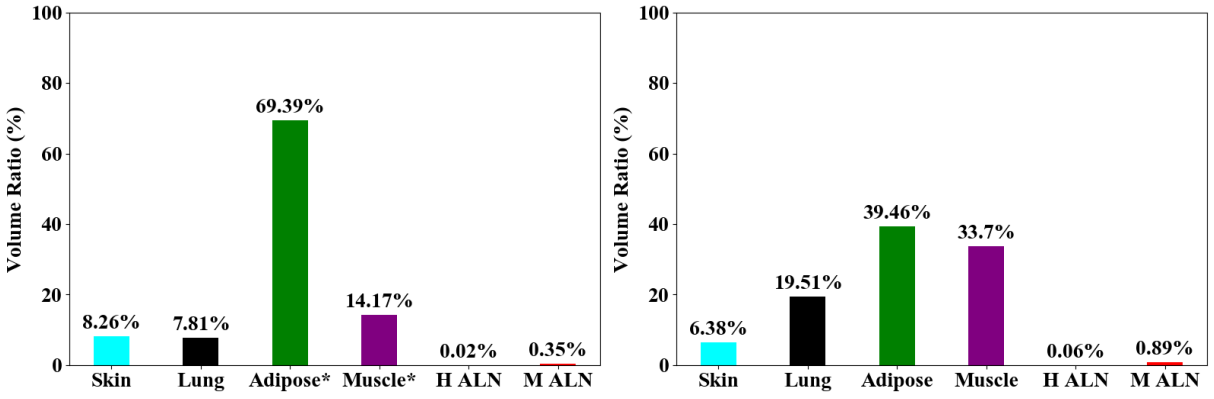

Figure B.2: Ratio between the volume of each tissue type and the total volume of: (a) the whole model and (b) restricted to the axillary region of AR_001. The asterisk (*) means that other tissue types may have been included in the calculation, such as fibroglandular tissue. H means Healthy and M means Metastasised.

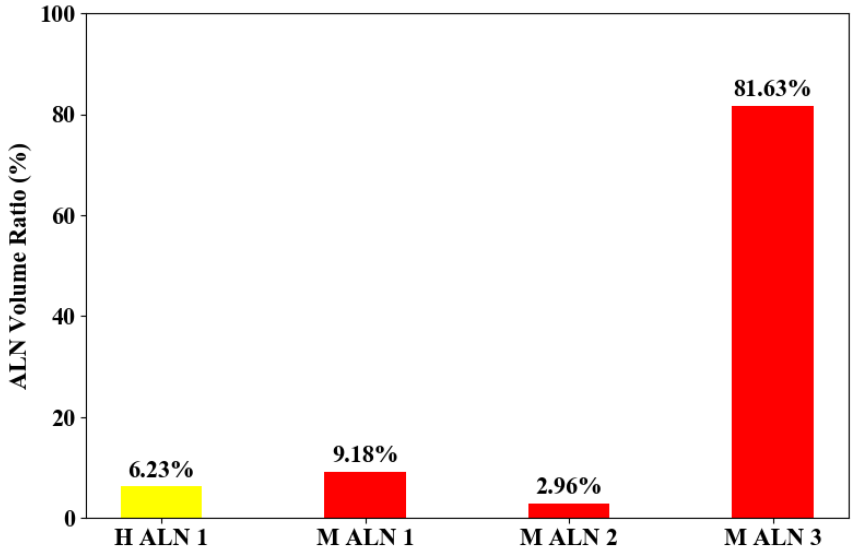

Figure B.3: Ratio between the volume of each ALN and the total volume of ALNs. H means Healthy and M means Metastasised.

B.2.2 Dielectric Properties

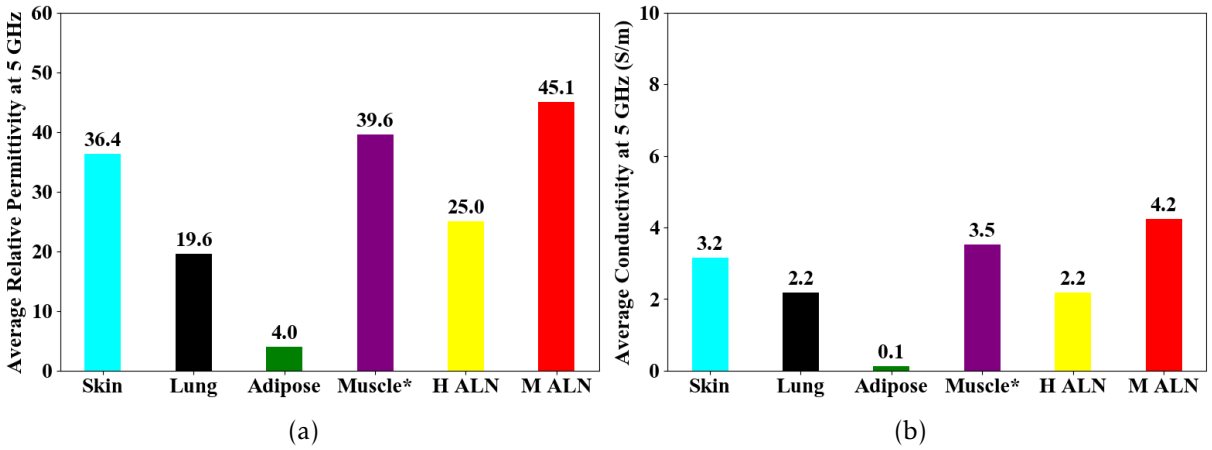

Figure B.4: Average (a) relative permittivity and (b) effective conductivity of each tissue type at 5 GHz considering MRI-intensity-based dielectric properties map. The asterisk (*) means that other tissue types may have been included in the calculation, such as fibroglandular tissue. H means Healthy and M means Metastasised.

B.3 Left Axillary Region Model

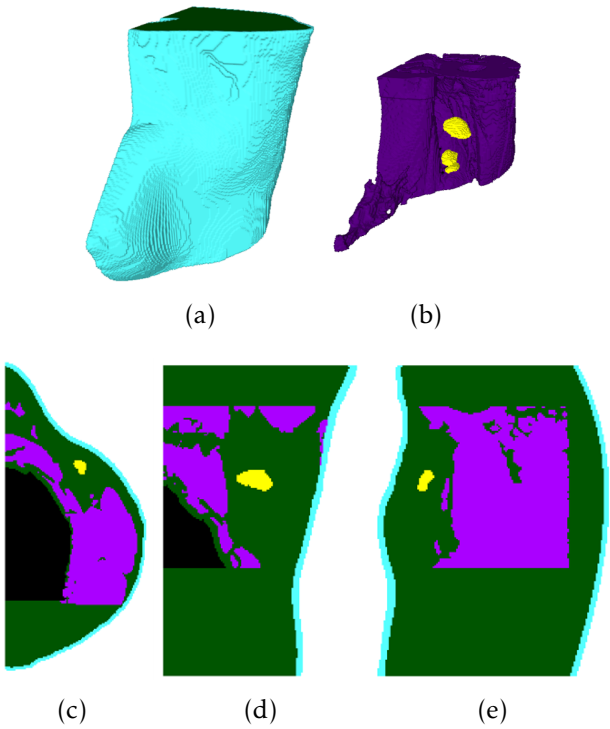

Figure B.5: Left axillary region model of AR_001 in: (a) 3D with all tissues, (b) 3D without skin nor adipose tissue, (c) axial, (d) coronal, and (e) sagittal planes. Blue represents the skin, green represents the adipose tissue, purple represents the muscle and fibroglandular tissue, black represents the lung cavity, and yellow represents the healthy ALNs.

- Available Files:
  1. AR_001_L_skin (.mat/.raw/.stl)
  2. AR_001_L_skin_filled (.stl)
  3. AR_001_L_adipose (.mat/.raw/.stl)
  4. AR_001_L_adipose_filled (.stl)
  5. AR_001_L_lung (.mat/.raw/.stl)
  6. AR_001_L_muscle (.mat/.raw/.stl)
  7. AR_001_L_h_aln (.mat/.raw/.stl)
  8. AR_001_L_label_map (.mat/.raw)
  9. AR_001_L_weight_map (.mat/.raw)
- Grid Size: $190 \times 298 \times 126$ (Axial × Coronal × Sagittal)
- Voxel Size: $0.9965 \times 0.9965 \times 1$ mm^3 (Axial × Coronal × Sagittal)
- Number of Healthy Lymph Nodes: 3
- Number of Metastasised Lymph Nodes: 0

B.3.1 Volume Ratios

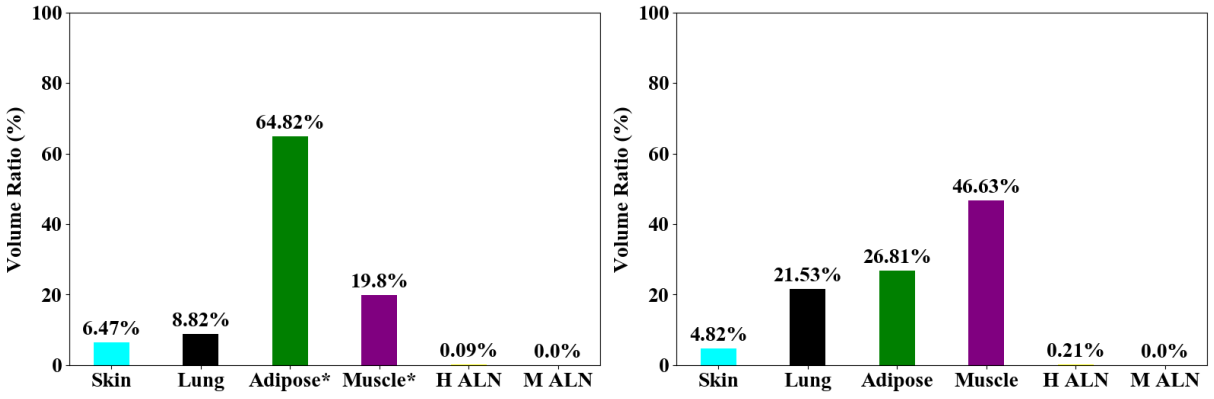

Figure B.6: Ratio between the volume of each tissue type and the total volume of: (a) the whole model and (b) restricted to the axillary region of AR_001. The asterisk (*) means that other tissue types may have been included in the calculation, such as fibroglandular tissue. H means Healthy and M means Metastasised.

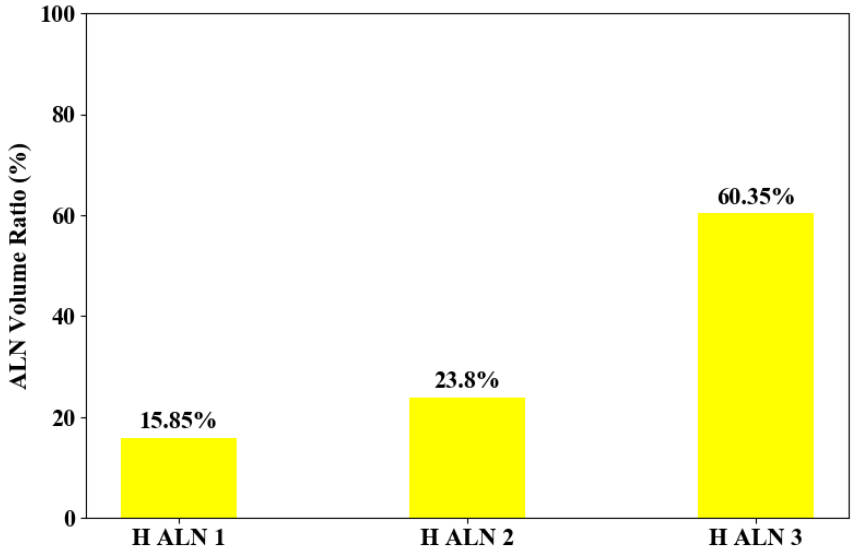

Figure B.7: Ratio between the volume of each ALN and the total volume of ALNs. H means Healthy.

B.3.2 Dielectric Properties

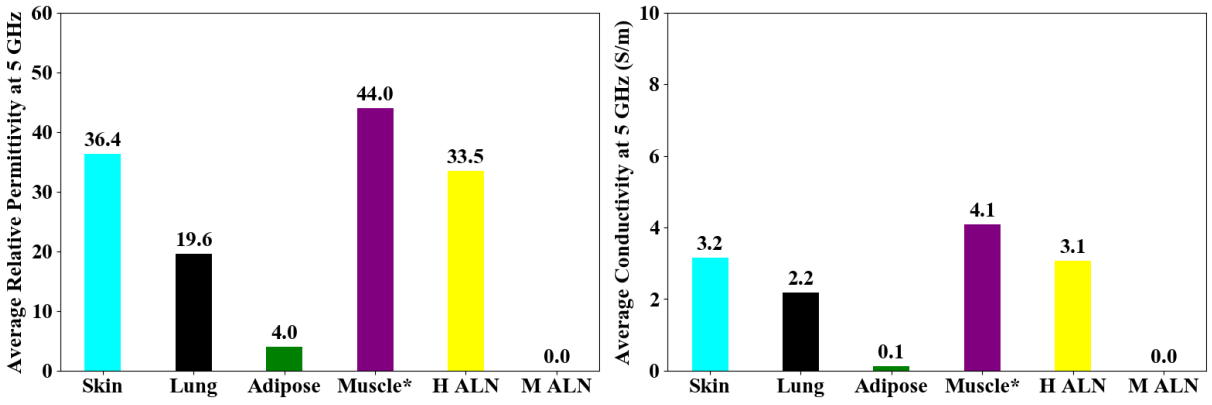

Figure B.8: Average (a) relative permittivity and (b) effective conductivity of each tissue type at 5 GHz considering MRI-intensity-based dielectric properties map. The asterisk (*) means that other tissue types may have been included in the calculation, such as fibroglandular tissue. H means Healthy and M means Metastasised.

C | Model AR_002

This appendix shows the details of the axillary region models AR_002 developed using the methodology presented in Chapter 4.

C.1 Patient Details

- Body Mass Index: 24
- Age: 40
- Approximate Skin Thickness: 3 mm

C.2 Right Axillary Region Model

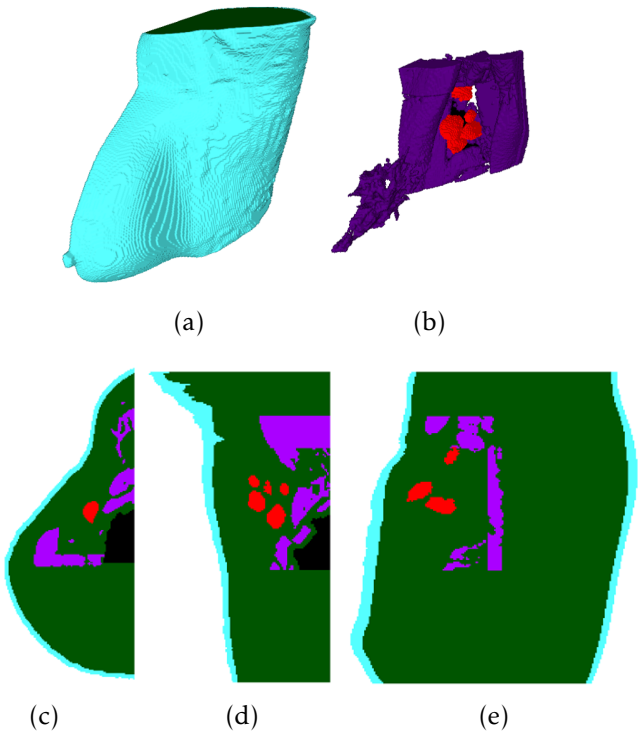

Figure C.1: Right axillary region model of AR_002 in: (a) 3D with all tissues, (b) 3D without skin nor adipose tissue, (c) axial, (d) coronal, and (e) sagittal planes. Blue represents the skin, green represents the adipose tissue, purple represents the muscle and fibroglandular tissue, black represents the lung cavity, and red represents the metastasised ALNs.

- Available Files:
  1. AR_002_R_skin (.mat/.raw/.stl)
  2. AR_002_R_skin_filled (.stl)
  3. AR_002_R_adipose (.mat/.raw/.stl)
  4. AR_002_R_adipose_filled (.stl)
  5. AR_002_R_lung (.mat/.raw/.stl)
  6. AR_002_R_muscle (.mat/.raw/.stl)
  7. AR_002_R_m_aln (.mat/.raw/.stl)
  8. AR_002_R_label_map (.mat/.raw)
  9. AR_002_R_weight_map (.mat/.raw)
- Grid Size: $204 \times 297 \times 144$ (Axial × Coronal × Sagittal)
- Voxel Size: $0.9965 \times 0.9965 \times 1$ mm^3 (Axial × Coronal × Sagittal)
- Number of Healthy Lymph Nodes: 0
- Number of Metastasised Lymph Nodes: 6

C.2.1 Volume Ratios

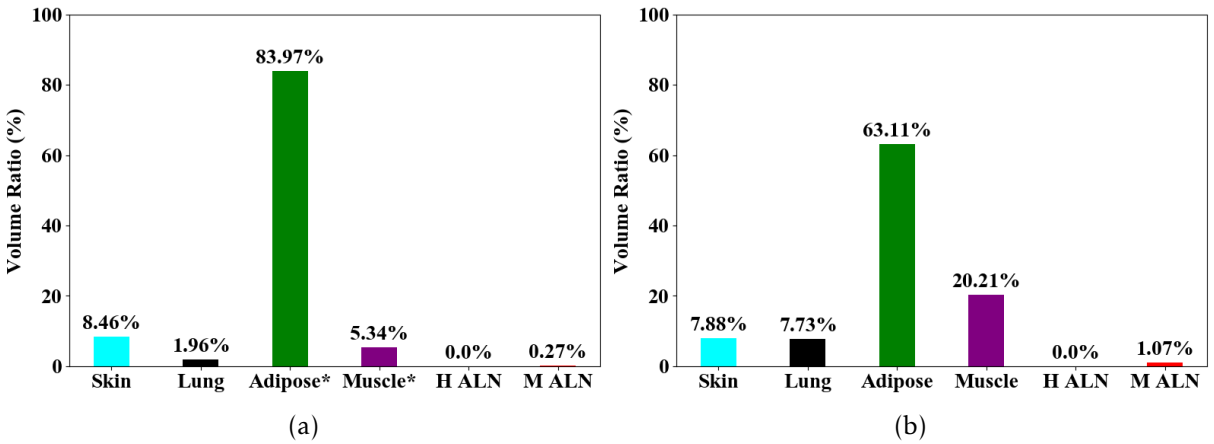

Figure C.2: Ratio between the volume of each tissue type and the total volume of: (a) the whole model and (b) restricted to the axillary region of AR_002. The asterisk (*) means that other tissue types may have been included in the calculation, such as fibroglandular tissue. H means Healthy and M means Metastasised.

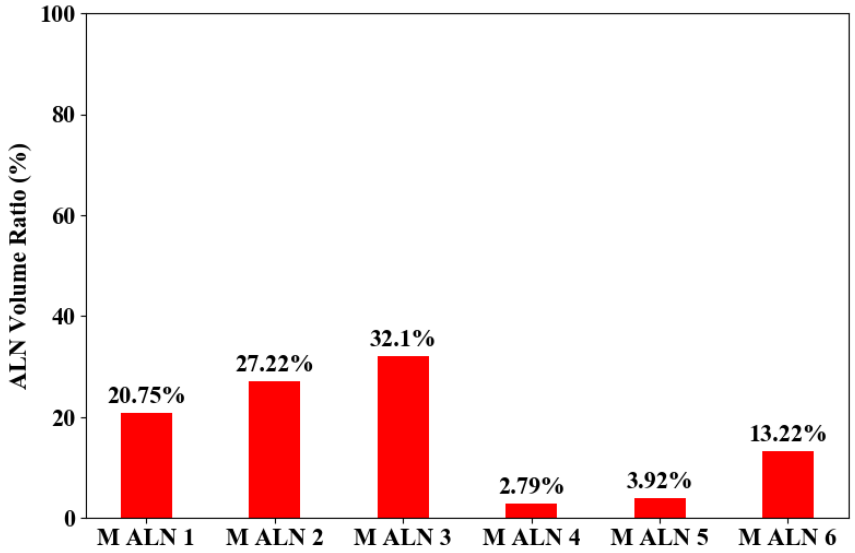

Figure C.3: Ratio between the volume of each ALN and the total volume of ALNs. M means Metastasised.

C.2.2 Dielectric Properties

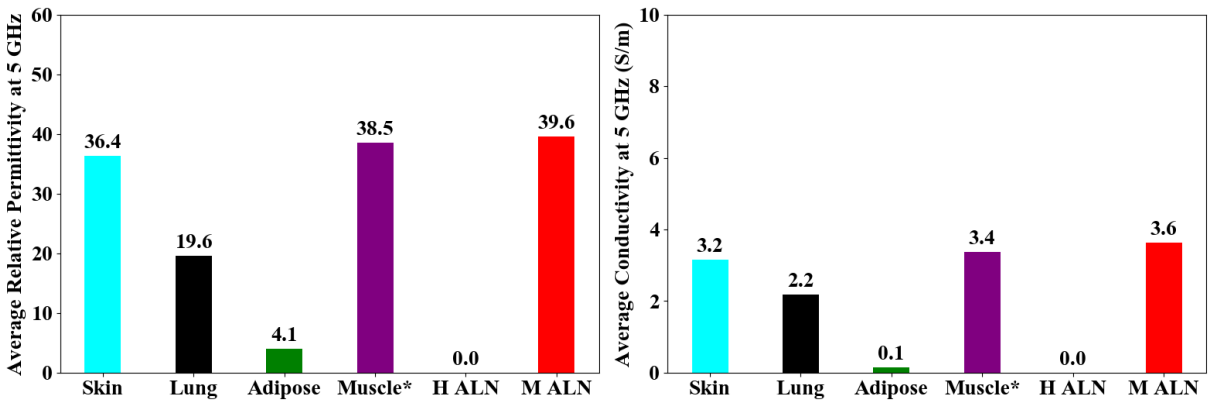

Figure C.4: Average (a) relative permittivity and (b) effective conductivity of each tissue type at 5 GHz considering MRI-intensity-based dielectric properties map. The asterisk (*) means that other tissue types may have been included in the calculation, such as fibroglandular tissue. H means Healthy and M means Metastasised.

C.3 Left Axillary Region Model

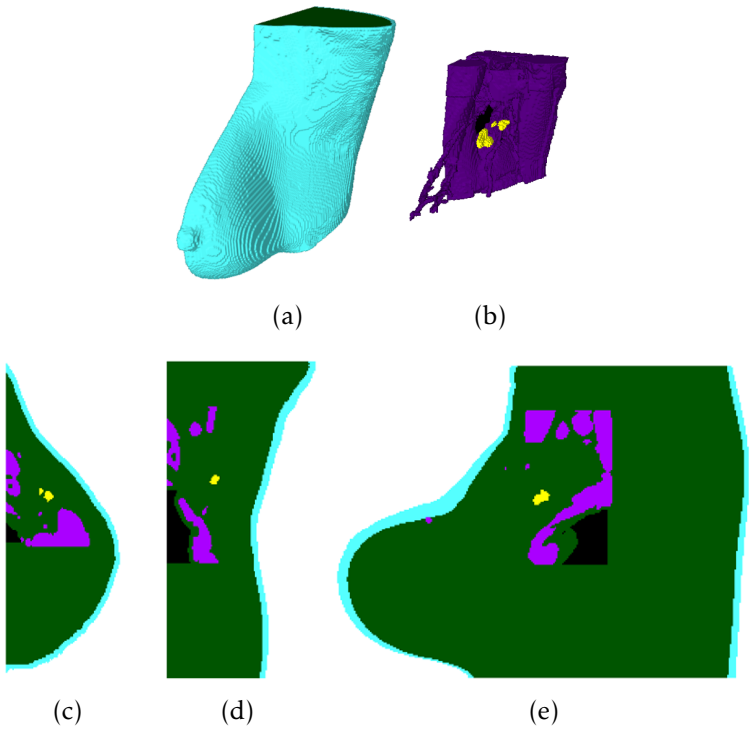

Figure C.5: Left axillary region model of AR_002 in: (a) 3D with all tissues, (b) 3D without skin nor adipose tissue, (c) axial, (d) coronal, and (e) sagittal planes. Blue represents the skin, green represents the adipose tissue, purple represents the muscle and fibroglandular tissue, black represents the lung cavity, and yellow represents the healthy ALNs.

- Available Files:

  1. AR_002_L_skin (.mat/.raw/.stl)
  2. AR_002_L_skin_filled (.stl)

3. AR_002_L_adipose (.mat/.raw/.stl)
4. AR_002_L_adipose_filled (.stl)
5. AR_002_L_lung (.mat/.raw/.stl)
6. AR_002_L_muscle (.mat/.raw/.stl)
7. AR_002_L_h_aln (.mat/.raw/.stl)
8. AR_002_L_label_map (.mat/.raw)
9. AR_002_L_weight_map (.mat/.raw)

- Grid Size: $204 \times 297 \times 105$ (Axial × Coronal × Sagittal)
- Voxel Size: $0.9965 \times 0.9965 \times 1$ mm^3 (Axial × Coronal × Sagittal)
- Number of Healthy Lymph Nodes: 4
- Number of Metastasised Lymph Nodes: 0

C.3.1 Volume Ratios

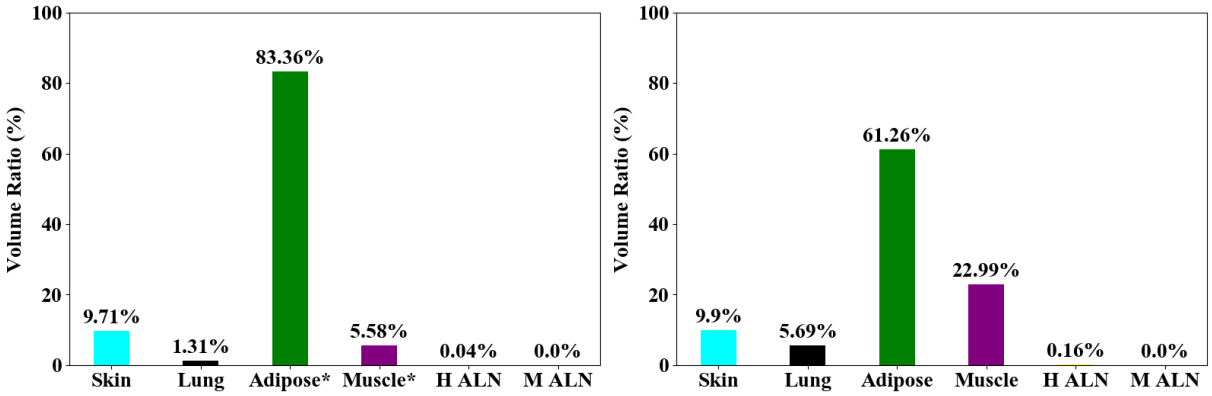

Figure C.6: Ratio between the volume of each tissue type and the total volume of: (a) the whole model and (b) restricted to the axillary region of AR_002. The asterisk (*) means that other tissue types may have been included in the calculation, such as fibroglandular tissue. H means Healthy and M means Metastasised.

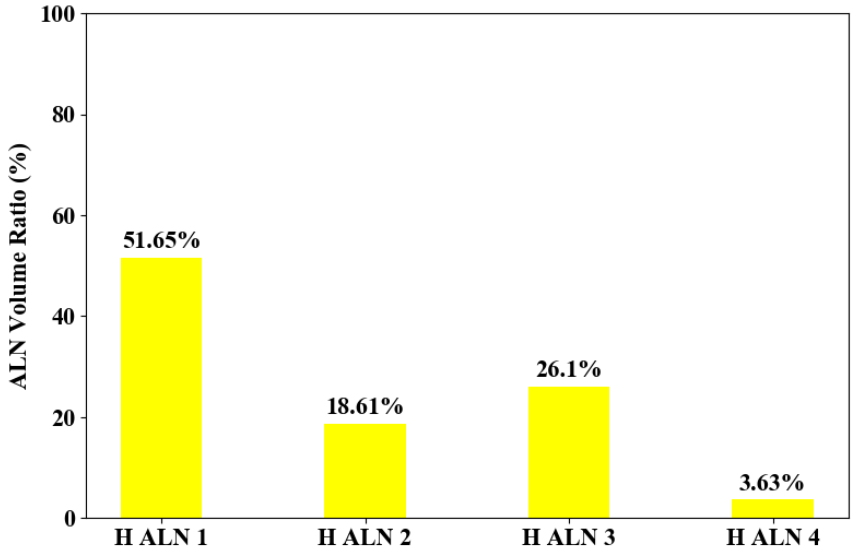

Figure C.7: Ratio between the volume of each ALN and the total volume of ALNs. H means Healthy.

C.3.2 Dielectric Properties

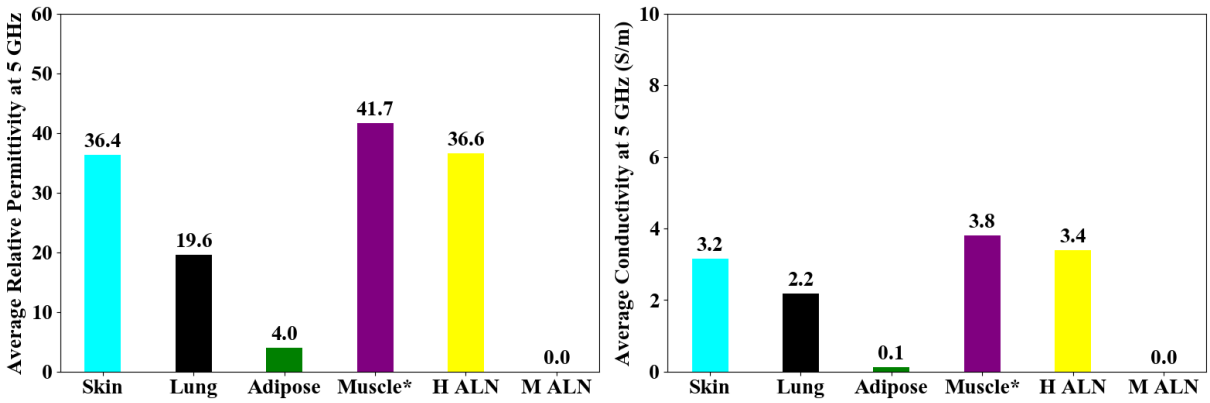

Figure C.8: Average (a) relative permittivity and (b) effective conductivity of each tissue type at 5 GHz considering MRI-intensity-based dielectric properties map. The asterisk (*) means that other tissue types may have been included in the calculation, such as fibroglandular tissue. H means Healthy and M means Metastasised.

D | Model AR_003

This appendix shows the details of the axillary region models AR_003 developed using the methodology presented in Chapter 4.

D.1 Patient Details

- Body Mass Index: 26
- Age: 57
- Approximate Skin Thickness: 3 mm

D.2 Right Axillary Region Model

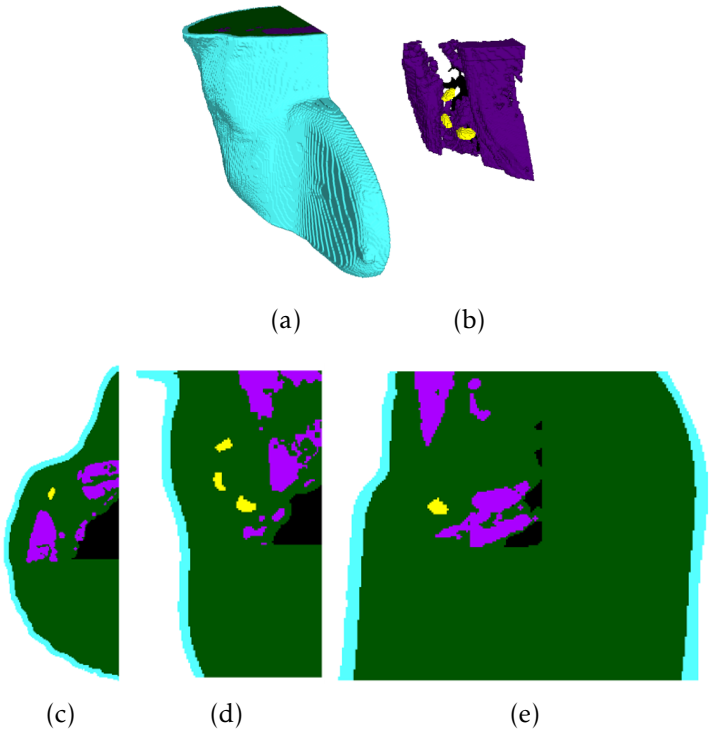

Figure D.1: Right axillary region model in: (a) 3D with all tissues, (b) 3D without skin nor adipose tissue, (c) axial, (d) coronal, and (e) sagittal planes of AR_003. Blue represents the skin, green represents the adipose tissue, purple represents the muscle and fibroglandular tissue, black represents the lung cavity, and yellow represents the healthy ALNs.

- Available Files:
  1. AR_003_R_skin (.mat/.raw/.stl)
  2. AR_003_R_skin_filled (.stl)
  3. AR_003_R_adipose (.mat/.raw/.stl)
  4. AR_003_R_adipose_filled (.stl)
  5. AR_003_R_lung (.mat/.raw/.stl)
  6. AR_003_R_muscle (.mat/.raw/.stl)
  7. AR_003_R_h_aln (.mat/.raw/.stl)
  8. AR_003_R_label_map (.mat/.raw)
  9. AR_003_R_weight_map (.mat/.raw)
- Grid Size: $169 \times 325 \times 114$ (Axial × Coronal × Sagittal)
- Voxel Size: $1.0764 \times 1.0764 \times 1$ mm^3 (Axial × Coronal × Sagittal)
- Number of Healthy Lymph Nodes: 3
- Number of Metastasised Lymph Nodes: 0

D.2.1 Volume Ratios

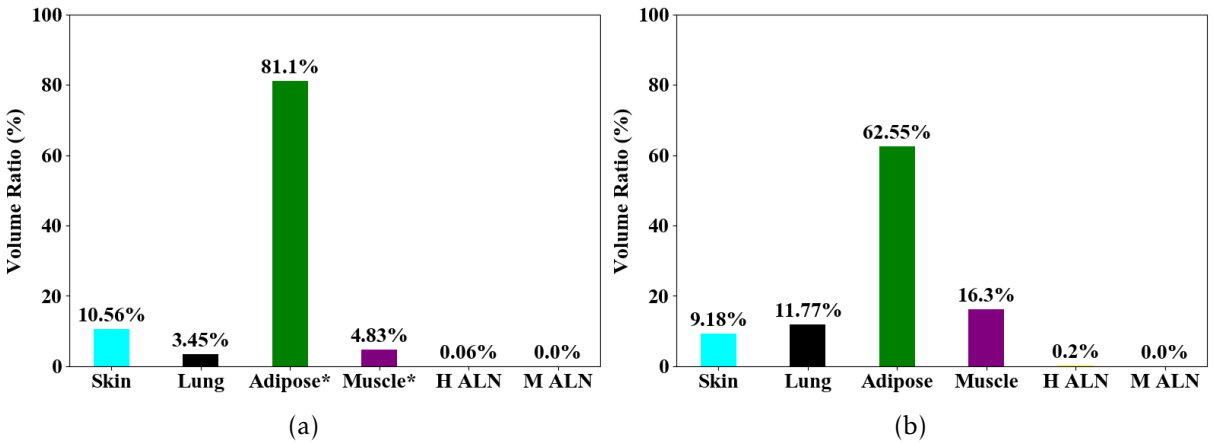

Figure D.2: Ratio between the volume of each tissue type and the total volume of: (a) the whole model and (b) restricted to the axillary region of AR_003. The asterisk (*) means that other tissue types may have been included in the calculation, such as fibroglandular tissue. H means Healthy and M means Metastasised.

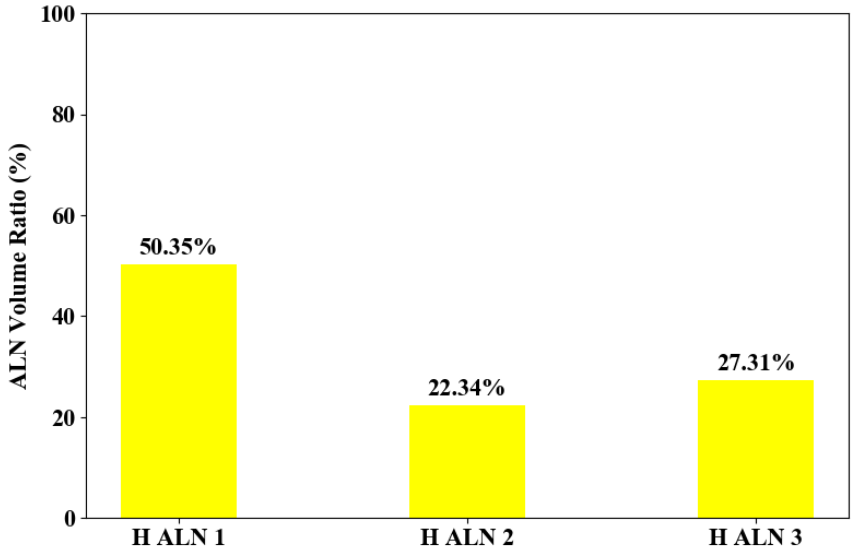

Figure D.3: Ratio between the volume of each ALN and the total volume of ALNs. H means Healthy.

D.2.2 Dielectric Properties

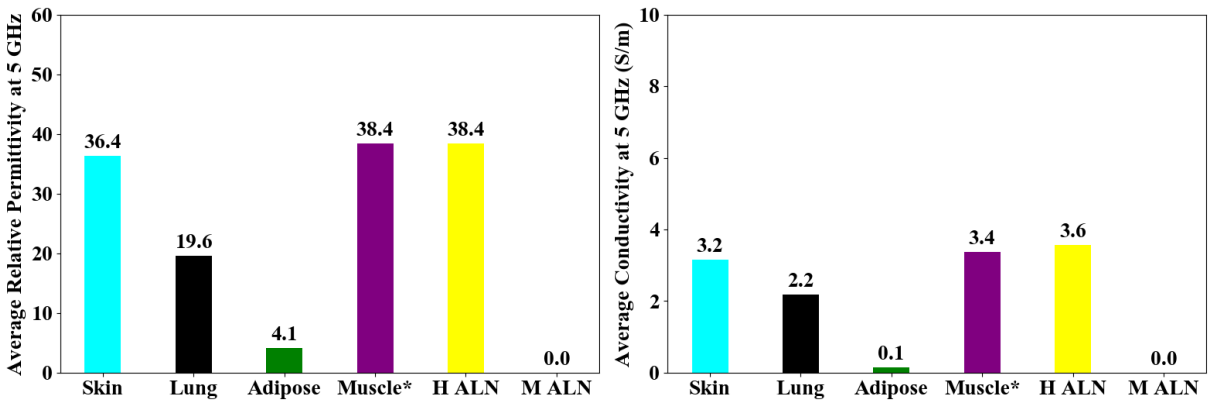

Figure D.4: Average (a) relative permittivity and (b) effective conductivity of each tissue type at 5 GHz considering MRI-intensity-based dielectric properties map. The asterisk (*) means that other tissue types may have been included in the calculation, such as fibroglandular tissue. H means Healthy and M means Metastasised.

D.3 Left Axillary Region Model

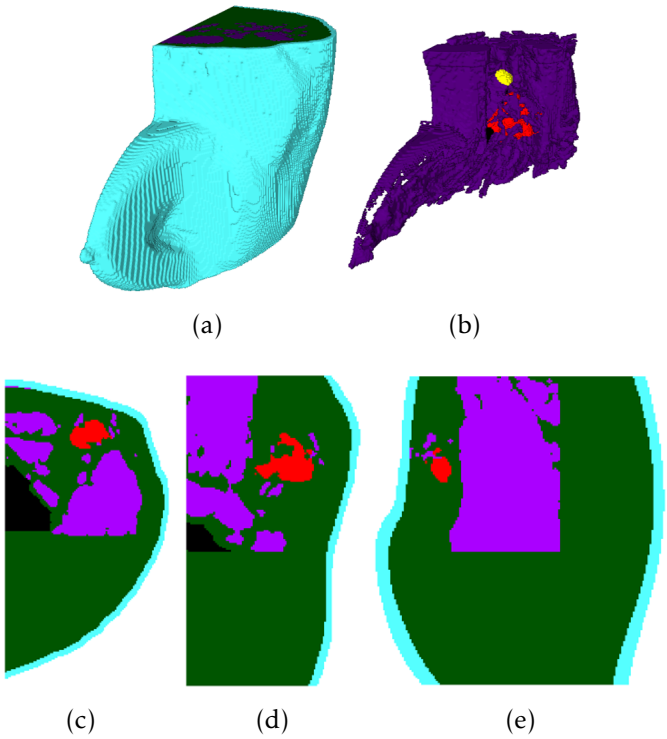

Figure D.5: Left axillary region model of AR_003 in: (a) 3D with all tissues, (b) 3D without skin nor adipose tissue, (c) axial, (d) coronal, and (e) sagittal planes. Blue represents the skin, green represents the adipose tissue, purple represents the muscle and fibroglandular tissue, black represents the lung cavity, yellow represents the healthy ALNs and red represents the metastasised ALNs.

- Available Files:

  1. AR_003_L_skin (.mat/.raw/.stl)
  2. AR_003_L_skin_filled (.stl)

3. AR_003_L_adipose (.mat/.raw/.stl)
4. AR_003_L_adipose_filled (.stl)
5. AR_003_L_lung (.mat/.raw/.stl)
6. AR_003_L_muscle (.mat/.raw/.stl)
7. AR_003_L_h_aln (.mat/.raw/.stl)
8. AR_003_L_m_aln (.mat/.raw/.stl)
9. AR_003_L_label_map (.mat/.raw)
10. AR_003_L_weight_map (.mat/.raw)

- Grid Size: $169 \times 325 \times 111$ (Axial × Coronal × Sagittal)
- Voxel Size: $1.0764 \times 1.0764 \times 1$ mm^3 (Axial × Coronal × Sagittal)
- Number of Healthy Lymph Nodes: 1
- Number of Metastasised Lymph Nodes: 1 Matted

D.3.1 Volume Ratios

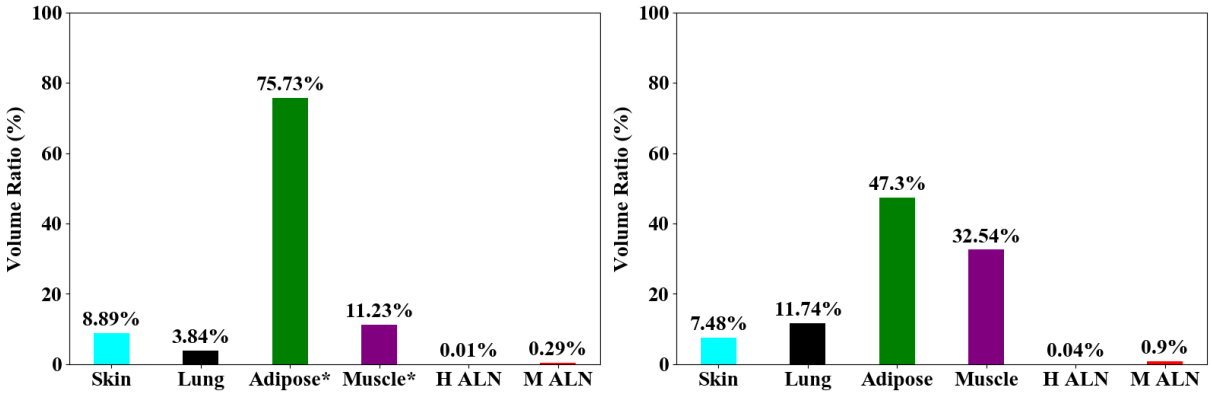

Figure D.6: Ratio between the volume of each tissue type and the total volume of: (a) the whole model and (b) restricted to the axillary region of AR_003. The asterisk (*) means that other tissue types may have been included in the calculation, such as fibroglandular tissue. H means Healthy and M means Metastasised.

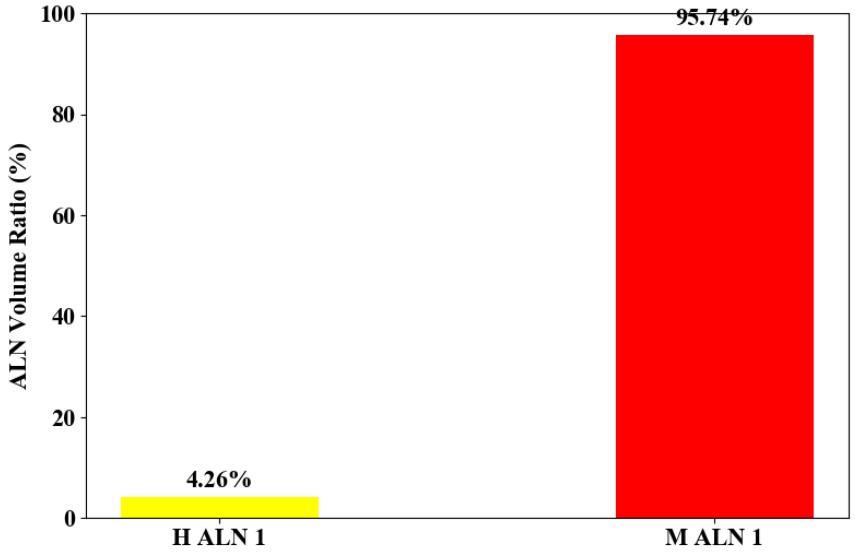

Figure D.7: Ratio between the volume of each ALN and the total volume of ALNs. H means Healthy and M means Metastasised.

D.3.2 Dielectric Properties

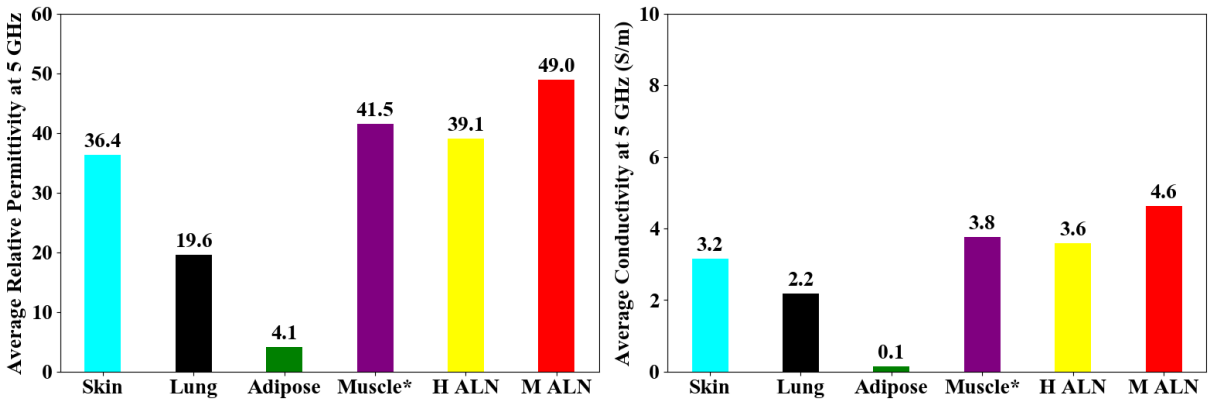

Figure D.8: Average (a) relative permittivity and (b) effective conductivity of each tissue type at 5 GHz considering MRI-intensity-based dielectric properties map. The asterisk (*) means that other tissue types may have been included in the calculation, such as fibroglandular tissue. H means Healthy and M means Metastasised.

E | Model AR_004

This appendix shows the details of the axillary region models AR_004 developed using the methodology presented in Chapter 4.

E.1 Patient Details

- Body Mass Index: 26
- Age: 79
- Approximate Skin Thickness: 3 mm

E.2 Right Axillary Region Model

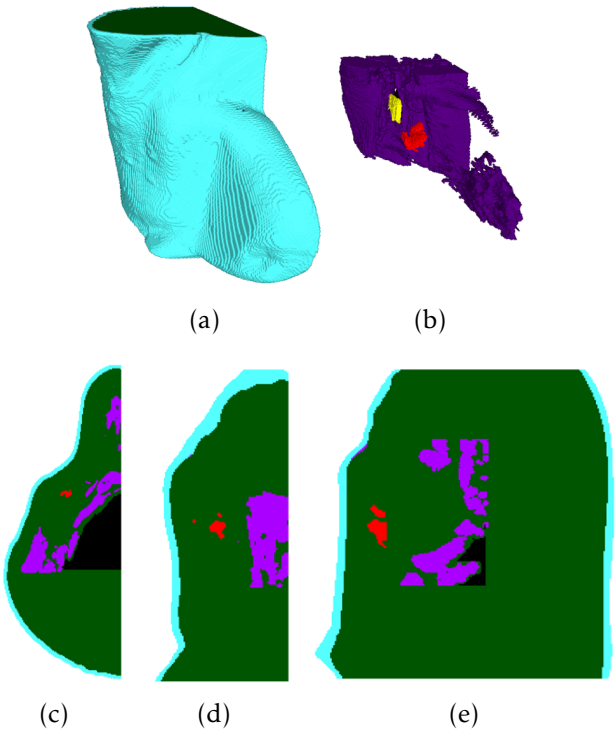

Figure E.1: Right axillary region model of AR_004 in: (a) 3D with all tissues, (b) 3D without skin nor adipose tissue, (c) axial, (d) coronal, and (e) sagittal planes. Blue represents the skin, green represents the adipose tissue, purple represents the muscle and fibroglandular tissue, black represents the lung cavity, yellow represents the healthy ALNs and red represents the metastasised ALNs.

- Available Files:
  1. AR_004_R_skin (.mat/.raw/.stl)
  2. AR_004_R_skin_filled (.stl)
  3. AR_004_R_adipose (.mat/.raw/.stl)
  4. AR_004_R_adipose_filled (.stl)
  5. AR_004_R_lung (.mat/.raw/.stl)
  6. AR_004_R_muscle (.mat/.raw/.stl)
  7. AR_004_R_h_aln (.mat/.raw/.stl)
  8. AR_004_R_m_aln (.mat/.raw/.stl)
  9. AR_004_R_label_map (.mat/.raw)
  10. AR_004_R_weight_map (.mat/.raw)
- Grid Size: $213 \times 360 \times 144$ (Axial × Coronal × Sagittal)
- Voxel Size: $0.9965 \times 0.9965 \times 1$ mm^3 (Axial × Coronal × Sagittal)
- Number of Healthy Lymph Nodes: 1
- Number of Metastasised Lymph Nodes: 2

E.2.1 Volume Ratios

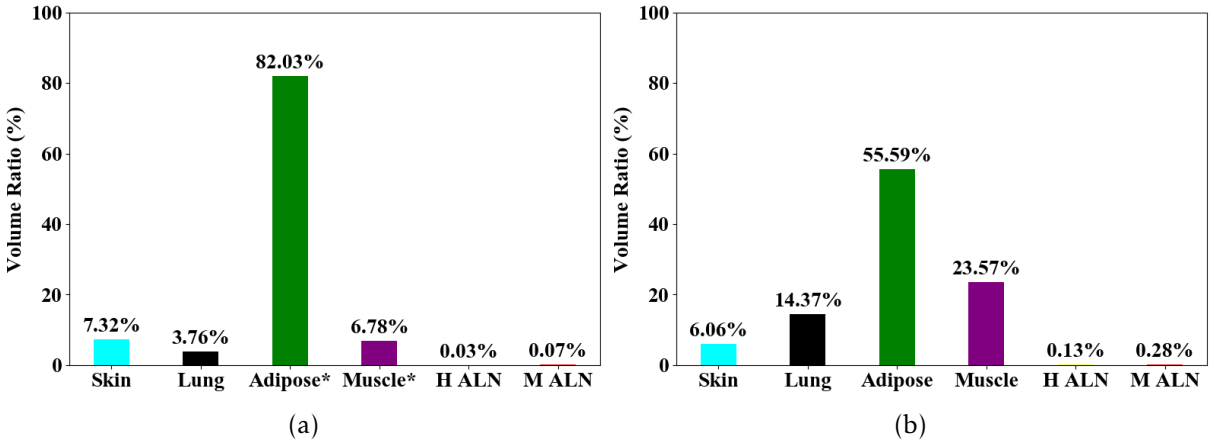

Figure E.2: Ratio between the volume of each tissue type and the total volume of: (a) the whole model and (b) restricted to the axillary region of AR_004. The asterisk (*) means that other tissue types may have been included in the calculation, such as fibroglandular tissue. H means Healthy and M means Metastasised.

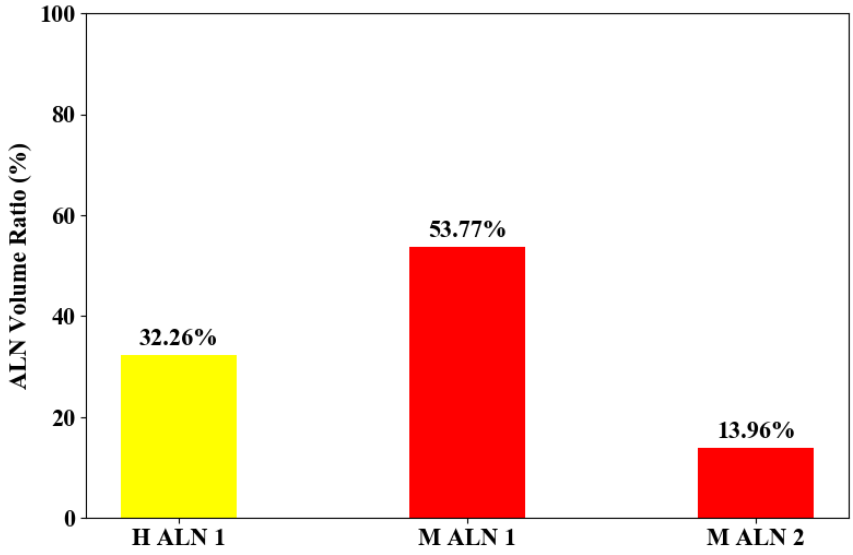

Figure E.3: Ratio between the volume of each ALN and the total volume of ALNs. H means Healthy and M means Metastasised.

E.2.2 Dielectric Properties

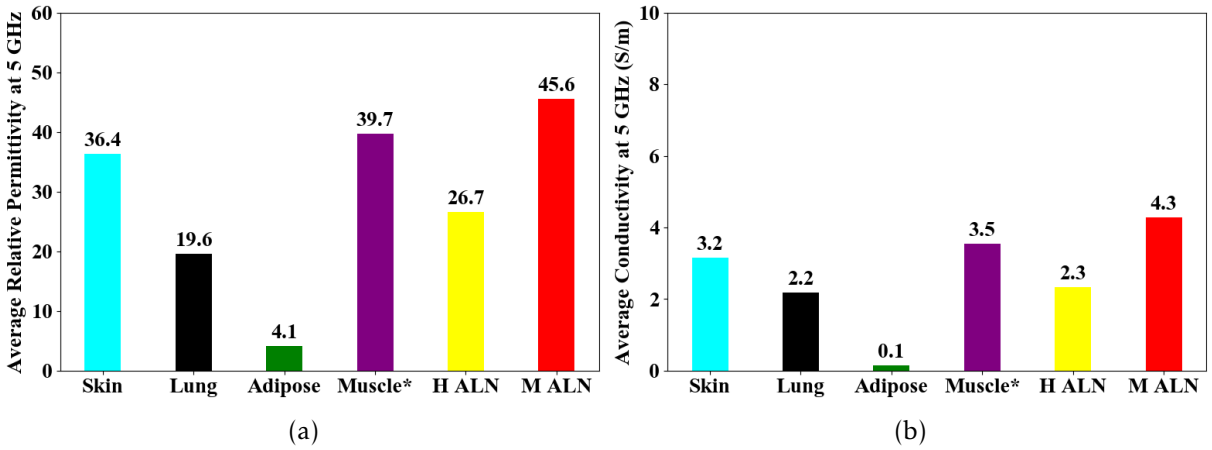

Figure E.4: Average (a) relative permittivity and (b) effective conductivity of each tissue type at 5 GHz considering MRI-intensity-based dielectric properties map. The asterisk (*) means that other tissue types may have been included in the calculation, such as fibroglandular tissue. H means Healthy and M means Metastasised.

E.3 Left Axillary Region Model

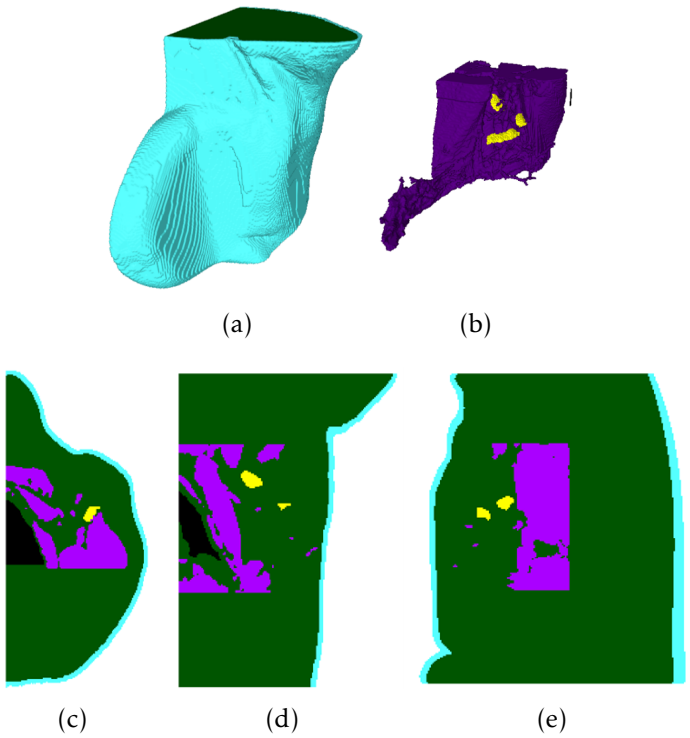

Figure E.5: Left axillary region model of AR_004 in: (a) 3D with all tissues, (b) 3D without skin nor adipose tissue, (c) axial, (d) coronal, and (e) sagittal planes. Blue represents the skin, green represents the adipose tissue, purple represents the muscle and fibroglandular tissue, black represents the lung cavity, and yellow represents the healthy ALNs.

- Available Files:
  1. AR_004_L_skin (.mat/.raw/.stl)
  2. AR_004_L_skin_filled (.stl)
  3. AR_004_L_adipose (.mat/.raw/.stl)
  4. AR_004_L_adipose_filled (.stl)
  5. AR_004_L_lung (.mat/.raw/.stl)
  6. AR_004_L_muscle (.mat/.raw/.stl)
  7. AR_004_L_h_aln (.mat/.raw/.stl)
  8. AR_004_L_label_map (.mat/.raw)
  9. AR_004_L_weight_map (.mat/.raw)
- Grid Size: $213 \times 360 \times 154$ (Axial × Coronal × Sagittal)
- Voxel Size: $0.9965 \times 0.9965 \times 1$ mm^3 (Axial × Coronal × Sagittal)
- Number of Healthy Lymph Nodes: 3
- Number of Metastasised Lymph Nodes: 0

E.3.1 Volume Ratios

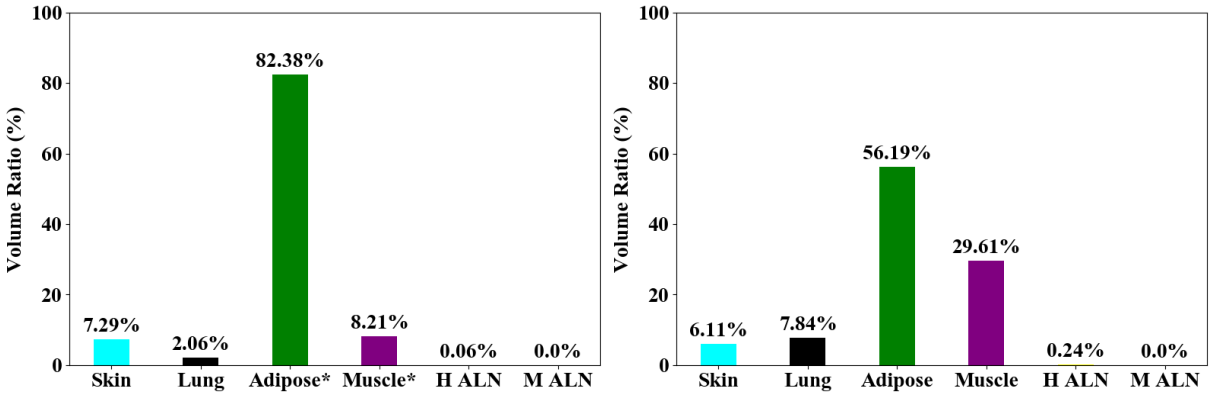

Figure E.6: Ratio between the volume of each tissue type and the total volume of: (a) the whole model and (b) restricted to the axillary region of AR_004. The asterisk (*) means that other tissue types may have been included in the calculation, such as fibroglandular tissue. H means Healthy and M means Metastasised.

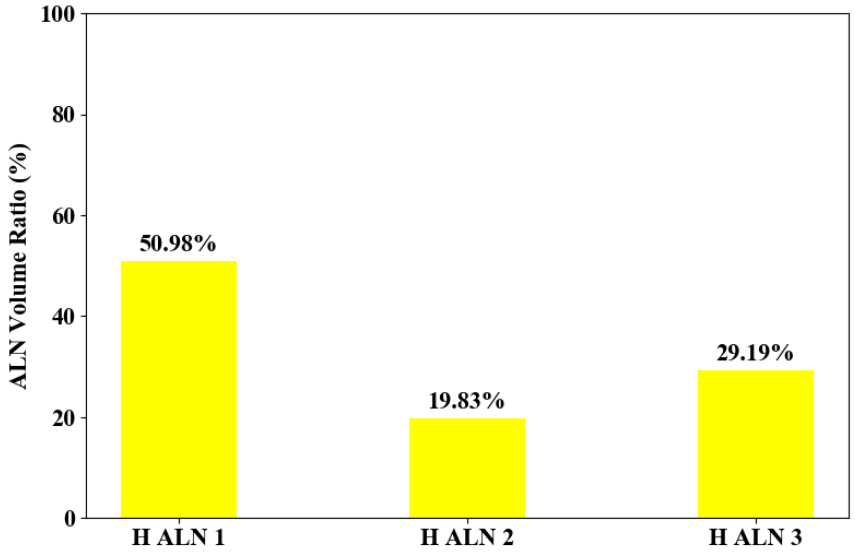

Figure E.7: Ratio between the volume of each ALN and the total volume of ALNs. H means Healthy.

E.3.2 Dielectric Properties

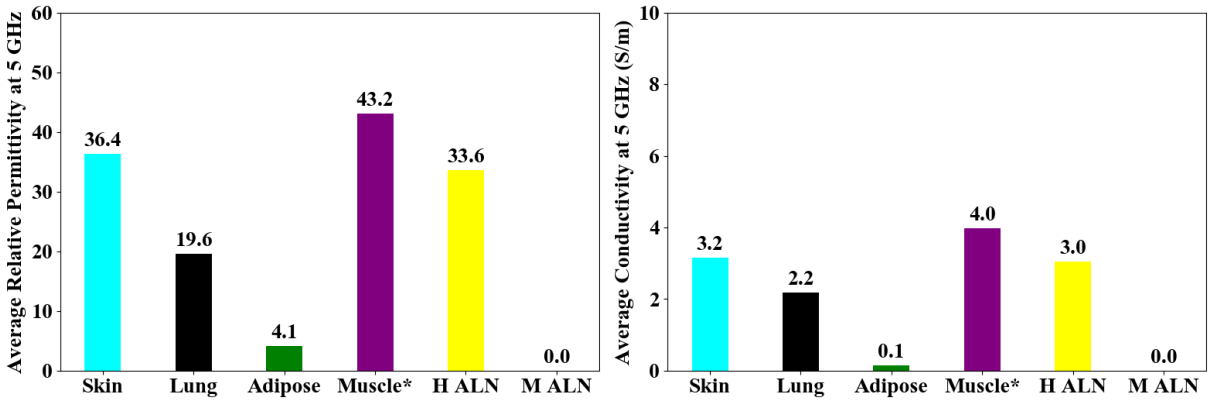

Figure E.8: Average (a) relative permittivity and (b) effective conductivity of each tissue type at 5 GHz considering MRI-intensity-based dielectric properties map. The asterisk (*) means that other tissue types may have been included in the calculation, such as fibroglandular tissue. H means Healthy and M means Metastasised.

F | Model AR_005

This appendix shows the details of the axillary region models AR_005 developed using the methodology presented in Chapter 4.

F.1 Patient Details

- Body Mass Index: 31
- Age: 67
- Approximate Skin Thickness: 3 mm

F.2 Right Axillary Region Model

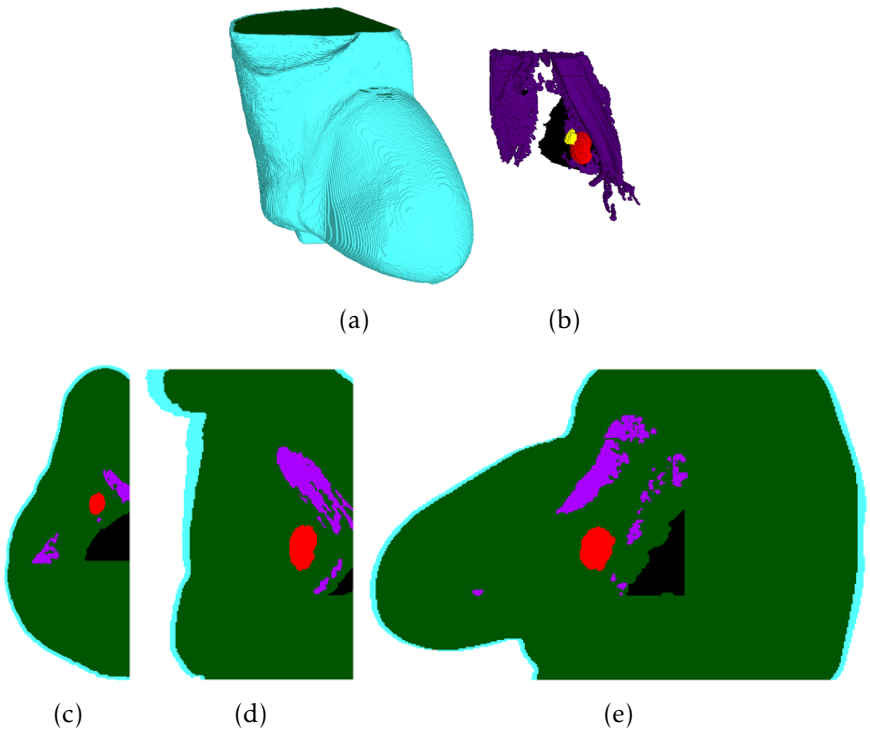

Figure F.1: Right axillary region model of AR_005 in: (a) 3D with all tissues, (b) 3D without skin nor adipose tissue, (c) axial, (d) coronal, and (e) sagittal planes. Blue represents the skin, green represents the adipose tissue, purple represents the muscle and fibroglandular tissue, black represents the lung cavity, yellow represents the healthy ALNs and red represents the metastasised ALNs.

- Available Files:
  1. AR_005_R_skin (.mat/.raw/.stl)
  2. AR_005_R_skin_filled (.stl)
  3. AR_005_R_adipose (.mat/.raw/.stl)
  4. AR_005_R_adipose_filled (.stl)
  5. AR_005_R_lung (.mat/.raw/.stl)
  6. AR_005_R_muscle (.mat/.raw/.stl)
  7. AR_005_R_h_aln (.mat/.raw/.stl)
  8. AR_005_R_m_aln (.mat/.raw/.stl)
  9. AR_005_R_label_map (.mat/.raw)
  10. AR_005_R_weight_map (.mat/.raw)
- Grid Size: $217 \times 443 \times 169$ (Axial × Coronal × Sagittal)
- Voxel Size: $0.9965 \times 0.9965 \times 1$ mm^3 (Axial × Coronal × Sagittal)
- Number of Healthy Lymph Nodes: 1
- Number of Metastasised Lymph Nodes: 1

F.2.1 Volume Ratios

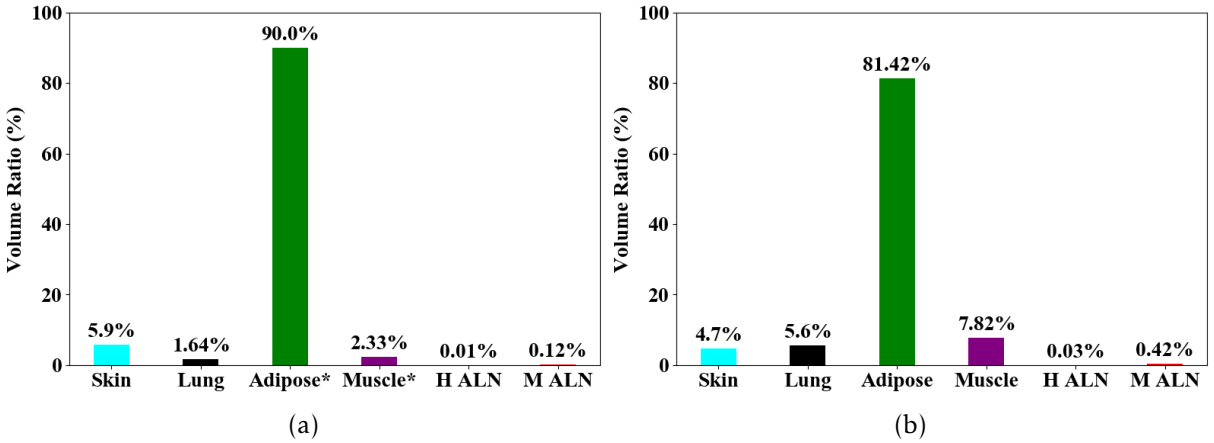

Figure F.2: Ratio between the volume of each tissue type and the total volume of: (a) the whole model and (b) restricted to the axillary region of AR_005. The asterisk (*) means that other tissue types may have been included in the calculation, such as fibroglandular tissue. H means Healthy and M means Metastasised.

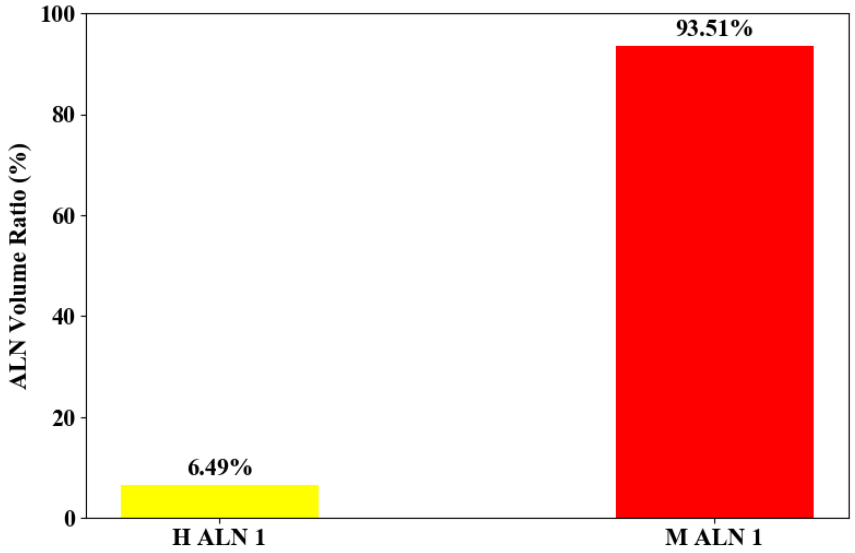

Figure F.3: Ratio between the volume of each ALN and the total volume of ALNs. H means Healthy and M means Metastasised.

F.2.2 Dielectric Properties

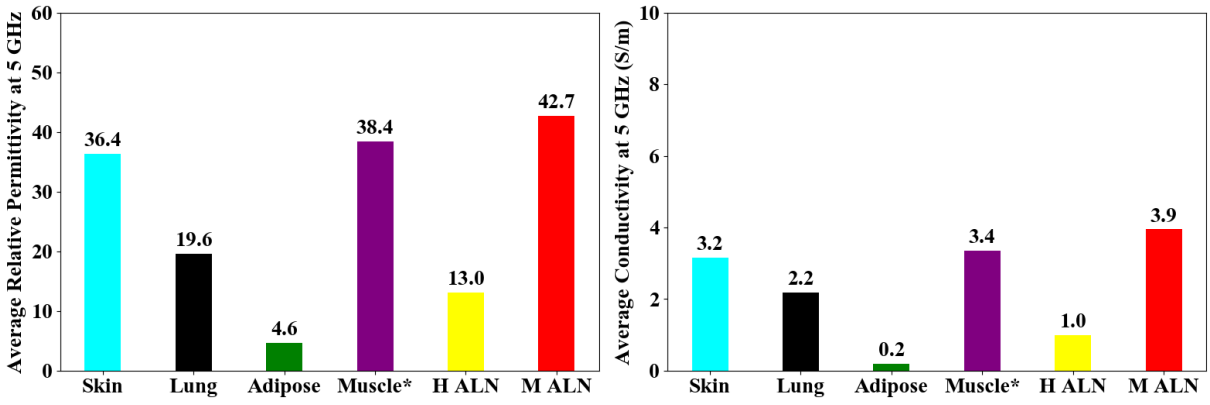

Figure F.4: Average (a) relative permittivity and (b) effective conductivity of each tissue type at 5 GHz considering MRI-intensity-based dielectric properties map. The asterisk (*) means that other tissue types may have been included in the calculation, such as fibroglandular tissue. H means Healthy and M means Metastasised.

F.3 Left Axillary Region Model

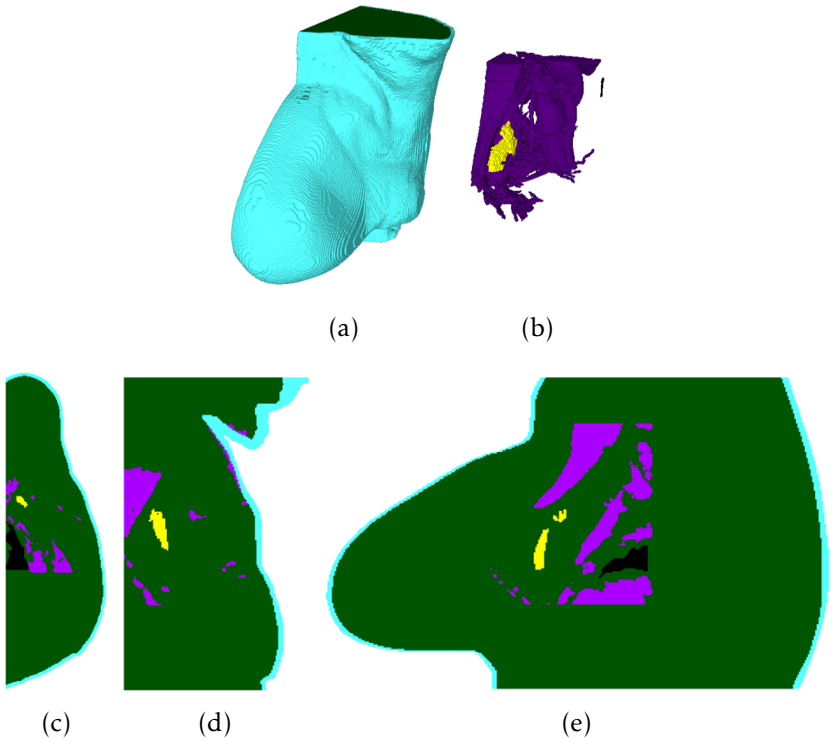

Figure F.5: Left axillary region model of AR_005 in: (a) 3D with all tissues, (b) 3D without skin nor adipose tissue, (c) axial, (d) coronal, and (e) sagittal planes. Blue represents the skin, green represents the adipose tissue, purple represents the muscle and fibroglandular tissue, black represents the lung cavity, and yellow represents the healthy ALNs.

- Available Files:
  1. AR_005_L_skin (.mat/.raw/.stl)
  2. AR_005_L_skin_filled (.stl)
  3. AR_005_L_adipose (.mat/.raw/.stl)
  4. AR_005_L_adipose_filled (.stl)
  5. AR_005_L_lung (.mat/.raw/.stl)
  6. AR_005_L_muscle (.mat/.raw/.stl)
  7. AR_005_L_h_aln (.mat/.raw/.stl)
  8. AR_005_L_label_map (.mat/.raw)
  9. AR_005_L_weight_map (.mat/.raw)
- Grid Size: $217 \times 443 \times 138$ (Axial × Coronal × Sagittal)
- Voxel Size: $0.9965 \times 0.9965 \times 1$ mm^3 (Axial × Coronal × Sagittal)
- Number of Healthy Lymph Nodes: 2
- Number of Metastasised Lymph Nodes: 0

F.3.1 Volume Ratios

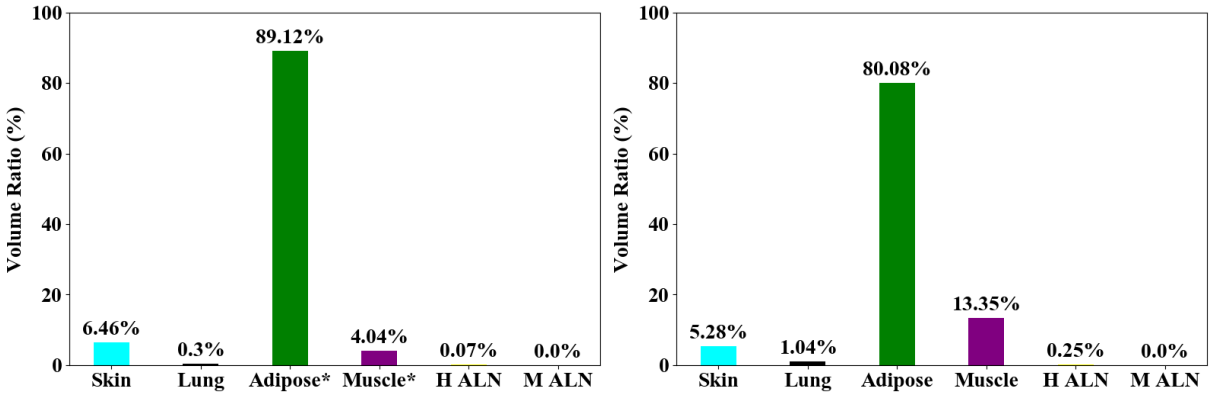

Figure F.6: Ratio between the volume of each tissue type and the total volume of: (a) the whole model and (b) restricted to the axillary region of AR_005. The asterisk (*) means that other tissue types may have been included in the calculation, such as fibroglandular tissue. H means Healthy and M means Metastasised.

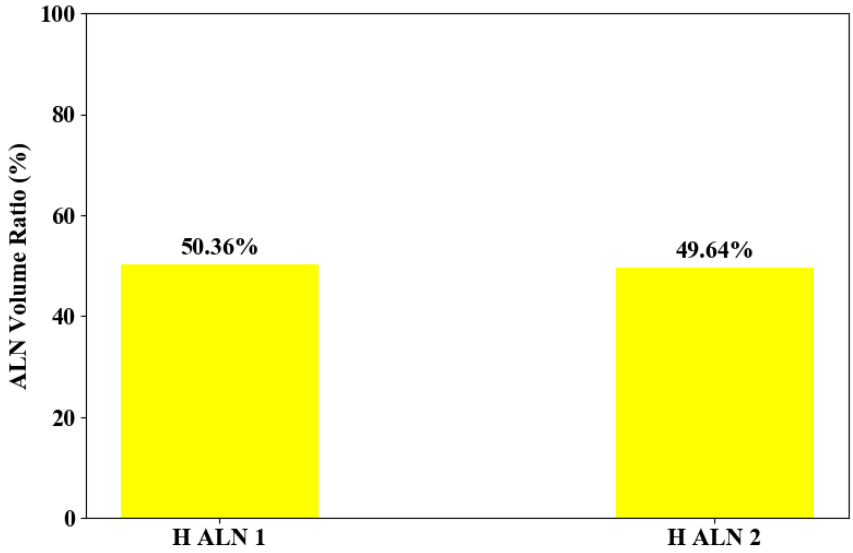

Figure F.7: Ratio between the volume of each ALN and the total volume of ALNs. H means Healthy.

F.3.2 Dielectric Properties

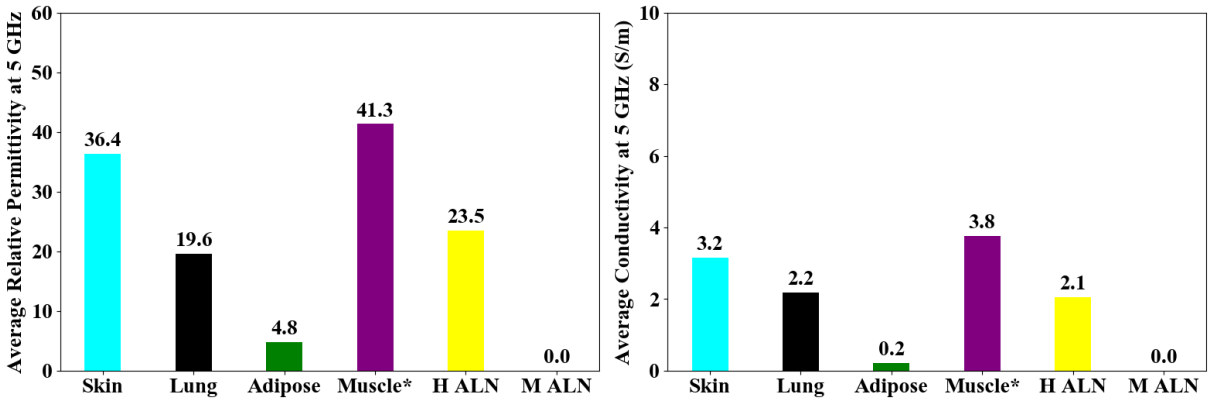

Figure F.8: Average (a) relative permittivity and (b) effective conductivity of each tissue type at 5 GHz considering MRI-intensity-based dielectric properties map. The asterisk (*) means that other tissue types may have been included in the calculation, such as fibroglandular tissue. H means Healthy and M means Metastasised.

G | Axillary Lymph Nodes Models Used for Machine Learning

This appendix shows images of all 60 Axillary Lymph Nodes (ALNs) models created for simulation of the reflected microwave signals, which were then used for classification between healthy and metastasised ALNs.

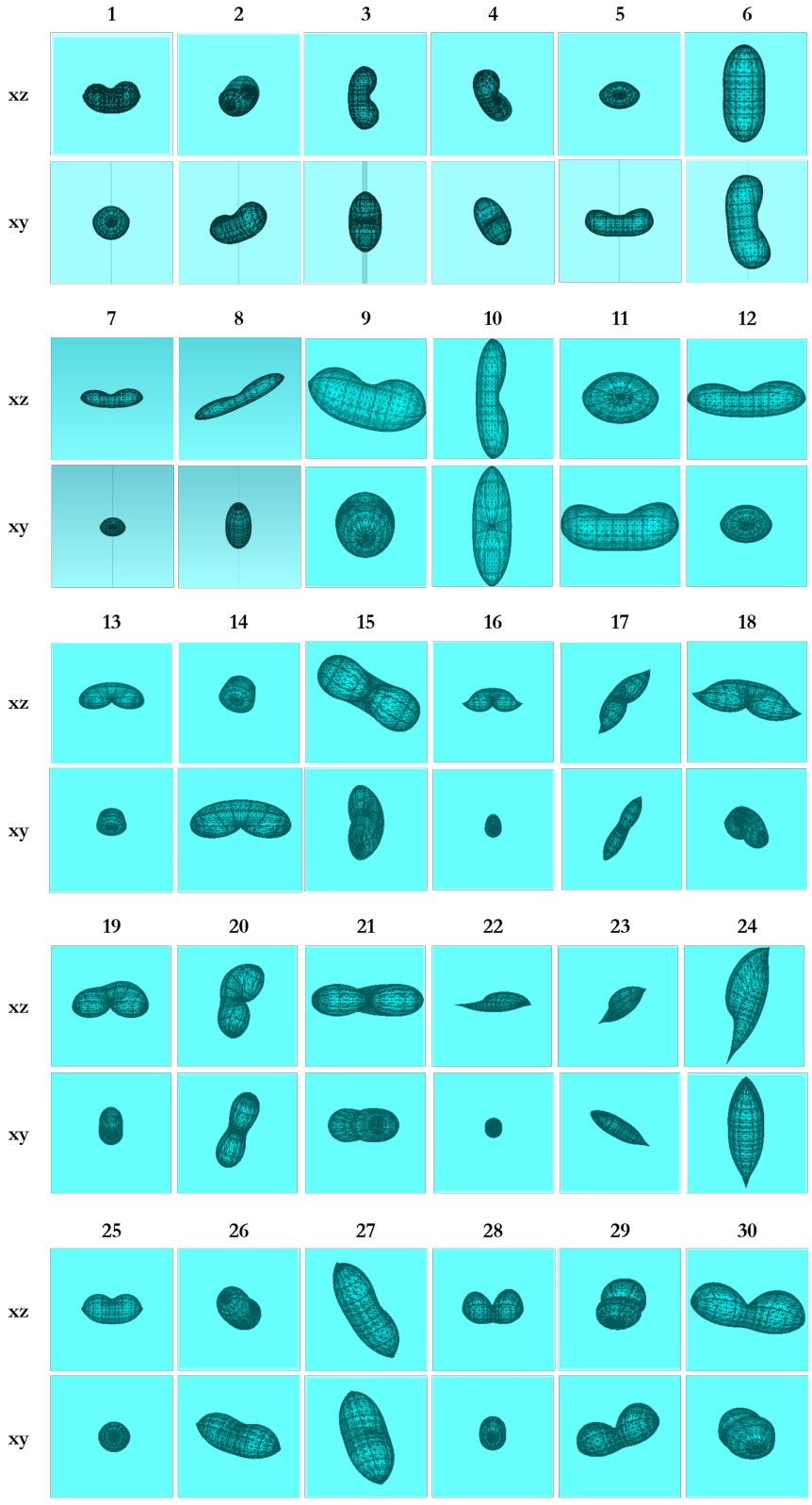

Figure G.1: Models of healthy ALNs in the *xz* and *xy*-planes of the setups reported in Chapter 6.

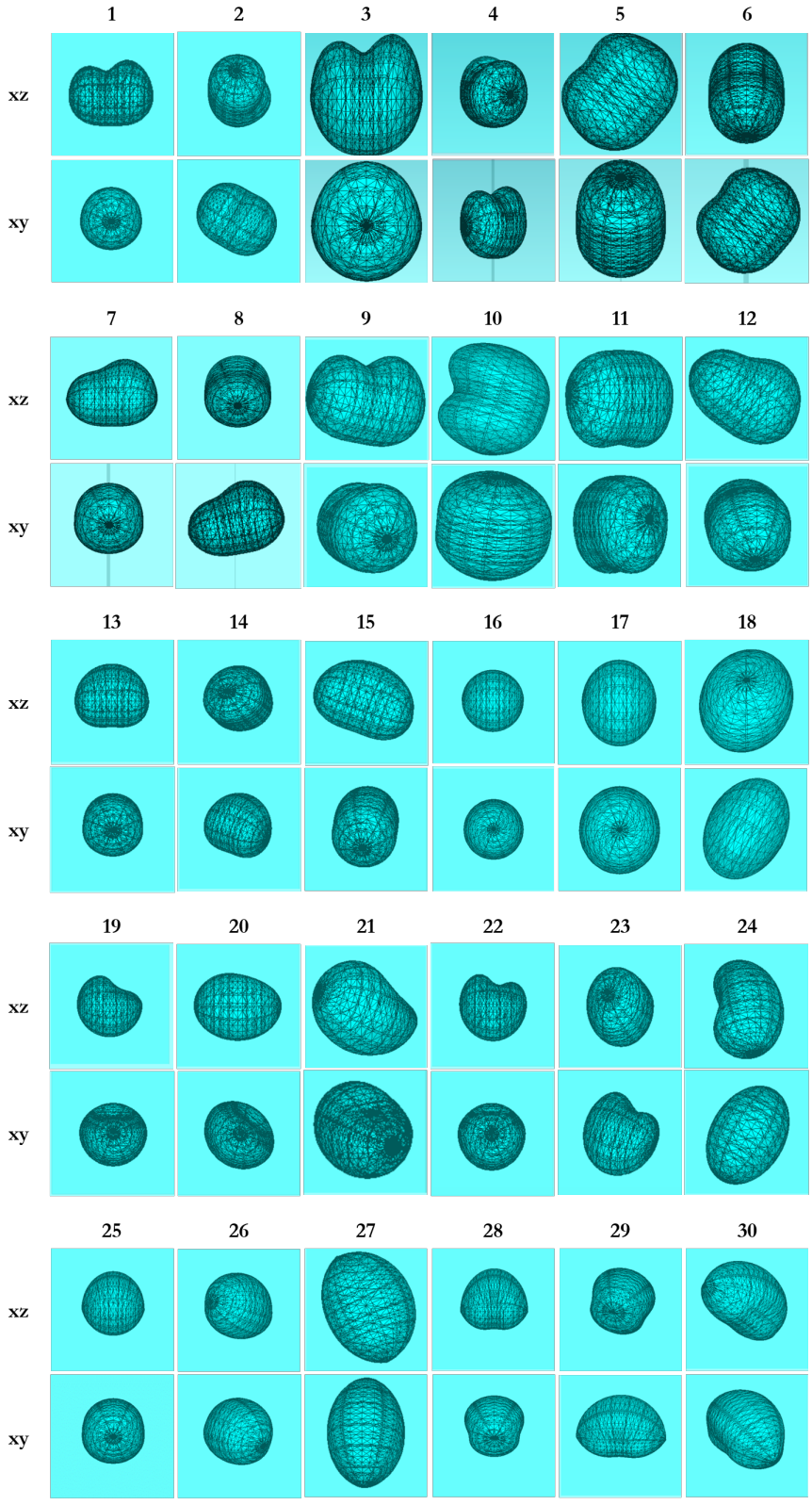

Figure G.2: Models of metastasised ALNs in the *xz* and *xy*-planes of the setups reported in Chapter 6.